January 2014

Experimental Study of the Displacements Caused by Cone Penetration in Sand

Mazhar Iqbal Arshad
Purdue University

Graduate School Form 30
(Revised 08/14)

PURDUE UNIVERSITY
GRADUATE SCHOOL
Thesis/Dissertation Acceptance

This is to certify that the thesis/dissertation prepared

By Mazhar Iqbal Arshad

Entitled
EXPERIMENTAL STUDY OF THE DISPLACEMENTS CAUSED BY CONE PENETRATION IN SAND

For the degree of Doctor of Philosophy

Is approved by the final examining committee:

Rodrigo Salgado
Chair

Monica Prezzi

Terry R. West

Steve Wereley

To the best of my knowledge and as understood by the student in the Thesis/Dissertation Agreement, Publication Delay, and Certification/Disclaimer (Graduate School Form 32), this thesis/dissertation adheres to the provisions of Purdue University's "Policy on Integrity in Research" and the use of copyrighted material.

Rodrigo Salgado
Approved by Major Professor(s): _____

Approved by: Dulcy Abraham 10/15/2014
Head of the Department Graduate Program Date

EXPERIMENTAL STUDY OF THE DISPLACEMENTS CAUSED BY CONE PENETRATION IN SAND

A Dissertation

Submitted to the Faculty

of

Purdue University

by

Mazhar Iqbal Arshad

In Partial Fulfillment of the

Requirements for the Degree

of

Doctor of Philosophy

December 2014

Purdue University

West Lafayette, Indiana

To my wife Farhat and Son Mustafa

ACKNOWLEDGEMENTS

First of all, I am thankful to Almighty Allah (God) for his enormous blessings and mercy that showered on me, without which it was possible to complete this research work.

I am extremely grateful to my advisor, Professor Rodrigo Salgado, for his instrumental guidance, a continued source of encouragement and support to the success of this work. I am also thankful to Professor Monica Prezzi for her continuous inspiration, valuable ideas and encouragement throughout this study. I also thankful to my advisory committee members, Professors Steve Wereley and Terry R. West for their kind help in reading the manuscript for short time. I am escpecially grateful to Professor Steve Wereley for his valuable guidance during conceptual stages of this work.

I am greatly indebted to the Pakistan Army Corps of Engineers for providing me the financial support for initial years of my graduate studies. I also acknowledge Professor Monica Prezzi for the financial support during last two years of my study.

I am grateful to all my colleagues and friends whom I work with, during my stay at Purdue. Especially, my thanks to Dr.Khalid Mehmood Arif, Faraz S. Tehrani and Kader Sener for their help during my course of study. I am extremely grateful to Mr. Nate Scaggs of Peerless Pattern Inc., for his extended support and help with economical fabrication of the testing facility; without his assistance, it would not have been possible. My sincere gratitudes for Geotechnical Secretary, Catherine Ralston, and Sharon Nemeth, of the business office, for facilitating and extending help for enormous procurement needed for the development of the DIC chamber testing facility.

I extend my special appreciations for my wife Farhat Sultana, for her continues support, encouragement, care, and prayers during my study tenure at purdue. I am also extremely thankful to my brother Mr. Mian Ijaz Rabbani for providing me morale and financial support. I especially thank and dedicate success in my life to my beloved wife and son Mustafa, who shared with me the demanding last semesters of my graduate study at Purdue.

TABLE OF CONTENTS

Page

Page

Page

Page

Page

LIST OF TABLES

LIST OF FIGURES

Figure Page

Figure Page

Figure Page

Figure Page

Figure Page

Figure Page

Figure Page

Figure Page

ABSTRACT

Arshad, Mazhar Iqbal. Ph.D., Purdue University, December 2014. Experimental Study of the Displacements caused by Cone Penetration in Sand. Major Professor: Rodrigo Salgado.

As more advanced theoretical methods become available for solution of the complex cone penetration (CPT) boundary-value problem, it is essential to develop methods to validate those solutions experimentally. A large scale model penetrometer testing facility, consisting of a half-circular calibration chamber with digital image correlation (DIC) capability, was developed for experimental simulation of cone penetration. The flat side of the chamber is transparent, made of Plexiglass. In individual tests, sand samples are prepared inside the half-circular chamber by pluviation; the half-circular cone is then pushed into the sand model flush against the Plexiglas, with the penetration process digitally imaged for DIC analysis. The displacement data obtained from DIC analysis provided valuable insights into the cone penetration boundary-value problem. Experiments with three different types of silica sands show that sand crushability influences the slip pattern around the advancing cone and also the cone penetration resistance. The derived strain paths show that very complex modes of deformation are experienced by the soil elements in close proximity of the penetrometer tip. The close-up imagery of the interface zone provided useful information for understanding the model penetrometer-sand interface behavior. The series of cone penetration tests conducted in layered sand profiles show that the sensing and development depths are dependent upon the position of weak and strong layers with respect to the direction of the advancing cone. The observed influence zone as interpreted from DIC analysis is smaller than stated in the literature.

CHAPTER 1. INTRODUCTION

1.1 Problem Statement

The cone penetration test (CPT) has gained tremendous importance in site characterization owing to its simplicity, speed, continuous soil profiling and well established cone resistance-based correlations for soil property estimation and pile design. Typically, the test is performed by hydraulically pushing a steel probe with 60° conical tip with a cross sectional area of 10 cm^2 at a standard penetration rate of 20 mm/s. During the penetration process, tip cone resistance (q_c) and sleeve friction (f_s) are measured continuously for soil profiling and engineering properties estimation. The soil classification and engineering properties are related to the measured tip cone resistance and sleeve friction developed through empirical, analytical or numerical means or a combination of these methods. Direct correlations are more appealing due to their simplicity, but most direct correlations have been developed empirically, which limits their general applicability.

Many researchers have worked on this problem, proposing various analytical and numerical solutions to predict cone penetration resistance in sands (e.g., Durgunoglu & J. K. Mitchell, 1976; Teh, 1987; Yu & Houlsby, 1991; Collins et al., 1992; Salgado, 1993; Berg et al., 1996; Susila & Hryciw, 2003; Huang et al., 2004; Tolooiyan & Gavin, 2011; Yu et al., 2012). Each of these solutions suffers from specific shortcomings (Salgado, 2013):

a. limit equilibrium-inspired solutions are speculative because of the absence of a free boundary where stresses are known and because of the need for assuming a slip mechanism in the immediate neighborhood of the cone;
b. cavity expansion solutions are themselves rigorous, but the calculation of penetration resistance from cavity limit pressure requires an approximation;
c. finite element analysis (FEA) requires modeling of soil-steel contact and must rigorously deal with the large mesh distortions that develop near the cone; to date, only simple soil models have been used and particle crushing has yet to be considered;
d. discrete element modeling (DEM) cannot handle a large domain and is limited in modeling particle shape and crushing.

As theoretical modeling of the cone penetration problem becomes more rigorous and produces accurate solutions of the cone penetration process, it is important to have companion experimental studies that can used to validate these theoretical solutions. In the past decade, particle image velocimetry (PIV) and digital image correlation (DIC) have gained attention in experimental geomechanics for modeling complex boundary value problems. Earlier work includes the use of the PIV technique to study the displacement of soil surrounding a model “pile” during penetration under plane-strain conditions White and Bolton (2004). In an attempt to model three-dimensional penetration, Liu (2010) performed centrifuge cone penetration tests under axisymmetric conditions combined with PIV image analysis. However, in most of the tests, deep penetration of the cone was accompanied by significant intrusion of sand particles between the cone and the transparent observation window, reducing the accuracy of the results to be useful in theoretical validation. Sophisticated experiments without these shortcomings are needed to produce reliable experimental data for validation of theoretical aspects of the problem.

1.2 Research Objectives

The main goal of the present research was to develop a sophisticated test facility for experimental simulation of the cone penetration process. The scope of the research work presented in this thesis includes:

1. Design and development of the half-circular calibration chamber with capability for image acquisition during half-cone penetration. This task was subdivided into :
    - Design and develop half-circular model probes with suitable instrumentation;
    - Develop a surcharge system for application of stress on top of the sample;
    - Develop a dedicated image acquisition system for imaging of the penetration process.
2. Study the displacements caused by cone penetration in uniform and layered sands in order to:
    - Visualize and understand the cone penetration process in uniform sand;
    - Investigate the development of cone penetration resistance when cone passes between two layers.

1.3 Thesis Outline

This thesis consists of eight chapters. The outline of each chapter is as follows:

Chapter 2 presents a comprehensive literature review of studies of cone penetration resistance in uniform and layered soil. The methods of CPT-based prediction of pile design are presented.

Chapter 3 presents the details of the experimental methodology adopted.

Chapter 4 provides the details of the development and design aspects of the half-circular calibration chamber testing facility.

Chapter 5 discusses the testing program.

Chapter 6 presents the model penetrometer test results in uniform sand with different densities, sand type and penetrometer type.

Chapter 7 discussed the development of cone penetration resistance in layered sand samples and Chapter 8 summarizes the conclusions drawn from this research and makes recommendations for future work.

CHAPTER 2. LITERATURE REVIEW

2.1 Introduction

Salgado (2013) reviewed theoretical and experimental studies of cone penetration, and the first half of this chapter follows closely that publication. The basic aim of site investigation is to gain knowledge of a soil profile and obtain relevant soil properties for economical and reliable geotechnical design. Specifically with respect to the solution of piling engineering problem, two approaches are common in practice: one direct design based on in-situ testing and indirect design based on theoretical, experimental or empirical correlations between soil properties and in-situ and/or laboratory testing. Among the available in-situ test methods, the cone penetration test (CPT) is one of the most commonly used site investigation tools. The CPT is not only useful in continuous soil profiling but in the design of foundation elements. For pile analysis and design, CPT-based direct methods are most appealing due to their simplicity. These are often empirical or semi-empirical correlations relating the cone resistance to pile resistance. This approach has the limitation that correlations are developed by relating the pile load tests to cone resistance under specific soil conditions. They may not be suitable to other soil types involves or conditions. A general applicable approach would be one in which correlations were developed based upon sound theoretical solutions for prediction of cone penetration and pile resistance. For this more refined interpretation of the soil CPT profile, a rigorous theoretical and experimental research is needed. The apparent simple problem of the CPT actually hides considerable complexity. This complexity arises due to the complexity of cone penetration process itself, which involves a large-displacements, and large strains and induces significant shearing and very large stresses in the soil.

Rigorous solution of such a boundary-value problem requires sophisticated algorithms and an equally sophisticated constitutive model to capture the response of the soil. Because of these extreme challenges, various types of simplifications of the problem have been adopted. These challenges also invite high-quality experimental work to validate the theoretical work or produce alternatives on its own. In this chapter, we will review the theoretical and experimental work undertaken for solution of CPT boundary-value problems and their prediction of cone and pile resistance in uniform and layered soil profile.

2.1.1 Cone Penetration Test (CPT)

The cone penetration test (CPT) was early used in the 1930s in the Netherlands for the assessment of bearing layers for pile foundations. The cone penetration test (CPT) is now one of the most widely used test for continuous soil profiling and in situ determination of soil properties. Typically the test is performed by hydraulically pushing a steel probe with 60 degree conical tip at the end and a cross sectional area of 10 cm^2 at a standard penetration rate of 20 mm/s. During the penetration process, tip cone resistance (q_c) and sleeve friction (f_s) are measured continuously. The CPT equipment has undergone tremendous development, and wide range of sensors is available today for special soil parameter estimation. The standard measurements are cone tip resistance and sleeve friction. The components of an electrical cone are shown in figure 2.1.

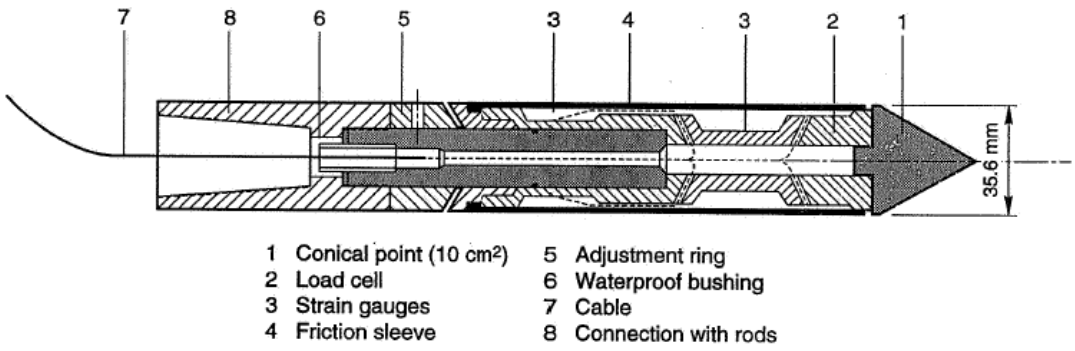

(a)

(b)

Figure 2.1(a) Components of electrical cone (deRuiter, 1971), and (b) Purdue CPT rig.

2.2 Cone Resistance Predictions

2.2.1 Theoretical Methods

Yu and Mitchell (1998) and Salgado (2012) have given the detailed review of previous theoretical and experimental works undertaken for solution of CPT boundary-value problem. We will here briefly discuss various theoretical approaches used for prediction of cone penetration resistance.

2.2.1.1 Bearing Capacity Methods

Analysis of the cone penetration process was first regarded as a bearing capacity problem. In bearing capacity approach, the collapse load of a deep circular foundation in the soil is assumed to be equal to its cone resistance. Limit equilibrium and slip-line analysis approaches were used to determine the collapse load.

2.2.1.1.1 Limit Equilibrium

In the limit equilibrium method, firstly the failure mechanism is assumed and then the global equilibrium in the soil mass is sought in order to derive the collapse load (Yu & Mitchell, 1998). The soil is modeled as rigid-plastic material with a yield criterion such as Tresca or Mohr-Coulomb criterion for derivation of the limit load. The equilibrium condition and the yield criterion satisfy only along the slip surface. The shape factor is introduced to relate the collapse load to cone penetration resistance.

2.2.1.1.2 Slip Line Method

In the slip-line method, as stated by Yu and Mitchell (1998), the plastic equilibrium is sought in soil mass using a yield criterion such as the Mohr-Coulomb or Tresca criterion and associated equations of equilibrium. This plastic equilibrium yields the basic differential equilibrium equations of the problem. A slip-line network on the basis of slip-line field theory is constructed from the derived differential equations and then the collapse load is obtained.

A major limitation of bearing capacity methods is that they do not take account for real soil stress-strain and volumetric behaviors.

2.2.1.2 Cavity Expansion Methods

In this method, the cone penetration is considered as deep indentation problem, in which the pressure required to indent on elastic-plastic medium is proportional to that required to expand the cavity of cone volume under same conditions. Two steps are needed to predict the cone resistance from the cavity expansion pressure: first is cavity creation or limit pressure must be computed, then limit pressure must be related to cone resistance (Salgado, 2012).

Earlier cavity expansion analysis in sand (Vesic, 1972; Ladanyi & Johnston, 1974) were based on linear elastic-plastic model with a von Mises failure criteria. Cavity expansion analyses involving more realistic soil stress-strain models in sand have been done in recent past (notably, Yu & Carter, 2006; Yu & Houlsby, 1991; Collins et. al., 1992; Salgado, 1993; Salgado & Randolph, 2001).

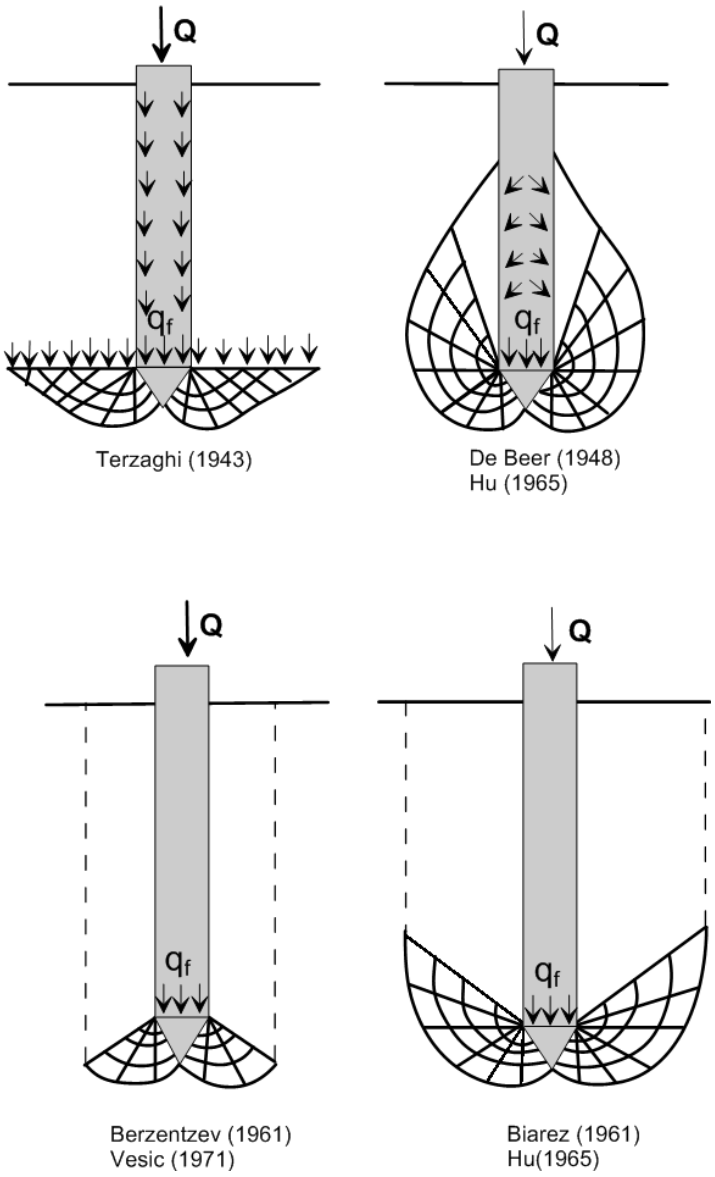

Figure 2.2 Assumed failure mechanisms for deep penetration (Durgunoglu & Mitchell, 1976)

Most recently, Salgado and Prezzi (2007) presented a concise cone penetration resistance analysis, in which limit pressure is calculated using the cavity expansion analysis of Salgado and Randolph (2001) and cone resistance is calculated from cavity limit pressure considering the true interface friction angle between the cone and soil and considering the stress rotation around the cone during the penetration process. At present, rigorous analysis of cavity expansion is possible. However, some approximation is introduced in the step of relating the cone resistance to the limit pressure obtained in cavity expansion analysis. As indicated by Salgado (2012), there is no consensus in the literature on how to link the cavity limit pressure to cone resistance. Some advocate direct use of spherical cavity limit pressure (Ladanyi & Johnson 1974). Mitchell and Keaveny (1986) suggested that the cylindrical cavity limit pressure gives a better prediction for cone penetration resistance for less compressible soils and spherical limit pressure better approximates it for more compressible soils. Table 2.1 presents some relationships that have been proposed to relate cavity expansion pressure to cone resistance, and Figure 2.3 shows the assumed failure mechanism adopted in derivation of these relationships.

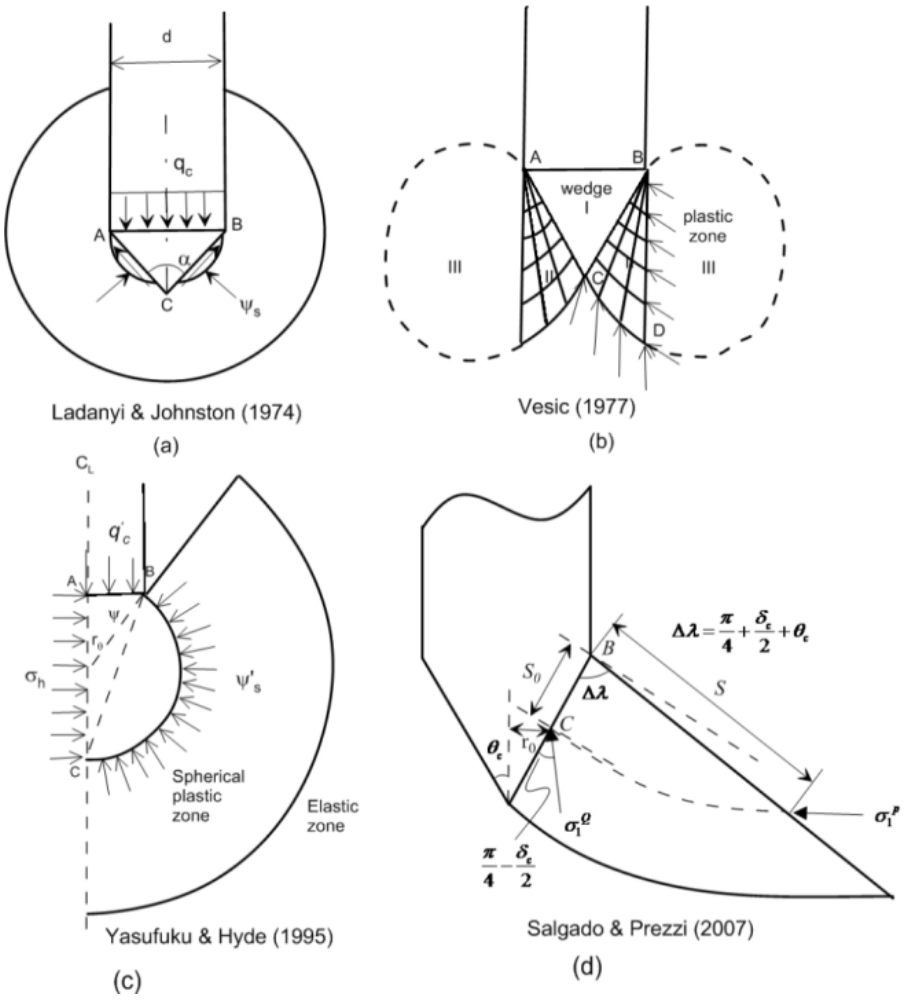

Figure 2.3 Assumed mechanisms of cone penetration (Yu and Mitchell 1998; Salgado and Prezzi, 2007)

Table 2.1 Summary of cavity expansion solutions (Yu and Mitchell, 1998).

Authors	Methods and Assumptions	Main Conclusions
Ladanyi & Jaohnson (1974)	The normal stress on the cone face is assumed to equal to spherical cavity limit pressure as shown in Figure 2.4(a)	$q_c' = N_q.\sigma_{v0}'$ where $N_q = \frac{(1+2K_0)A}{3}[1+\sqrt{3}\tan(\lambda\phi')]$ q_c' : Cone Resistance ; N_q : Cone Factor σ_{v0}' : Vertical effective stress A: $P_{limit} / \sigma_{mean}'$ λ : Cone roughness factor ϕ' : Effective friction angle
Vesic (1972,1977); Chem &Juang (1996)	The cone resistance is related to spherical cavity limit pressure with assumed failure mechanism of Figure 2.4 (b)	$N_q = \left(\frac{1+2K_0}{3-\sin(\phi')}\right)\exp[(\pi/2-\phi')\tan(\phi')]$ $\times\tan^2(45+\frac{\phi'}{2})(I_{rr})^n$
Yasufuku & Hyde (1995)	Cone resistance is related to spherical limit pressure in for compressible sand using simple failure mechanism Figure 2.4(c)	$N_q = \frac{(1+2K_0)A}{3(1-\sin\phi')}$
Salgado & Prezzi (2007)	Cone resistance is related for freshly deposited uncemented silica sand to the cylindrical cavity expansion using the slip pattern of Figure 2.4(d).	$\frac{q_c}{p_A} = 1.64\exp\left[0.1041\phi_c + (0.0264-0.0002\phi_c)D_R\right]\left(\frac{\sigma_h'}{p_A}\right)^{0.841-0.0047D_R}$ P_A: Reference stress ϕ_c: critical state friction angle D_R: Relative density σ_h: Lateral effective stress

2.2.1.3 Strain Path Methods

Baligh (1985) first proposed the strain path method, which considers the cone penetration problem as a steady-state flow problem that may be viewed from the perspective of the cone as soil flowing past the penetrometer. The soil is considered a viscous fluid, and the flow field is established from a potential function that does not depend on strength, only on relative positions from the cone tip. The key assumption of the method is that the streamlines can be estimated around the penetrating cone without rigorous consideration of the constitutive behavior of the soil because the problem is kinematically over constrained. This is more applicable to un-drained penetration in clays, where the volume conservation holds well, whereas, in drained penetration in sands,

estimating streamlines is difficult due to dilatant/contractive behavior of sands. Figure 2.4 shows the strain contours around a 60-degree cone derived using strain path method (Teh, 1987).

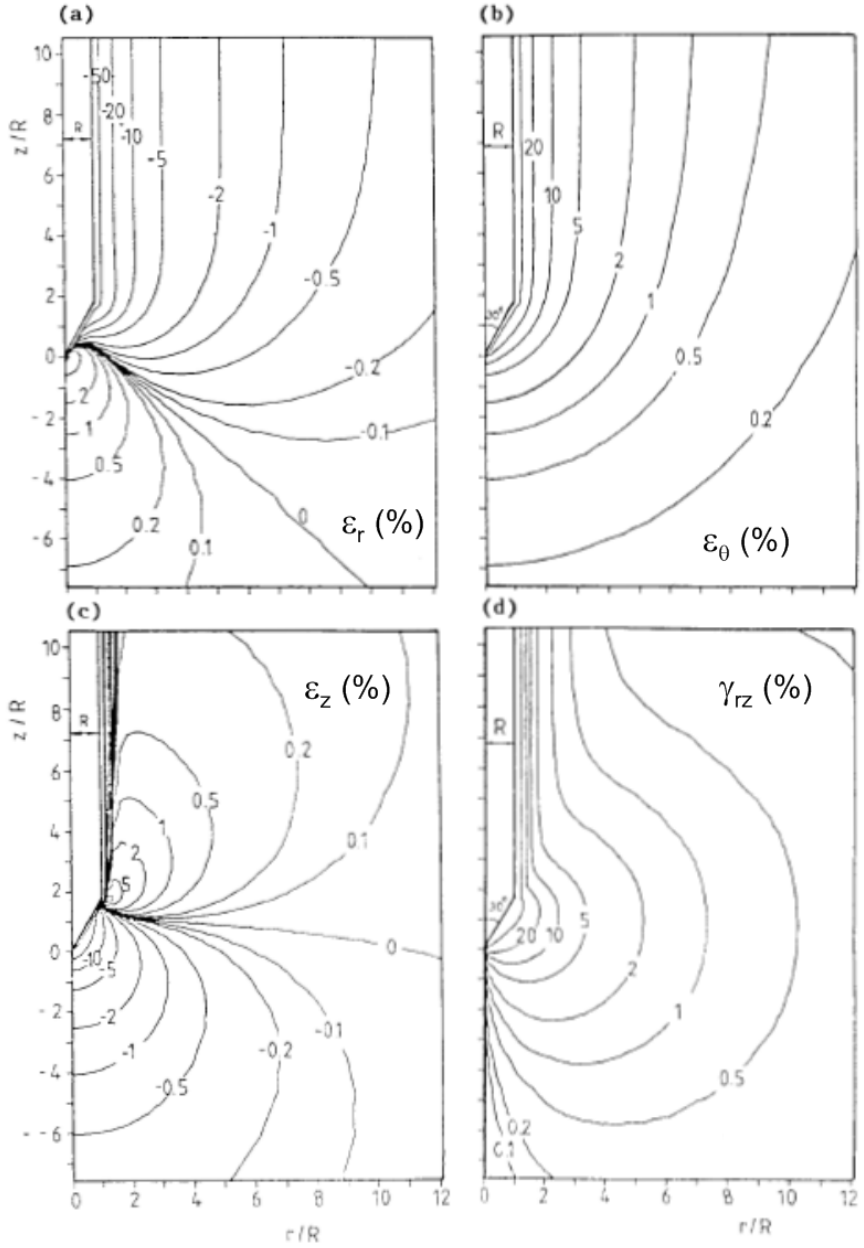

Figure 2.4 Strain contours around a 60-degree penetrometer (Teh, 1987)

2.2.1.4 Finite Element Methods

Cone penetration involves large deformation of the soil and significant shearing at the interface between the soil and the penetrometer. The stresses associated with cone/pile penetration are extremely large (BCP Comittee, 1971) inducing particle crushing coupled with large deformation. Modeling of the cone penetration problem in a rigorous manner requires an accurate modeling of the interface between the cone and soil, the modeling of the large shear deformation around the cone, and of the particle crushing behavior near the cone-soil interface.

Modeling large deformation associated with cone penetration problem, involves large distortion of the mesh, which can affect the accuracy of the results or even not produce any. To overcome this difficulty of mesh distortions, various approaches have been adopted. Berg,et.el. (1996) used the Eulerian formulation of cone penetration problem, in that the cone was modeled as fixed boundary in a pre-bored hole and the soil moves upward as in strain path method. As the material stream upward it gets displaced by the fixed cone and corresponding stresses and strains are calculated till steady state is reached. As indicated by Salgado (2012) the Eulerian formulation has the shortcoming that it cannot easily handle boundaries that may be moving across the mesh.

Huang et al. (2004) used updated Lagrangian approach and performed displacement controlled finite element analysis. The soil behavior was modeled using a simple elastic-perfectly plastic Mohr-Columb yield criterion. Finite sliding frictional contact was used to model the penetrometer soil interface.

Susila & Hryciw (2003) and Tolooiyan & Gavin (2011) used the arbitrary Lagrangian-Eurliean (ALE) formulation in their finite element analyses. Both used the Drucker-Prager yield criterion. The cone tip interface was modeled by master-slave kinematic contact algorithm. The frictional resistance was considered along cone tip and sleeve. The interface friction angle (δ) was taken as 50% of the critical state friction angle.

Ahmadi (2000) performed cone penetration using finite difference technique using FLAC with updated Lagrangian approach. The radial and vertical displacements were specified at cone-soil interface nodes to create the cavity for cone. A simple Mohr

Coulomb elastic-plastic soil model was used and the interface friction between cone and soil was not considered ($\delta=0$) in their analysis.

All numerical studies so far have relied on simple soil models. Interface modeling was mostly neglected. The particle crushing behavior modeling as observed below the pile/penetrometer (White & Bolton, 2004) was not accounted for in any of these studies. Moreover, no experimental solution to the cone penetration boundary-value problem exists to compare theoretical solutions against.

2.2.1.5 The Discrete Element Method (DEM)

Discrete Element Method (DEM) has also been used to study the cone penetration problem. The DEM is based upon particulate mechanics with the equation of motion solved for individual particle contact forces. The properties are characterized by diameter, mass and density. The inter-particle contact is modeled through normal and shear stiffness and damping. Huang et al. (1993) coupled the DEM and the boundary element method (BEM) to study the cone penetration in 2D axi-symmetry of the problem. The cone size was 5 mm in radius and soil particles were modeled as disks with 0.8 mm diameter.

The shortcoming of DEM analysis is that it is computationally intensive (Yu et al., 2012); therefore these analyses are performed for reduced model domains, which means that there are scale effects. The other aspect is that soil particles are not spheres and the shape of particles will affect the inter-particle contact forces.

2.2.2 Experimental Methods

2.2.2.1 Calibration Chamber Testing

Calibration chamber testing provides an effective way for study the cone penetration resistance in sand. In calibration chamber test a large cylindrical sand sample is prepared under controlled condition and CPT is performed to develop the empirical correlations between cone resistance and various soil properties. Calibration chamber testing is performed in four steps (Salgado,1993, 2013);

- Soil sample preparation (air pluviation is the standard method of sample preparation)
- Consolidation (application of stress boundary conditions)
- Cone penetration testing
- Disassembling

The sample is prepared by air pluviation method, the desired density is achieved by controlling the sand deposition rate and fall height. There are two types of calibration chamber, one type has flexible walls sample housed by rubber membrane, to which lateral is applied. The other type of calibration chamber has rigid walls, with lateral displacement not allowed. Depending on the chamber, four different types of boundary conditions can be applied in a test (Salgado, 2012), as shown in table 2.2.

There are three types of empirical correlations developed as result of calibration chamber testing (Yu and Mitchell, 1998): (1) correlation in terms of relative density; (2) correlation in terms of friction angle; and (3) correlation in terms of state parameter.

Table 2.2 Calibration chamber boundary conditions (Salgado, et.al 1998)

Boundary Condition	Lateral	Top/Bottom
BC1	Constant Stress	Constant Stress
BC2	Strain = 0	Strain = Zero
BC3	Strain = 0	Constant Stress
BC4	Constant Stress	Strain = 0

According to Salgado (2013) relationship to cone resistance to soil state and intrinsic variables is:

$$q_c = \mathbf{q_c}\,(D_R, \sigma'_h, \text{intrinsic properties, structure}) \qquad (2\text{-}1)$$

The cone resistance increases with increase of relative density and horizontal effective stress. The cone resistance also strongly depends upon the soil intrinsic variables such as the critical state friction angle and particle compressibility and crushability. The cone resistance increases with increasing critical-state friction angle and

decreases with increasing compressibility/crushability. Other soil structure parameters such as fabric and cementation, also affect the cone resistance. Table 2.3 shows summary of various correlations proposed based upon the calibration chamber testing. The major limitation of these correlations is that they are based upon clean, freshly deposited sand. Another fact is that the calibration chamber is of limited size, and there are chamber size and boundary effects on measured cone resistance. The cone resistance measured in the calibration chamber differs from that in the field, with the magnitude of the difference depending upon boundary type and soil initial state. Various correlations have been developed to link the cone resistance in calibration chamber to the cone resistance in the field (Salgado et al., 1998; Mayne & Kulhawy, 1991; Pournaghiazar et al., 2012).

Table 2.3 Summary of empirical correlations for cone resistance

Authors	Methods and Assumptions	Cone Resistance or Cone Factor
Houlsby & Hitchman(1988)	The cone resistance is assumed to be dependent upon horizontal stress and density	$\frac{q_c}{P_A} = A(\frac{\sigma'_{h0}}{P_A})^{0.6}$ q_c : Cone Resistance σ'_{h0} : horizontal effective stress A: Density dependant coeficient
Jamiolkowski (1988)	The cone resistance is assumed to be mainly dependent of mean stress and soil density	$q_c = \frac{205}{P_A}(\frac{\sigma'_m}{P_A})^{0.51}\exp(\frac{2.93D_R}{100})$ $\sigma'_m = \frac{1}{3}(\sigma'_{v0} + 2\sigma'_{h0})$
Houlsby & Hitchman(1988)	The cone resistance is assumed to be primarily dependent upon horizontal stress and soil friction angle	$q_c = \sigma'_{ho}\exp\left[0.16(\phi' - 9^\circ)\right]$ σ'_{ho} = Initial horizontal stress ϕ' = Peak friction angle
Been et al. (1987)	The cone resistance is assumed to be dependent upon mean effective stress and soil state parameter	$q_c = N_q \cdot \sigma'_{vo}$ $N_q = \frac{1+2K_0}{3}[1 + K\exp(-m\xi)]$ ξ = State parameter
Yu et al. (1996)	The cone resistance is dependent upon cylindrical cavity limit pressure and soil state parameter	$\frac{q_c}{\psi'_{\lim}} = \exp(1.542 - 3.37\xi)$

2.2.2.2 Centrifuge Testing

No correlation for cone resistance has been developed from centrifuge testing. Most of the focus in centrifuge testing has been on investigation of the boundary and particle scale effects, stress normalization (Gui, et al., 1998) and the dependence of penetration resistance on rate on penetration resistance. There are two limitations of centrifuge testing: first, very fine sand is used to maintain the similitude conditions that limits their field applicability; second, particle size effects come in play in centrifuge through the dilation process in shear bands (Foray, 1991, Bałachowski, 2007, Loukidis & Salgado, 2008, Salgado, 2013). Balachowski (2007) investigated the particle size effects by using a single cone penetrometer, with two different gradations of sand with the same mineralogy with three different stress levels. He concluded that no significant effect is likely present if the ratio of the model cone diameter to D_{50} exceeds 20.

Bolton & Gui (1993) and Bałachowski (2007) studied the size effects and concluded that the diameter ratio of container to cone (D/dc) should be greater than 40 to avoid any size effects.

2.2.3 Penetration Resistance in Layered Soil

In case of layered soil, the penetration resistance may be affected near interfaces between weak and strong layers. There is some penetration depth required for the cone to fully develop the cone resistance that would be expected for given layer. In this section, we will review how this problem of penetration resistance in layered soil has been studied both from the experimental and theoretical points of view.

2.2.3.1 Calibration Chamber Testing

There are very few studies conducted in calibration chambers to investigate layering effects. P. van den Berg (1994) studied the penetration resistance in two-layered soil in a rectangular glass chamber of size 400 x 400 x1000 mm without surcharge for validation of their numerical analysis. Two experiments were reported, with kaolin clay over Eastern Scheldt sand and sand over clay. A standard 36mm-diameter cone was used at the center of the chamber with penetration rate of 2 cm/sec. Their results show that the

cone senses the strong sand layer at a distance of 0.5 diameters from the interface and requires 5-6 cone diameters penetration beyond the interface to reach steady-state cone resistance. In sand over soft clay, the cone senses the soft clay layer 4-5 cone diameter ahead of the interface and requires a penetration of 2-3 times the cone diameter below the interface to reach steady state. Figure 2.5 shows the cone resistance profiles of their tests. Results were affected by the fact the penetration is shallow and by size effects.

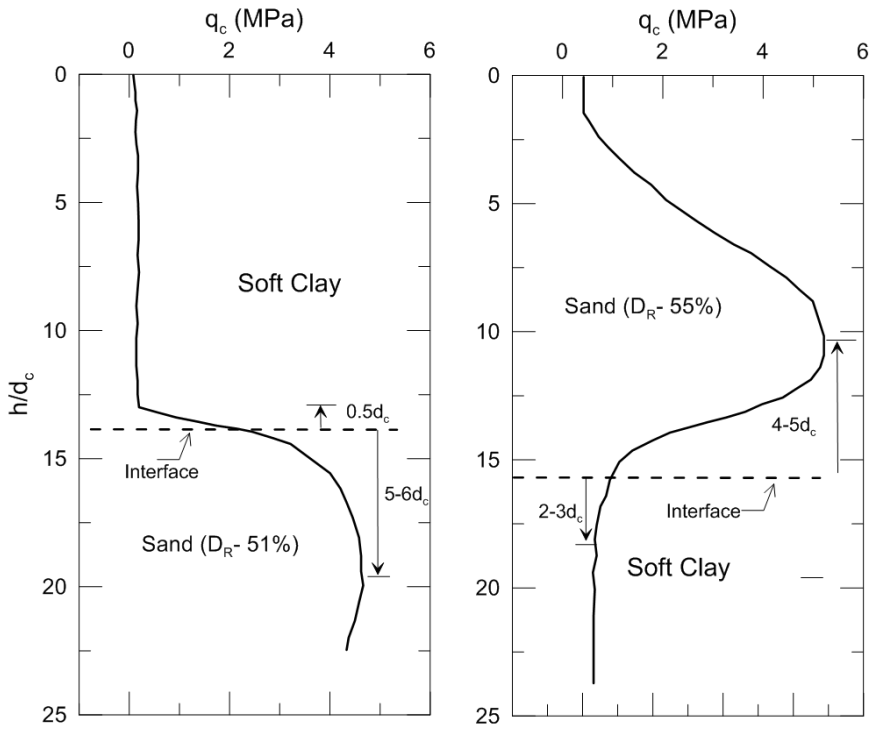

Figure 2.5 Penetration resistance in layered soil (P. van den Berg, 1994)

Houlsby et al. (1988) conducted calibration chamber tests to study the effect of artificial cementation in carbonate sand on model pile bearing resistance. Jacked and preinstalled model pile tests were performed. The tests were terminated on rupture of the cemented sand layer, thus no insight on development of base resistance beyond that is available. They concluded that the model pile senses the cemented strong layer at a distance of 2.5 pile diameters ahead of the interface. The increase in thickness of the strong cemented layer increases the base resistance. The tests conducted with different stress level show no effect of stress on pile sensing distance.

2.2.3.2 Centrifuge Testing

A few centrifuge tests have been conducted to investigate the cone resistance development in layered soil profiles. Gui et al. (1998) conducted a series of cone uplift tests to investigate the development depth in a uniform sand layer. They concluded that a penetration of 5 cone diameters is required to develop the steady-state cone resistance in uniform layer, irrespective of penetration direction.

Xu & Lehane (2008) performed a total of four centrifuge tests with flat end penetrometer in three two-layer soil samples and one three layer sample. Two samples were of two layers with silica sand having different densities. One test was with three layeres of sand with different densities and one test with clay underlying saturated sand. Their results indicate that the cone sensing and development depths are different depending upon the orientatin of weak and strong layer. As shown in Figure 2.6 the sensing depth varies from 2 to 8 diameters for the sand samples, depending on sand densities, and 14 diameters for the sample with sand and clay layers. The development depth ranges from 2 to 6 diameters for sand samples but is about 1 diameter for the sand over clay sample. The sensing and development depths were found to be affected by the direction of penetration (from weak layer to strong layer and vice versa).

2.2.3.3 Theoretical Studies

Study of the effect of layering has mostly been attempted through analytical and finite element methods. An early analytical attempt was to predict the cone resistance in layered soil based upon Boussinesq's half space elastic deformation solution (Vreugdenhil et al., 1994). The authors predicted the cone resistance in multi layered system depending upon elastic shear stiffness ratios of these layers, by considering the displacement compatibility of the interfaces. Their analysis neglected the plastic deformation developed during cone penetration.

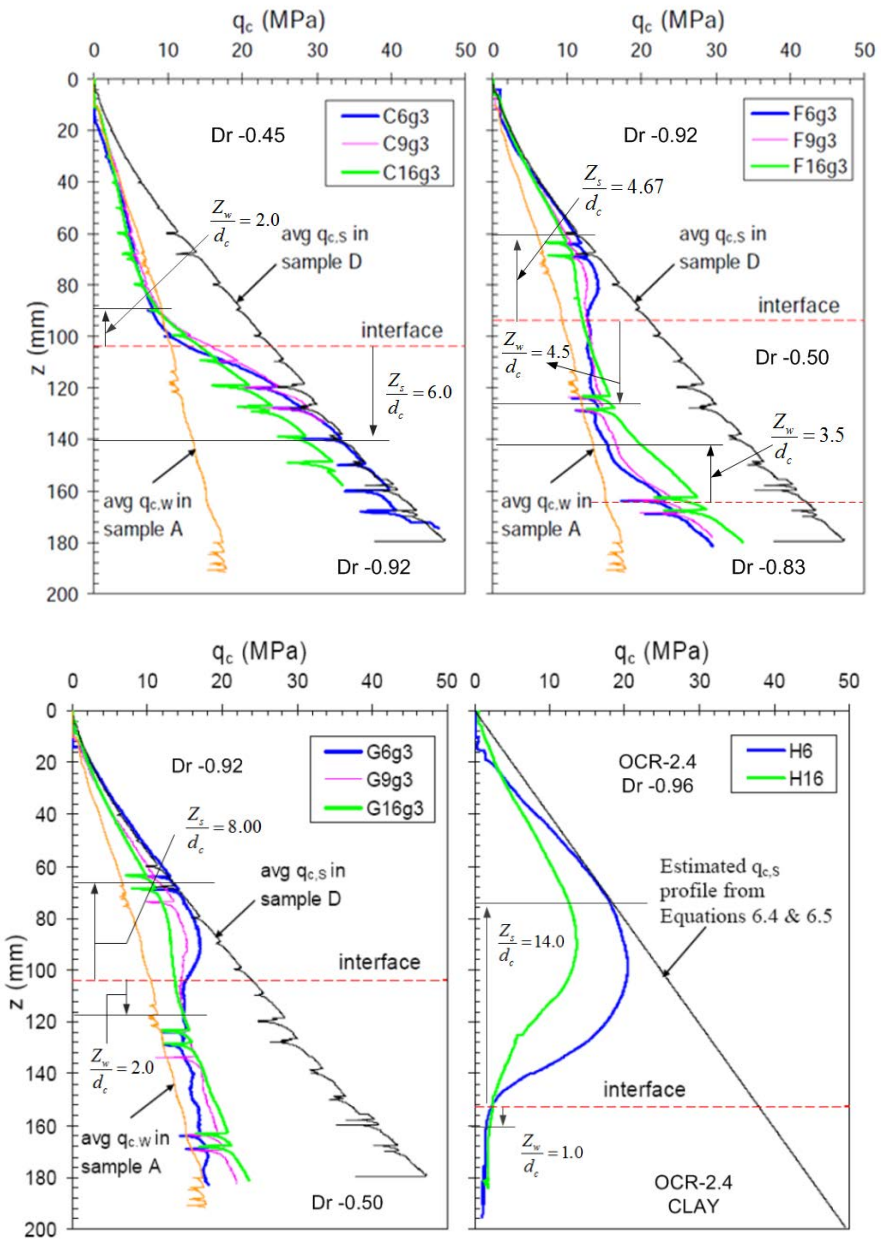

Figure 2.6 Sensing and development depth in layered soil profile (Xu, 2007)

Yang (2006) study the influence zone for base resistance of pile in clean and silty sand using spherical cavity expansion analysis. The author assumed a failure pattern similar to that of Yasufuku & Hyde (1995) as shown in Figure 2.7. The analytical relationships for influence zone above and below the pile tip were proposed from spherical cavity limit pressure. It was concluded that, in clean sand, the influence zone below the pile tip is 5.5 times the pile diameter and is 2.5 times the pile diameter above

the pile tip. For silty sand, the influence zone is 3.5 times the pile diameter below the pile tip, and 1.5 times the pile diameter above the pile tip.

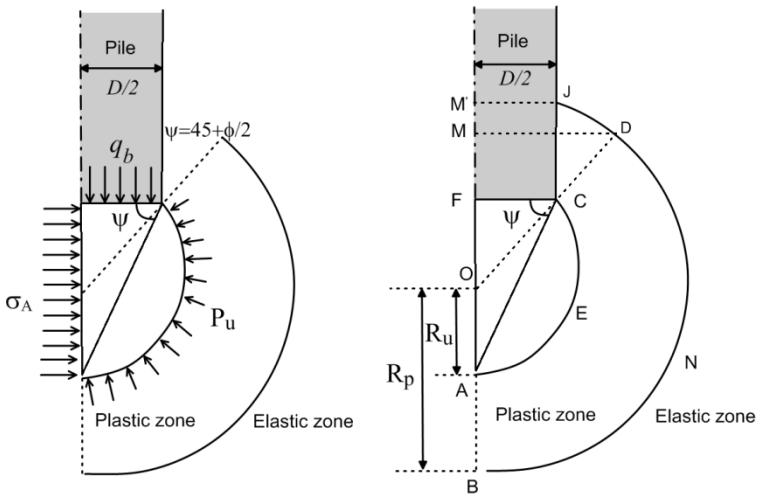

Figure 2.7 Influence zone below pile tip (Yang, 2006)

Van Den Berg, et al. (1996a) performed large-displacement finite element analysis in layered soil using Arbitrary Lagrangian Eulerian (ALE) technique. The sand constitutive behavior was modeled using the Drucker-Prager yield criterion with a non-associated flow rule and a Von Mises criterion is used to model undrained clay behavior. For clay over sand layer, a development depth of 4 cone diameters is required to fully develop the cone resistance within the sand. They also concluded that this development distance depends upon the stiffness ratios; for example, sand to clay stiffness ratio of 2.5, the development depth is 3 cone diameters, whereas, for stiffness ratio of 4, that increases to 5 cone diameters. For sand over clay layer, the cone senses the clay layer 4 cone diameters ahead of the interface. However, as the author emphasized, the material properties adopted specially the stiffness ratio have a great effect on the results.

Ahmadi & Robertson (2005) performed finite difference analysis of cone penetration in two-layered soil profiles. They used updated Lagrangian approach, with arbitrary displacement specified on cone-soil interface nodes with vertical to horizontal displacement ratio of 0.6 in order to match the experimental displacement pattern observed by Berg (1996). Summary of their results on cone influence zone is shown in

Table 2.4. They concluded that the influence zone ahead and behind the advancing cone depends upon relative stiffness and horizontal effective stress. They also concluded that the influence zone decreases with increasing horizontal effective stress due to less dilation of sands.

Table 2.4 Reported cone influence zones by Ahmadi & Robertson (2005)

Test condition	Density, D_R (%)	Sensing depth (d_c)	Development depth (d_c)
Loose over dense	30/90	4.2	10
Dense over loose	90/30	18	8.4
Medium dense over loose	50/30	10	3.5
Loose over medium dense	30/50	5.5	6
Medium dense sand over clay	50/S_u=20 kPa	10	1.7
Clay over medium dense	s_u = 20 kPa/50	1.5	6
Clay over dense	s_u = 20 kPa/50	2	14

Their results show a very large influence zone as compared to experimental evidence. The authors have also investigated the presence of a thin strong layer sandwiched between soft clay layers. They concluded that the development of full resistance within a sand layer requires a minimum thickness of 7 cone diameters for loose sand and as much as 28 cone diameters for dense sand. A thin layer correction factor is also proposed based upon the thin layer thickness.

Xu & Lehane (2008) studied the penetration resistance in two-layered soil profiles by numerical spherical cavity expansion analysis using the PLAXIS finite element code. They used Plaxis non-linear hardening soil model based on the Mohr-Columb yield criterion with dilation cut off to model the constitutive behavior of the sand. The obtained cavity limit pressure is assumed to be an estimate of the cone tip resistance using the relationship proposed by Randolph et al. (1995). Two types of layered soil profiles were modeled: (1) strong over weak and (2) weak over strong. They created the cavity at different distances from the interface in strong and weak layers, cavity limit pressures

were obtained and the corresponding tip resistances were calculated. In this way, they studied the effect of proximity to the interface on strong and weak layer tip resistances. Their numerical model is as shown in Figure 2.8.

They proposed an equation based on the ratio of the steady-state cone resistances in the weak layer to that of strong layer ($\eta_{\min} = q_{c,w} / q_{c,s}$) for predicting the cone resistance profile in the transition zone that extends above and below the interface. The ratio of cone resistance in the transition zone to that of the steady-state resistance in the strong layer is defined as:

$$\eta = \frac{q_c}{q_{c,s}} = \eta_{\min} + (1-\eta_{\min}) \exp\left[-\exp(A_1 + A_2 \frac{H}{D}) \right] \qquad (2\text{-}2)$$

The equation is applicable for $0.01 < \eta < 0.9$, where A_1 and A_2 are coefficients defined as follows:

$$A_1 = -0.22 \ln \eta_{\min} + 0.11 \le 1.5 \qquad (2\text{-}3)$$

$$A_2 = -0.11 \ln \eta_{\min} - 0.79 \le -0.2 \qquad (2\text{-}4)$$

The sensing depth in weak layer is very small and they proposed different relationships for the sensing depths and development depths. For con resistance ratio of 0.02, this equation implies that the sensing depth in very weak layer is less than 2 cone diameters and the development depth in strong layer is 12 cone diameters.

$$\frac{Z_s}{D} = 1.4 - 2.5 \ln \eta_{\min} \qquad (2\text{-}5)$$

$$\frac{Z_w}{D} = 1.4 - 0.26 \ln \eta_{\min} \qquad (2\text{-}6)$$

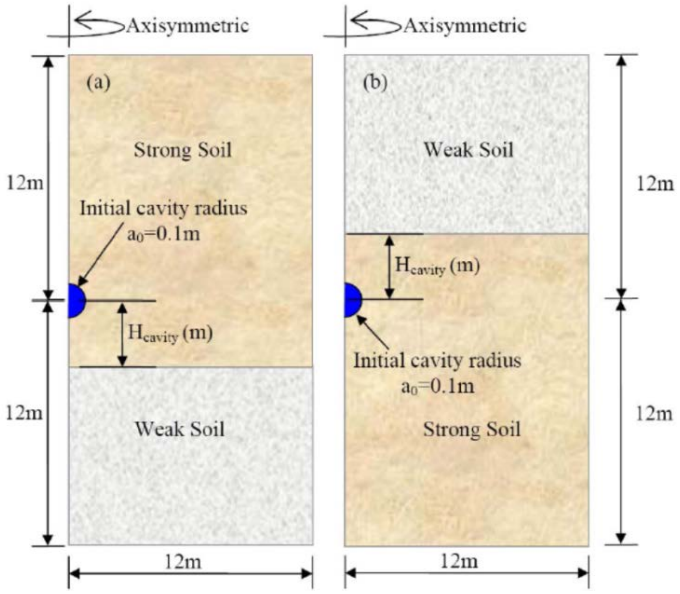

Figure 2.8 Schematic of two-layered model (Xu, 2007)

2.3 Prediction of Pile Resistance

2.3.1 Sources of Pile Resistance

Axially loaded piles support the load from the superstructure (Q_t) through basically two mechanisms: (1) friction between the pile shaft and surrounding soil (shaft resistance Q_s) and (2) compressive resistance at the pile base called (base resistance Q_b) (Salgado, 2008).

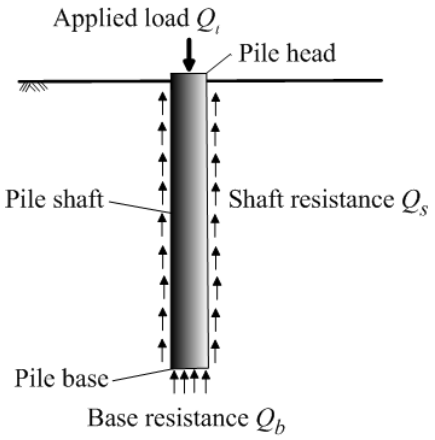

Figure 2.9 Sources of pile resistance (Salgado, 2008)

As the load increases at the pile head, the pile settlement increases until eventually the pile plunges and the pile shaft and base resistances reach their limit values. During this loading process, a thin shear zone devolps around the pile shaft. Because this zone is so thin, even very small pile movements generate large shear strains in this shear zone, leading to full moblization of the limit shaft resistance Q_{sL}. In contrast to shaft resistance, mobilization of base resistance requires a subtantial soil compression, and significant pile settlement is required. Therefore, the ultimate load Q_{ult} criteria is used to define the capacity of a pile. Among various ultimate load criteria, the 10% relative pile settlement criteria is widely used. In case of 10% relative settlement criteria, Q_{ult} is load corresponding to pile head settlement equal to 10% of pile diameter. The base resistance Q_b corresponding to 10% pile head settlement is often defined as the ultimate pile base resistance Q_{bult}.

The ultimate total resistance Q_{ult} of the pile is the sum of ultimate base resistance $Q_{b,ult}$ and limit shaft resistance Q_{sL} of the pile (Salgado, 2008):

$$Q_{ult} = Q_{bult} + Q_{sL} = q_{bult} A_b + \sum_{i=1}^{n} q_{sLi} A_{si} \qquad (2\text{-}7)$$

where q_{bult} is the ultimate unit base resistance, q_{sLi} is the limit unit shaft resistance along the interface of the pile with soil layer *i*, A_b is the area of the pile base; A_{si} is pile shaft area interfacing with soil layer *i*, and n is the number of soil layers crossed by the pile.

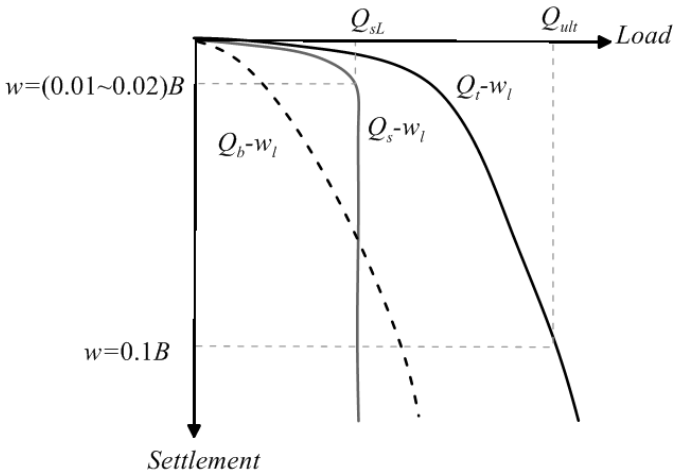

Figure 2.10 Typical load settlement curve (Salgado et al., 2011)

2.3.2 Relationship to Pile Installation and Loading

A pile can be constructed by creating a cavity in soil and in situ casting of concrete or grout, in which case it is classified as a non-displacement pile, or by driving/jacking a steel or precast concrete element into the ground, in which case it is called a full displacement pile. The method of pile installation affects the in situ state of the soil surrounding pile. The pile response to structural loading differs depending on the type of the pile and the method of its installation. Jacked piles are installed either in one continuous stroke or through a number of jacking strokes. CPT is considered a scaled-down pile load test due to the similarity between certain pile installation methods and cone penetration. Figure 2.11 illustrates this similarity and shows certain key variables for the CPT and a jacked pile.

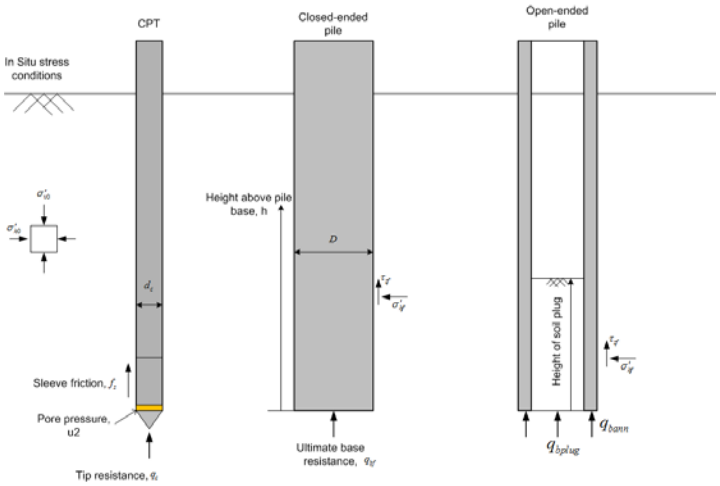

Figure 2.11 CPT analogy to jacked pile (White, 2003)

2.3.3 Prediction of Base Resistance

For a displacement pile, the limit unit base resistance q_{bL} at a certain depth within a given soil layer is approximately equivalent to the cone penetration resistance q_c of the same soil layer at that depth (Salgado, 2008). There are two types of methods, for estimation of unit base resistance of a pile. The in situ test-based method, which directly correlates the q_{bL} with $q_{c,}$ and soil property based methods, in which the basic soil properties are used as input variables.

2.3.3.1 In-Situ Test Based Methods

The general expression for linking $q_{b,ult}$ of a pile to q_c is (Salgado, 2008):

$$q_{b,ult} = C_b \cdot q_c \tag{2-8}$$

where C_b is suitable reduction factor applied to cone resistance depending on the pile type, installation method and other factors such as scale effects, partial mobilization, embedment depth and thin layer effects.

2.3.3.1.1 Scale Effects

Various averaging techniques have been proposed to account for scale effects due to local inhomogeneity and the different sizes of the cone penetrometer and a pile. An average q_c is used to correlate with the pile base resistance. Three averaging techniques are recommended in the literature (Bustamante & Gianselli, 1982; Jardine et al., 2005; Lehane et al., 2005, Salgado, 2008; Lehane, 2012): (1) taking the mean q_c value in the zone 1.5 pile diameters above and below the pile tip, (2) Taking average q_c value 1 pile diameter above and 1.5 pile diameter below the tip, and (3) the so-called "Dutch" averaging technique, used for highly variable cone resistance profiles for calculating the average q_c within an influence zone of 4 pile diameters below and 8 pile diameters above.

2.3.3.1.2 Partial Mobilization

The ultimate base resistance of driven piles corresponding to a displacement equal to 10% of the pile diameter will typically be less than the cone resistance q_c. The reduction factor depends upon the soil below the pile tip. Lee and Salgado (1999) have proposed a density-dependent reduction factor for sands.

2.3.3.1.3 Partial Embedment

A pile has greater diameter than the cone, so it needs a deeper embedment into a layer in order to mobilize the full strength of that layer. The embedment depth required for development of the full strength of the bearing layer can be referred to as the "development depth". When the pile is embedded in the layer less than this development depth, the pile base resistance will be affected by the layer above. Similarly, the close proximity of an underlying weak layer also affects the mobilization of the pile base resistance.

Table 2.5 shows the reduction factor for base resistance calculation from q_c for displacement piles.

Table 2.5 Design value of C_b (modified from Salgado, 2008)

Pile Type	C_b	Source
Driven Pile	$C_b = 0.35 - 0.5$	Chow (1996)
	$C_b = 0.4$	Randolph (2003)
	$C_b = \begin{cases} 0.32 - 0.7 \text{for } D_R = 30\% \\ 0.27 - 0.57 \text{for } D_R = 50\% \\ 0.24 - 0.5 \text{for } D_R = 70\% \\ 0.20 - 0.43 \text{for } D_R = 90\% \end{cases}$	Lee & Salgado (1999) Basu et al. (2005)
	$C_b = 1.02 - 0.0051 D_R$	Foye et al. (2009)
	$q_{bult} = [0.5 - 0.25.\log(D / d_c)] q_{cave}$ D: Pile diameter d_c : Cone diameter q_{cave} : Average q_c ± 1.5D	Jardine et al. (2005) ICP Method
	$\frac{q_{bult}}{q_{cb,avg}} = 0.6$ $q_{cb,avg}$: Dutch averaging technique used for for $q_{cb,avg}$ in highly variable cone resistance profile , otherwise same as ICP method	Lehane et al. (2005) UWA Method

2.3.3.2 Soil Property- Based Method

The limit base resistance q_{bL} can be considered approximately equal to the cone penetration resistance q_c. Salgado & Prezzi (2007) proposed the following relationship for calculation of limit base resistance q_{bL}:

$$\frac{q_{bL}}{p_A} = 1.64 \exp\left[0.1041\phi_c + \left(0.0264 - 0.0002\phi_c\right) D_R\right] \left(\frac{\sigma'_h}{p_A}\right)^{0.841 - 0.0047 D_R} \quad (2\text{-}9)$$

where ϕ_c is critical-state friction angle, D_R is the relative density expressed as a percentage and σ'_h is effective in situ horizontal stress prior to installation. For an ultimate unit base resistance q_{bult} defined as that causing a settlement of 10% of the pile diameter. Salgado (2008) proposed a density-dependent correction factor to account for this partial mobilization:

$$q_{bult} = q_{b,10\%} = [1.09 - 0.007 D_R] q_{bL} \quad (2\text{-}10)$$

2.3.4 Prediction of Shaft Resistance

As a pile is loaded axially, limit shaft resistance q_{sL} develops due to shearing between the pile and the soil. This shearing resistance depends upon the normal stress acting on interface and interface friction coefficient between the soil and the pile shaft (Salgado, 2008). Mathematically, it can be expressed as:

$$q_{sL} = \sigma'_n \tan\delta = (K\sigma'_{v0}) \tan\delta = (K \tan\delta)\sigma'_{v0} = \beta\sigma'_{v0} \quad (2\text{-}11)$$

where K is the coefficient of lateral earth pressure at limit condition, δ is the mobilized interface friction angle and σ'_{v0} is the vertical effective stress before the pile installation at the depth where shaft resistance is calculated. The normal stress acting on the interface strongly depends upon the pile installation method and initial soil state. For displacement piles, the normal stress acting along the interface varies similarly to cone resistance q_c as observed in field tests (Lehane, 2012). Therefore, the normal stress acting on interface can be linked directly with cone resistance q_c.

In the direct design approach, the relationship between the shaft resistance and the cone resistance takes following form (Salgado, 2008):

$$q_{sLi} = c_{si} q_{ci} \quad (2\text{-}12)$$

Table 2.6 shows the summary of methods available for calculation of limit shaft resistance.

Table 2.6 Methods for limit shaft resistance calculation (after Salgado, 2008)

Method	C_s	Source
Empirical	$C_s = \begin{cases} 0.008 \text{ for open ended steel piles} \\ 0.012 \text{ for precast concrete piles} \\ 0.018 \text{ for Franki and timber piles} \end{cases}$	Schmertmann (1978)
	$C_s = \begin{cases} 0.004\text{-}0.006 \text{ for } D_R \le 50\% \\ 0.004\text{-}0.007 \text{ for } 50\% < D_R \le 70\% \\ 0.004\text{-}0.009 \text{ for } 50\% < D_R \le 90\% \end{cases}$	Lee & Salgado (2003) For close-ended piles
	$C_s = \begin{cases} 0.004 \text{ for clean sand} \\ 0.0057 \text{ for silty sand} \\ 0.0069 \text{ for silty sand with clay} \end{cases}$	Aoki &Velloso (1975)
Semi-empirical	$q_{sL} = \sigma'_{rf} \tan\delta$ $\sigma'_{rf} = \sigma'_{rc} + \Delta\sigma'_{rd}$ $\sigma'_{rc} = 0.029 q_c \left(\frac{\sigma'_{v0}}{P_A}\right)^{0.13} \left[\max\left(\frac{2h}{B}, 8\right)\right]^{-0.38}$ $\Delta\sigma'_{rd} = \frac{4GR_{avg}}{R}$ $G = q_c \left[0.0203 + 0.00125\frac{q_c}{\sqrt{P_A \sigma'_{v0}}} - 1.21\times10^{-6}\frac{{q_c}^2}{P_A \sigma'_{v0}}\right]$	Jardine et al. (2005) ICP Method σ'_{rc} : Normal stress acting on shaft at end of the pile installation $\Delta\sigma'_{rd}$: Normal stress increase due to dilation G : Shear stiffness
	$\sigma'_{rc} = 0.03 q_c \left[\max\left(\frac{h}{B}, 2\right)\right]^{-0.5}$ $G = 185 q_c \left[\frac{q_c / P_A}{\sqrt{\sigma'_{v0} / P_A}}\right]^{-0.75}$	Lehane et al. (2005) UWA Method Similar to ICP method
Property-based method	$q_{sL} = 0.02 \tan\delta \left[1.02 - 0.0051 D_R\right] q_{bL}$ *where* $q_{bL} \approx q_c$: $\frac{q_{bL}}{P_A} = 1.64 \exp\left[0.1041\phi_c + (0.0264 - 0.0002\phi_c) D_R\right] \left(\frac{\sigma'_h}{P_A}\right)^{0.841 - 0.0047 D_R}$	Salgado (2008)

2.3.4.1 Friction Fatigue

The process of progressive reduction in normal stress acting on pile-soil interface at a given soil horizon with the further penetration of a pile is referred to as “friction fatigue” (Heerema, 1980). The friction fatigue depends upon the number of shearing cycles involved during pile installation. White & Bolton (2004) suggested that soil is crushed at the pile tip, and this material ‘coats’ the shaft as it penetrates. The possible migration of crushed particles along the interface would cause soil ‘relaxation’ away from the interface. This, in turn, leads to reduction of the normal stress acting on the shaft. Randolph et. al (1994) argued that the shaft friction degradation rate in driven piles depends also on other factors, such as the compressibility/particle crushability along the shaft, the pile surface roughness, incremental driving energy and the effective displacement ratio at pile tip.

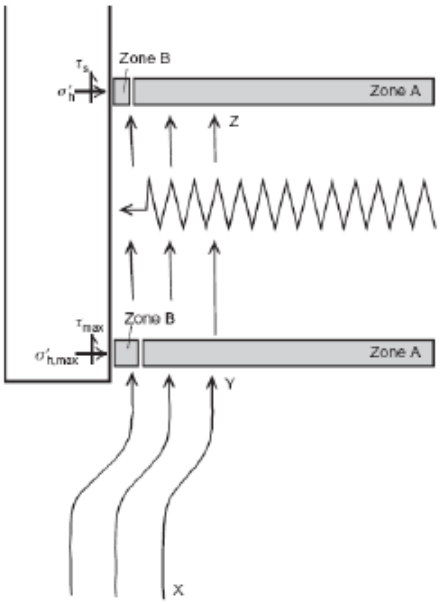

Figure 2.12 Kinematics of friction fatigue (White & Bolton, 2004)

2.4 Experimental Observation of Displacement Field during Model Pile/ Penetrometer Installation

One possible route for solving the complex CPT boundary-value problem experimentally is to quantify the soil displacement through visual observation during penetrometer installation. Various researchers in the past have employed the visual technique to observe the soil movement near the model pile/penetrometer. These studies mostly produced qualitative information on the displacement field during cone penetration. Today, with availability of advanced imaging capturing and analysis tools (like digital Particle Image Velocimetry (PIV) and Digital Image Correlation (DIC) techniques), it is possible to measure the soil displacement with improved precision (White 2000). It is now plausible to solve boundary value problems like the pile/penetrometer installation experimentally (complete solution would require a constitutive model to integrate strains obtained experimentally or experimental measurement of stresses). In this section, we will review previous research conducted to observe soil movement around an advancing pile or penetrometer. We will divide the studies into two categories: (1) experimental studies with real soil and (2) experimental studies with artificial soil.

2.4.1 Experiments with Real Soil

2.4.1.1 X-Ray Radiography and Computed Tomography

A series of model pile tests are reported by Robinsky & Morrison (1964). These tests used dry silica sand, with pile installation by jacking. An X-ray method was used to track the movement of lead shots embedded in the soil model. The resulting displacement vectors were used to deduce contours of volumetric strain. Figure 2.13 is a radiograph of a typical pile tip showing the displacement pattern of sand in its immediate vicinity. A zone approximating the shape of a cone is found beneath the pile extending downwards from the edges of the pile. This technique only yields qualitative information about the displacement field.

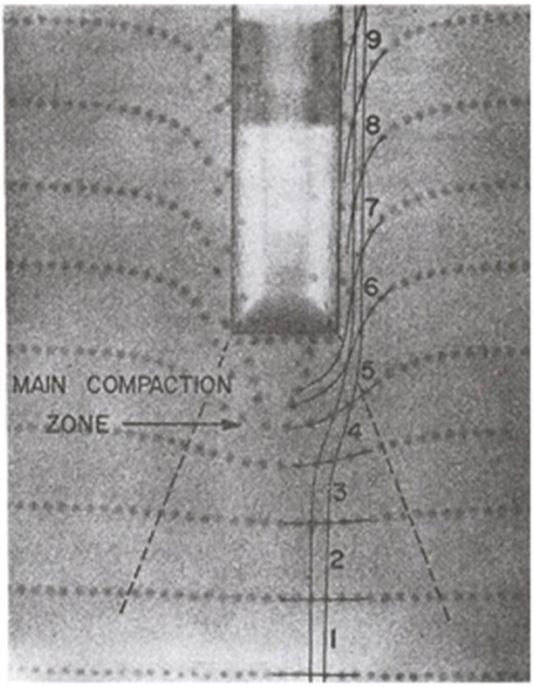

Figure 2.13 Radiograph of pile tip showing the compaction zone below pile base (Robinsky & Morrison, 1964)

Kobayashi & Fukagawa (2003) conducted a series of cone penetration test in Toyoura sand using lead markers and iron powder spread in the soil. X-Ray Computed Tomography (CT) Scan was used to capture the images during cone penetration. Figure 2.14(a) shows the experimental set up. Three penetrometers of 16 mm diameter with different tip geometries were used. They observed that a narrow cone produced mostly radial displacement but a blunt tip produced a prominent vertical bulb. Figure 2.14(b) shows the effect of cone tip geometry on deformation pattern. Continuous observation of cone penetration was not possible due to long CT scanning time required for high-resolution still images and the poor resolution of X-ray TV motion pictures. Still images were acquired during discrete “instants” during penetration. The displacement resolution in this technique depends upon the lead markers density.

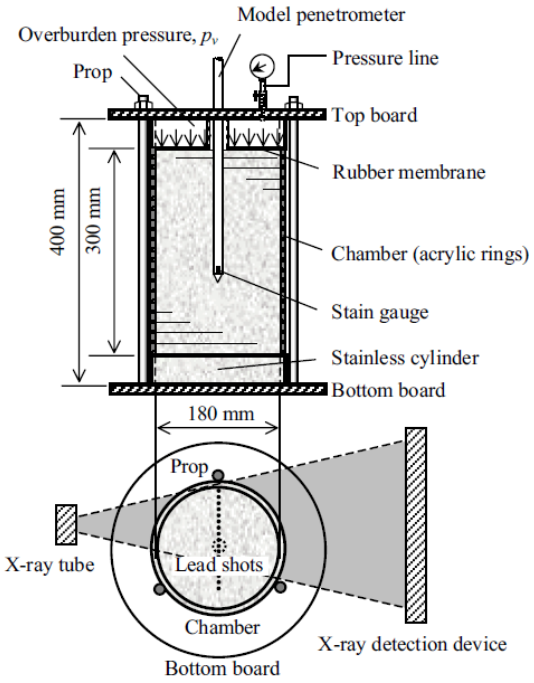

(a)

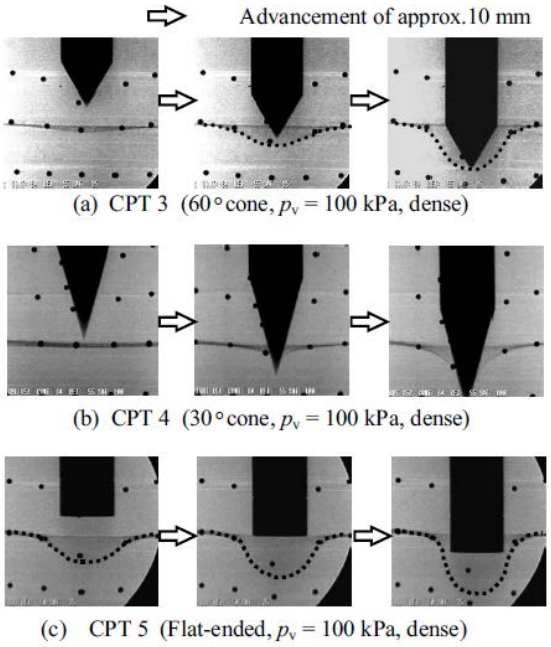

(b)

Figure 2.14 (a) Test set up and (b) deformation characteristics around cone tip (Kobayashi & Fukgawa, 2003)

Cheng et al. (2005) conducted 3D X-ray tomography during miniature cone penetration tests to observe the density changes during the penetration process. A small flexible wall chamber 100 mm in diameter and 200 mm in height was used. The surcharges of 80 and 40 kPa were applied through vacuum. A miniature cone of 6 mm diameter was used for penetration tests in fine sand samples having D_{50} of 0.15 mm. The X-ray imaging was performed at the start and at certain intervals during cone penetration. Image subtraction and x-ray attenuation was used to estimate the density changes. They observed dilation up to 2.5 cone diameters around the penetrometer and a slight increase in density (compression) was observed elsewhere. Samples were prepared with two initial densities: 1.61 g/cm^3 and 1.54 g/cm^3. Figure 2.15 shows the spatial distribution of density after 100 mm of the cone penetration.

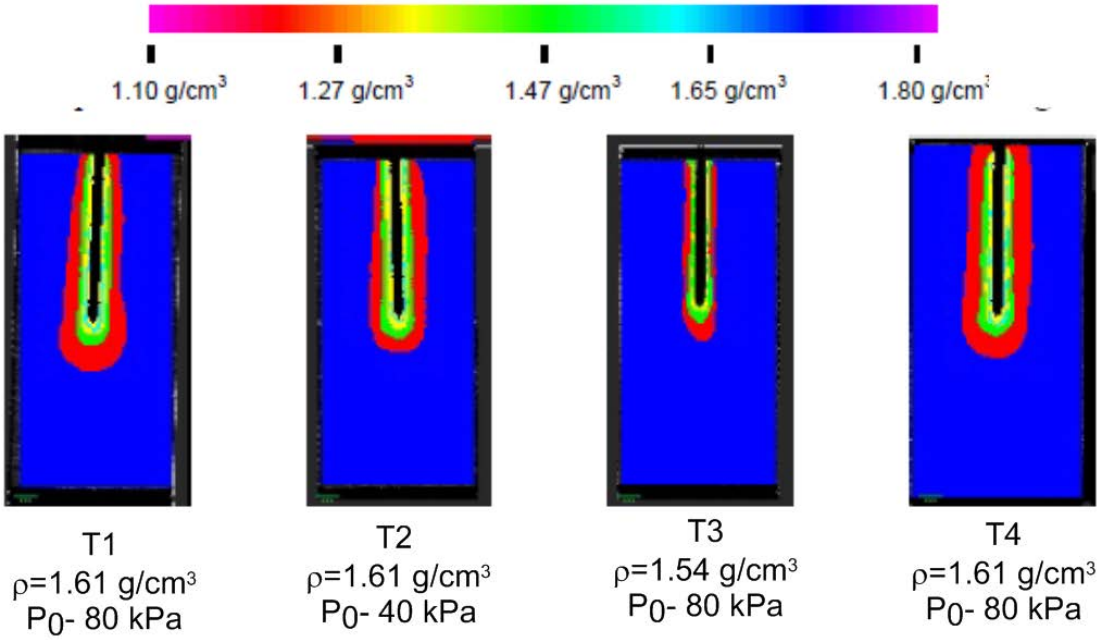

Figure 2.15 Density changes during miniature cone penetration (Cheng et al., 2005)

2.4.1.2 Colored Sand Layers

Yasufuku & Hyde (1995) used layers of sand with different colors to examine the displacement around a pre-installed 20 mm diameter pile in a split cylindrical chamber. Three sands of different crushability (Dogs Bay carbonate sand, Masado crushed granite sand and Aoi silica sand) were tested in a small calibration chamber with diameter of 330 mm and height of 500 mm. They concluded that the deformation 'bulb' beneath the pile tip strongly resembles that generated by spherical cavity expansion in an infinite medium. Based on this observation, the authors suggested that spherical cavity expansion theory is a suitable analytical method to predict the end bearing capacities of piles in crushable sands. The method provided only qualitative information about the failure mechanism.

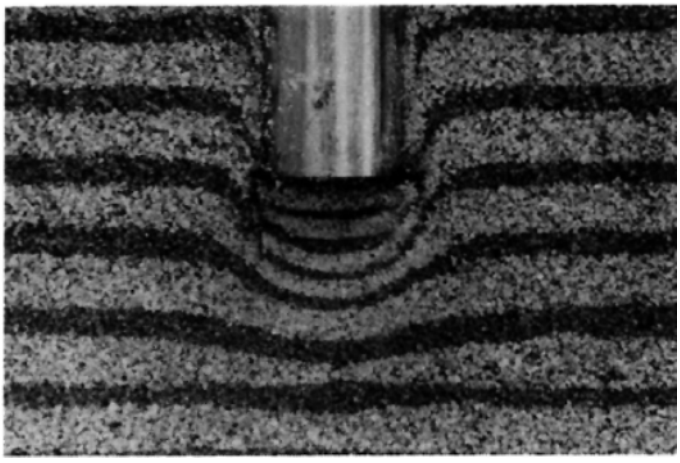

Figure 2.16 Pile tip failure mechanism observed by Yasafuku & Hyde (1995)

2.4.1.3 Target Markers Tracking

Li et al. (2010) studied the displacement field during penetration of a model pile with diameter equal to 40 mm in medium dense sand over rubber powder used to simulate a soft soil. The rectangular chamber size was 1.0 x 0.6 x 1.2 m. Red and blue-colored sand markers were placed at regular intervals in order to observe the displacement field during pile penetration. The displacement field was obtained by tracking these colored sand markers through digital images. Figure 2.17 shows the radial and vertical displacement distributions. They concluded that the radial extent of the region where horizontal displacements are observed is 5-7 times the pile diameter. They

suggested that the displacement field below the pile tip is similar to that for spherical cavity expansion. The experiments were conducted at low stress level and their results are representative of shallow penetration. Displacement measurement accuracy and resolution with this type of target tracking technique can be affected by the disappearance of colored sand markers, especially in the high shear zones near the pile tip.

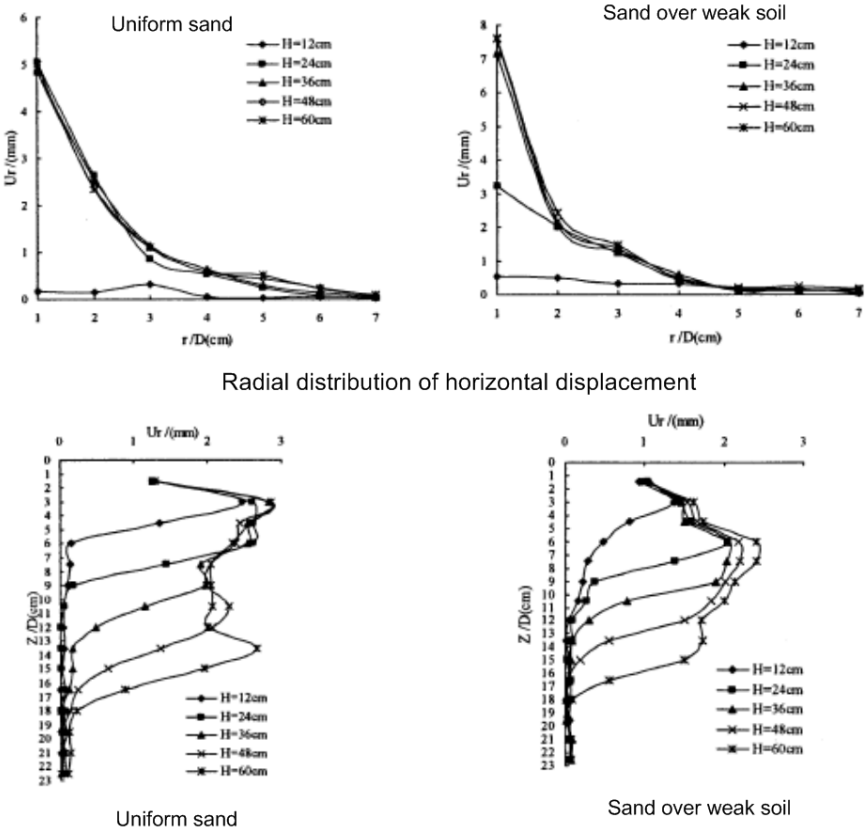

Figure 2.17 Radial and vertical distribution of horizontal displacement (Li et al., 2010)

2.4.1.4 Stereo-Photogrammetric Method

Gupta (1992) used the stereo-photogrammetric technique to observe the displacement field around a model cone penetrometer during penetration in loose and medium dense sand samples. The surcharge of 25 kPa was applied on the top of the soil sample of size 1000 × 500 × 650 mm. The 36-mm-diameter half cone was initially clamped with glass to prevent particle intrusion. The soil displacements were obtained

using the “false relief technique”, where the false height in a stereo image is proportional to the in-plane displacement in the sand. Figure 2.18 shows the finite strains obtained after the penetration depth of 10 times the cone radius. The accuracy in displacement measurement was reported by the author as 7%. The author concluded that a spherical cavity expansion takes place below the cone tip.

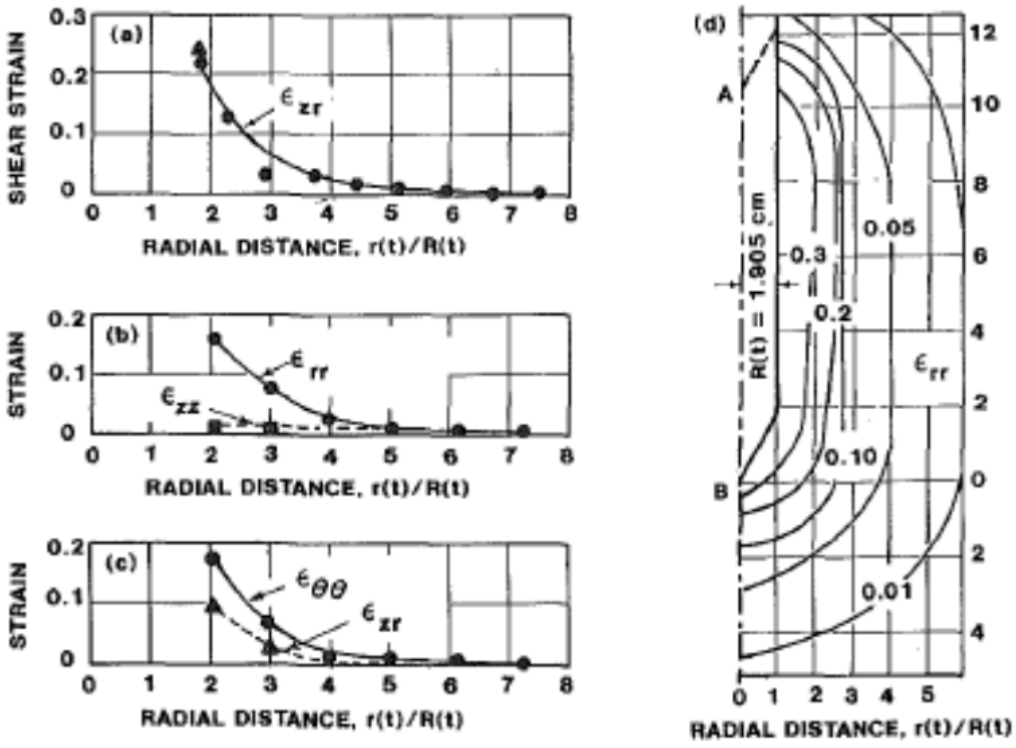

Figure 2.18 Strain distribution during cone penetration (Gupta, 1992)

2.4.1.5 Laser Speckle Inferometry Technique

De Pater & Nieuwenhuis (1987) used Laser Speckle Inferometry to investigate the displacement field around a model cone penetrometer. They used a standard 36-mm-diameter cone penetrometer in a rectangular tank with size $800 \times 400 \times 400$ mm. The cone was firmly pressed against the glass wall to prevent sand intrusion. Double exposure photographs were made on high-resolution film. The inference patterns were created by passing a laser beam through negative. The sand displacements were measured by measuring the distances between inference patterns. Figure 2.19 shows the typical double exposure cone image during penetration and the obtained displacement field around a

constricted cone. The accuracy of this technique depends upon the formation of inference patterns, which do not form clearly in dry sand. A cylindrical cavity expansion was inferred from the observed displacement field.

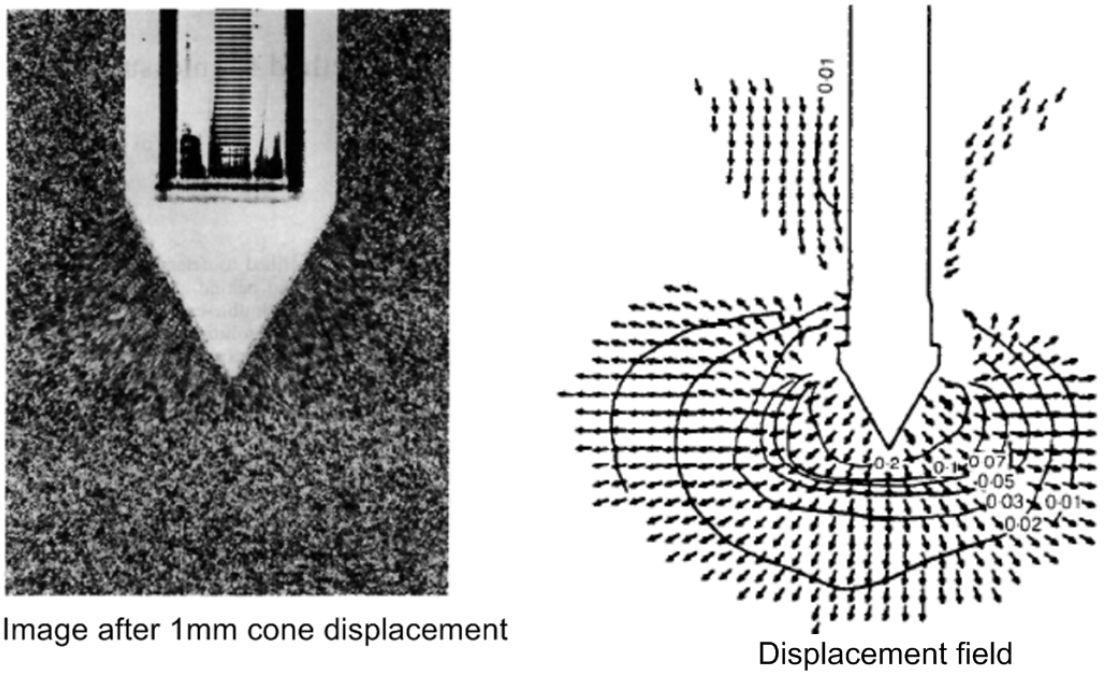

Figure 2.19 Displacement pattern around cone penetration in loose sand (De Pater & Nieuwenhuis, 1987)

2.4.1.6 Particle Image Velocimetry (PIV)

White & Bolton (2004) pioneered the use of the PIV technique in geotechnical modeling. The PIV technique was used to obtain the displacement and strain paths during model pile installation in a plane-strain calibration chamber with dimensions given by 1000 ×750 × 50 mm. Two piles of different breadths (32 mm & 16 mm) were used. Two off-the-shelf digital cameras (2MP Kodak DC280) were used to photograph the pile installation process at a frame rate of 0.5 frames/s. The principles of close-range photogrammetry were used for camera calibration. Two testing sands (crushable Dog's Bay carbonate sand and Leighton Buzzard silica sand) were used in their study. A surcharge of 50 kPa was applied on the top of the sample to simulate the deep pile penetration. The work mainly focused on deducing the strain paths below the pile base.

Only a few displacement paths were reported. An example of incremental displacement field below the model pile base is shown in Figure 2.20.

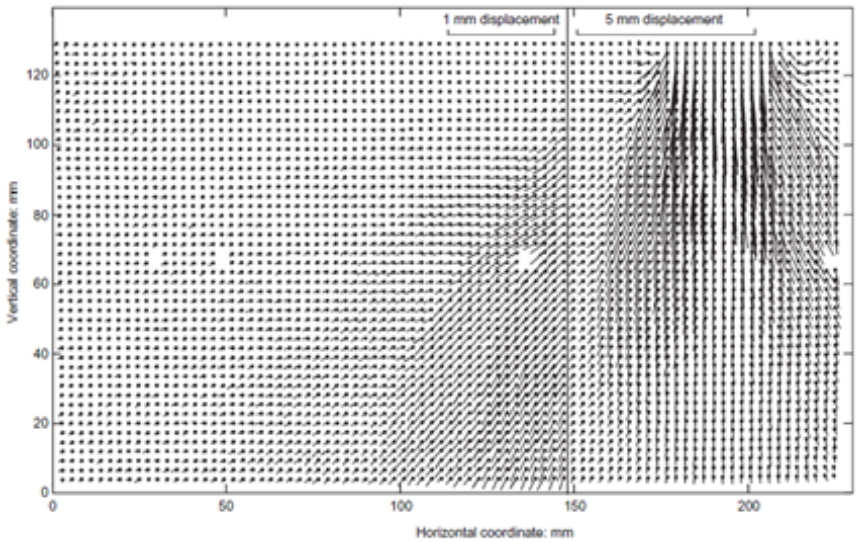

Figure 2.20 Incremental displacement field below pile base (White & Bolton, 2004)

The study of White and Bolton (2004) provided the extremely useful insights of displacement pile behavior. Due to the plane strain loading in the experiments, the displacements resulting from the experiments are greater than for a real pile. For PIV analysis, they used a Fast Fourier Transform (FFT)-based correlation tracking scheme, which is explained later in section 3.3.2. The particle tracking scheme used does not account for interrogation window deformation, which can affect the accuracy of results near the pile tip, where the soil experiences large shearing and rotation. The strain calculations relied on constant-strain triangular elements. Owing to the very dense spacing of these elements the “gauge length” for strain calculation is too small than the representative equivalent volume (REV) (Davis & Selvadurai, 1996) for a continuum behavior prediction for geomechanics.

Liu (2010) conducted a PIV study of cone penetration in the centrifuge. A PIV analysis similar to that of White & Bolton (2004) was used. Their model consisted of a 500-mm diameter half-circular sand sample. A half-circular penetrometer with the diameter equal to 12 mm was used. Leighton Buzzard silica sand with D_{50} of 0.5 mm

with minimum particle size of 0.3 mm was used. Two digital cameras (Canon Power shot S70) were used for taking frames of the penetration. The image capture rate was 0.2 frames/s. Displacements at the same radial distances from the cone were much smaller than for the plane strain model. The author concluded that the displacement pattern resembles that from spherical cavity expansion below the cone tip and that from cylindrical cavity expansion above the cone tip. The derived strain paths were much less in magnitude than observed for the plane strain case. Their results are however more likely to have been influenced by an increased refraction effect due to the inclined camera position with reference to the observation plane. Considerable sand intrusion was also observed in their tests during deep penetration, which may influence the accuracy of the results. The PIV analysis done has the same limitations as that of White and Bolton (2004). Figure 2.21 shows a typical image obtained at deep penetration.

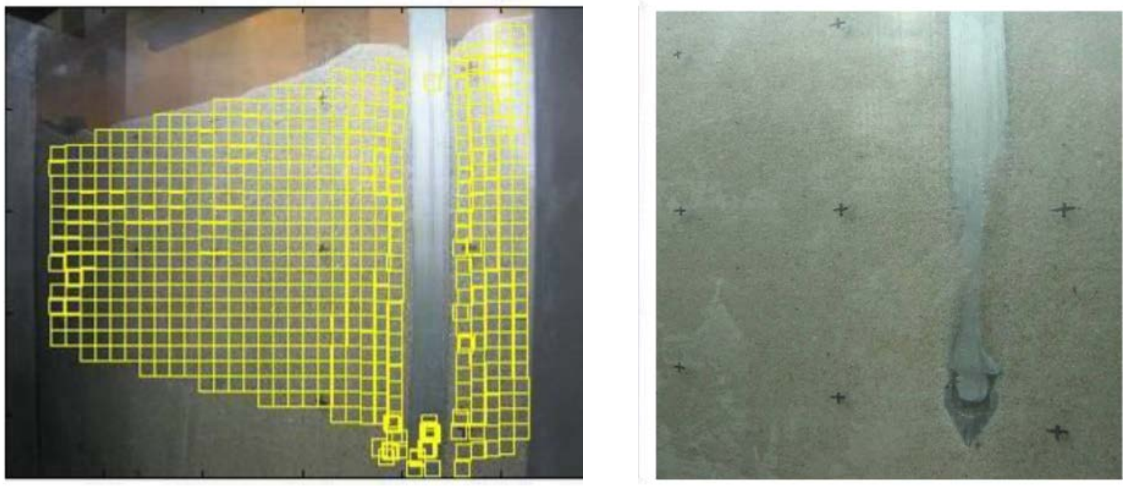

(a) (b)

Figure 2.21 Centrifuge cone penetration experiment: (a) typical image with PIV mesh (b) intrusion at deep penetration (Liu, 2010)

2.4.2 Experiments with Artificial Soil

2.4.2.1 Photo-elasticity

Allersma & Broere (2002) studied the stresses around cone penetration using a plane strain model and photo elasticity. The model size was 285 × 250 mm with thickness of 50 mm. Crushed glass with particle size between 2 and 3 mm was used as

the granular material. A surcharge of 150 kPa was applied at the top of the sample. The magnitudes and directions of principle stresses were deduced using photo-elasticity relationships. The maximum stress was observed below the tip. Their results are affected by scale effects and the difference between crushed glass and real sand. Figure 2.22 shows the stress pattern and principal stresses directions around the penetrometer.

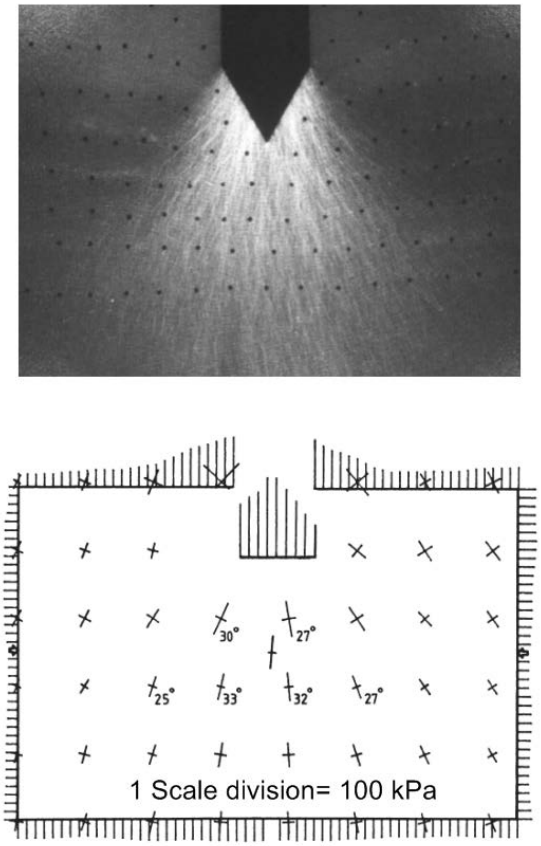

Figure 2.22 Stress pattern distribution and principal stress directions around model probe (Allersma & Broere, 2002)

2.4.2.2 Video-Extensometer

Lehane & Gill (2004) used amorphous fumed silica as a transparent soil using paraffin oil and mineral spirit as the pore fluid. The artificial soil was created to model clay behavior. The tracking targets are of 2mm black spherical beads placed at desired locations within the sample. The specimen was consolidated to 270 kPa and then unloaded to 0.7 kPa. A flat-end penetrometer of 6.35 mm radius was pushed into a soil

tank of size 160 × 280 × 800 mm. The penetrometer was pushed manually with average speed of 0.06 mm/s to achieve undrained penetration. They concluded that the radial distribution of displacement compares well with estimates of cylindrical cavity expansion theory and field data, as shown in Figure 2.23.

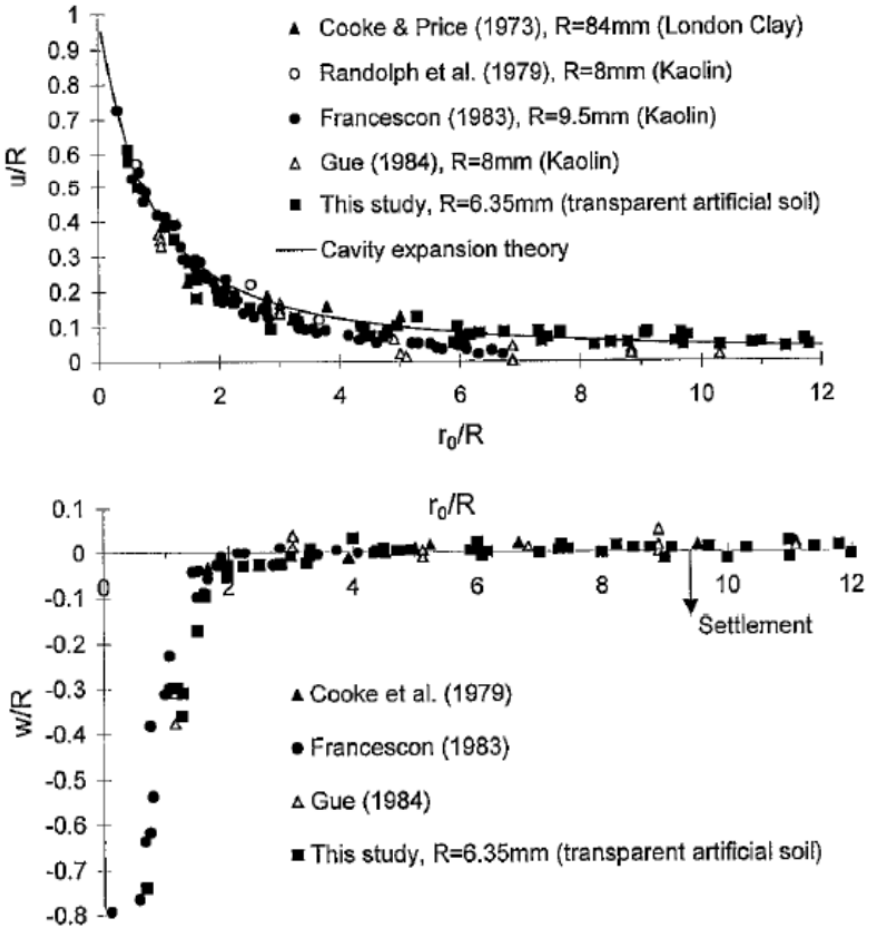

Figure 2.23 Radial distribution of normalized displacement during cone penetration (Lehane & Gill, 2004)

2.4.2.3 PIV in Transparent Soil

Ni et al. (2010) used artificial soil similar to Lehane & Gill (2004) to model miniature pile penetration in clay. A scale model of size 100 × 100 × 300 mm was used with an 8-mm diameter probe. The specimen was consolidated to 40 kPa and then unloaded to 8 kPa. Their experimental set up consists of a classical PIV test set up as used in experimental fluid mechanics. Light-reflecting seeding particles were used to

enhance the texture of the transparent clay. A laser beam was used to produce the light sheet for illumination of observation plane. A Canon 350D 8-megapixel digital camera was used for image capturing during the model pile penetration with 0.8 frames/s. The PIV software of White & Bolton (2004) was used for PIV analysis.

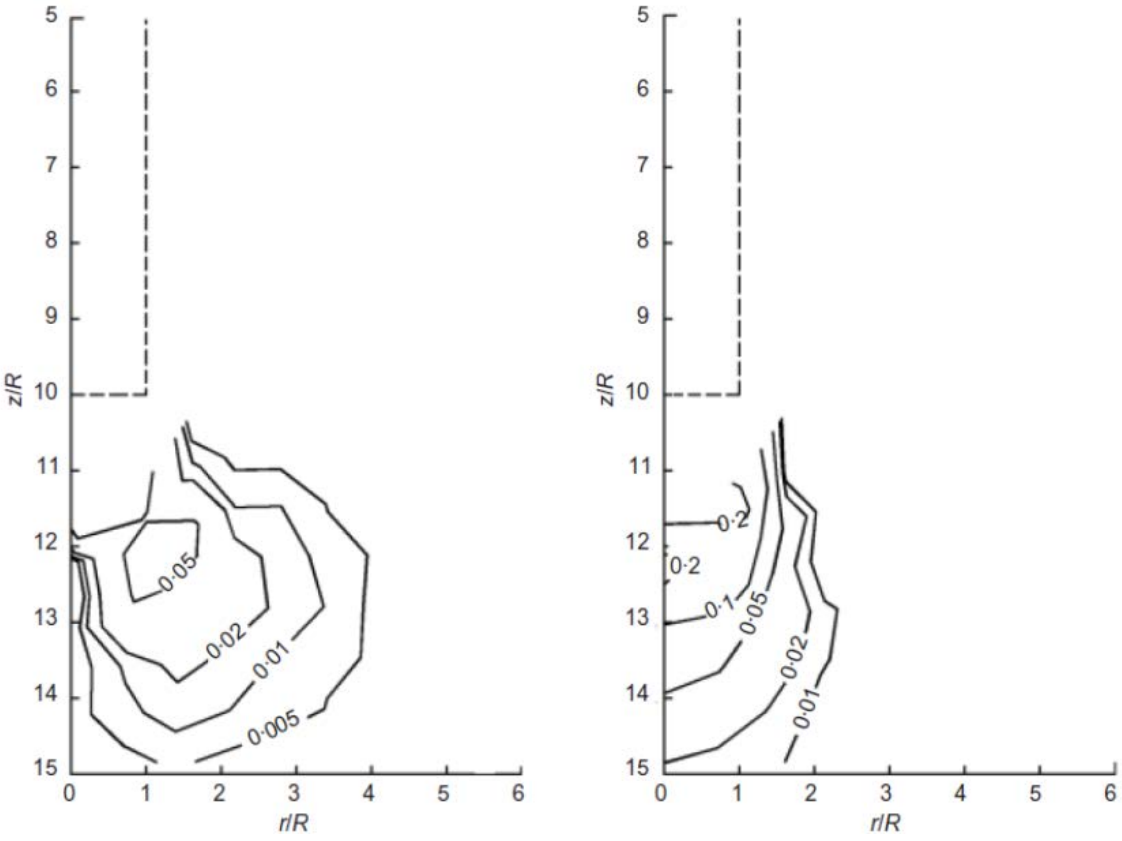

Figure 2.24 Normalized radial and vertical displacement during model pile penetration in transparent soil (Ni et al., 2010)

2.5 Summary

In this chapter, we reviewed the various experimental and theoretical approaches adopted for solution of the cone penetration boundary-value problem. The following major conclusions can be drawn:

- The theoretical prediction of cone penetration has improved from early theoretical models of limit equilibrium to current cavity expansion analysis. Various approximations have been used for linking the cavity limit pressure to cone resistance. No rigorous theoretical solution for this problem exists. Particle crushing has not yet been modeled rigorously.
- Strain path methods, in which soil streamlines are considered to be independent of soil strength, are applicable to clay but not to sand.
- Finite element studies have mostly relied on simple constitutive relationships and accurate modeling of interface and particle crushing is still a challenge. There is no reliable experimental study available for validation of these numerical results.
- The effect of soil layering on penetration resistance has mostly been studied theoretically. The theoretical results are inconsistent in terms of sensing and development depths. Very few experimental studies have been conducted in layered soil profiles.
- Various image analysis techniques have been employed in the past to study the displacement field during penetrometer installation. An advanced tracking algorithm to overcome the rotation and shearing effects of soil particles is needed for acceptable accuracy in displacement measurements, particularly in the intensive shearing zone around the cone tip.

CHAPTER 3. EXPERIMENTAL METHODOLGY

3.1 Introduction

Experimental solution of the cone penetration boundary value problem requires the precise measurement of soil displacements. In order to pursue that goal, a rigorous and robust measurement methodology is needed. A review of available measurement techniques concluded that existing PIV/DIC techniques, with improvements to improve the accuracy and overcome limitations, were the best approach. This chapter describes the experimental methodology adopted. The measurement accuracy of the DIC, the adopted technique, is evaluated and the performance of DIC is compared to other correlation methods. The suitability of 2D DIC for axisymmetric boundary value problem is evaluated. The key parameters influencing the DIC analysis are studied and a systematic approach is used to deduce these parameters. The new experimental methodology combines three techniques: the digital image acquisition, the DIC technique and the camera calibration based on principles of close-range photogrammetry.

3.2 Experimental Concept

3.2.1 Calibration Chamber and Centrifuge Testing

Calibration chamber testing has been extensively used in the past (Bellotti et al., 1982; Parkin, 1988; Houlsby & Hitchman, 1988; Ghionna & Jamiolkowski, 1991; Huang & Hsu, 2011) to study cone penetration resistance in sands under known density and boundary stress conditions. Calibration chamber testing is subject to boundary and size effects due to the limited size of the chamber. These boundary effects can be minimized by choosing the appropriate chamber to cone diameter ratio.

The calibration chamber testing represents a “point” in the field. In contrast, centrifuge testing tends to model a complete field soil profile.

In centrifuge testing, a miniature cone is used; therefore, the scale effects specific to cone tip resistance are present (Balachowski, 2007). To minimize these scale effects while conforming to similitude requirements, finer sand is preferred. The finer material will exhibit slightly different mechanical behavior than that of normal-sized sand. The centrifuge testing also suffers from boundary effects similar to those observed in calibration chamber testing, so an appropriate container to penetrometer diameter ratio is also needed (Gui et al., 1998). Due to the miniature size of the penetrometer in centrifuge testing, scale effects are unavoidable in sleeve friction owing to the dilation process in the shear band that forms next to the cone (Foray, 1991). Another shortcoming of centrifuge testing is the presence of a slightly inclined stress field from the center due to rotational acceleration (Taylor, 1995).

The main goal of this research is to measure the displacement field in the sand around a penetrometer during penetration by viewing the sand deformation process through transparent windows. The finer material used in the centrifuge tests will have greater likelihood of intrusion between the penetrating probe and viewing window. The other technical challenge is the transmission of large volume of high-resolution image data through slip rings; to circumvent this, image data is stored onboard and the user has no control of it during the test. The effect of the high acceleration on the digital camera sensor may result in increased image distortion. The size limit of the centrifuge testing platform also restricts the flexibility of camera positioning with respect to the model, which is desirable to achieve the optimum focus distance for minimization of image distortion. A calibration chamber offers the user better control of all sensors during the entire duration of the test. The great advantage of possibility of conducting a number of penetration tests in one sample in the centrifuge would not be available given the displacement measurement requirement of this research. After considering the relative merits of centrifuge and calibration testing, a calibration chamber with application of surcharge is the appropriate choice of modeling cone penetration for this research.

3.2.2 Axisymmetric Boundary Conditions and its validity

The viewing of the penetration process allows three types of configurations: an axisymmetric half-circular model, an axisymmetric quadrant model and a plane strain model as shown in Figure 3.1. The choice between these three configurations was made based on: representation of field boundary conditions; influence of boundary wall frictions on observed penetration behavior and optimum utilization of existing calibration chamber testing facility. The axisymmetric boundary condition can be achieved in a half-circular model or a quadrant model. The half-circular model is the obvious choice because it will have less wall friction and boundary effects on the penetration mechanism.

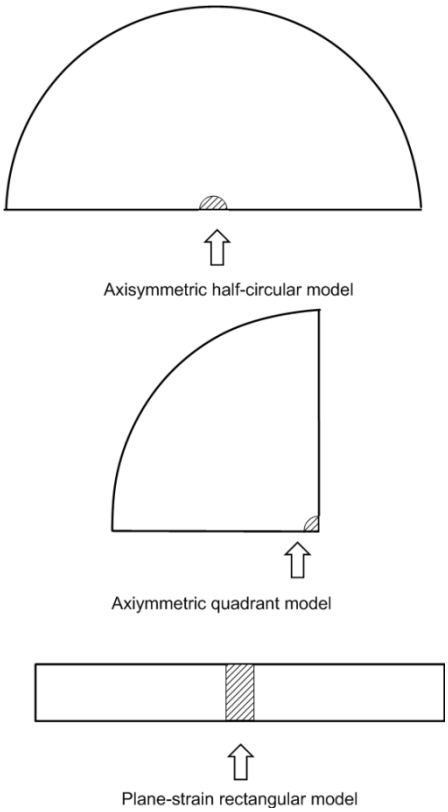

Figure 3.1 Possible boundary conditions for viewing penetration process

The half-circular axisymmetric model against a viewing window is extremely challenging to achieve because of high chances of ingress of sand between the penetrometer and viewing window. The geometry of the model alone will not guarantee the axisymmetric penetration process unless the geometry of the penetrometer tip

facilitates the soil flow in a symmetric manner. Therefore, a half-circular penetrometer with half-conical tip is desired to ensure the axisymmetric boundary condition at the penetrometer tip. For flat-ended penetrometers, a slight distortion in the symmetric soil flow will be observable below the tip.

3.2.3 Design Requirements for Experimental Set Up

The geotechnical chamber designed in this research aimed at observation of cone penetration with measurement of the soil displacements field. The goal was to solve the CPT boundary value problem experimentally. The experimental set up designed should fulfill the following considerations for attainment of the desired aim:

- Maintenance of axisymmetric boundary conditions
- Minimization of boundary influence
- Minimization of wall friction influence on penetration mechanism
- Sufficient imaging resolution and capture rate
- Sufficient Measurement Precision. The image resolution must be sufficient to resolve the individual sand grain. This is achieved by requiring that an individual grain be viewed within an array of at least of 3×3 pixels to ensure minimum grey level intensity sampling in order to obtain sub-pixel level accuracy (Schreier et al., 2009). The image system should have sufficient capturing speed so that it can image the cone penetration process at least twice as fast as the penetration rate in order to reproduce the cone penetration process more accurately. The deformation measurement technique must have sufficient precision to capture the lowest relevant strain during the cone penetration process throughout the field of view. Figure 3.2 presents the strain ranges experienced during various geotechnical processes. For cone penetration testing, the strain levels at ultimate failure are of 8-150% range. In order to observe the pre-failure behavior, the lowest strain level of interest in CPT is of the order of 0.8%, so the deformation measurement system should detect at least this 0.8% strain.

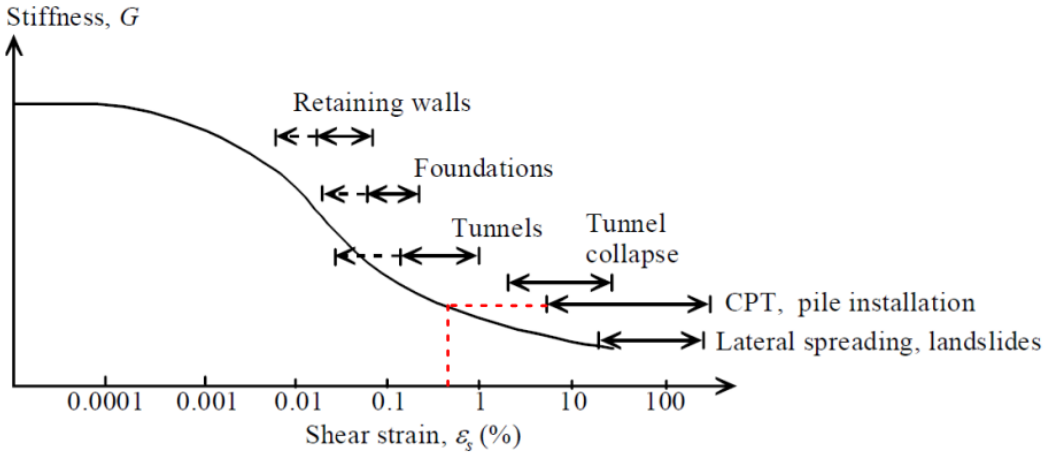

Figure 3.2 Strain levels in geotechnical world (After Mair, 1993)

3.2.4 Components of Experimental Methodology

The components of experimental methodology designed to perform the present research includes the axisymmetric half-circular calibration chamber, the digital image capturing system for recording of penetration process, the techniques to obtain the soil displacement from the recorded digital images, the measurement and the post processing tool for strain evaluation. Figure 3.3 shows the components of experimental methodology adopted. The design and fabrication of needed hardware for accomplishment of this research are discussed in detail in Chapter 4. In the present chapter, we will focus on techniques implemented to obtain the soil displacement field.

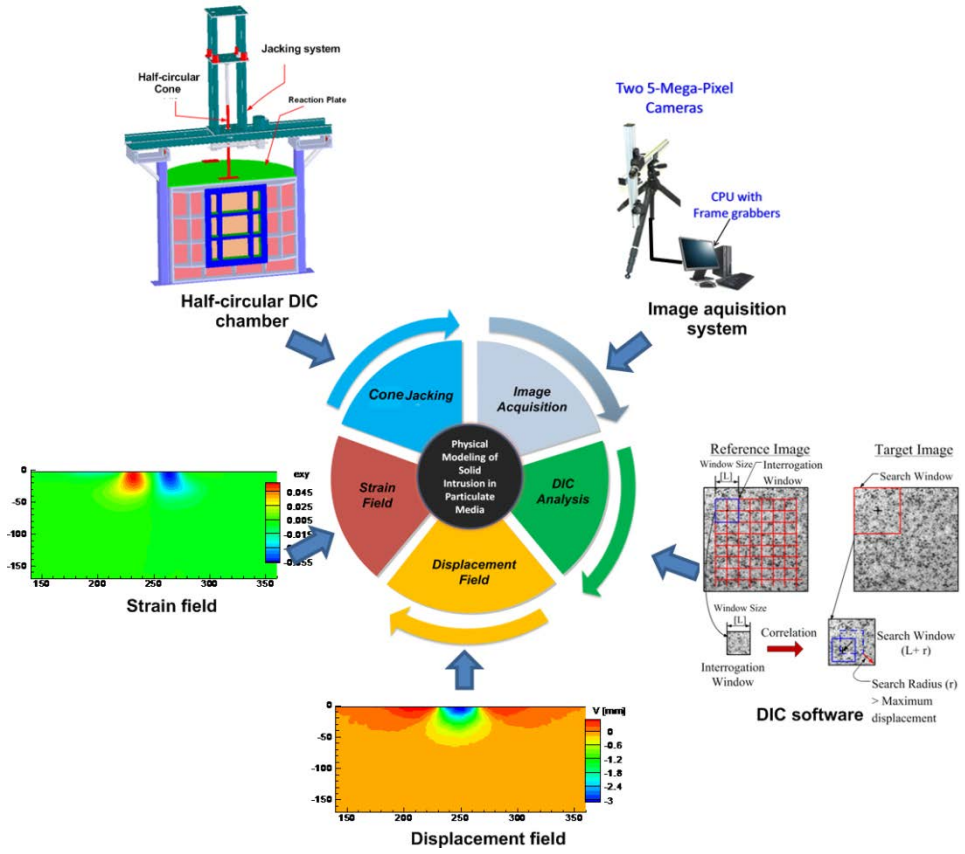

Figure 3.3 Components of experimental methodology

3.3 Soil Displacement Measurement Technique

3.3.1 Digital Imaging

The first step in image-based displacement technology is the digital image recording during a test event. A monochrome digital image camera records the reflected light from the object through a charge coupled device (CCD) or a complementary metal oxide semiconductor (CMOS) sensor by converting the incoming light into a number of electrons through photo-electricity. The image sensor consists of an array of numbers of pixels, defining the resolution of that image sensor (for example a 5-Megapixel or 5-MP sensor consists of 2592 × 1944 pixels). Depending upon the amount of charge collected, an intensity value is assigned to that pixel. The mosaic of pixel intensity forms the image. The pixel intensity values are stored as two dimensional matrices in digital form. A typical 8-bit format image has pixel intensity range from 0-255, where 0 represents pure

black and 255, white. Due to the workings of the various components of the camera, such as the analog-to-digital converter, transistors, amplifiers and electronic circuit wiring, the intensity value of pixel is not always the same and is subject to some random noise with time even under constant light exposure. The random noise can be assessed for a digital camera by taking the image in a dark room with the lens cap on, thereby preventing the light from reaching the image sensor. Figure 3.4 shows the random noise of the camera used in this research; a 10% random intensity noise was observed.

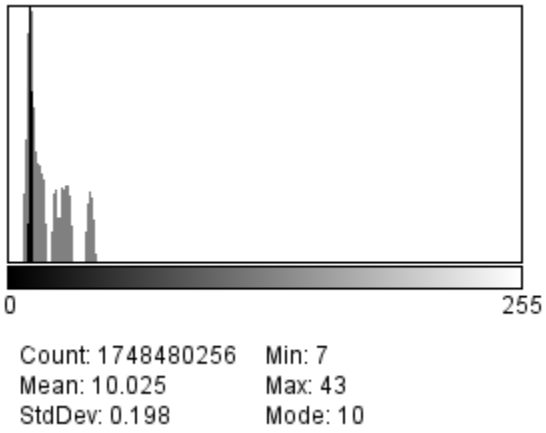

(a)

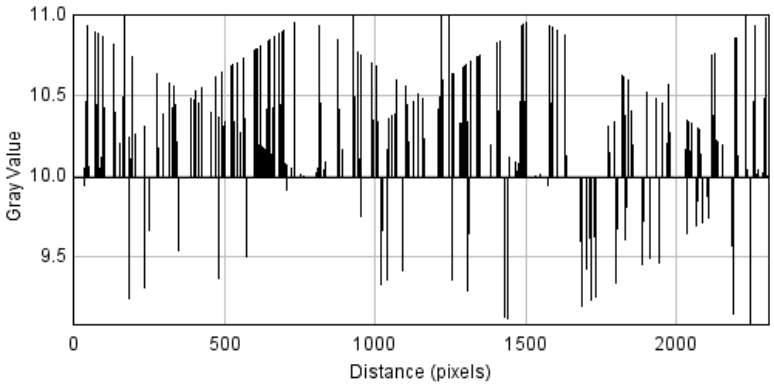

(b)

Figure 3.4 Random intensity noise of a digital camera: (a) histogram and (b) linear profile.

3.3.2 Digital Image Correlation Technique

The digital image correlation (DIC) technique is a non-contact optical method employed in experimental mechanics to obtain full-field surface displacements of a specimen during a loading event. A similar technique, called Particle Image Velocimetry (PIV), is employed in experimental fluid mechanics for obtaining the velocity field in a fluid. Both techniques rely on digital imaging of the specimen during loading and obtaining the displacement field through correspondence. The unique correspondence between a sub set of an image before loading (reference image) and after loading (deformed image) requires the specimen surface to exhibit random, non-repeating and isotropic textures called the speckle pattern (Schreier et al., 2009).

The basic principle of DIC is that the area of interest in the reference image is divided into a virtual grid. The spacing of the grid defines the measurement resolution. The displacement calculations are made at each node of the grid by tracking the same points (pixels) from the reference image to that in the deformed image. To compute the displacement at point $P(x_0,y_o)$, a square subset window of length L consisting of (2M+1) × (2M+1) pixels centered at point P is defined in the reference image. The corresponding location of the subset window is searched for in the deformed image. The degree of similarity between the reference and target subset windows is evaluated using a predefined correlation criterion. The matching procedure is completed by searching for the pixel position in the deformed window leading to a peak in the correlation coefficient. A pixel grouping, which corresponds to a particle grouping, is referred to as a domain *subset* in the DIC literature or a *window* in PIV literature. This thesis will use DIC terminology from this point on. The displacement vector of a subset is obtained from the difference between the coordinates of the centers of the subset in the original configuration and the corresponding subset in the deformed configuration as determined using a peak correlation algorithm. Figure 3.5 shows the graphical representation of the image correlation process for a single subset. The detailed theoretical aspects of DIC are covered in Schreier et al. (2009), which readers may consult for further understanding of the subject.

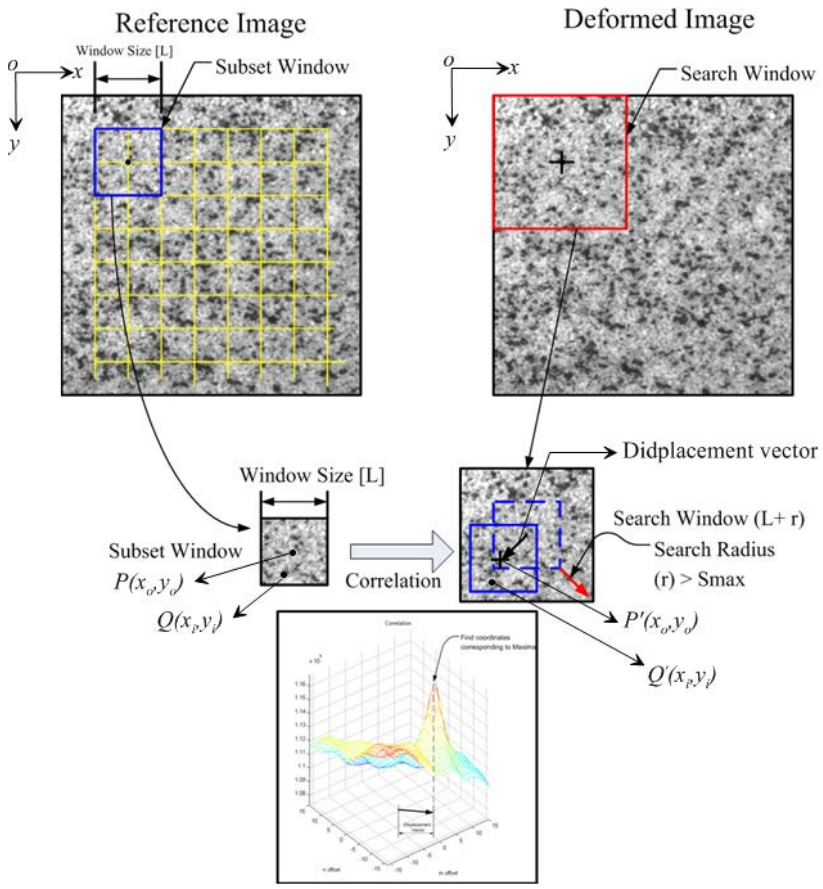

Figure 3.5 Image correlation procedure for a subset

3.3.2.1 Template Matching Criterion

There are two types of criterion for template matching of a small subset (n pixels size) of the reference image and the corresponding displaced and deformed subset of the deformed image. One criterion is based on cross-correlation (CC) tracking and the other is based on minimization of the grey value difference (SSD) between the two images. The pixel grey level intensity is represented by discrete spatial domain functions f_i in the original, undeformed image and g_i in the deformed image. The basic assumption in this technique is that the pixel grey level intensity magnitudes in images after deformations remains essentially the same (except for Gaussian random noise). Table 3-1 lists specific criteria commonly used in DIC analyses.

Table 3.1 Summary of common correlation criteria (After Pan, 2010)

Cross-correlation (CC)	Sum of squared difference (SSD)	Performance
$C_{CC} = \sum f_i g_i$	$C_{SSD} = \sum (f_i - g_i)^2$	Sensitive to all changes of deformed subset intensity
$C_{NCC} = \frac{\sum f_i g_i}{\sqrt{\sum f_i^2 \sum g_i^2}}$	$C_{NSSD} = \sum \left(\frac{f_i}{\sqrt{\sum f_i^2}} - \frac{g_i}{\sqrt{\sum g_i^2}} \right)^2$	Insensitive to scale changes of deformed subset intensity
$C_{ZNCC} = \frac{\sum \overline{f}_i \overline{g}_i}{\sqrt{\sum \overline{f}_i^2 \sum \overline{g}_i^2}}$	$C_{ZNSSD} = \sum \left(\frac{\overline{f}_i}{\sqrt{\sum \overline{f}_i^2}} - \frac{\overline{g}_i}{\sqrt{\sum \overline{g}_i^2}} \right)^2$	Insensitive to scale and offset changes of deformed subset intensity

In Table3-1: $\overline{f} = \frac{1}{n}\sum_{i=1}^{n} f_i,\ \overline{g} = \frac{1}{n}\sum_{i=1}^{n} g_i,\ \overline{f}_i = f_i - \overline{f},\ \overline{g}_i = g_i - \overline{g}$

Pan (2010) and Wereley (2010) have shown that both types of criterion are related and can be deduced from each other. For example, the zero normalized sums of squared difference (ZNSSD) criterion is related to the zero normalized cross-correlation (ZNCC) criterion as follows:

$$C_{ZNSSD} = \sum \left(\frac{\overline{f}_i}{\sqrt{\sum \overline{f}_i^2}} - \frac{\overline{g}_i}{\sqrt{\sum \overline{g}_i^2}} \right)^2 = \sum \left(\frac{\overline{f}_i^2}{\sum \overline{f}_i^2} - 2\frac{\overline{f} \cdot \overline{g}_i}{\sqrt{\sum \overline{f}_i^2}\sqrt{\sum \overline{g}_i^2}} + \frac{\overline{g}_i^2}{\sum \overline{g}_i^2} \right) \tag{3-1}$$

$$C_{ZNSSD} = 2 - 2\frac{\sum \overline{f} \cdot \overline{g}_i}{\sqrt{\sum \overline{f}_i^2}\sqrt{\sum \overline{g}_i^2}} = 2(1 - C_{ZNCC}) \tag{3-2}$$

3.3.2.2 Subset Shape Function

The imaging template matching criteria discussed so far are suitable for determination of average in-plane displacements (translations) of typically square subsets of two images. In the case of complex displacement fields, with which compression, elongation, shear and rotation are non-negligible; the initially square subset in the reference image does not remain square and gets distorted and rotated considerably in the subsequent deformed images. To account for subset deformation, an appropriate shape

function is introduced into correlation algorithms to transform the pixel coordinates of the reference subset into the coordinates of the deformed image. In this way, the desired matching accuracy is achieved even in very complex displacement fields. Wereley & Gui (2003) also proposed an iterative window deformation cross-correlation algorithm in which the interrogation window coordinates are interpolated in the deformed image by decomposing the initial iterative displacement into the translation (average displacement) and the shear part and applying the window shifting and shearing in the subsequent iterations. The proper choice of a subset shape function is essential for improved precision in displacement measurement. Therefore the knowledge of expected displacement a priori or an iterative correlation scheme is necessary for displacement measurement in a complex displacement field.

Schreier et al. (2009) showed that, even for very small rotation angles, de-correlation takes place as can be seen in the plot of correlation coefficient residuals versus rotation angle shown in Figure 3.6 which is obtained by rotating the image at its center incrementally and performing the image correlation using the sum-of-squared-difference criterion.

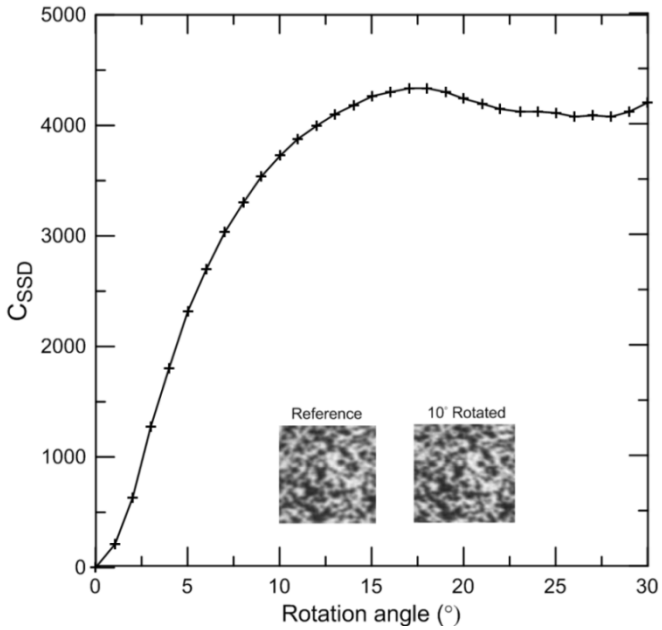

Figure 3.6 De-correlation due to rotation (after Schreier et al., 2009)

Various subset shape functions have been proposed in the literature for accounting for subset/window deformation. Wereley & Gui (2003) used a four-point bilinear interpolation method for subset deformation. Polynomial shape functions are used for increasingly complex subset deformation. A zero-order polynomial shape function represents pure rigid body translation, a first-order polynomial function or affine transformation can be used for translation, rotation and shear; quadratic and higher-order shape functions can be used for more complex displacement fields. White & Bolton (2004) found that a soil element located near the tip zone of the model pile during installation undergoes rotation of up to 30 degrees with intense shearing; therefore, a higher-order subset shape function is needed for DIC analysis during penetrometer installation.

3.3.2.3 Sub-Pixel Displacement Measurement

Various algorithm have been proposed in the literature for sub-pixel displacement estimation as discussed by Pan et al. (2009). The two most widely used sub-pixel displacement measurement methods are the iterative spatial domain cross-correlation algorithm and the peak-finding algorithm. In the iterative cross-correlation algorithm, the relative deformation of subset in the deformed image is taken into account through interpolation of light intensity of deformed images, by using a suitable subset shape functions. It makes the correlation function as a continuous non-linear function rather than a discrete correlation function otherwise, and the displacement at the sub-pixel level is automatically calculated during the iterative solution procedure. On the other hand, the peak-finding algorithm detects the location at which peak correlation occurs for a local discrete correlation matrix. The least square fitting or interpolation is used to approximate the local correlation matrix and the peak position of approximated curve is taken as sub pixel displacement. The VIC 2D, a commercial digital image correlation software used in this study utilizes the iterative spatial domain cross-correlation technique for calculation of sub-pixel displacements.

3.3.3 2D DIC vs. Stereo DIC

Two-dimensional (2D) DIC is suitable for planar tests, in which there is no excessive out-of-plan-displacement. Otherwise, stereo/3D DIC is preferred for displacement measurement accuracy. In the chamber set up used in the present research, the soil displacement observation is done on a planar surface in which, for the axisymmetric penetration problem, no out-of-plane-displacements are expected. Experimentally, negligible out-of-plane soil displacements may be occur due to the deformation of the observation window under the large stresses developing below the penetrometer tip. In order to quantify these out of plane displacements, we also performed one penetration test with 3D DIC. The stereo images were recorded during re-jacking of a penetrometer using Correlated Solutions 3D DIC system. The image correlation analysis was performed using VIC3D software. Only the top observation window was imaged during the test as two digital cameras are required for 3D DIC for imaging of a single observation plane. Figure 3.7 shows the images acquired in both cameras during the penetration test, the contour plot and the radial distribution of the out-of- plane-displacement after a penetration depth of 5 times the penetrometer diameter. It can be seen that the out of plane displacement is very small (of the order of 0.08mm). The deformation of the Plexiglas window is of same order as that calculated from FEM analysis of the calibration chamber front wall, as discussed later in section 4.2.3.2.

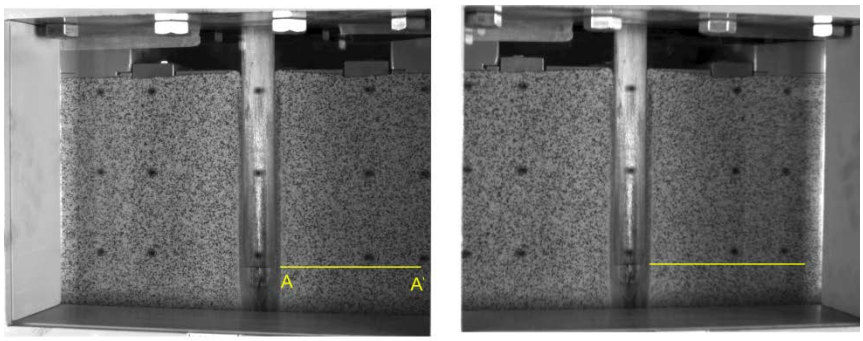

(a)

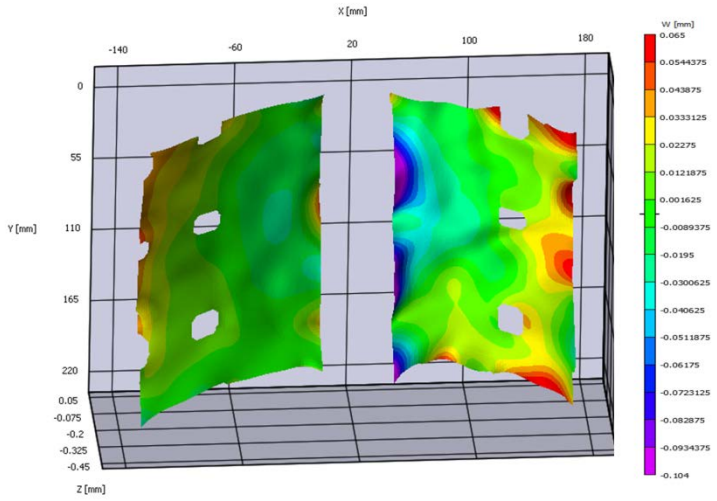

(b)

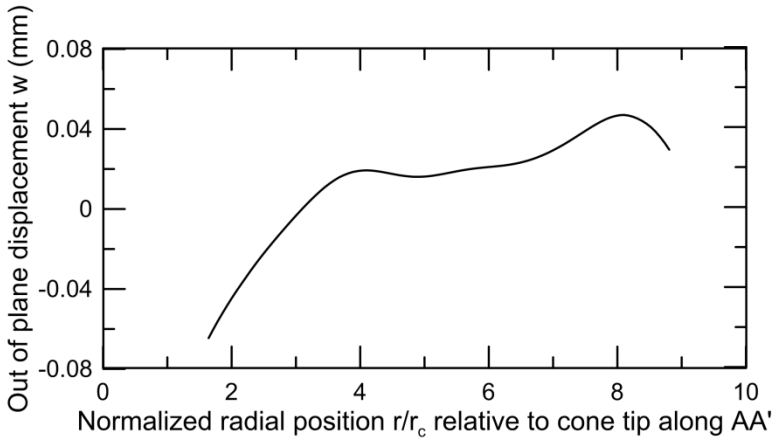

(c)

Figure 3.7 3D DIC results: (a) stereo images during cone penetration, (b) contour plot and (c) radial distribution of out-of-plane displacement.

3.3.4 Performance and Accuracy of Correlation Functions

The predictive performance of correlation functions was compared using synthetic PIV recordings. The complex 4-roll mill flow was simulated similarly to done by Wereley & Gui (2003) using the EDPIV software. The synthetic image recordings were of digital resolutions of 1024×1024 pixels. The particle size was 2-5 pixels and the maximum displacements of 6.5 pixels were present at the corners of the simulated image. The particle density was 0.0195 particle/pixel and about 20 particles were present in a 32×32 pixel window. Figure 3.8 shows the simulated image pair and vector plot of applied flow. Two correlation functions were tested: the central difference interrogation (CDIC) correlation with 4-point image correction and zero-normalized sum of squared difference (ZNSSD) with affine transformation (bilinear interpolation) of subset shape function. The side length of the subset was varied between 8 pixels and 64 pixels. Figure 3.9 shows the comparison of the normalized error in horizontal and vertical displacements using both correlation criteria. The ZNSSD criterion performs slightly better for smaller size of the subsets. For subset sizes equal to 32 pixels and larger, the performance of both correlation functions is comparable. The effect of subset shape functions was also studied by performing the correlation using the ZNSSD criteria with linear and quadratic shape functions. The higher-order subset shape functions produced less error for smaller subset windows but the subset shape function effects are negligible for larger subset sizes. The results have shown that the increased window size with low-order subset shape function yields similar accuracy as use of 2^{nd} order subset shape function. These observations show that until a suitable REV for the material is reached, it is not possible to accurate capture the displacement field in a continuum sense.

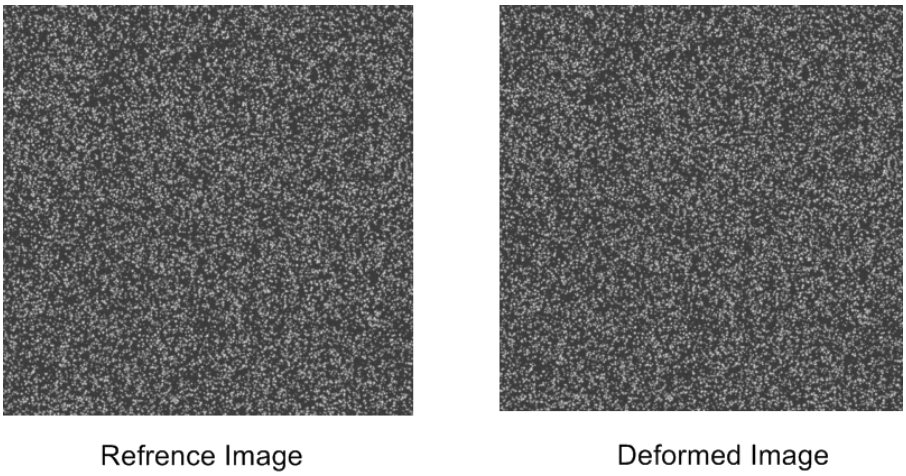

(a)

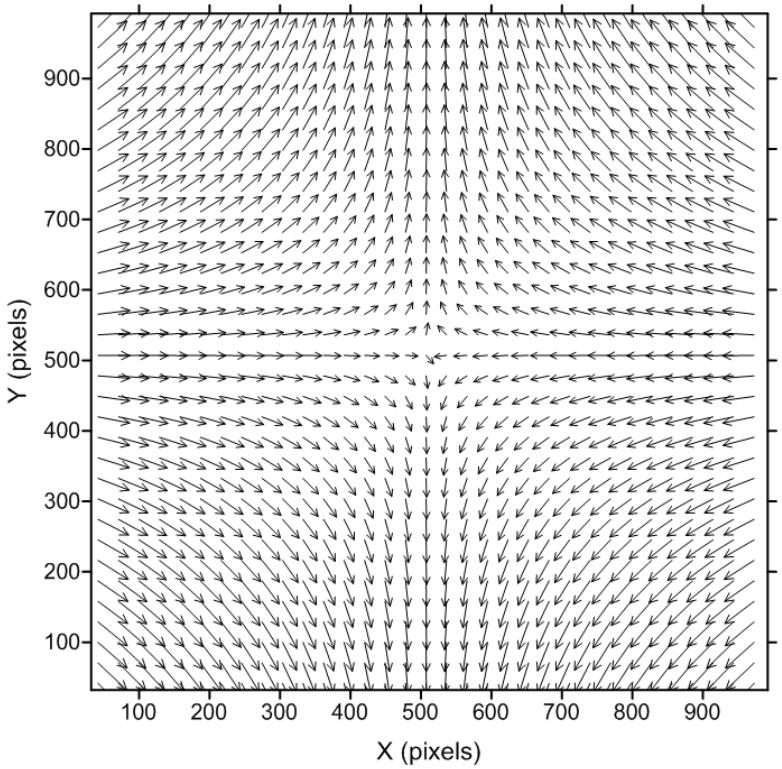

(b)

Figure 3.8 Correlation function test: (a) simulated image pair, and (b) applied complex flow.

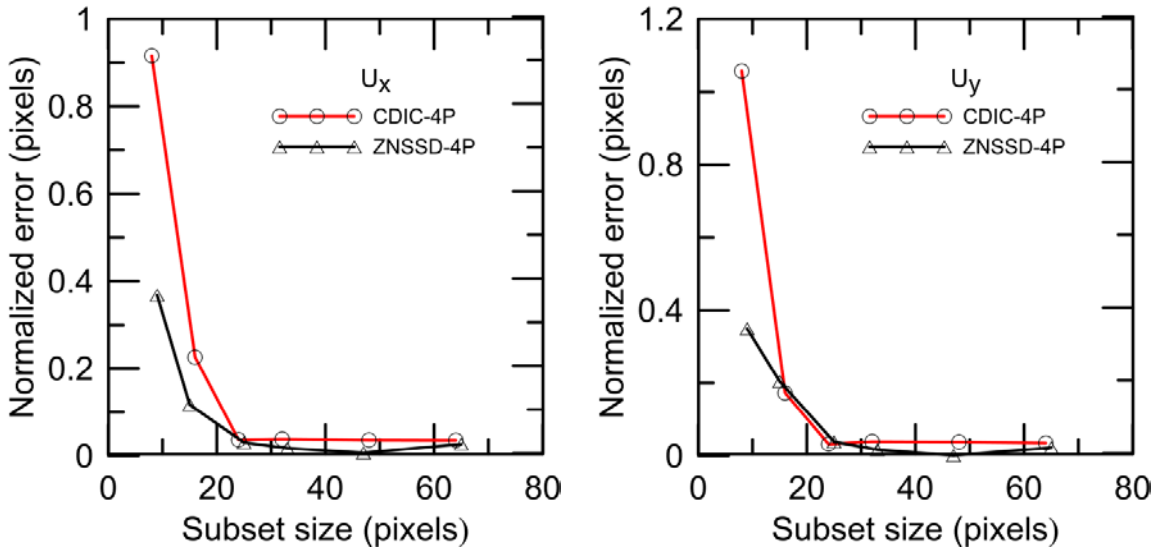

(a)

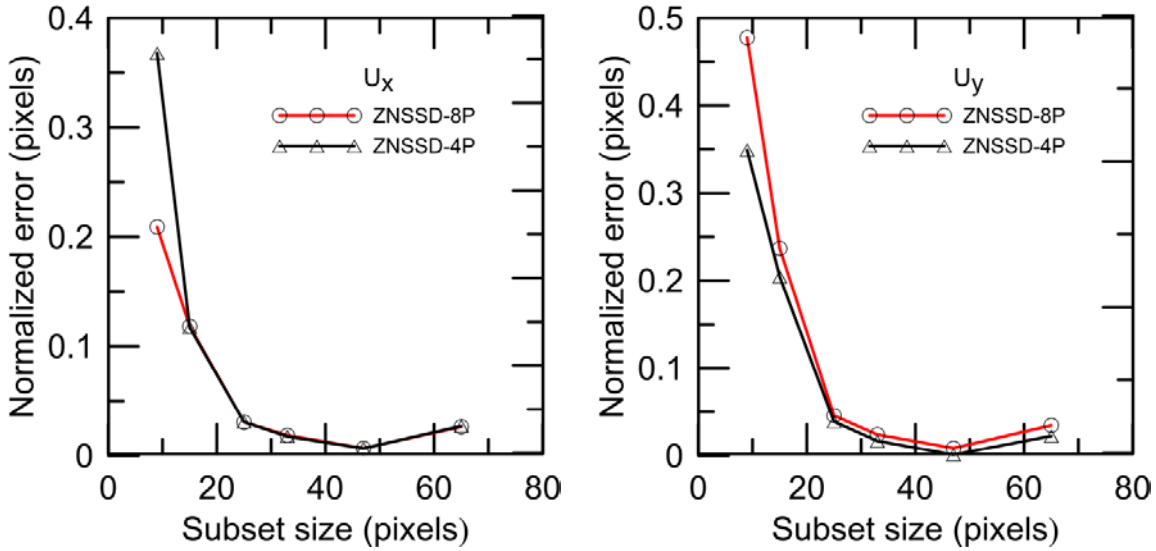

(b)

Figure 3.9 Comparison of correlation criterion: (a) CDIC vs. ZNSSD, and (b) influence of subset shape functions.

3.3.5 Optimization of DIC/PIV Parameters for Sand

As the soil deformation during cone penetration process is not known a priori, the assessment of the accuracy of DIC measurement is difficult. To overcome this, a simple translation test for a small soil sample was designed to obtain optimized correlation parameters and estimates of measurement error. The transparent translation box, 100 × 50 mm in size, was designed to apply horizontal and vertical translation to a soil sample. The transparent soil box was mounted on a 3-axis micrometer optical stage. Translational increments of 0.025 inch (0.625 mm) were applied. Images were recorded at each increment. The total translation applied was more than 15 mm (the radius of the cone penetrometer used in this study) to account for large displacement expected in actual cone penetration test. Figure 3.10 shows the experiment test set up. Both artificially textured and natural color sand samples were tried.

Different correlation algorithms were tested for each set of images of the natural-color sand and the textured sand samples. A 1% pixel accuracy criterion was used in all methods. The correlation algorithms tested are as follows:

a. central difference interrogation correlation with continuous window shifting (CWS) and 4 point image correction (CDIC-4P);
b. central difference interrogation correlation with CWS and 9-point image correction (CDIC-9P);
c. central difference interrogation correlation tracking with CWS and 4-point image correction (CDIC-Corr tracking); and
d. normalized sum of square difference with 4-point optimized subset shape function (NSSD-DIC).

Overall, a displacement accuracy of 8 microns was achieved for the textured sand sample, whereas a 27-micron displacement accuracy was observed for natural color sand. The errors of linear camera calibrations are neglected. The effect of subset size was also investigated by changing subset size between 8 and 128 pixels. Figure 3.11 shows the RMS error plot for both the textured and the natural-color sand sample. The test results

indicate that that a smaller RMS error is observed for textured sand then for naturally colored sand due to improved texture contrast.

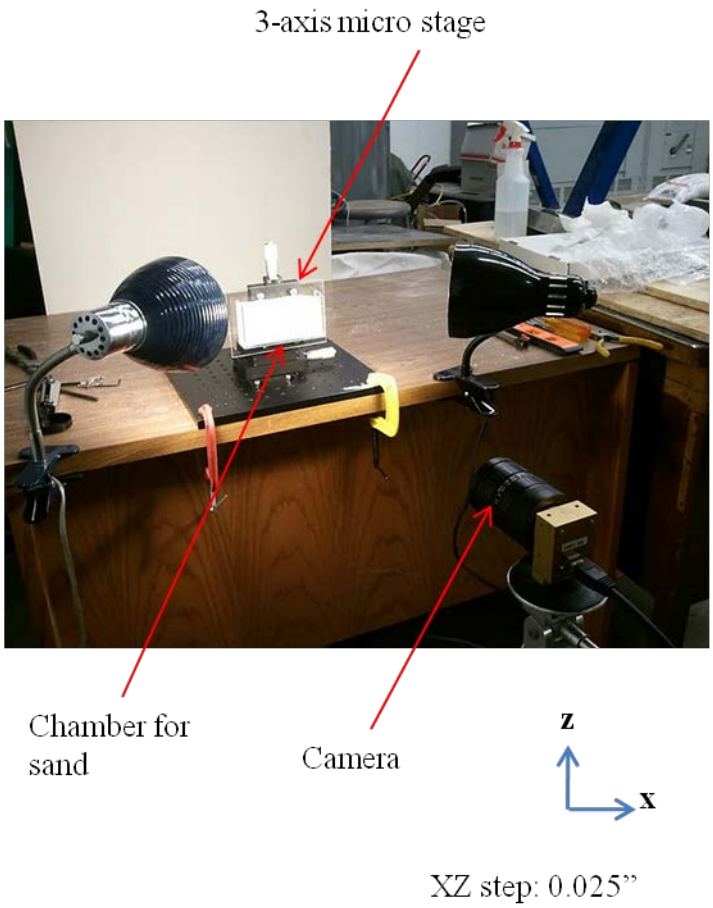

Figure 3.10 Simple translation test set up

The displacement measurement error decreased with increasing size of the subset. As the subset size increased beyond 32 pixels, the gain in accuracy is not large but computation time increases substantially. These tests clearly indicated that the use of textured sand is beneficial for improved accuracy especially during the analysis of a large number of images collected during actual cone penetration test. The NSSD showed better correlation results and is the preferred choice for image correlation analysis.

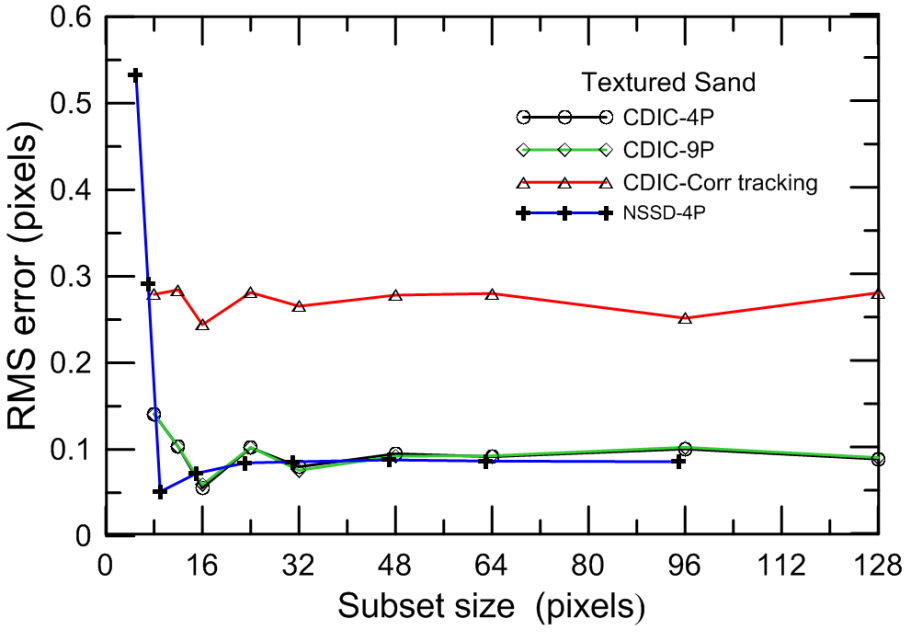

(a)

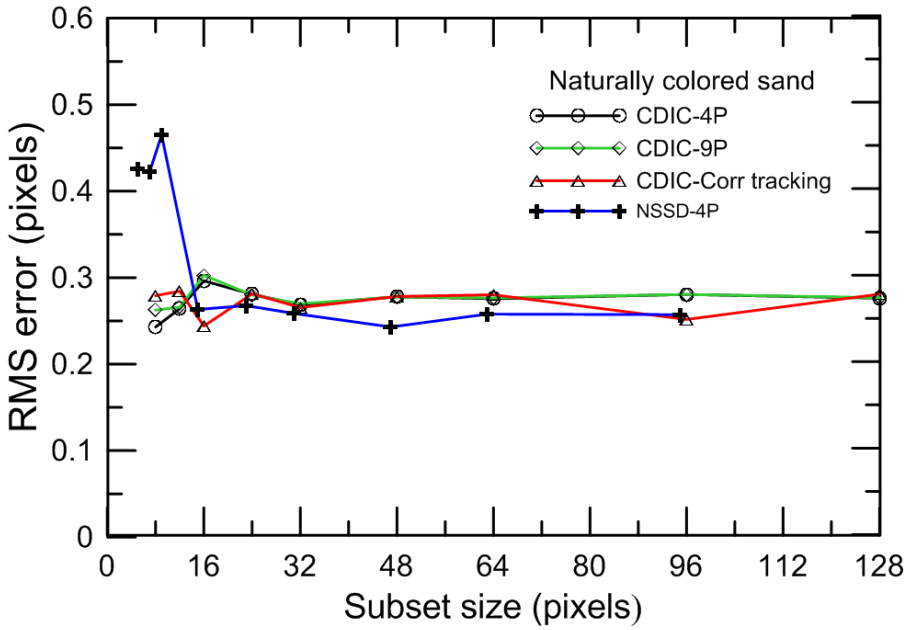

(b)

Figure 3.11 Displacement RMS error plot for translation test: (a) textured sand, and (b) naturally colored sand.

Since incremental correlation is required to be performed during a penetration test, error accumulation is a potential problem. The total error in the displacement field can be minimized by selecting the optimum number of images for incremental correlation

analysis instead of using the entire set of images collected during the penetration test. Out of average 1500 images recorded during each penetration test, every fifth image was used for DIC analysis. This image increment was optimized by trial and error for achieving the desired correlation accuracy (not to be affected by particle disappearance from view due to large displacement increments) and minimizing the accumulation of error.

3.3.6 Sources of Errors in Displacement Measurements

3.3.6.1 Effects of Particle Disappearance from View

The presence of intense shearing and rotation around the penetrometer tip can displace some particles out of plane (i.e., a colored sand particle may move behind the white sand particles or vice versa), which means that they appear in one but not both images to correlate. In order to quantify the particle disappearance effect, we manually replace the grey level intensity of a 2×2 pixels region in a template image of 50×50 pixels randomly. The average dark sand grey level particle intensity, found to be 83, was replaced by the bright sand particle grey level intensity of 230 and vice versa. The correlation coefficient (C_{NCC}) was determined by performing normalized cross correlation (NCC) between the original and the modified subset. In a second experiment, the regions selected for intensity change were matched particle shape closely. Figure 3.12 shows that the correlation of confidence level less than 90% takes place when the percentage of the area modified in the above manner is greater than 3% of the subset area or 3-4 sand particles disappear from view.

To see how many particles were going out of view in an actual cone penetration experiment, we monitored closely along the cone tip the movement of the sand particles. It took 10 penetration increments (images) for complete disappearance of the 3-4 sand particles in a region of 100 ×100 pixels. The incremental correlation coefficient achieved between two successive images was 0.9456 due to the intensity normalization procedure in the correlation criteria. Therefore, in the incremental correlation, the effect of particle disappearance is negligible. With regards to particle rotation, we observed that, with the large mean stresses around the cone tip, the interlocking effect prevents particle rotation, and the effect of rotation is therefore negligible and does not need to be corrected for.

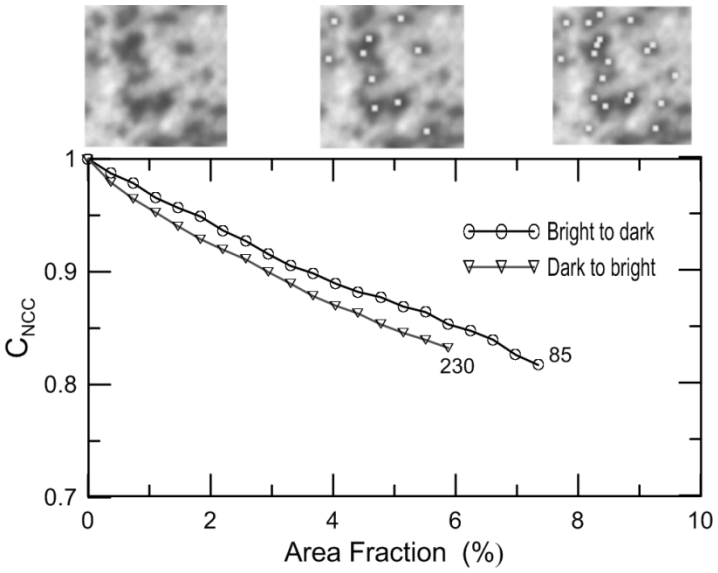

(a)

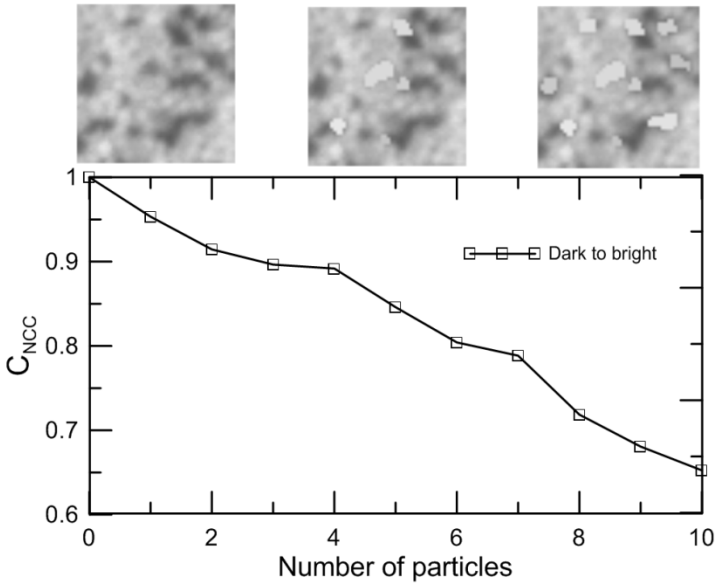

(b)

Figure 3.12 Effect of particle disappearance on image correlation: (a) comparison of dark and bright particles disappearance, and (b) effect of number of particles

3.3.6.2 Effect of Glass Scratching

The scratching of the glass viewing window will affect the accuracy of measurements by creating stationary speckle patterns that do not move with the soil. In case this scratching becomes excessive, it creates a masking effect and the measured soil displacement accuracy in the scratched zone will be compromised. In order to assess the

maximum effect of glass scratching, a badly scratched glass (glass sheet after 6 trial penetration tests) was placed behind the viewing window. A rectangular penetrometer painted with a speckle pattern was caused to slide against the scratched glass in the empty chamber. The incremental DIC analysis was performed on 230 images. The known penetrometer travel distance was compared with that calculated using DIC. A maximum error of 0.375mm was observed after penetrometer movement of 95.45mm. To separate the accumulated error due to incremental correlation, the initial image was also correlated with the final image and the resulting error was 0.29mm. This additional error was avoided by frequent change of glass sheet after 1-2 penetration tests depending upon observed scratching of glass. Figure 3.13 shows the scratched zone of glass window and measurement results.

3.3.6.3 Effect of Illumination

The non-uniform illumination of the measurement plane can cause systematic error on DIC measurement. Moreover, the heat generated due to illumination may affect the image sensor and can cause additional distortions in the images. To reduce this effect we used Compact Fluorescent Lights (CFL) not to generate additional heats as compared to Halogen flash lights. The use of reflectors with careful light alignment was made to distribute the lights evenly and the duration of illumination was kept to a minimum by keeping the lights on only during the penetration tests.

The effects of light offset and variation in scale were also minimized by adopting the robust DIC correlation criteria of Zero Mean Normalized Sum of Squared Difference (ZNSSD), which take into accounts light variation effects.

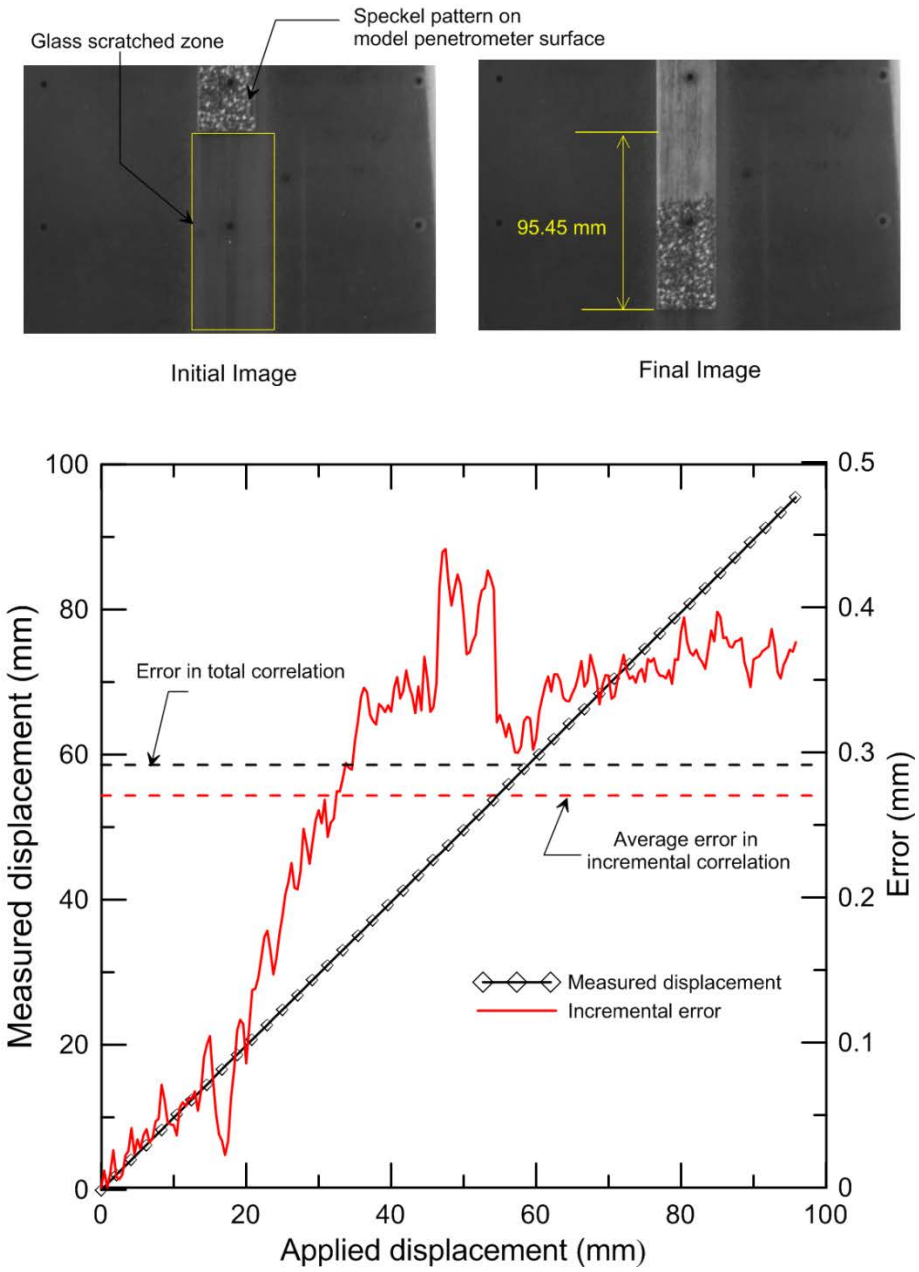

Figure 3.13 Displacement errors due to glass scratching

3.3.6.4 Effect of Lens Distortion

The common lens suffers from radial and tangential distortion caused by the location of the aperture stop during image capture and the distance between the image and object. These distortions appear as a variation in image scale at the radial distance from the optical axis that usually aligns with the center of the image provided image

plane and lens center are coplanar. If the magnification increases with the distance from the optical axis, pincushion (radial) distortion takes place (Figure 3.14). When the magnification decreases with the distance from the optical axis, barrel (tangential) distortion takes place. These distortions will induce errors in DIC measurements not only in spatial position but also in measured displacements. The relative displacement from the optical axis due to lens distortion induces pseudo strains and displacements. The effect of lens distortions can be minimized by selecting a telocentric lens or a high-quality lens with optimized distance from the object. This optimized distance can be experimentally determined so that the aperture coincides with the lens position. Another possible method is to use camera calibration in order to account for lens distortions in DIC measurements. In order to quantify distortions of the camera lens used in this experimental set up, we performed camera calibration with three different distances between the object and the lens.

The distortion calibration target grid (obtained from US Max Levy) was placed in front of and behind the glass viewing window without disturbing the lens focus, and images of the calibration target were obtained. In this way we investigated the effect of thick viewing window on lens distortions. The Heikkila camera calibration model (Heikkilä & Silvén, 1997) and their online published MATLAB software was used for calibration. The circular control points in image space were located using the geoCENTROID software (White et al., 1999). The details of the camera model adopted are explained later in Section 3.4. Table 3.2 shows the radial and tangential coefficients obtained from calibration tests. The lens distortions in air and behind the glass were similar, except in close range calibration, when the radial distortions increased. These results indicate that the thick viewing window that we have used had only marginal effect on image distortion because of the large distance between the viewing window and the camera. In all penetration tests, we positioned the camera at a distance of 1200mm from the viewing window and accurately aligned the cameras with the observation plane using a three-axis level and a cross-hair target.

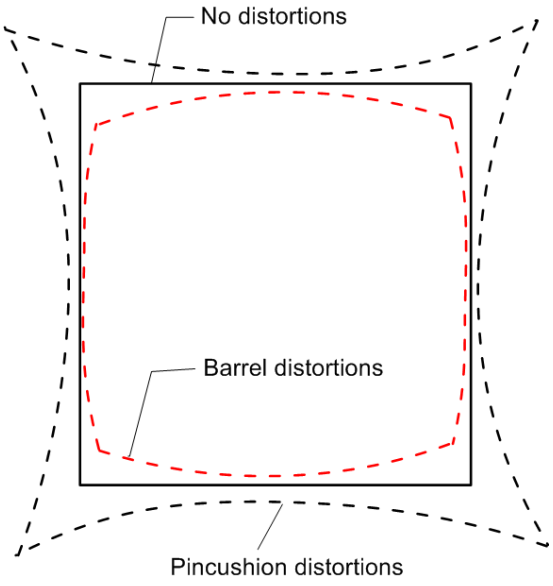

(a)

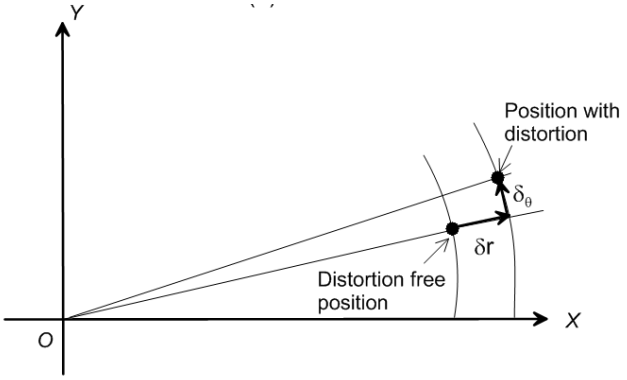

(b)

Figure 3.14 Lens distortions: (a) barrel and pincushions distortions (b) effect on DIC displacement.

Figure 3.15 shows the calibration target grid used and the radial distortion map in calibration test 1 performed behind the glass.

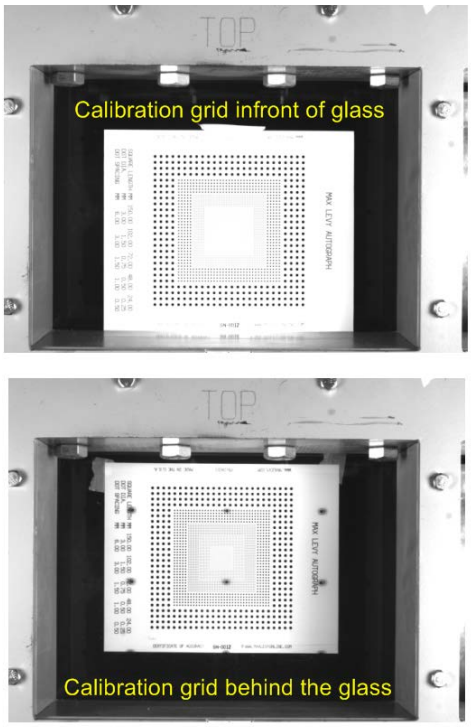

(a)

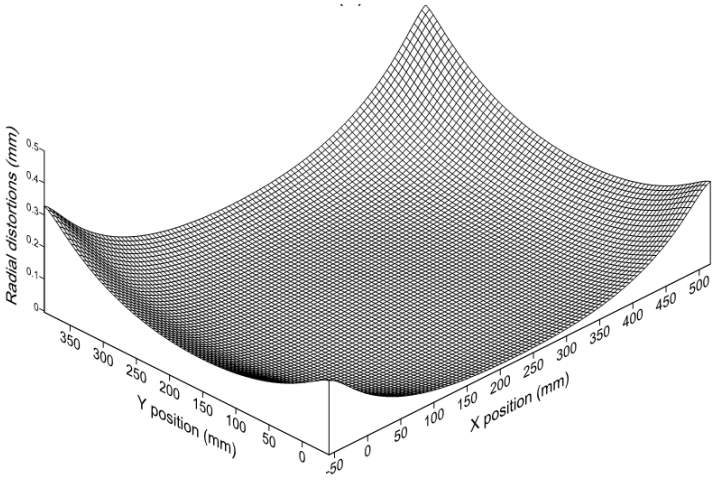

(b)

Figure 3.15 Camera calibration test: (a) calibration grid in front of and behind the glass, and (b) the radial distortion map for the target grid positioned behind the glass.

Table 3.2 Typical lens distortions in air and behind the viewing window

Distortion coefficients (mm)	Object to camera distance (mm)					
	1000		1200		1400	
	Air	Glass	Air	Glass	Air	Glass
Radial						
k_1	-6.58e-05	-6.64e-04	-8.35e-05	8.74e-05	-2.17e-04	-2.12e-04
k_2	-1.78e-05	1.65e-04	-7.86e-06	-1.48e-05	2.11e-06	6.28e-07
Tangential						
p_1	5.53e-04	5.24e-04	5.12e-04	5.01e-04	5.99e-04	6.28e-04
p_2	4.76e-04	3.39e-04	4.73e-04	5.49e-04	5.54e-04	5.46e-04

3.3.6.5 Effect of Refraction

The presence of the Plexiglas viewing window between the camera and sand observation plane will induce three types of distortions (Salma et. al, 1980): (1) displacement of image plane, (2) radial distortions, and (3) deterioration of image quality. The glass plate does not change the focus length when the optical axis is normal to soil observation plane. For increasing incidence angles (measured from the optical axis), the image point is displaced radially outward. The outward image displacement would induce a pseudo strain due to relative difference of radial displacement caused by the refraction. This additional radial distortion as shown in Figure 3.16 can be calculated from Snell Law using (Gardener & Bennete 1927):

$$\alpha_r = mt\left(\tan\beta' - \frac{\tan\beta}{n}\right) \tag{3-3}$$

where m is the scale ratio (the ratio of the size of the image in pixels to the object size in length units), t is the thickness of the glass sheet, n is the refractive index of the glass sheet and

$$\sin\beta / \sin\beta' = n \tag{3-4}$$

In the typical experiment done in the course of the present research, the field of view is 450 × 337 mm, the image sensor size is 5.7 × 4.28mm (so the magnification *m* is 5.76), the camera lens has a fixed focal length of 12.5mm, the half-field angle β is 12.25 degrees, and the thickness *t* of the Plexiglas and glass sheet (with refractive index *n* =1.50) is 82.45 mm. The maximum error in the radial displacement at extreme points of the image can be calculated as 0.153 mm or 0.882 pixels. To reduce the refraction distortion, two possibilities exist: placement of a compensation glass plate of appropriate thickness (*t/m*) between the camera lens and the image plane or consideration of the additional radial distortion component in camera calibration. We used a target marker behind the thick PlexiglasPlexiglas sheet for calibration before every test; this corrects for the combined effect of lens and refraction distortions. Moreover, we optimized the distance between the camera and object (1200 mm) so that minimal refraction effect took place.

In order to estimate the combined lens and refraction image distortion effects that would happen in the absence of calibration, we acquired a sequence of images of a stationary soil sample. The DIC analysis was performed on this set of images. The resultant displacement and induced pseudo strains contour plots are shown in Figure 3.17. It is evident the relative combined noise of refraction and light intensity changes are of the order of 0.010% strain, which is negligible. The distribution of displacement and strain across the width of the image is also shown in Figure 3.17.

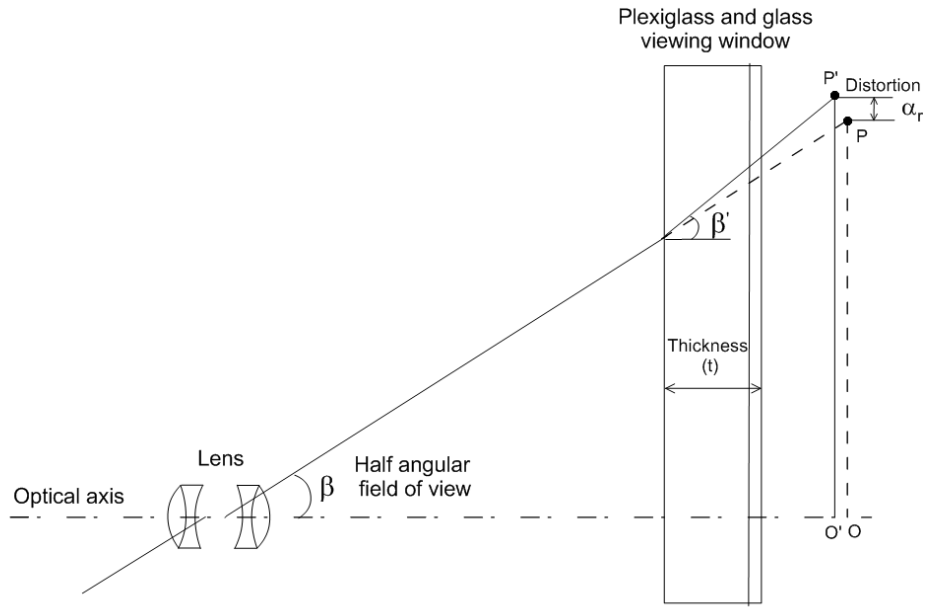

(a)

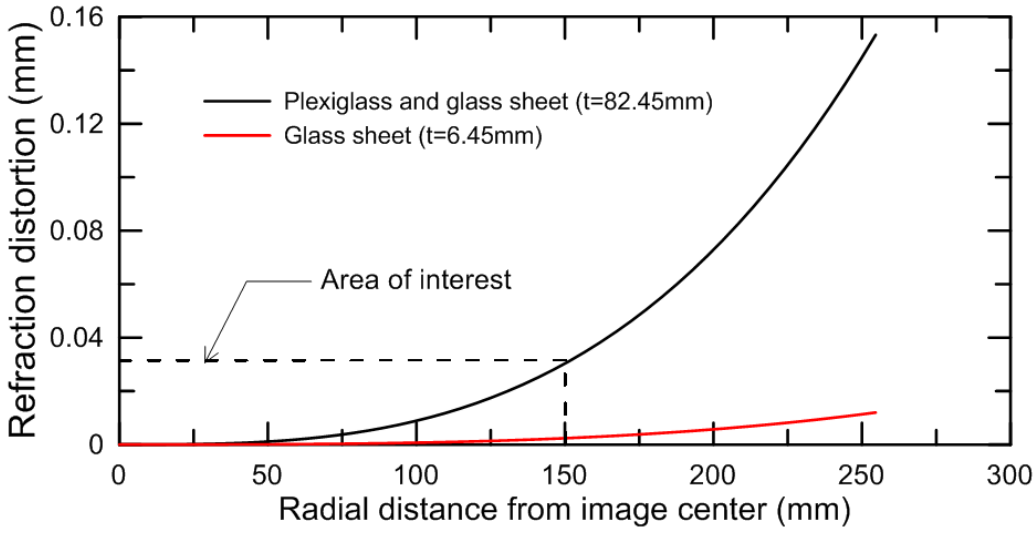

(b)

Figure 3.16 Effects of refraction: (a) radial distortion (b) expected radial distortion with increasing distance from optical axis.

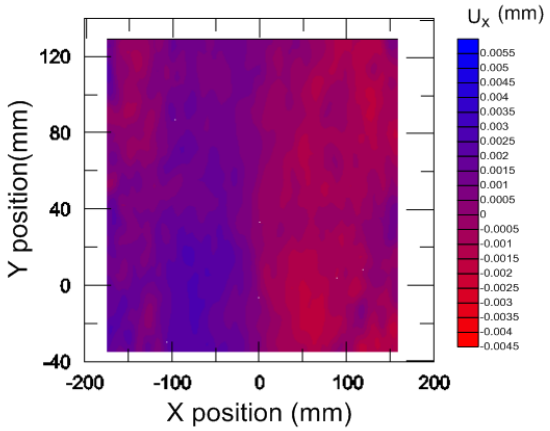

(a)

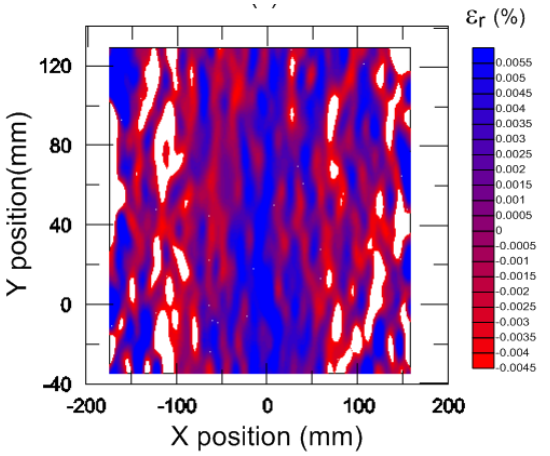

(b)

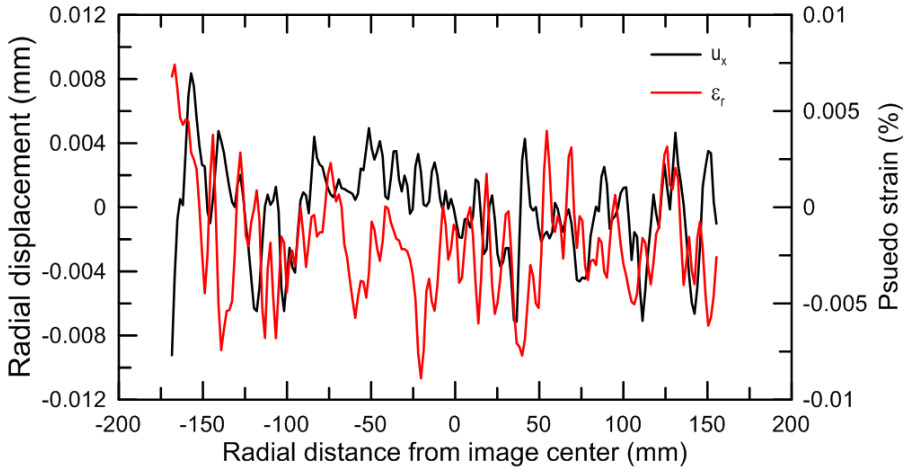

(c)

Figure 3.17 Refraction effects: (a) radial displacement, (b) radial strains, and (c) profile along width of image.

3.4 Camera Calibration Model

The classical pinhole camera model is based on perspective projection. The conversion from world coordinates to image space and vice versa needs three geometric transformations: between world and camera coordinates; between the camera and image coordinates; and between the image and sensor coordinates. Figure 3.18 shows the simple perspective model of a camera using front image plane projection. A point *M* having world coordinates (*X*, Y, *Z*) projects on image space through the pinhole perspective center R_c located in the camera coordinate system (*x*,*y*,*z*). The corresponding point in image space is *m* with coordinates system (x_i, y_i) with units of pixels. The origin of the image coordinate system lies at the optic axis. The image space point *m* also corresponds to a sensor point m_s with physical coordinates of (x_s, y_s) having metric units.

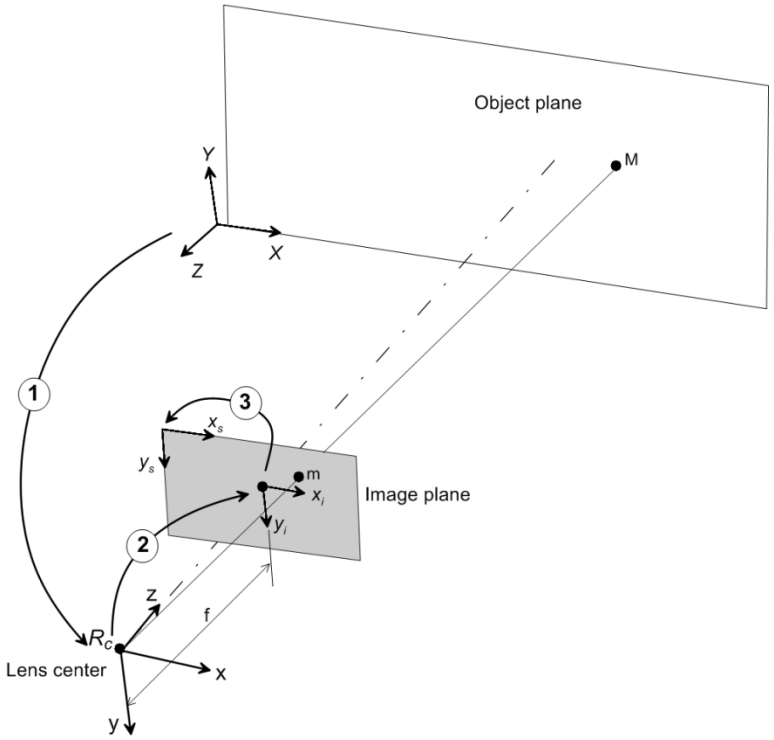

Figure 3.18 Pinhole camera model and three transformations

The first transformation between world and camera coordinates requires the rotation matrix [**R**] and translation vector **t**. The point *M* in world coordinate system can be converted to camera system origin R_c using homogenous coordinates as:

$$M = \begin{Bmatrix} x \\ y \\ z \\ 1 \end{Bmatrix} = [\mathbf{R}] \cdot \begin{Bmatrix} X \\ Y \\ Z \\ 1 \end{Bmatrix} + \mathbf{t} = \begin{pmatrix} \mathbf{R} & \mathbf{t} \\ 0 & 1 \end{pmatrix} \begin{Bmatrix} X \\ Y \\ Z \\ 1 \end{Bmatrix} \tag{3-5}$$

where rotation matrix:

$$[\mathbf{R}] = \begin{pmatrix} R_{11} & R_{12} & R_{13} \\ R_{21} & R_{22} & R_{23} \\ R_{31} & R_{32} & R_{33} \end{pmatrix} \tag{3-6}$$

and translation vector **t** is

$$t = \begin{Bmatrix} t_x \\ t_y \\ t_z \end{Bmatrix} \tag{3-7}$$

The second transformation is of point **M** in World coordinates expressed in the camera lens/projective center (*x, y, z*) to point *m* on the 2D image plane using camera pinhole camera model (see Figure 3-18) and homogeneous coordinates as:

$$\alpha \begin{Bmatrix} x_i \\ y_i \\ 1 \end{Bmatrix} = \begin{pmatrix} f & 0 & 0 \\ 0 & f & 0 \\ 0 & 0 & 1 \end{pmatrix} \begin{Bmatrix} x \\ y \\ z \end{Bmatrix} \tag{3-8}$$

where α is the scale factor between object and image coordinates and *f* is the focal length.

The transformation of image space coordinates on to local origin of sensor at top left corner is obtained by relating the image coordinates through the principal point (C_x ,C_y), that lies on optical axis. The parameters S_x and S_y are the horizontal and vertical scale factors expressed in pixels/unit length to convert metric dimension of sensor into pixels. In homogenous coordinates the image space coordinates are related in sensor coordinates expressed in pixels coordinates as:

$$\begin{Bmatrix} x_s \\ y_s \\ 1 \end{Bmatrix} = \begin{pmatrix} S_x & 0 & -S_x c_x \\ 0 & S_y & -S_y c_y \\ 0 & 0 & 1 \end{pmatrix} \begin{Bmatrix} x_i \\ y_i \\ 1 \end{Bmatrix} \tag{3-9}$$

Finally the combined transformation of world coordinates will be related to pixels coordinates for orthogonal camera sensor as:

$$\alpha \begin{Bmatrix} x_s \\ y_s \\ 1 \end{Bmatrix} = \begin{pmatrix} fS_x & 0 & C_x & 0 \\ 0 & fS_y & C_y & 0 \\ 0 & 0 & 1 & 0 \end{pmatrix} \begin{pmatrix} R & t \\ 0 & 1 \end{pmatrix} \begin{Bmatrix} X \\ Y \\ Z \\ 1 \end{Bmatrix} \tag{3-10}$$

where, C_x = -$S_x c_x$ and C_y = -$S_y c_y$.

In two-dimensional image correlation, if we assume the origin of the World coordinates to match that of the object and is located at the optical axis than the rotation tensor is identity and the sensor plane is normal to object plane (no skew is present in image) as shown in Figure 3.19, then the relationship between object coordinates to sensor position are simplified using the direct linear transformation (DLT) as proposed by Abdel-aziz I. & Karara M. (1971) to:

$$\begin{Bmatrix} x_s \\ y_s \end{Bmatrix} = \begin{Bmatrix} \left(\frac{fS_x}{Z}\right) X \\ \left(\frac{fS_y}{Z}\right) Y \end{Bmatrix} + \begin{Bmatrix} c_x \\ c_y \end{Bmatrix} = \begin{Bmatrix} s_x X \\ s_y Y \end{Bmatrix} + \begin{Bmatrix} c_x \\ c_y \end{Bmatrix} \tag{3-11}$$

where s_x and s_y are number of sensors per unit object length on the image plane in the horizontal and the vertical directions respectively. Four camera instinct parameters (s_x, s_y, c_x and c_y) are needed to relate the object coordinate with image plane coordinates.

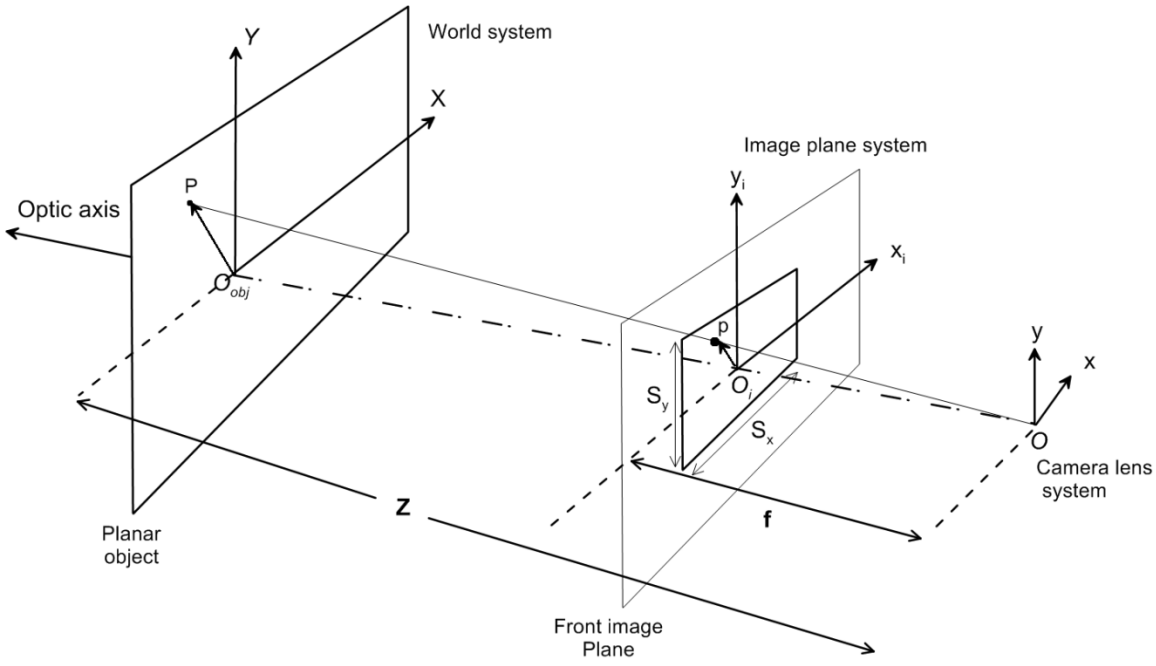

Figure 3.19 2D imaging of planar object and affine transformation of object point P on image plane point p (after Schreier et al., 2009)

3.4.1 Lens Distortions

The radial lens distortion displaces the point in the image plane radially from the optical axis. To account for the radial distortion of the image, additional radial distortion coefficients k_1 and k_2 are determined. The resultant additional displacement of the image point due to radial distortion can be found using the relationship proposed by Salma et al. (1980) as:

$$\begin{Bmatrix} \Delta x_{s-r} \\ \Delta y_{s-r} \end{Bmatrix} = \begin{Bmatrix} x_s \left(k_1 r^2 + k_2 r^4 \right) \\ y_s \left(k_1 r^2 + k_2 r^4 \right) \end{Bmatrix} \tag{3-12}$$

where r is the radial distance from the principal point, the center of the image at the optical axis for a coplanar image plane and lens center :

$$r = \left(x_s^{\,2} + y_s^{\,2} \right)^{1/2} \tag{3-13}$$

The tangential distortion is modeled similarly to the radial distortion: two tangential distortions parameters p_1 and p_2 allow calculation of the tangential component of the lens distortion through:

$$\begin{Bmatrix} \Delta x_{s-t} \\ \Delta y_{s-t} \end{Bmatrix} = \begin{Bmatrix} 2p_1 x_s y_s + p_2\left(r^2 + 2x_s r^2\right) \\ p_1\left(r^2 + 2y_s r^2\right) + 2p_2 x_s y_s \end{Bmatrix} \tag{3-14}$$

The total distortion is the summation of the radial and tangential distortions. For camera calibration with distortion, in addition to the instinct parameters (s_x, s_y, c_x and c_y), four extra lens distortion parameters (k_1, k_2 , p_1 and p_2) are to be determined. A total of 8 parameters are needed to define the image-object space transformation matrix for a 2D object plane which is perpendicular to the optical axis. The iterative solution is employed from known control points in object space to determine this transformation matrix. Once the transformation matrix is found, then any point coordinates in the image can be converted to corresponding object coordinates.

3.4.2 Camera Calibration Procedure

The goal of camera calibration is to determine the camera instinct and lens distortion parameters to convert the image pixel coordinates to object coordinates. To derive the camera parameters, a set of 45 image control points were printed on a transparent laminating film using 1440 DPI printer. The calibration target film covers the entire inner surface of the glass that is in direct contact with the Plexiglas.

The first step in calibration procedure is the precise location of control points in image space. The centroids of these control points were obtained using the Matlab geoCENTROID software (White et al., 2003). The precise image pixel coordinates are determined using intensity threshold criteria; an error in location less than 0.5 pixels was considered acceptable. The object space coordinates of these control points are printed on a calibration sheet and were checked for presence of any printing errors through a commercial calibration grid.

These control points were then used to establish the camera calibration parameters using the camera calibration toolbox for Matlab (Heikkilä & Silvén, 2000). The inverse model of the camera calibration tool was used to estimate the projection error. The amount of radial, tangential and total distortion can be determined through the camera calibration toolbox. The images are corrected for distortions before DIC analysis using the camera calibration toolbox (imcorr function of toolbox). A polynomial is fit according to the control point coordinates and pixel coordinates to get the image-to-object scale, which was chosen by minimizing the projection error of the projected world coordinates as compared to the original world coordinates. This procedure was followed for all tests. The complete camera calibration procedure is illustrated in Figure 3.20.

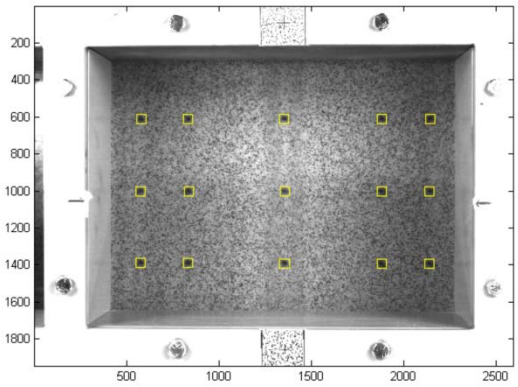

(a)

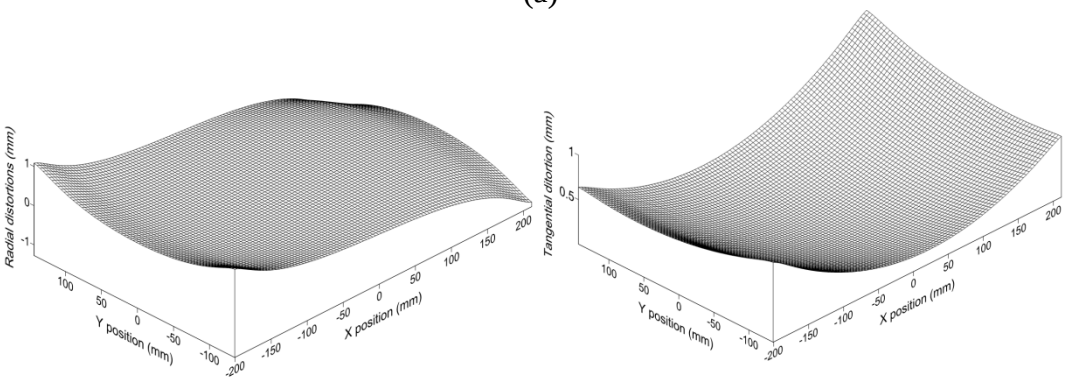

(b)

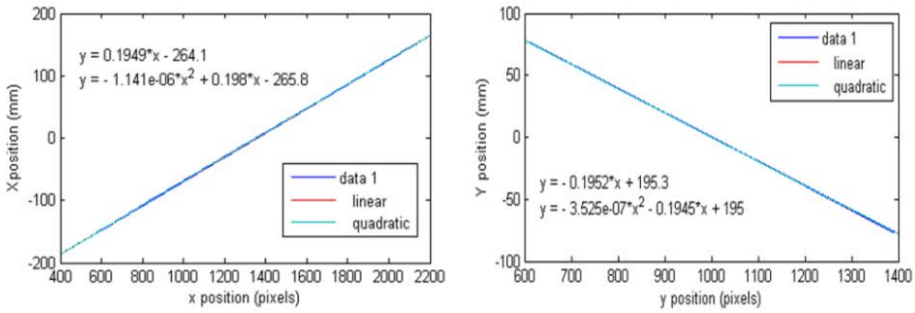

(c)

Figure 3.20 Camera calibration steps: (a) detection of control markers in image space, (b) deducing the camera instinct parameters and image correction, and (c) polynomial fit to corrected image coordinates (pixels) and object coordinates (mm).

3.5 Post Processing for Strain Field

The DIC analysis yields displacement data that can be post-processed to determine the strain field. Quadrilateral elements, such as Q_4, Q_8 and Q_9, could be used for derivation of the strain field. The problem with such a formulation is that the measurement grid of displacement is few sand particles (3-4 sand particles) spacing, which is approximately 2-3 mm, and the gauge length is too small to respect the continuum assumption for a representative element volume. The resultant strain field will be noisy. To overcome this, a more robust strain field calculation procedure was adopted using the commercial DIC software VIC2D.

In this approach, VIC-2D uses a square strain window of size $N \times N$ displacement measurement points that equals or exceeds $20 \times D_{50}$ was defined as user input. This size of strain window corresponds to a representative element volume (REV) for a coarse-grained material treated as a continuum. In VIC-2D, the displacement field obtained from the image correlation within the strain window is fit locally with a quadratic shape function:

$$u(x,y) = \beta_1 + \beta_2 x + \beta_3 y + \beta_4 xy + \beta_5 x^2 + \beta_6 y^2 \quad \text{(3-15)}$$

$$v(x,y) = \beta_7 + \beta_8 x + \beta_9 y + \beta_{10} xy + \beta_{11} x^2 + \beta_{12} y^2 \quad \text{(3-16)}$$

The unknown parameters β_i are computed through least-square fitting of equation 3-15 and 3-16 of the measured displacement data. For estimation of these twelve parameters, a minimum of 12 measurement points are required (this requires minimal strain window of size 5×5 displacement points).

$$E(\beta) = \sum_{i=1}^{N} \left(F(x_i, \beta) - f(x_i) \right)^2 \quad \text{(3-17)}$$

where x_i is location of measurement point, $f(x_i)$ are the displacement measurements at locations x_i, and $F(x_i, \beta)$ is the fitted model as function of unknown parameters β. Once the local surface fit is obtained, the estimates for local derivatives can be computed.

The derivatives of displacements are calculated at the center of the strain window (Figure 3.21) as:

$$\frac{\partial u}{\partial x}(x^{CP}, y^{CP}) = \beta_2 + \beta_4 y^{CP} + 2\beta_5 x^{CP} \tag{3-18}$$

$$\frac{\partial u}{\partial y}(x^{CP}, y^{CP}) = \beta_3 + \beta_4 x^{CP} + 2\beta_6 y^{CP} \tag{3-19}$$

The VIC-2D utilizes continuum mechanics formulation for deformations to obtain the Green-Lagrange strain tensor (Sutton, Orteu, & Schreier, 2009), by relating the un-deformed (X) to deformed states (x) of a subdomain (comprising displacement data points array (**d**) of user-defined strain window) through deformation gradient tensor **F** as:

$$x = \mathbf{F}(X) \tag{3-20}$$

where **F** is defined as:

$$\mathbf{F} = I + \nabla \mathbf{d} \tag{3-21}$$

The I is an identity matrix and $\nabla \mathbf{d}$ is displacements derivatives and these are obtained by differentiating the least square surface fit of each displacement component over the defined strain-window (equal to REV) as discussed earlier:

$$\nabla \mathbf{d} = \begin{bmatrix} \frac{\partial u}{\partial X} & \frac{\partial u}{\partial Y} \\ \frac{\partial v}{\partial X} & \frac{\partial v}{\partial Y} \end{bmatrix} \tag{3-22}$$

The Green-Lagrange tensor **E** is obtained from the Right Cauchy-Green strain tensor **C** through:

$$\mathbf{E} = \frac{1}{2}(\mathbf{C} - \mathbf{I}) \tag{3-23}$$

where:

$$\mathbf{C} = \mathbf{F}^T \mathbf{F} \tag{3-24}$$

The components of Green-Lagrange tensor **E** is obtained in terms of displacements gradients components as:

$$E_{rr} = E_{xx} = \frac{\partial u}{\partial X} + \frac{1}{2}\left[\left(\frac{\partial u}{\partial X}\right)^2 + \left(\frac{\partial v}{\partial X}\right)^2\right] \tag{3-25}$$

$$E_{zz} = E_{yy} = \frac{\partial v}{\partial Y} + \frac{1}{2}\left[\left(\frac{\partial u}{\partial Y}\right)^2 + \left(\frac{\partial v}{\partial Y}\right)^2\right] \tag{3-26}$$

$$E_{rz} = E_{xy} = \frac{1}{2}\left(\frac{\partial u}{\partial Y} + \frac{\partial v}{\partial X}\right) + \left[\left(\frac{\partial u}{\partial X}\frac{\partial u}{\partial Y}\right) + \left(\frac{\partial v}{\partial X}\frac{\partial v}{\partial Y}\right)\right] \tag{3-27}$$

The circumferential strain $E_{\theta\theta}$ is independent of θ due to axial symmetry of the problem and was obtained from radial displacements using the finite strain formulation:

$$E_{\theta\theta} = E_3 = \left(1 + \frac{u}{r}\right)^2 - 1 \tag{3-28}$$

The volumetric strain was obtained from the principal strains:

$$E_{vol} = (1 + E_1)(1 + E_2)(1 + E_3) - 1 \tag{3-29}$$

Similarly the local rigid body rotation θ of sub-domain/strain window is obtained from the polar decomposition of F into the stretch tensor U and rotation tensor R as:

$$\mathbf{U} = \mathbf{C}^{1/2} = \left(\mathbf{F}^T\mathbf{F}\right)^{1/2} \tag{3-30}$$

$$\mathbf{R} = \mathbf{F}\mathbf{U}^{-1} = \begin{bmatrix} \cos\theta & -\sin\theta \\ \sin\theta & \cos\theta \end{bmatrix} \tag{3-31}$$

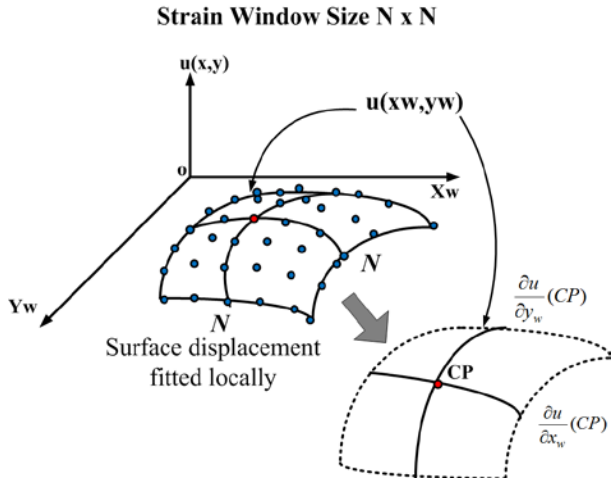

Figure 3.21 Local least square fitting for displacement derivatives

3.6 Summary

A new experimental methodology has been adopted to study the soil displacement field around the cone penetrating in sand; the methodology is based on the DIC technique. Various parametric experiments were performed for assessing the accuracy of DIC correlation algorithms, and key parameters influencing the accuracy of DIC analysis results were identified and optimized. The key factors affecting the displacement accuracy were investigated, and procedures were adopted to minimize these effects. Robust strain calculation procedures were adopted to obtain realistic strain fields subject to the size of the REV for particulate media.

CHAPTER 4. DEVELOPMENT OF AXISYMMETRIC CALIBRATION CHAMBER FOR DIC APPLICATIONS

4.1 Introduction

The literature review presented in Chapter 2 indicated that the solution of the cone penetration boundary value problem is plausible experimentally. Previous research on observation of the displacement field during installation of a model pile/penetrometer was hampered by limitations of the displacement measurement system, the plane strain boundary condition or sand ingress between the penetrometer and viewing glass. There is no theoretical solution that for the cone penetration problem, and no experiments have been reported in the literature on truly axisymmetric cone penetration. Furthermore, there is no established knowledge of how penetration resistance is affected by the proximity of soil layer interfaces. In order to study such questions, an axisymmetric calibration chamber testing facility for DIC analysis of cone penetration was designed and developed. This chapter provides a detailed description of the design, fabrication and instrumentation of different components of the system.

4.2 Design of Half-Circular Calibration Chamber

4.2.1 Design Considerations

The experimental concept and desired requirements for the experimental test set up were discussed in detail in section 3.2. We will next discuss how those requirements were met during design and fabrication of the half-circular calibration chamber.

4.2.1.1 Boundary and Scale Effects

The size of the half-circular calibration chamber and half-circular cone penetrometer were chosen to minimize boundary and scale effects. The avoidance of scale effects requires use of a cone penetrometer that is sufficiently greater than the size of the sand particles of the test sand. If the penetrometer is too large with respect to the chamber, excessive boundary effects will develop, so an appropriate chamber to probe diameter ratio is needed. In the literature for dense silica sands, a range of 50–100 of chamber to probe diameter ratios have been suggested to minimize boundary effects (Ghionna & Jamiolkowski, 1991, Foray, 1991, Mayne & Kulhawy, 1991, Schnaid & Houlsby, 1991, Salgado et al., 1998, Ahmadi & Robertson, 2008, Wesley, 2011 and Pournaghiazar et al., 2012). Gui et. al (1998) proposed that a probe to diameter ratio of 40 for dense sand in centrifuge testing is sufficient to avoid the size effects. Based on the literature, we considered that a chamber to probe diameter ratio of 50 is adequate to minimize boundary effects while keeping tests practical. The selected half-circular chamber diameter was 1.6m. A larger chamber size would be uneconomical in terms of fabrication and testing costs. The selected chamber size is greater than the largest size (1.2 m) used to perform most of the calibration chamber studies reported in the literature (Ghionna & Jamiolkowski, 1991).

4.2.1.2 Bottom Boundary Effects

The height of the calibration chamber should allow sufficient offset between the final cone penetration tip positions and the rigid base of the calibration chamber to avoid any influence of the rigid boundary on penetration resistance. At the same time, sufficient cone penetration should be allowed for full development of cone resistance in the soil sample. Gui et al. (1998) proposed that the minimum development penetration depth

required for cone resistance in uniform sand is 5 times the cone diameter (d_c) and the cone tip should be at least 10×d_c away from any rigid boundary to avoid any influence on cone penetration resistance. By considering this, we selected the chamber height of 1250mm, which allows the net cone penetration depth of 22 cone diameters.

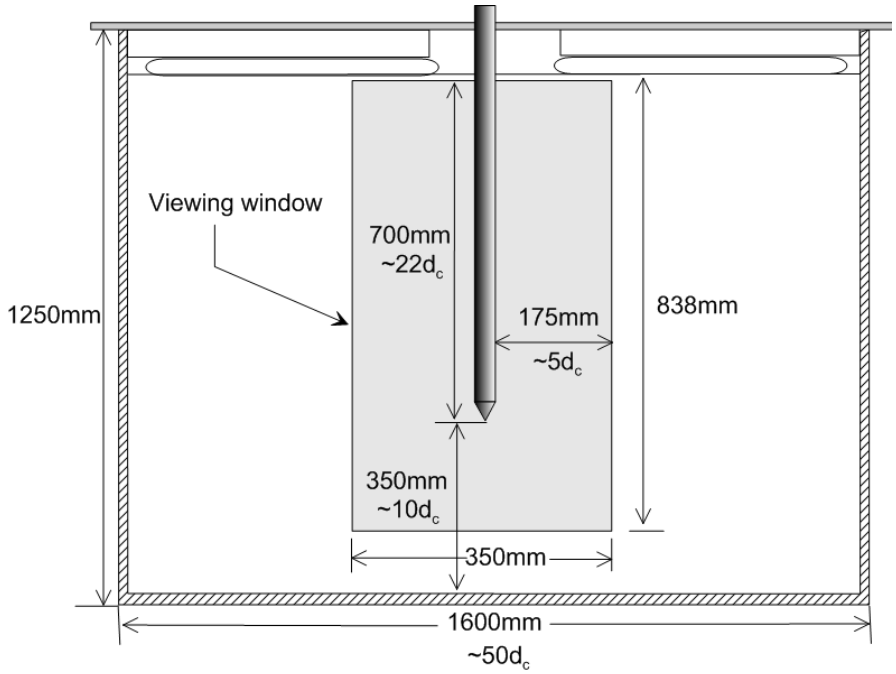

Figure 4.1 Half-circular calibration chamber sizing

4.2.1.3 Minimal Deflection of Front Observation Wall

The half-circular cone penetration in soil was to be performed against a Plexiglass viewing window. Owing to the very large stresses appearing below the cone tip during penetration, the viewing window will undergo large deflections even before the arrival of the cone tip if it is not adequately designed against these high stresses. A large deflection of the viewing window would have two adverse effects: (1) creation of conditions that do not correspond to the problem to be modeled and (2) creation of a small gap that would allow sand ingress between the Plexiglass wall and the probe, resulting in non-observation of the probe during penetration. Therefore, it was necessary to design the front wall to be sufficiently strong to resist the expected high stresses and meet the

stringent requirement of very minimal wall deflection. A combination of Plexiglass thickness with a reinforcing steel frame was used to achieve this goal.

4.2.1.4 Maximizing the Sand Displacement Observation Area

Since a steel frame was used to help keep Plexiglass deformation minimal, some loss of viewing area was unavoidable. However, it was essential to maintain the required image to object resolution in order to achieve sub-pixel resolution accuracy in displacement measurement, as discussed in section 3.3.2.3. It was also essential that the displacement field be viewable on both sides of the symmetry axis. From past studies (Gupta, 1992; Kobayashi & Fukagawa, 2003; Liu, 2010) minimal displacements were observed at the radial distance of 10 times the cone radius (r_c) from the cone penetration path. Accordingly, we designed the chamber so that the soil observation area has a width of 350 mm, corresponding to $10r_c$ ($5d_c$) (for a cone with diameter equal to 31.75mm) on each side of the cone.

4.2.2 Initial Prototyping and Modifications

The biggest challenge posed in the design was how to ensure maintenance of a 1m-long mechanical contact between the penetrometer and the viewing glass window during the penetration process within the tolerance of 100μm (the smaller sand particle size observed after sieving), in order to prevent sand ingress between the penetrometer shaft and the viewing window. The other uncertainty was the distribution of normal stress acting on the viewing window during penetration. A rectangular model penetrometer with flat end was considered initially for testing purposes. Figure 4.2 shows the rendering of the initial calibration chamber and images of the initial penetration tests.

A series of trial tests was done with the flat-end penetrometer, but deep penetration was not achieved. The sand ingress started at penetration depths of 5-6 “diameters” of the penetrometer and the tests were unsuccessful. Various trial solutions, including installation of a thin foam on the penetrometer face to be in contact with Plexiglass sheet to overcome any Plexiglass sheet deformation during penetration, use of magnets flush with the Plexiglass sheet and use of a 1-mm-thick guide channel were

attempted. The trial of a small probe-size guide channel was able to prevent sand ingress from the sides but not at the base of the penetrometer.

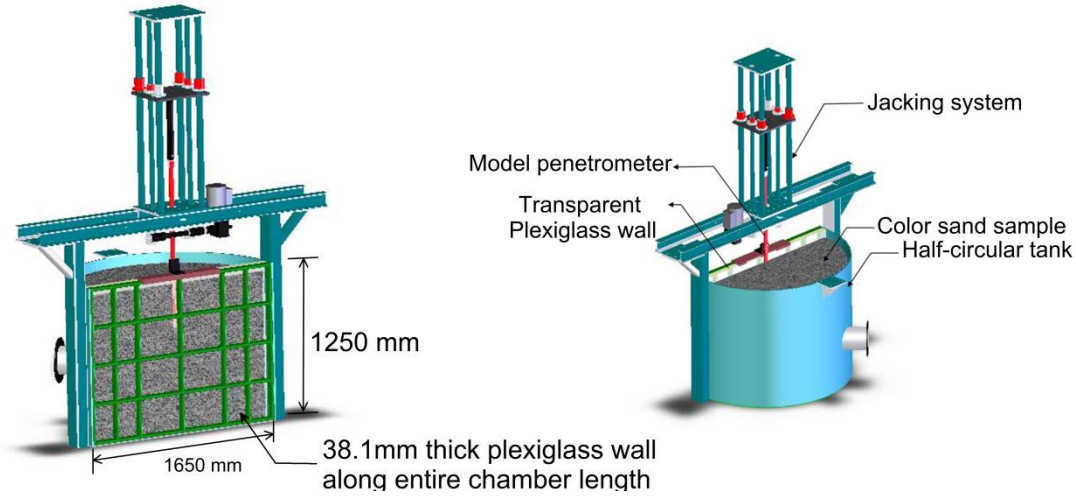

(a)

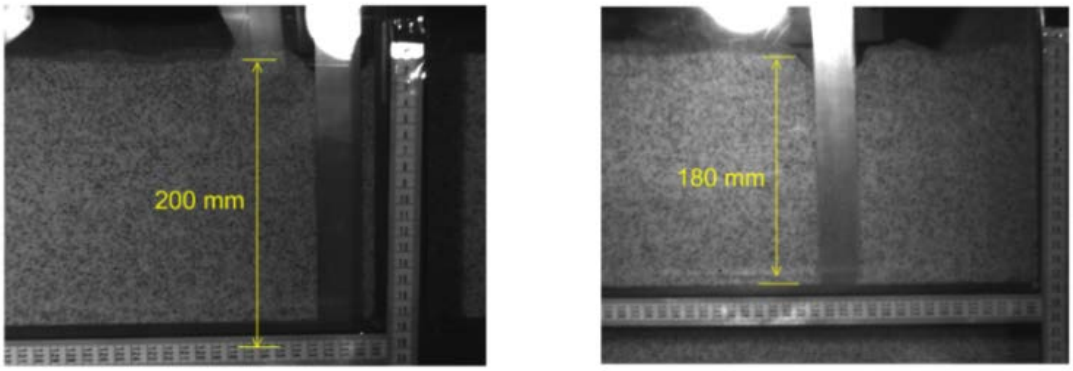

(b)

Figure 4.2 Initial prototyping: (a) chamber design, and (b) initial penetration tests.

4.2.2.1 The First Modification: A Roller Assembly with Guide Sleeve

A lateral roller support to press the penetrometer against the Plexiglass sheet and a rectangular guide sleeve using Ferlon bearing were fabricated to ensure precise alignment of the model penetrometer during installation. This modification also did not improve the length of penetration without sand ingress perhaps because greater

deformation induced in the Plexiglas wall by the lateral pressure. Figure 4.3 shows that the penetration depth of 200mm was achieved with the use of a roller assembly.

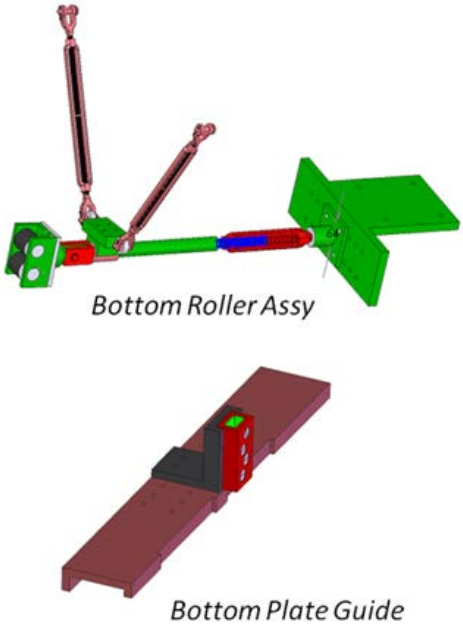

(a)

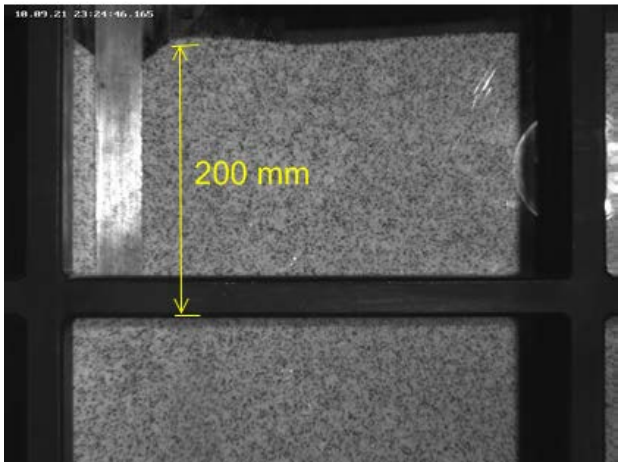

(b)

Figure 4.3 The first modification: (a) A roller assembly with guide sleeve, and (b) penetration result after modification.

4.2.2.2 Experimental Evaluation of Normal Stress and the Plexiglass Wall Deformation

In order to measure the stresses acting on the Plexiglass wall during penetration, we used a Prescale™ pressure-indicating film, which is a single-use film that displays the contact pressure through peak pressure snap shots through developed color intensity. The pressure-indicating film was installed at different penetration depths on the inner sides of the Plexiglass sheet to measure the normal pressure acting on the Plexiglass observation window. Two Prescale™ films with two different resolutions of 4LW (50-400 kPa) and LLLW (200-600 kPa) were used to estimate the normal pressure. Figure 4.4 shows the film installation and pressure measured at different penetration depths.

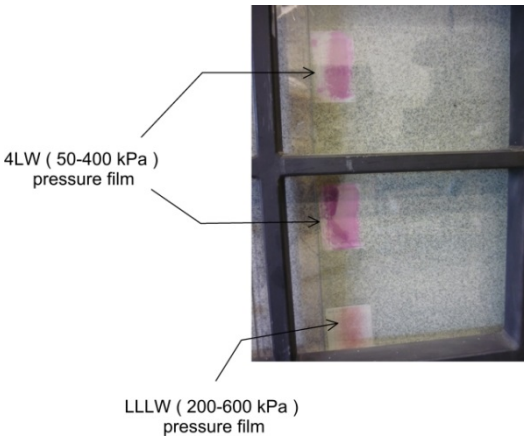

(a)

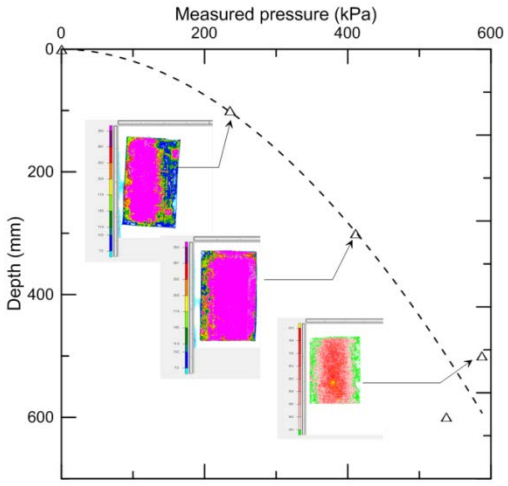

(b)

Figure 4.4 Pressures from pressure-indicating films for a sample with no surcharge: (a) film installation along penetration path (b) average pressure measured.

The Plexiglass wall deformation during penetration was also monitored using an NDI OPTOTRACK motion tracking system having measurement resolution of 0.01mm. A total of 16 wired strobe tracker targets were installed on the Plexiglass wall and dynamic tracking of these targets were done during the penetrometer installation. The maximum Plexiglass wall deformation measured was 0.46mm. Even the supporting frame was deforming during the penetration and a maximum deformation of 0.36mm in the frame was observed. From these experiments, it was concluded that the Plexiglass observation windows needed to be redesigned to withstand the high pressures with minimal deformation. Figure 4.5 shows the OPTOTRACK targets arrangement and the measurement results.

4.2.2.3 Trial with Modified Penetrometer Tip Geometry

It was judged that the penetrometer with a flat end led to non-symmetric soil flow around the tip and that the sand-probe frictional resistance at the flat end led to a resultant force at the tip that forced the penetrometer tip to drift away from the Plexiglass sheet, thus causing the sand ingress. To validate this hypothesis, we performed one penetration test with a rounded tip. The penetration without sand ingress increased to 430mm (Figure 4.6), and it was decided to modify the penetrometer tip geometry to a half-cone shape to ensure symmetric soil flow below the penetrometer tip.

4.2.3 Final Design of Calibration Chamber and Additional Modifications

4.2.3.1 Chamber Description

The final design consists of a large half-circular calibration chamber with diameter equal to 1680mm and height equal to 1250mm. The general layout is shown in Figure 4.7. The calibration chamber consists of a modified front wall assembly, a 12.5-mm-thick half-circular chamber steel wall, a removable jacking system, a mechanical positioning system and a surcharge system consisting of a bottom plate, a top reaction lid and a half-circular air bladder. For sand drainage after completion of a test, a sluice gate valve was provided at the bottom of the chamber.

(a)

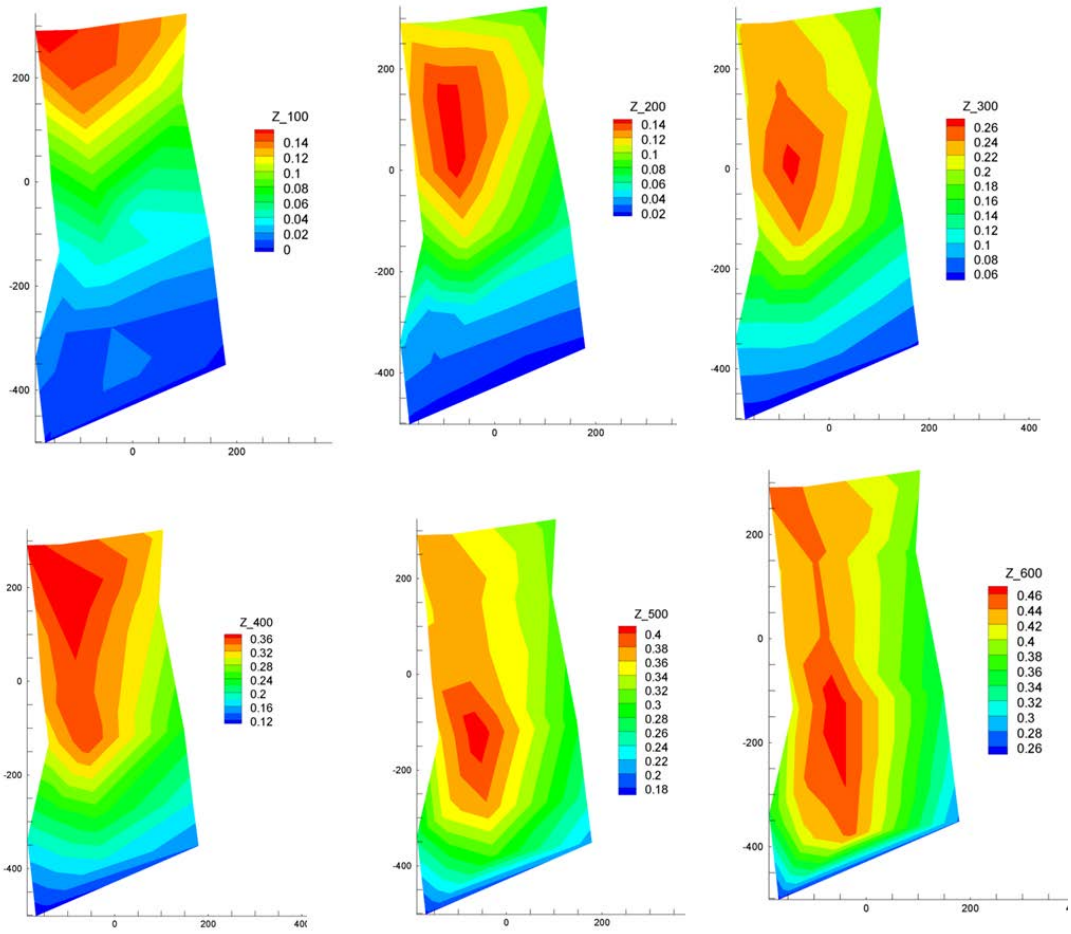

(b)

Figure 4.5 Measurement of Plexiglass wall deformation: (a) OPTOTRACK tacking targets arrangement (b) Plexiglass sheet deformation contours vs. cone penetration depth.

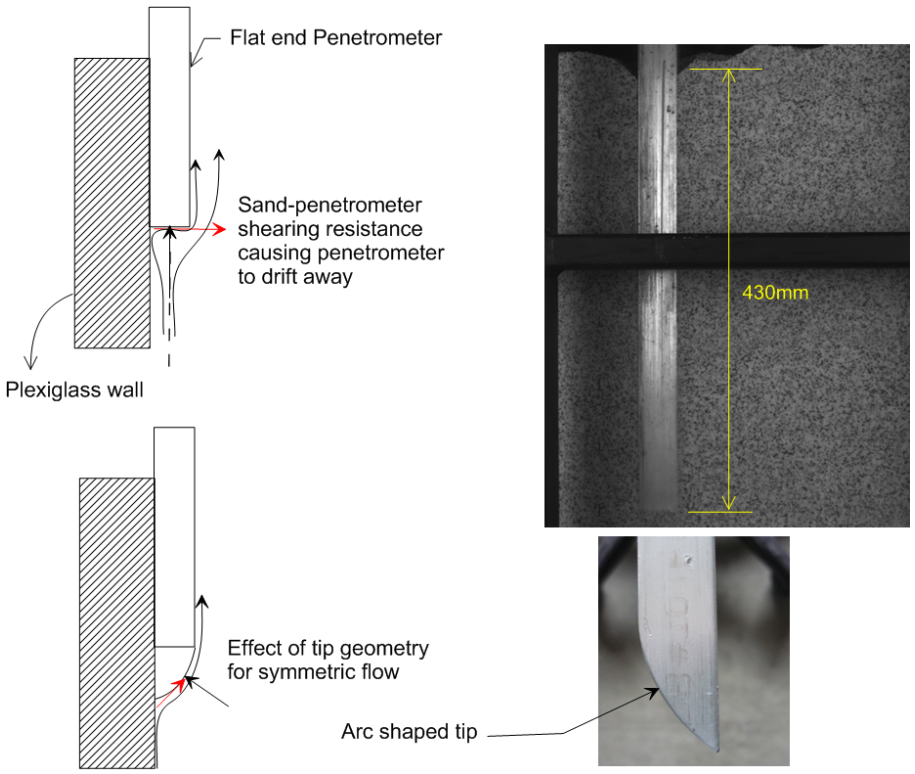

Figure 4.6 Arc-shaped tip geometry and improved penetration depth

Three Plexiglass observation windows of size 352×252 mm were provided in the center of the front wall to allow imaging of the entire penetration process. The cone penetration mechanism can be observed for penetration depths up to $45r_c$ within a viewing window extending to either side of the cone penetration path up to $10r_c$. The size of the observation window can be extended for testing under low surcharge with the removal of a front-wall stiffener assembly.

The other components of the testing facility include an ACME screw jacking system, a half-circular sand pluviator, an overhead hoist crane for material handling, and an image acquisition system. All of these components except ACME screw jacking system were designed by the author and fabrication was done by the Peerless Pattern Machine Shop Inc. This new testing system was developed as part of the existing large-scale model pile testing facility at the Bowen laboratory, Purdue University.

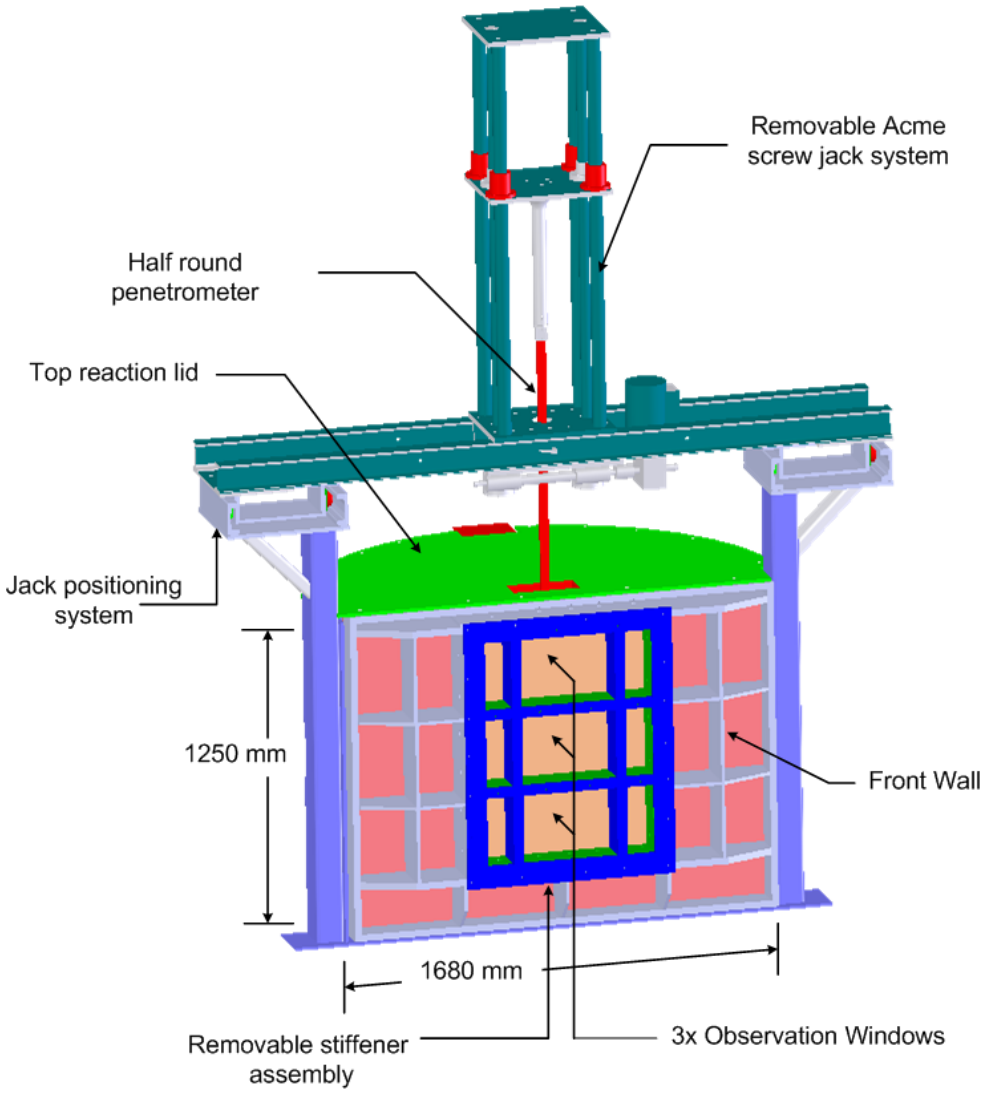

Figure 4.7 Description of modified calibration chamber

4.2.3.2 The Front Wall Assembly Design

The critical component of the testing chamber was the design of the front-wall assembly, which housed the Plexiglass viewing window (with the dimensions of 610 × 915 mm) at the center. The foremost requirement in the design was minimization of deformation of the front wall to prevent the intrusion of sand particles between the penetrometer and the Plexiglass as discussed in section 4.2.1.3. Maximum wall deformation occurs in the vicinity of the pressure bulb that forms below the cone penetrometer tip. Three different wall assembly configurations, as shown in Figure 4.8,

were considered and modeled using the commercial finite element code ABAQUS. For each wall assembly configuration, the thickness of the Plexiglass window was taken as 38.1 mm, 50.8 mm and 76.2 mm. In each model, two different surcharge values (applied on the top of the sample) of 50 kPa and 100 kPa were simulated. The selection of final wall assembly configuration was made to optimize fabrication cost. A 6.35-mm-thick annealed glass sheet was used as a non-structural member, positioned flushed with the Plexiglass sheet to prevent its scratching.

The stresses on the wall due to cone penetration were estimated using the cavity expansion and penetration resistance analysis program CONPOINT (Salgado & Prezzi, 2007). Normal stresses acting on the Plexiglass were estimated based on the assumption that the lateral stress below the cone tip was equal to the limit cylindrical cavity pressure. Figure 4.9 shows the loading conditions considered in analysis.

The radial and vertical variation of hoop stresses (acting normal to the Plexiglass) was done using the analytical field option available in ABAQUS. The penetrometer loading was modeled at its final penetration depth, about two thirds of the depth from the top of the chamber. Since only the front wall was modeled, instead of the complete chamber, appropriate displacement boundary conditions were applied to model the weld and bolt connections at the ends of the wall and the front reinforcing assembly. The bolts were modeled using point-to-surface contact options with influence zone equal to the bolt length. The mechanical properties of the Plexiglass, annealed glass and carbon steel used in the model were provided by the manufacturers. Figure 4.10 shows the deformed shape of the adopted front wall assembly under 50 kPa surcharge. The maximum calculated wall deformation was 0.095 mm ($\text{deflection/wall height} = 0.0001$).

An exploded view of the adopted chamber design and an image of the fabricated front wall assembly are shown in Figure 4.11.

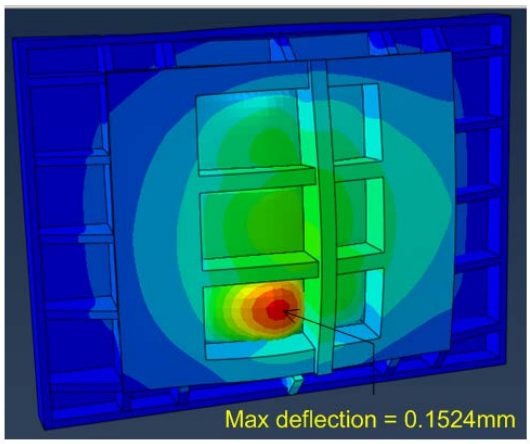

(a)

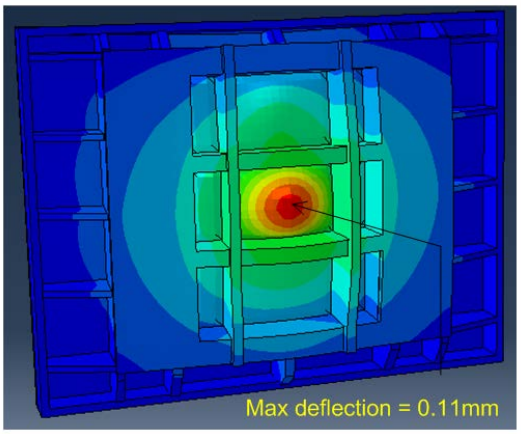

(b)

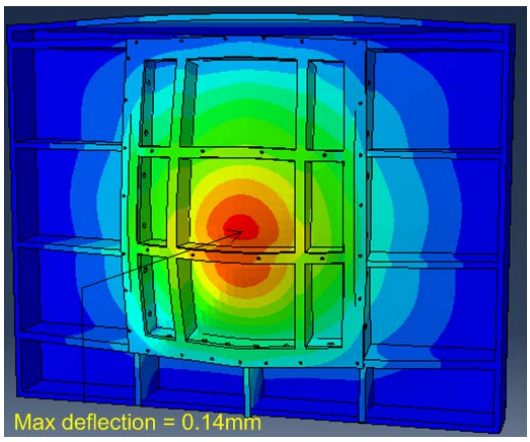

(c)

Figure 4.8 Different front wall assembly design layouts considered: (a) off-center viewing window, (b) symmetric layout with welded connection, and (c) symmetric layout with bolted connections.

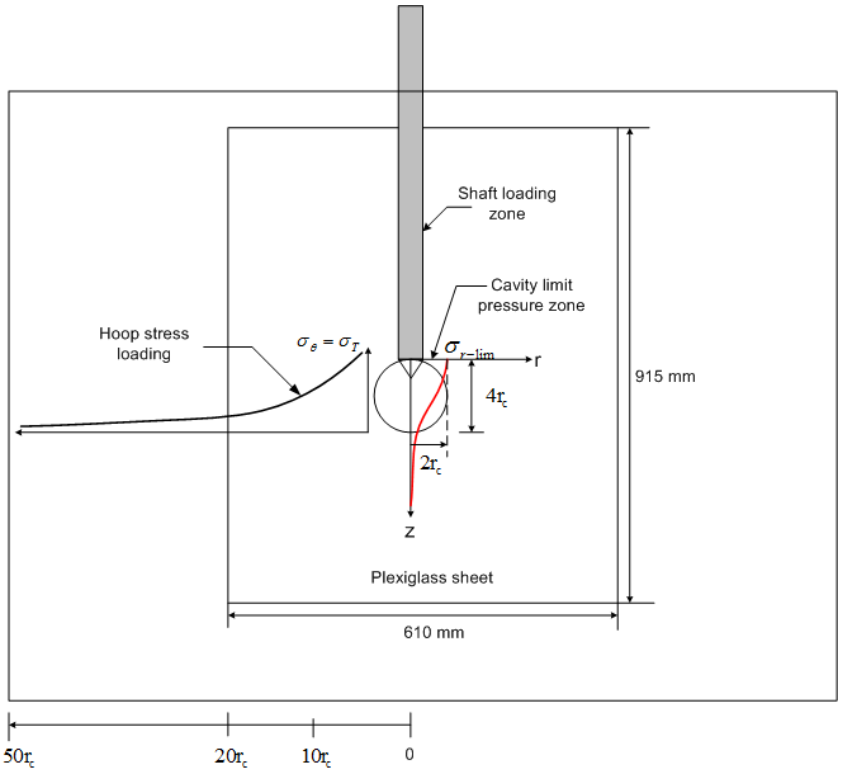

Figure 4.9 Loading conditions considered in front wall assembly design

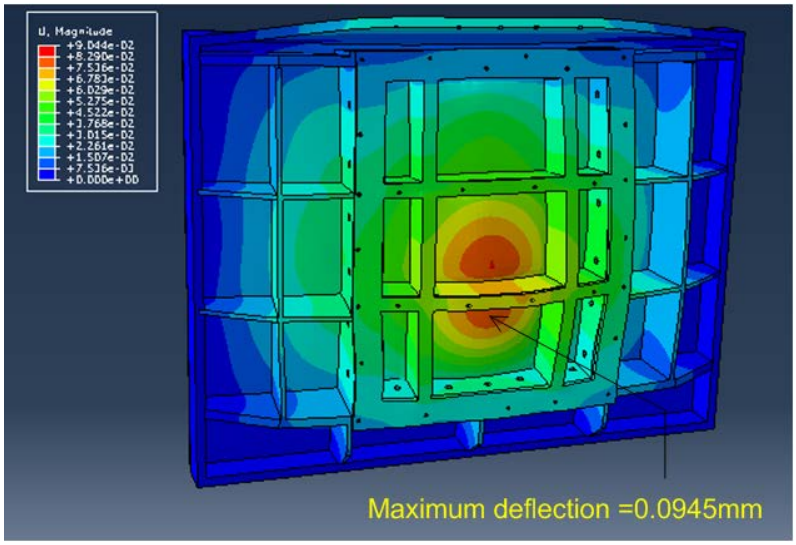

Figure 4.10 Deformed shape of adopted front wall assembly

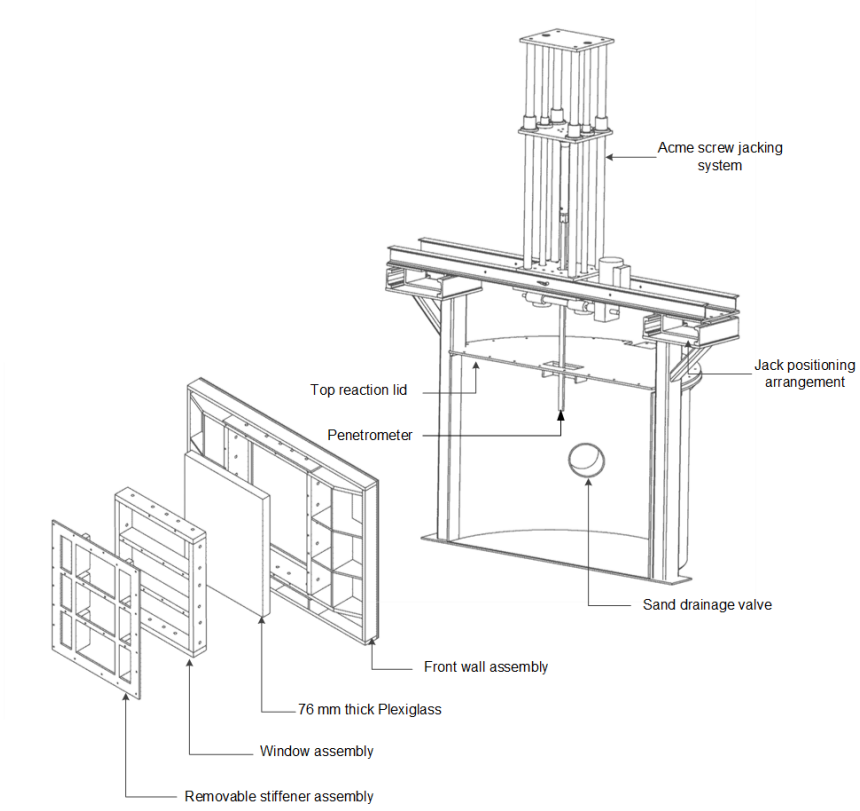

(a)

(b)

Figure 4.11 Adopted chamber design: (a) exploded view of chamber (b) image of front wall assembly after fabrication.

4.2.3.3 Additional Measures for Preventing Sand Ingress during Penetration

In addition to proper design of the chamber, additional measures were also adopted during fabrication for preventing the sand ingress between glass and penetrometer in penetration tests.

4.2.3.3.1 Machining and Polishing of Plexiglass Sheet

Very precise machining was required to make the surface of the Plexiglass sheet flat. After machining, the Plexiglass was polished by Pease Plastics Inc. to make it transparent and remove any machining marks.

4.2.3.3.2 Design of Cam Follower Roller Assembly

A roller assembly consisting of three sets of Cam-Followers (NHK-Model CF18) was designed and fabricated to slightly press the probe against the glass sheet and to ensure precise guidance of the penetrometer during penetration. The roller assembly was removable and was designed to be mounted on the tank top lid as shown in Figure 4.12.

Figure 4.12 Cam-follower roller assembly

4.2.3.3.3 Jacking System Positioning and Alignment Arrangement

A positioning system was designed to move the jacking system mounting platform for positioning the jacking system precisely with reference to the glass sheet. A mechanical adjustment handle with a fine-pitch threaded shaft allow the movement of the jack mounting plates with a resolution of 2.5mm per turn. This precise positioning of the jacking system ensured perfect initial contact of the flat side of the penetrometer with the glass sheet. Any small angular deviation would cause sand ingress along the shaft and below the penetrometer tip. The positioning system consists of 4 sets of heavy duty roller bearings (Pacific Bearings Model-HVB-056) and two parallel 16-inch U-channel guide rails (Model HVR-2). The jack system has axial load capacity of 80 kN. Figure 4.13 shows rendering of the bearing and a photograph of the jack positioning system.

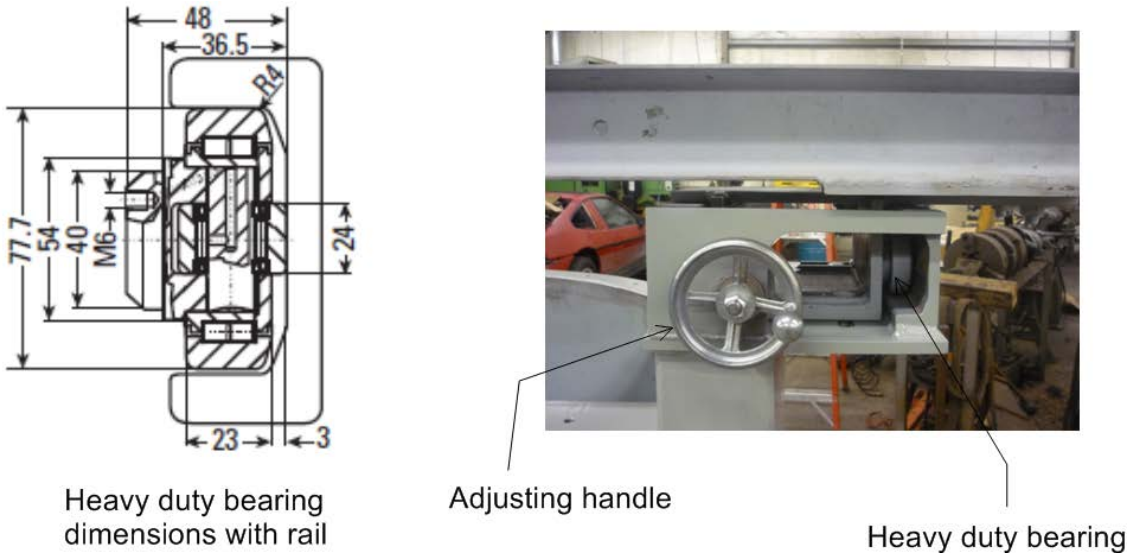

Figure 4.13 Jack positioning and alignment system

4.3 Design of Half-Circular Sand Pluviator

An important aspect of calibration chamber testing is formation of uniform and reproducible sand samples at a desired density. Air pluviation is the favored sample preparation method in calibration chamber testing for dry sand due to its simplicity and its emulation of the natural deposition process (Brandon & Clough, 1991). The pluviation method offers several advantages over vibrating or tamping techniques, including very good uniformity, less segregation of particles, no particle crushing, good density control and repeatability. Two types of pluviation systems are used for sample preparation: stationary pluviation or traversing spreader system (Salgado et al., 1998b). The desired relative density is achieved by controlling the deposition flow rate through shutter opening sizes and hole patterns at a certain fall heights. Fall height has little to no effect on the relative density of the sample for heights greater than the critical fall height, which is the height beyond which sand particles fall at their limit velocity, being acted upon by zero resultant force due to balancing air drag forces and gravity (Rad & Tumay, 1987).

We designed and built the half-circular pluviator system shown in Figure 4.14. The pluviator diameter is 1500 mm; being slightly smaller than the chamber diameter, it can move inside the tank so that a constant fall height can be maintained. The pluviator consists of a half-circular steel cylinder 150 mm in height to which a perforated steel plate was welded at the bottom. Another perforated acrylic plate having the same hole pattern and diameter (hole diameter = 10mm) was attached in a rotating recess at the bottom of the steel plate. The pluviator is open and ready to pluviate sand when both hole patterns are aligned. The pluviator can hold a sand volume of up to 0.5 m3. Two No. 6 diffuser sieves, with opening size of 3.125 mm, are also attached in a staggered fashion at the bottom of the shutter plate.

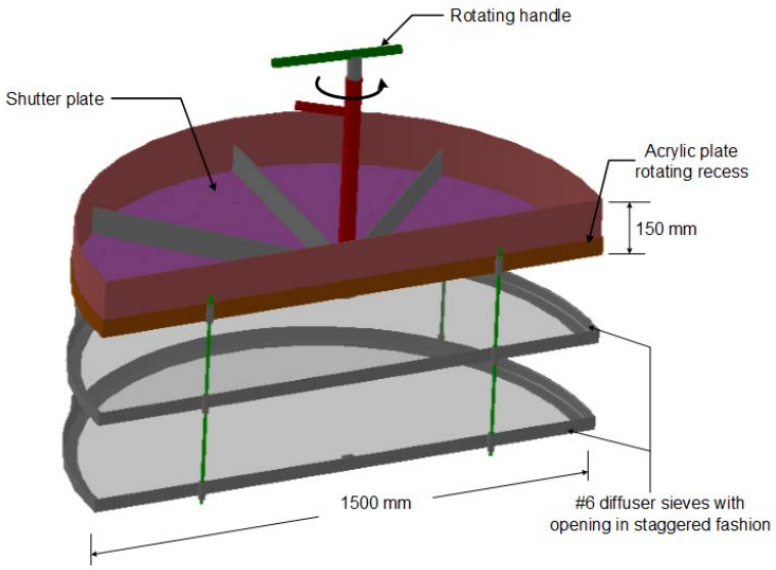

(a)

(b)

Figure 4.14 Half-circular pluviator: (a) exploded view (b) picture after fabrication.

In order to prepare a sample, the pluviator is attached to a gantry with a chain-hoist crane. The chain hoist allows the adjustment of the sand falling height, while the gantry with the attached casters can be moved freely so that the pluviator can be placed above the soil tank during pluviation, or away from it after sample preparation. For

sample preparation, the sand stored in bags is first placed in the pluviator using the overhead chain-hoist crane. The shutter plate is then opened and sand is released from the holes in it. The influence zone of the sand falling jets depends upon the height between the shutter plate and the diffuser sieves (this height was selected such that the sand falling jets would overlap slightly near the boundary walls of the chamber). Figure 4.15 shows how the relative density of the sample increases with increases in the sand fall height. Dense sand samples are prepared with double diffuser sieves, which slow down the rate of deposition. Target densities of 85%, 65% and 45% were achieved by varying the fall height and by using different combination of diffuser sieves.

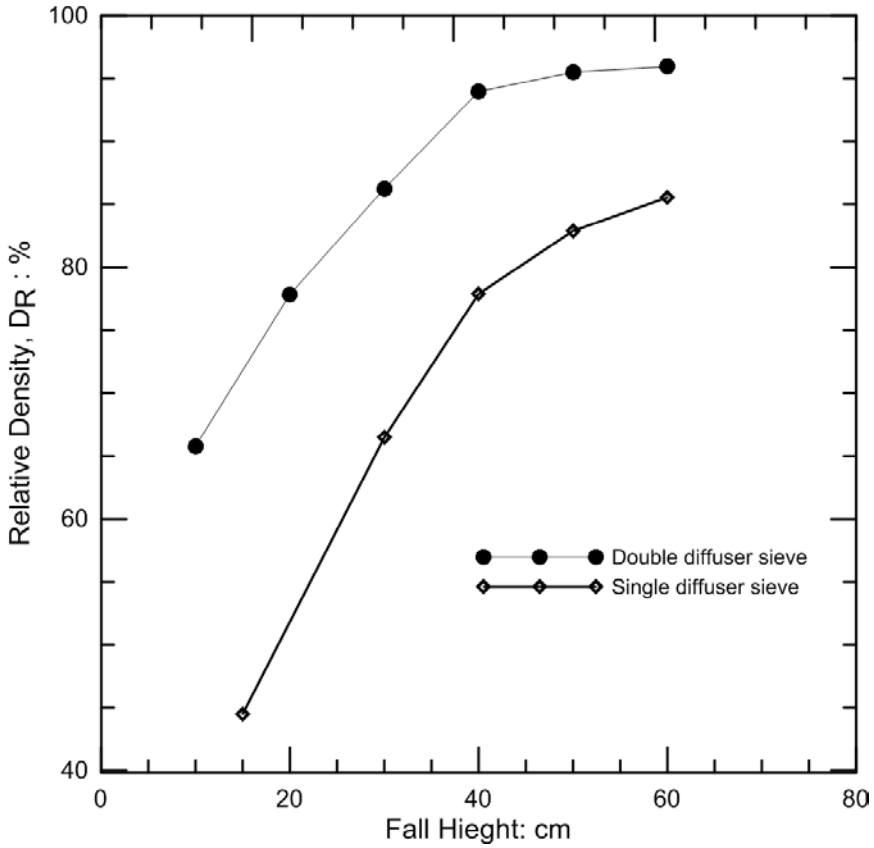

Figure 4.15 Relative density vs. fall height

4.4 Model Half-Circular Cone Penetrometer

4.4.1 Design and Instrumentation

In this study, we used penetrometers with two different diameters: 31.75mm and 19.04mm. The model cone penetrometers were fabricated from custom-shaped, half-circular sections of brass used in naval ships guard railings. The length of each penetrometer was 914mm. The bottom of each penetrometer was designed to accommodate different tip geometries. A 60-degree half-conical and a flat end tip were machined for installation at the bottom of penetrometer. An 8mm diameter hole was gun drilled in the large penetrometer for passage of instrumentation wires. Two kind of instrumented half-cone tips were used for the penetration tests. Initially, we installed 350 ohms full bridge strain gauges on a column welded behind a half-cone tip to form a column load cell for measuring the tip resistance. The performance of this tip sensor was variable due to the influence of bending strains related to the shape of the cross section. To improve that, a new tip was fabricated to house a miniature 10-kN compression load cell model LC307-5K manufactured by Omegadyne Inc, USA. The tip was attached to the penetrometer bottom using two M5 bolts. A small gap was allowed between the bottom of the penetrometer and the conical tip to allow the load cell diaphragm deflection and to avoid preloading of the load cell due to over torqueing of the tip attachment bolts. This gap was filled by the Silicon sealant 3145 RTV MIL-A-46146 manufactured by Dow Corning. The cone tip connecting bolt heads present on the cone tip surface were filled with automobile body putty and the tip surface was leveled and smoothed. Figure 4.16 shows the images of the penetrometer and different tips used.

To measure the total cone resistance during installation, a miniature in-line compression-tension load cell of 20-kN (model LC-202 manufactured by Omegadyne, Inc. USA) was installed. A special coupling was designed and fabricated connecting the penetrometer head and jacking system. Figure 4.17 shows the image and coupling arrangement.

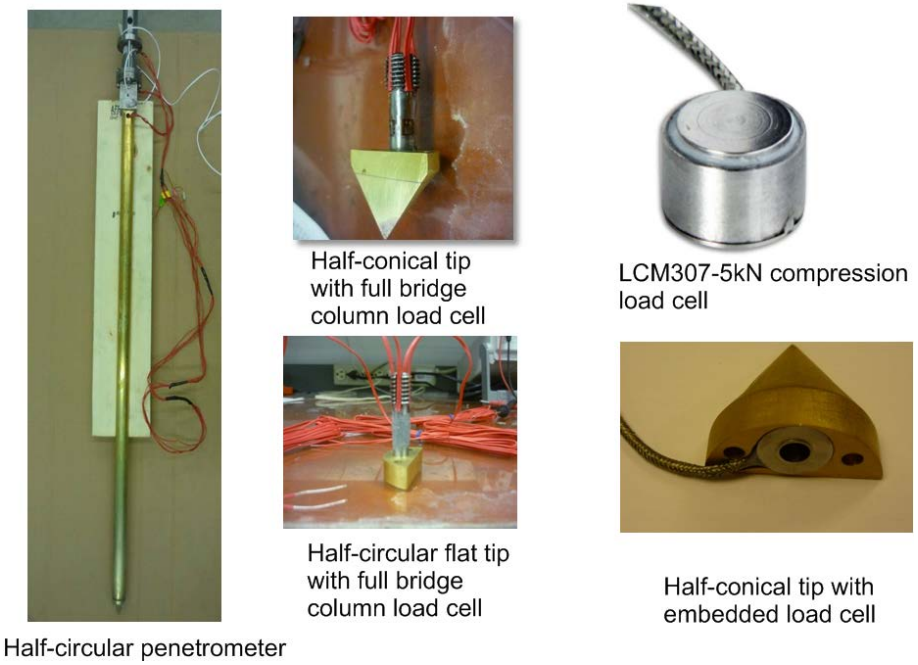

Figure 4.16 Half-circular model penetrometer with different end tips

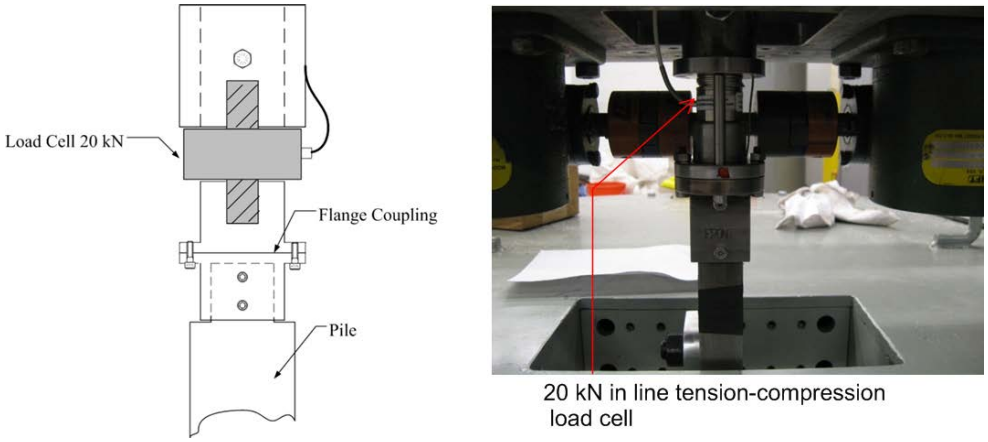

Figure 4.17 In-line 20-kN tension-compression load cell coupling arrangement

4.4.2 Penetrometer Tip Load Cell Calibration

The load cell was housed in the penetrometer tip as shown in Figure 4.16. The load cell was calibrated using a very short penetrometer using the same load cell coupling as would be used in an actual test in the loading frame. Known incremental loads were applied and the corresponding output voltage was recorded using a 20-bit data acquisition

system with measuring range set to 0.1 volts. A special bottom support was fabricated to house the conical tip, and the cone tip was snug fit in the half-cone housing. A small hole was drilled at the bottom of the housing to prevent damage to the tip. Figure 4.18 shows the testing arrangement and the calibration results.

4.5 Jacking System

A 25-ton jacking system consisting of two Acme screw jacks with a dedicated motor controller is used to perform the cone penetration tests at a constant penetration rate. The screw jacks are powered by a 0.5 HP, 1725 RPM three-phase motor through two external gear boxes with a reducer ratio of 25:1. Motor speed control is achieved through a Lenze ACtech SCM005S frequency inverter. Two limit switches were installed at both ends of the jack travelling distance. The maximum speed of the jacking system is 50mm/min. Two-way jacking cycles are possible through manual control using upward and downward jogging switches. The jack uses four guide sleeve linear motion bearings mounted on shafts to ensure minimum compliance, accurate and vibration-free motion. The jack is removable and used only for cone penetrometer or model pile installation after sample preparation. For accurate alignment of the cone or model pile with respect to the viewing window, jack supporting platforms placed on top of the testing chamber were made adjustable through a PCB linear bearing and a mechanical controller as described in section 4.2.3.3.3. Figure 4.19 shows the schematic of the jacking system and image of the jack in mounted position.

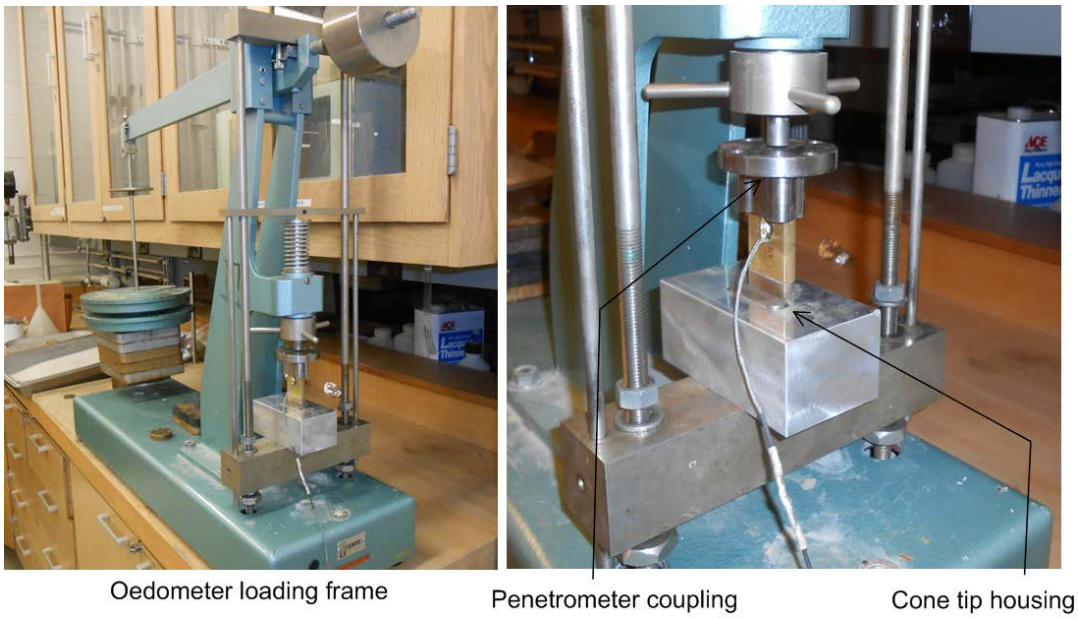

(a)

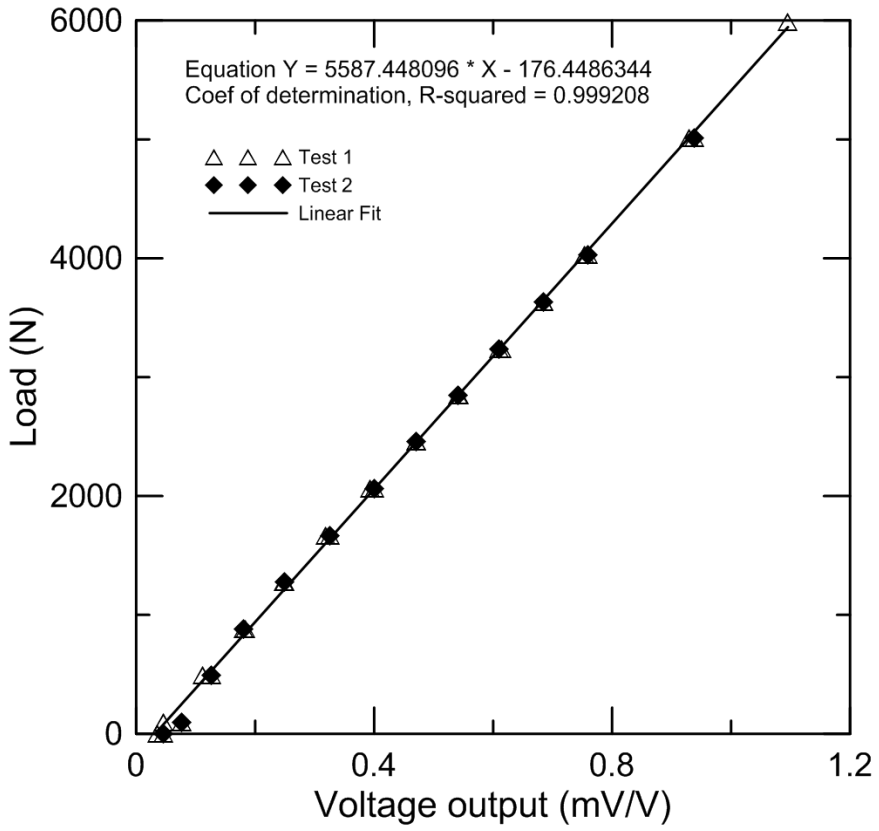

(b)

Figure 4.18 Penetrometer tip load cell calibration: (a) test arrangements (b) calibration results.

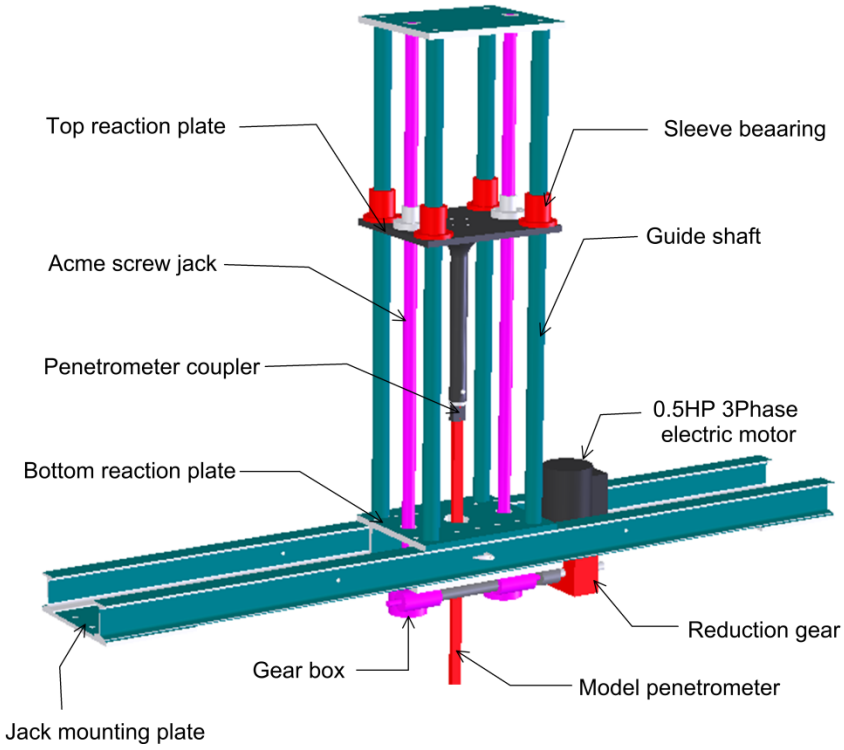

(a)

(b)

Figure 4.19 Components of jacking system (a) schematic (b) image of jack mounted on calibration chamber.

4.6 Surcharge System

A special half-circular air bladder, manufactured from Weiler Rubber Tech, LLC, enabled application of a uniform surcharge on top of the sand sample. The pressure bladder has a diameter of 1530 mm and it covers almost the entire area of sample, except the small area where the cone or model pile is pushed into the sample. For this purpose, the pressure bladder has a rectangular insert to allow insertion of a penetrometer or one or more model piles. For even distribution of pressure near the cone penetrometer, a bottom steel plate with cone entry points at specific locations is used. A top cover lid bolted at the top of the chamber provided reaction for the applied surcharge. The laboratory high-pressure air-line was used to inflate the rubber bladder. The pressure control was achieved by a dedicated pressure control panel using an air pressure gate valve operated manually. The feedback from the in-line pressure transducer allowed precise adjustment of surcharge application. The pressure transducer also allowed the continuous monitoring of applied stress at the top of the sample during the entire duration of the test. Figure 4.20 shows the image of the half-circular bladder, and Figure 4.21 shows the schematic of the surcharge system.

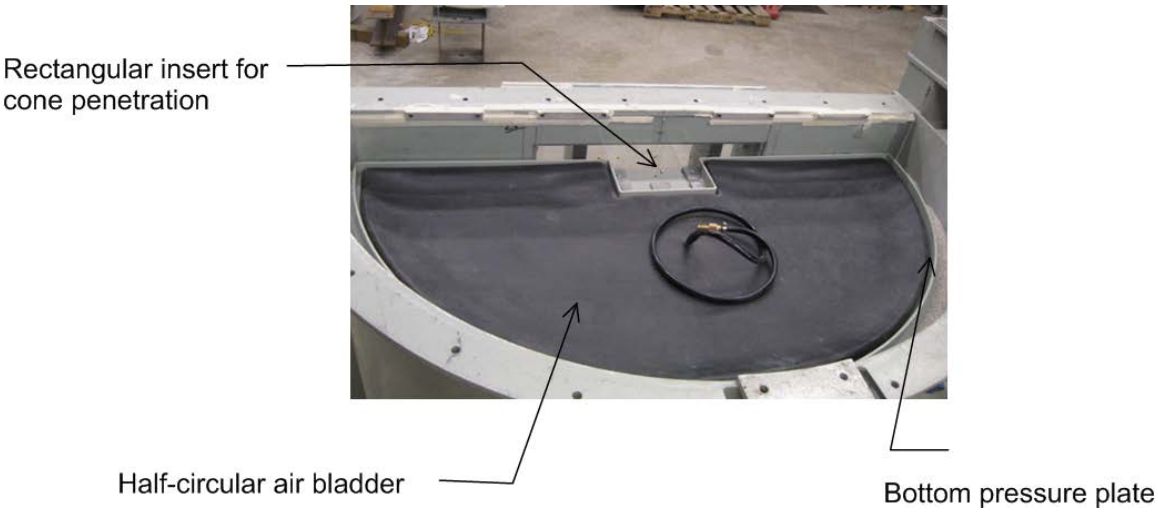

Figure 4.20 Half-circular air bladder for surcharge loading

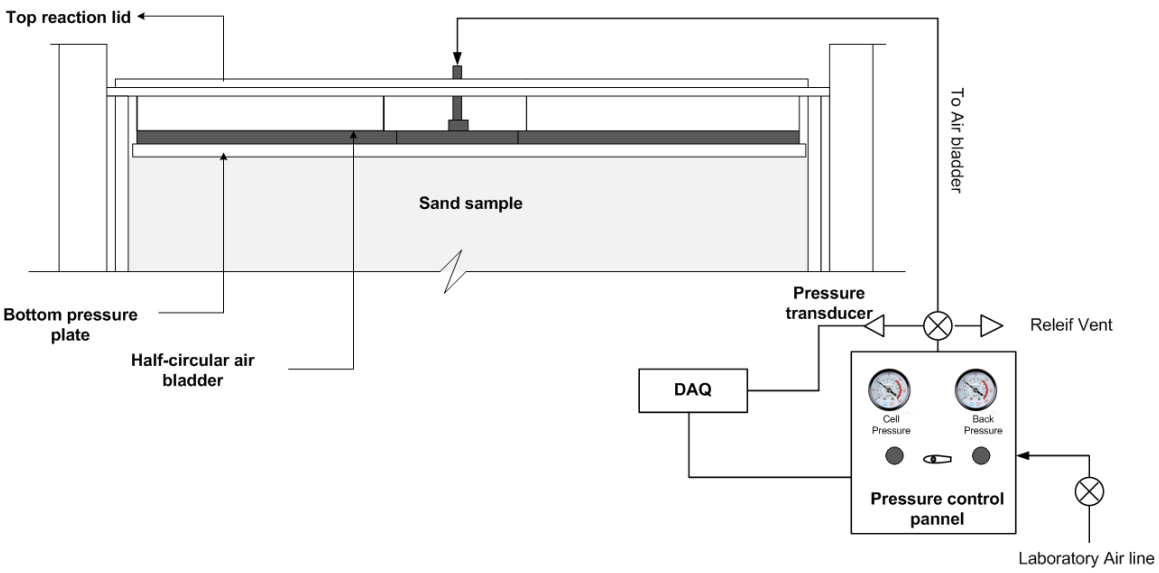

Figure 4.21 Schematic of surcharge system

4.7 Image Acquisition System

The dedicated image system used to image the cone penetration process consists of:

- three cameras with 5-Mega-Pixel (2592×1944 pixels) resolution with APTINA image CMOS MT9P031 sensors
- a PCI-express frame grabber capable of transferring sustained data up to 700MB/sec from four cameras simultaneously to two RAID arrays of 160 GB 1000RPM hard drives
- a dedicated PC
- three compatible FUJINON 12.5-mm fixed-focal-length, high-resolution C-mount lenses

The cameras were connected to frame grabbers using Ethernet RJ45 connector cables. The system can capture the images at full resolution up to 7frames/s. The imaging system has a camera control and acquisition software, XCAP from EPIX Inc., USA. The three cameras were mounted in series in the vertical direction using two multiple camera support bars. A heavy duty Monfrotto tripod equipped with a three-way pan head for precise leveling was used for camera support. Two light boxes with compact florescent lights were used for illumination. The images captured during each test were transferred

from RAID hard drives to external hard drives for DIC analysis and to create disk space for the next test. Figure 4.22 shows a picture of the image acquisition system.

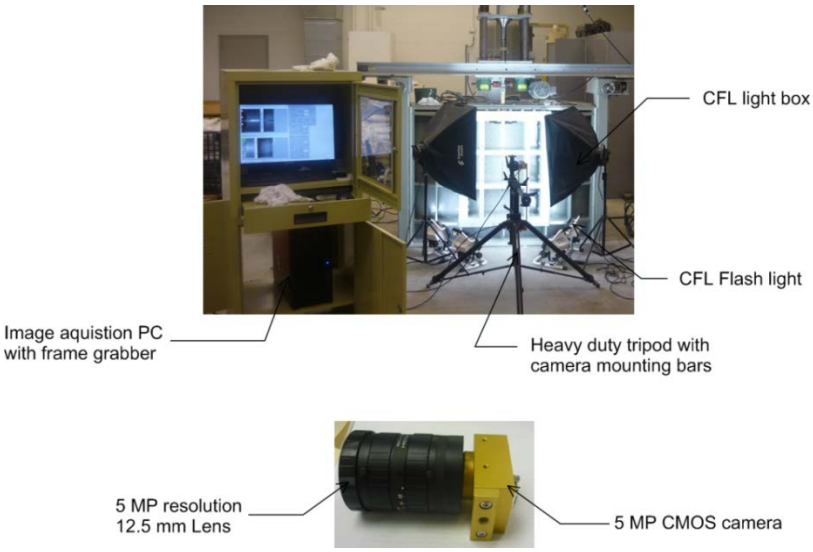

Figure 4.22 Components of image acquisition system

CCD sensor cameras are superior to CMOS sensor cameras because of the slightly better performance in terms of quantum efficiency and image quality, as shown in Figure 4.23. The maximum signal to noise ratio for the selected CMOS camera was 38.1dB; an alternative CCD camera would have a maximum signal-to-noise ratio of 41.67 dB. However, this 7% gain in quantum efficiency would come at an additional cost of 300%.

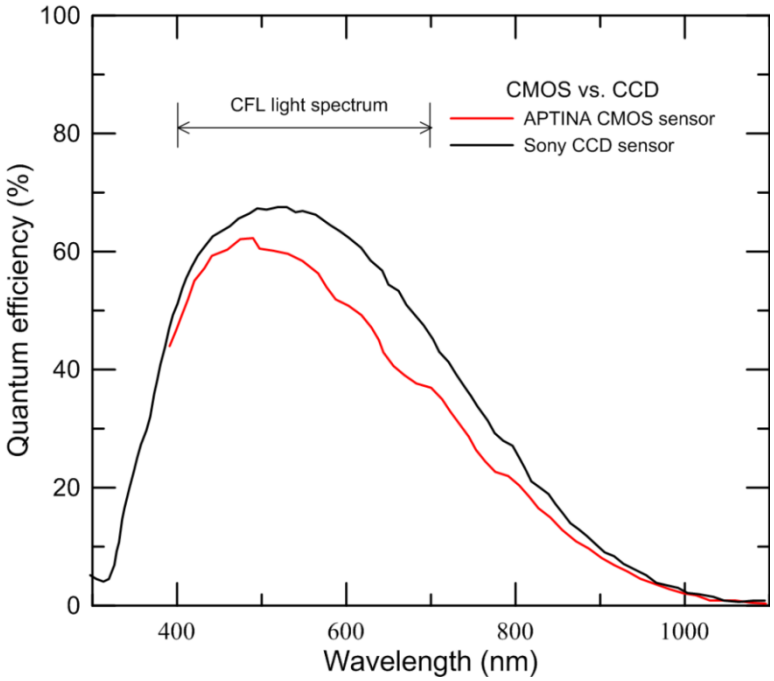

Figure 4.23 CCD vs. CMOS camera sensors (data from Epix Inc. and Pointgrey Inc.)

4.8 Data Acquisition System

A 16-bit Vishay System 5000 data acquisition system (DAQ) was used for measuring the penetrometer jacking force and tip load cell during penetration. Other sensors, such as pressure transducers and stress cells embedded in soil were also monitored using the same DAQ system. The DAQ system was synchronized manually with the image acquisition system to relate the sensor data with the images.

4.9 Overhead Hoist Crane for Material Handling

A 1-ton DAYTON overhead hoist crane was installed for material handling during sample preparation and emptying of the calibration chamber after completion of each penetration test. The hoist crane is positioned at the desired location by moving the hoist trolley along an H-beam rail (Figure 4.24).

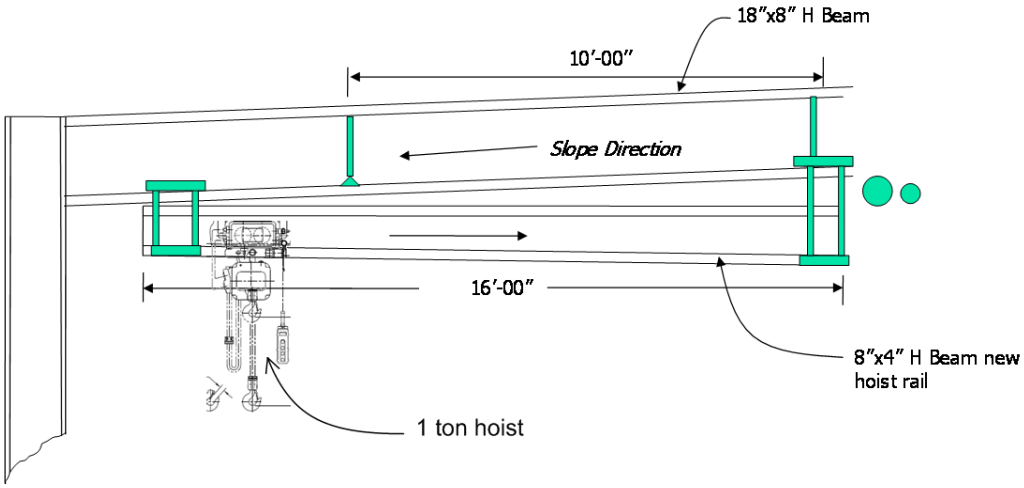

Figure 4.24 Installation of 1-ton hoist crane and rail

4.10 Summary

In this chapter, the development of an axisymmetric half-circular calibration chamber was presented. Various measures adopted for preventing sand particle ingress between the cone penetrometer and the viewing glass during cone penetration were described. The design of the various components of the test system was discussed. The model half-circular penetrometer was designed to accommodate different tip geometries. The penetrometer tip was instrumented with different load measurement sensors, and the calibration of these sensors was described. The jacking system used to install the penetrometer was carefully designed to ensure absolutely vertical penetration. A surcharge system with half-circular air bladder with pressure control was developed for application of different stress boundary condition at the top of the sample. A dedicated image acquisition system with suitable illumination arrangement for imaging of the cone penetration process was described.

CHAPTER 5. EXPERIMENTAL PROGRAM

5.1 Introduction

The literature review presented in Chapter 2 demonstrated that there is a lack of quality experimental work for solution of the CPT boundary value problem in uniform and layered soil profiles. A newly developed half-circular calibration chamber with added DIC capability as described in Chapter 4 provides means for solving the CPT boundary value problem experimentally. A series of half-circular cone penetration tests were performed to understand the penetration mechanism in uniform and layered sand. The effect of stress and relative density on sand movements has been studied. For layered samples, various combinations of sand relative densities have been used to model the two layered soil profile. In addition to conventional penetration resistance measurement, the cone penetration process has been imaged to generate the photographic data for soil displacement analysis. This chapter describes the test conditions and experimental procedures followed in the cone penetration and DIC testing program.

5.2 Test Conditions

5.2.1 Engineering Properties of the Test Sand

In this research, coarse-grained silica sand #2Q-ROK was the main test sand. The sand is commercially available from US Silica Company in large quantities. The sand is quarried from the Oriskany sandstone deposits at Berkeley Springs, West Virginia. The sand has angular particles and is composed mainly of quartz (98.0%) with traces of calcite; these characteristics make it slightly more susceptible to particle crushing than other silica sands. For comparison purposes, a few tests were also performed with two other silica sands: ASTM 20-30 sand, which has rounded particles and Ohio-Frac sand, which has sub-rounded particles.

ASTM 20-30 is clean sand mined from Ottawa, Illinois, and is composed of 99.8% quartz. Ohio-Frac sand is mined from the Sharon conglomerate formation at Thompson Ohio and consists of 99.7% quartz. These three sands are classified as poorly graded (SP) based on the unified classification system (ASTM D2487). The maximum and minimum densities of the sands were determined based on ASTM D4254 and ASTM D4253. The index properties of the testing sands are shown in Table 5.1. Figure 5.1 shows the grain size distribution curve for testing sands. In case of # 2Q-ROK sand, the sand was sieved in bulk from the Midwestern Industries screening facility to remove the fines. After a few initial penetration tests, the sieved sand was used within 10 cone diameters area around the penetration areas for all subsequent tests. This procedure was adopted to remove the fines generated due to particle crushing during each penetration test.

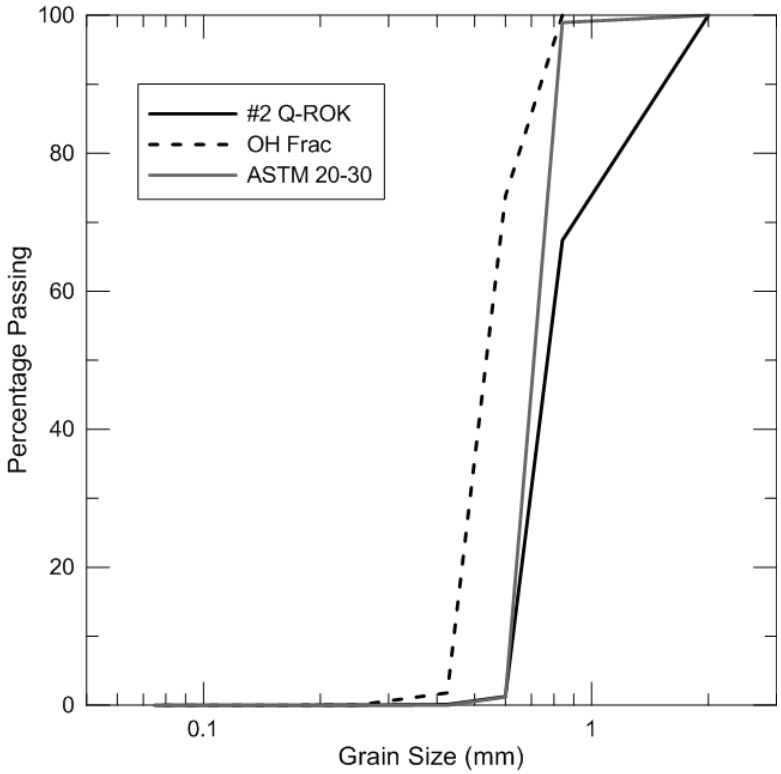

Figure 5.1 Particle size distribution of test sands

Table 5.1 Index properties of testing sands

Sand	Grain Shape	SiO_2 (%)	Specific Gravity (G_s)	D_{50} (mm)	Cu	e_{max}	e_{min}
#2 Q-ROK	Angular	99.0	2.65	0.78	1.43	0.998	0.668
ASTM 20-30[1]	Rounded	99.8	2.65	0.74	1.2	0.742	0.502
Ohio Frac	Sub-Angular	99.7	2.65	0.54	1.37	0.853	0.537

Figure 5.2 shows microscopic images of the test sands. We can see that #2 Q-ROK has angular particles, that ASTM 20-30 sand is rounded and that Ohio-Frac sand has sub-angular particles.

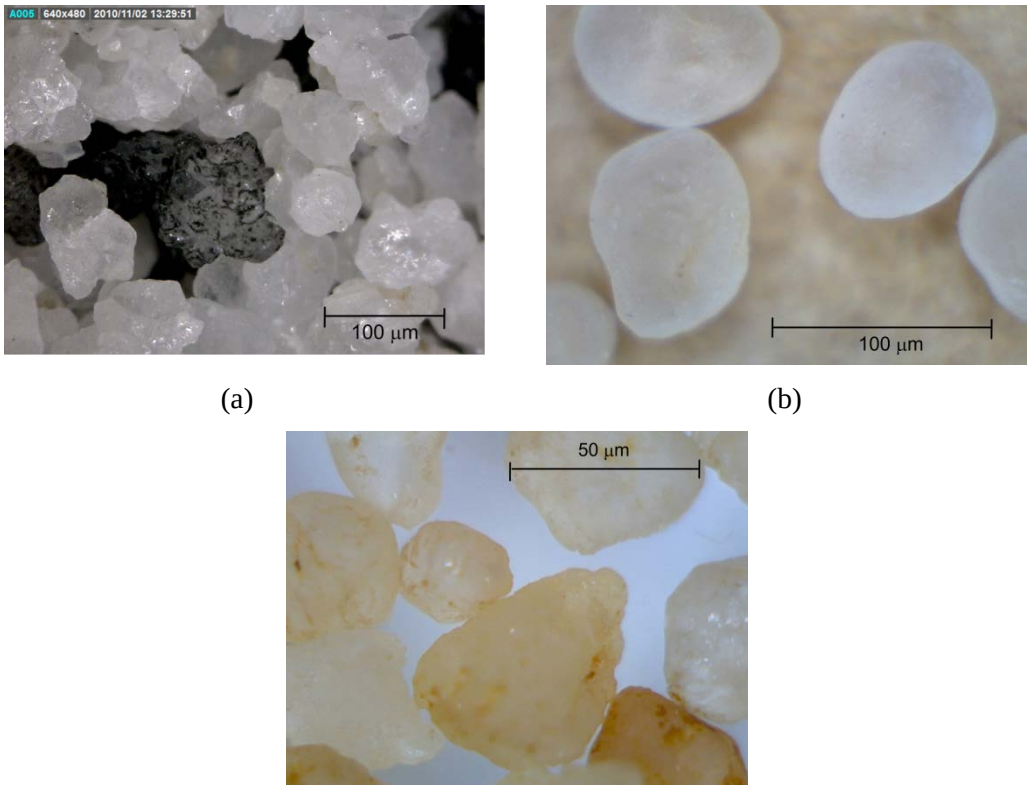

(a) (b)

(c)

Figure 5.2 Microscopic images of test sands: (a) #2 Q-ROK, (b) ASTM 20-30 and (c) Ohio Frac.

[1] Data from Chow (2001)

The peak and critical-state friction angles of #2Q-ROK sand were estimated from direct shear tests conducted in a 60mm square shear box. Two series of test were performed, one in loose sand (with density of 32±3%) and the other in dense sand (with density of 78±3%). The dense samples were prepared by using the air pluviation method, using a funnel and a diffuser sieve, with constant fall height of 300 mm. The loose samples were prepared with a funnel only and a fall height of 50 mm. The top of the sample was carefully leveled with wooden leveling device. The tests were conducted with normal stress ranging from 60 to 442 kPa. The estimated peak friction angle (ϕ_p) under these testing conditions is 40.3 degrees and the critical-state friction angle (ϕ_c) is 32.3 degrees. The test results are shown in Figure 5.3.

5.2.1 Crushability of Test Sands

From a crushability standpoint, coarse-grained soil particles range from extremely crushable to non-crushable. Crushability of sand depends on particle mineralogy, morphology, strength, and arrangement, and stress state (Mitchell & Soga, 2005; Hardin, 1985). More importantly, during a deep penetration process that induces both large mean and shear stresses below the cone tip or pile base, particle crushing is observed in almost all sands (BCP committee, 1971;White, 2002).

In order to compare the crushability characteristics of the silica sands considered in this study, one-dimensional compression tests (Figure 5.4(a)) were performed on very dense samples (D_R ~ 85%) with normal stresses of up to 10 MPa. The samples were prepared using air pluviation. The vertical displacement during the test was measured by LVDT after stabilization of displacement at the end of each load increment. In the case of #2Q-ROK, creep effects were observed, and it took more time for displacement to stabilize than for other sands. The sieving before and after the compression tests were done to assess the crushability. The relative breakage parameter B_r, as defined by Hardin (1985), was then used to provide an assessment of the crushability of these different sands. From the results of the one dimensional compression tests, the #2Q-ROK sand was categorized as a highly crushable sand, with B_r =10.51, the Ohio-Frac sand, as of intermediate crushability, with B_r = 2.56, and the ASTM 20-30 sand, as the least

crushable of the three silica sands, with B_r = 0.56. Figure 5.4(b) shows a comparison of the crushability of these three sands based on the percentages passing the #100 sieve after the one-dimensional compression tests.

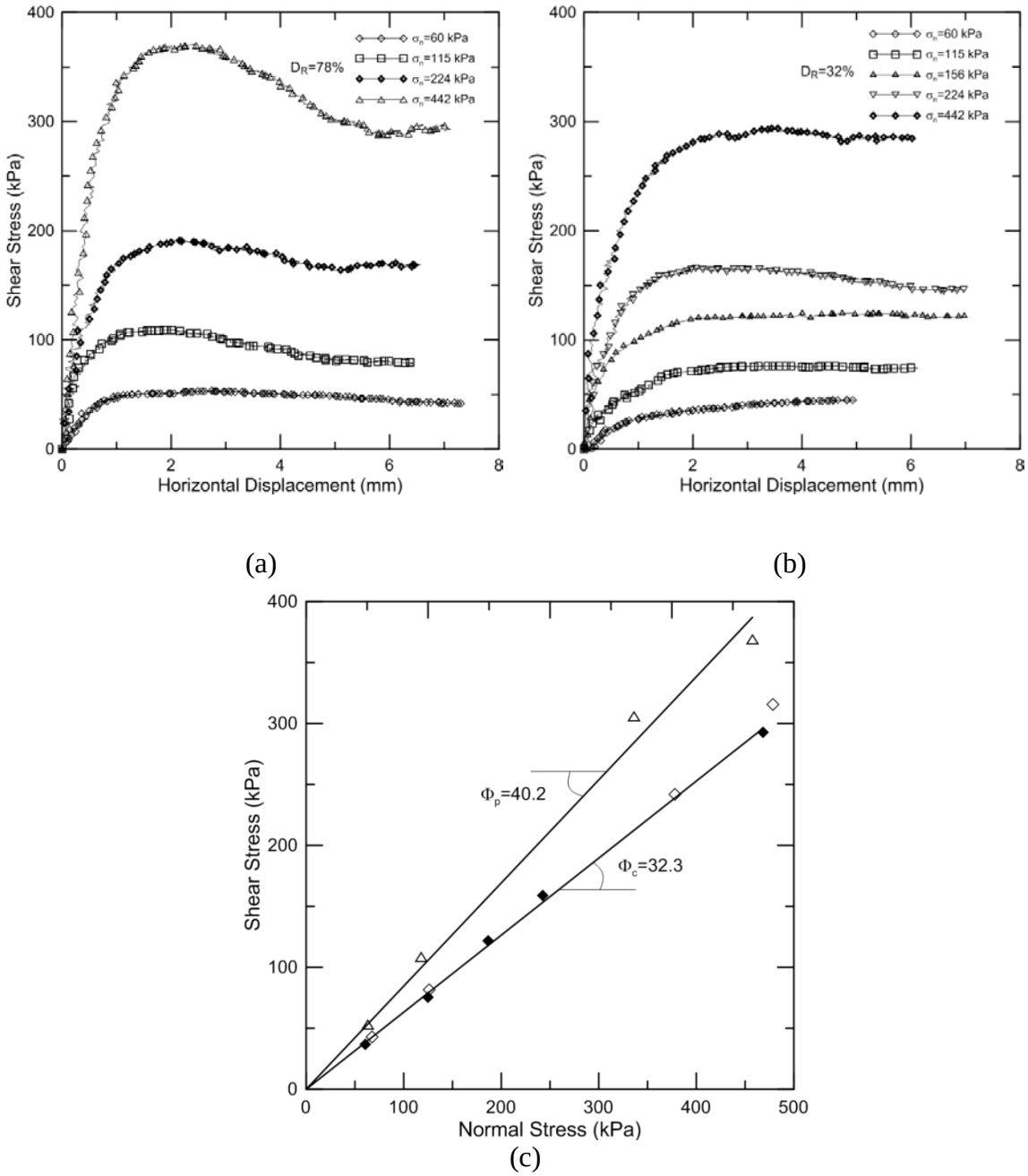

Figure 5.3 Direct shear test results

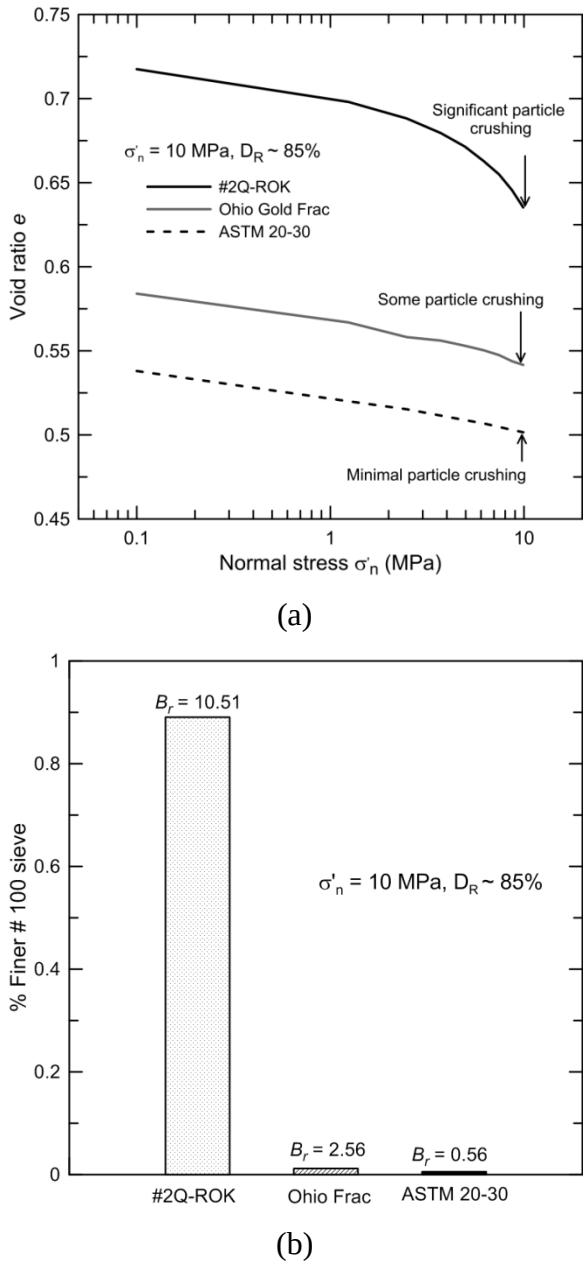

Figure 5.4 Crushability assessment of test sands: (a) 1D compression test results, and (b) comparison of % finer than # 100 sieve after compression testing.

5.2.2 Interface Friction between Penetrometer and Test Sand

The interface friction angle between sand and a brass plate of similar roughness as that of the model penetrometer was determined from direct shear tests. The 60mm-square shear box was used. The brass plate was made of the same material the cone. The surface roughness of the brass plate and model penetrometer were measured using an optical profilometer and found to be similar. The surface profile measurements will be discussed in detail in a later section.

The test sand used was #2Q-ROK with the same gradation as used in cone penetration testing. The engineering properties of the sand were already discussed in section 5.2. To determine the interface friction between sand and brass plate, only half of the shear box was filled with sand. The brass plate was placed at the bottom half of the shear box. The sand was placed in the upper half of the shear box with air pluviation, using funnel and a sieve with a constant fall height of 150mm. The medium dense sand samples were prepared with relative density (DR) of 65±2%. One test was also performed with sand sample retrieved after a penetration test in dense condition to see the effect of particle crushing on interface friction. The interface friction angle between the brass plate and the sand is found to be 21.6 degrees for normal stresses ranging from 60 to 442 kPa. The test conducted on the recovered sand sample shows similar results as those on virgin sand. Figure 5.5 shows the test arrangement and Figure 5.6 shows the test results.

5.2.3 Surface Roughness of Model Penetrometer

The surface roughness of the model penetrometer shaft and of the brass plate was measured using ZEMETRICS Zescope optical profiler. Separate measurements of surface roughness for the conical tip and shaft were made. Surface roughness is expressed as a single numeric parameter *Ra* which is measurement of surface finish, a quantitative calculation of the relative roughness of a linear profile or area under observation. At each measurement location an area of 745×745 microns was measured with 20× zoom lens.

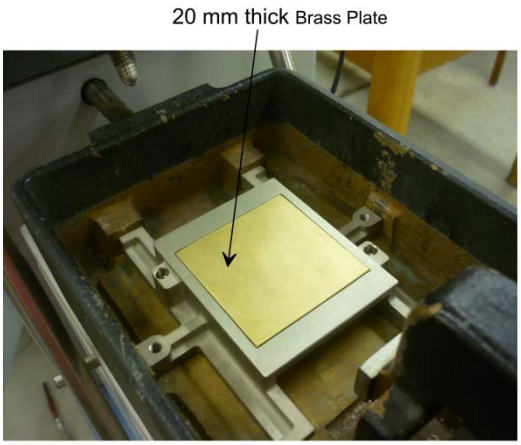

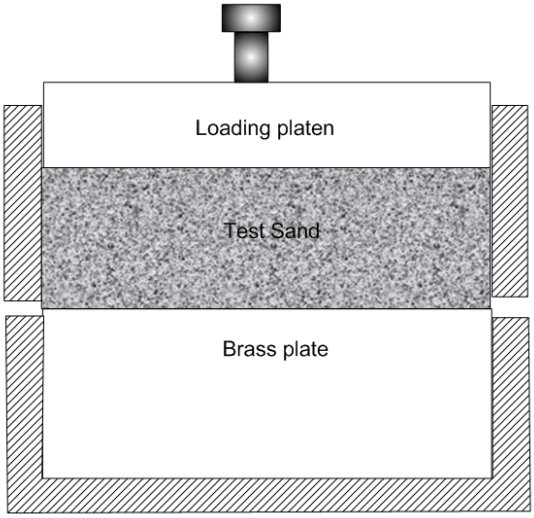

(a) (b)

Figure 5.5 Brass-sand interface friction test arrangements

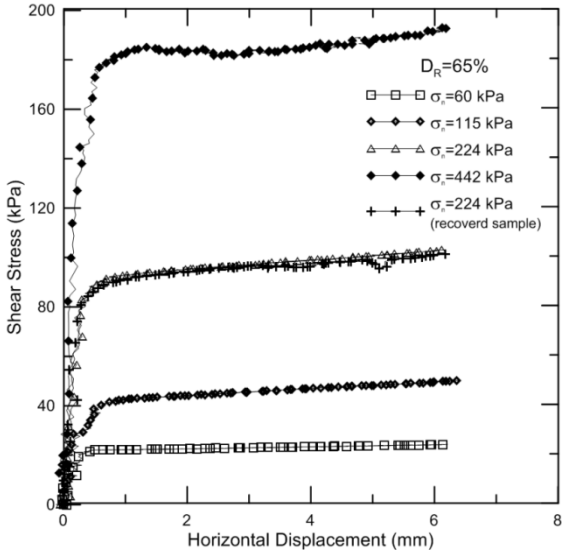

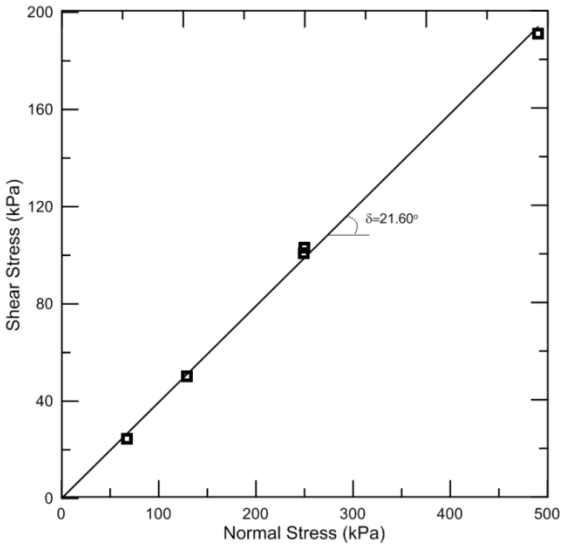

(a) Shear stress vs. horizontal displacement. (b) Shear stress vs. normal stress.

Figure 5.6 Interface friction between model penetrometer and #2Q-ROK sand

The average surface roughness R_a of brass plate and model penetrometer shaft were similar. The surface roughness of the conical tip was four times higher than the shaft. The average surface roughness R_a of the brass plate was 0.8138 microns and that of

the penetrometer shaft was 0.8360 microns. However, the cone tip surface roughness measured was 3.258 microns. This was due to the fact that measurements were made after few penetration tests and scratching of cone tip took place by the sliding of sand particles under extreme stress regime around the penetrometer tip. Figure 5.7 shows the surface roughness profile measurement results.

A bilinear relationship between interface friction angle (δ_{cv}) and normalized roughness defined as $R_n = R_a / D_{50}$ has been proposed by various researchers (Uesugi & Kishida, 1987 and Porcino et al., 2003) with the upper limit reached at $\delta_{cv} = \phi_c$. The friction coefficient between the brass plate and the # 2Q-ROK sand is in good agreement with these studies, as indicated in Figure 5.8.

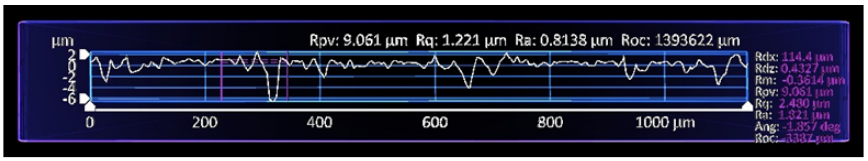

(a) Brass Plate Surface Profile.

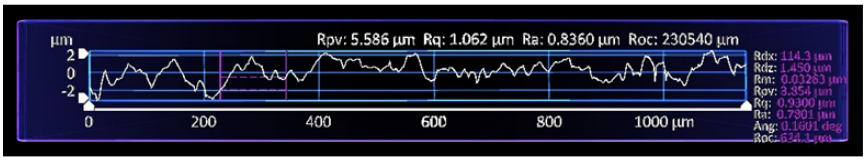

(b) Penetrometer shaft Surface Profile.

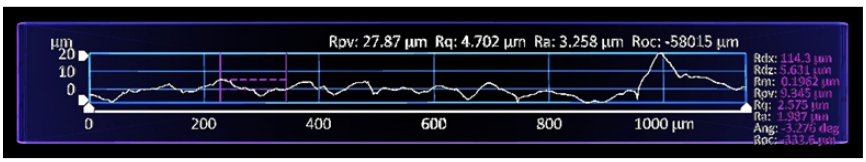

(c) Cone tip Surface Profile.

Figure 5.7 Surface profiles of brass plate and penetrometer

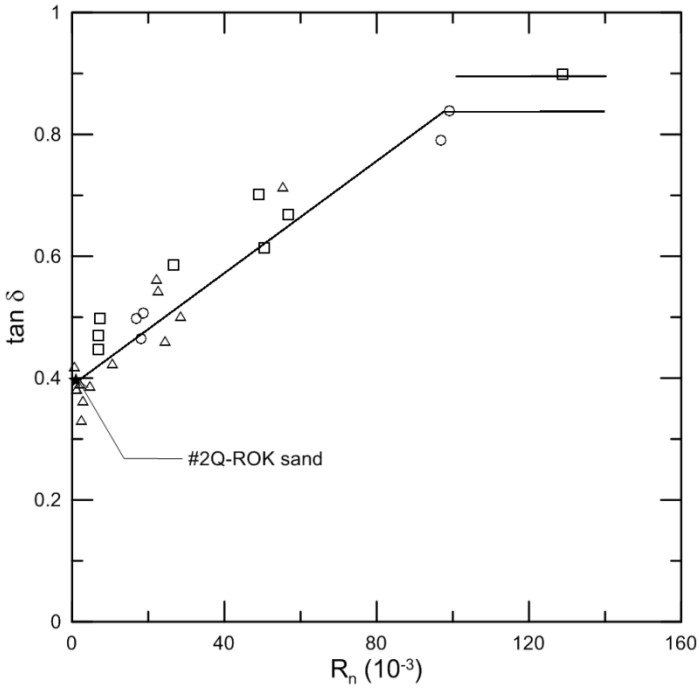

Figure 5.8 Normalized roughness vs. friction coefficient (Uesugi & Kishida, 1987)

5.2.4 Chamber Size and Boundary Effects

Penetration resistance measured in calibration chamber differs from that measured in the free field conditions due to boundary effects arising from the limited size of the chamber. It is well understood now that these boundary effects depend upon the initial soil state, defined primarily by density and stress level. Various experimental and theoretical studies have been conducted to evaluate the boundary effects under different soil and boundary conditions and to relate q_c in chamber testing to that in the field (Ghionna & Jamiolkowski, 1991, Foray, 1991, Mayne & Kulhawy, 1991, Schnaid & Houlsby, 1991, Salgado et al., 1998, Ahmadi & Robertson, 2008, Wesley, 2011 and Pournaghiazar et al., 2012). There is general agreement in the literature that the boundary effects can be minimized if the ratio of diameter of chamber to cone diameter ($d_{chamber} / d_c$) is kept above a certain threshold.

Parkin & Lunne (1982) suggested that boundary effects can be neglected for dense sand if ratio of chamber-cone diameter ratio is more than 50, whereas for loose sand a ratio equal to 21 is considered sufficient. Ghionna & Jamiolkowski (1991) stated

that for low and medium compressible silica sand, the calibration chamber diameter to cone diameter ratio should be greater than 60 for dense and very dense conditions in order to “eliminate” size effects. For loose sand, they concluded that a minimum ratio of 31-35 is desirable. They also highlighted the importance of compressibility and crushability in evaluating the calibration chamber size effects. A limiting value of 70 for calibration chamber-cone diameter ratio is considered sufficient by Mayne & Kulhawy (1991) in their empirical correlation based upon a calibration chamber test database.

Based upon cavity expansion solutions, Schnaid & Houlsby (1991) suggested that the chamber-cone diamter ratio should be atleast 50 to eliminate the size effects. Pournaghiazar et al. (2012) suggested a limiting value of cone-chamber diamter 70. Salgado et al. (1998) reported that the chamber-cone diameter ratio should be 25-125 depending upon the initial horizontal effective stress and density. The sand crushability factor is also another important aspect that has not been investigated much in any of these theoreitical or experimental studies. The sand crushability may have some influence on the required chamber-cone diameter ratio in order to avoid the boundary effects.

The diameter ratio is the most important factor for evaluation of size effects on penetration resistance measured in calibration chamber testing for all type of sands. In this research the chamber-cone diameter ratio is aproximately 52 or 87, for the large (32mm) and mini (19mm) cone penetrometers respectively. Moreover the main test sand used in this research is more crushable than sands used in past studies, therefore no apperciable size effects are present. In order to assess the size effects during cone penetration, miniature pressure transducers were also placed, in a few tests in the soil sample near the rigid boundry and on chamber boundary wall itself.Figure 5.9 shows the location of pressure sensors and radial stress measured during two penetration tests, conducted in dense over medium dense and medium dense over dense samples. From these results it is evident that some boundary effects are present in case of dense soil as a slight increase in horizontal stress can be seen as compared to initial horizontal effective stress. For medium dense samples, no increase of radial stress is observed. The radial stress measured inside the sand sample is much lower than stress measured at the hard boundary. It may be argued that the low stress values measured in sand mass are due to

the pressure sensor displacement during penetration, which may have affected sensor sensitivity.

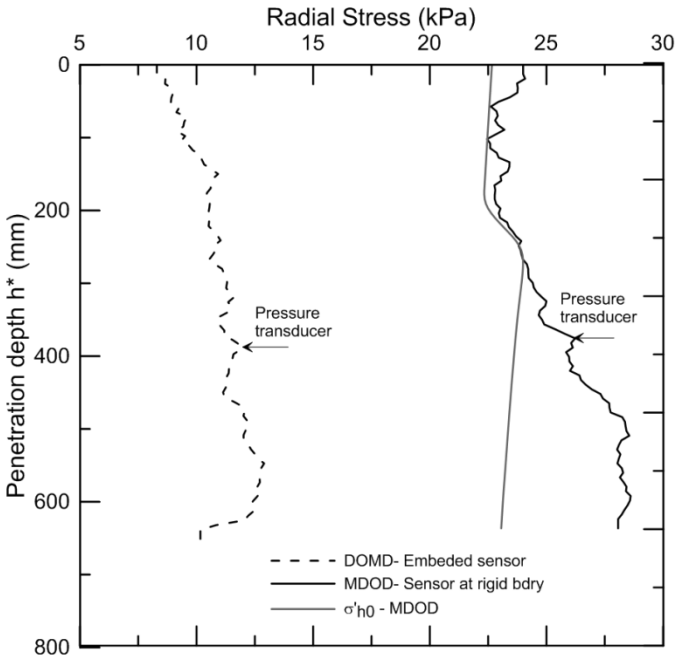

(a)

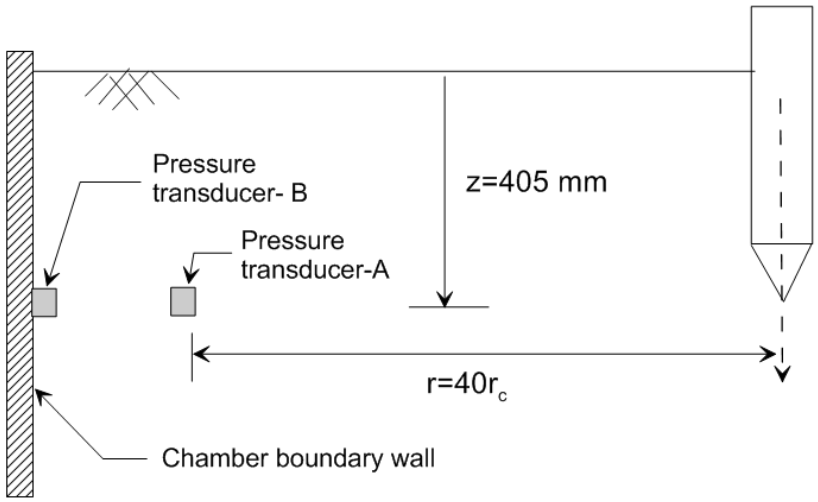

(b)

Figure 5.9 Assessment of boundary effects during cone penetration test

The proximity of the chamber base, a rigid boundary, can also result in increase in cone penetration resistance. To avoid the influence of base boundary effects on measured

tip resistance the cone tip final position should be sufficiently far from the base boundary. In order to assess the base boundary effects, a 20-kN load cell with diaphragm was mounted at chamber base directly below the cone penetration path. Any increase in vertical stress over the initial value would indicate the presence of boundary effects. Figure 5.10 shows the vertical stress measured at the chamber base versus cone penetration depth. These measurements shows that, for very dense sand samples, the significant base boundary effects are present when cone is located at the distance less than 15 cone diameters from the chamber base. For medium dense and loose test samples, the base boundary effects are negligible at the distances greater than 12.5 and 10 cone diameters from the base boundary, respectively.

5.2.5 Particle Size Effects

There are two facets of particle size effects: The first is related to the tip resistance. If the particle size to cone diameter ratio falls below a threshold for which the assumption of continuum no longer apply, particle size and arrangement will start influencing the tip resistance. Secondly, if a miniature cone is used, the shear banding and strain localization takes place along the model penetrometer shaft is of same size as for the prototype, and thus will result in increased frictional resistance due to increase in lateral stiffness (Foray, 1991).

In order to minimize these scale effects, limiting ratios of cone diameter to mean particle size (d_c / D_{50}) have been suggested in various studies. Gui et al. (1998) suggested that d_c / D_{50} should be greater than 20 to minimize the scale effects on tip resistance. Similarly Bałachowski (2007) also concluded that particle size effects appear if d_c / D_{50} is less than 20.

In this study we used two different model penetrometers with d_c / D_{50} ratios of 41 and 25. The ratio is greater than the suggested limit in literature; therefore it can be considered that particle size effects on cone tip resistance are avoided. With regards to side friction, some scale effects in the mini cone will be present since the cone diameter

is 19 mm, as compared to standard cone diameter of 36mm. In the case of the large cone used in this study, which has a diameter of 32 mm, the scale effects will be negligible.

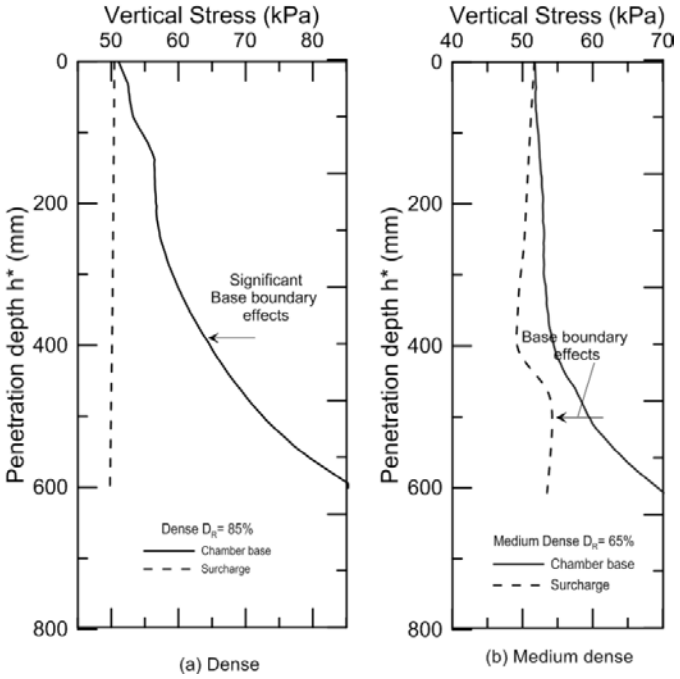

(a)

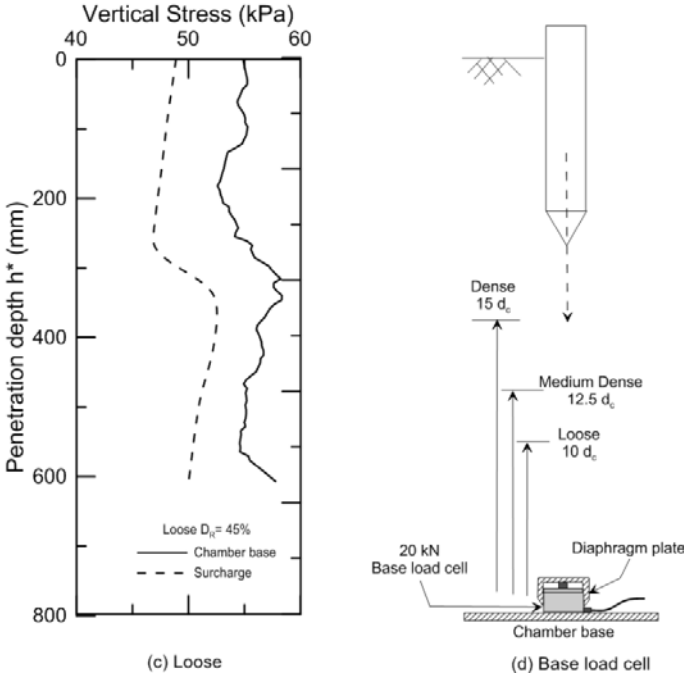

(b)

Figure 5.10 Chamber base boundary effects

5.2.6 Penetration Rate Effects

The standard penetration rate for cone penetration testing according to ASTM testing standard D5778 is 20 mm/s. In this study, the main objective was to deduce the displacement field from digital images acquired during the cone penetration process using the DIC technique as explained in section 3.3.2. The application of this technique requires a small cone penetration rate; therefore, the cone penetration rate selected in all tests was ~1mm/s (versus standard penetration rate of 20 mm/s). Moreover, the penetration rate effects on cone resistance in dry sand are insignificant, as reported in previous studies (Gui et al., 1999, Danziger & Janeiro, 2012), therefore it is perceived that the selected penetration rate will have no significant effect on measured tip resistance.

5.2.7 Effects of Glass Friction

In this study a half-circular model cone was penetrated in sand samples immediately by next to a glass viewing window so that imaging during the cone penetration process was possible. There are two forms of friction between the surfaces of an interface: static friction to overcome resistance to initiation of motion and the kinematic friction, which takes place during continued sliding. These types of possible kinematic frictional effects on testing results are discussed in the following sections.

5.2.7.1 Friction Effects on Cone Penetration Resistance

Two types of friction effects on measured cone tip resistance $q_{c,m}$ are present in CPT conducted in half-circular calibration chamber. The first effect is the decrease in tip resistance due to frictional force F_r between flat side of the half-circular cone with glass sheet, which prevents the deformation of diaphragm of load cell, seated behind the tip. The second effect is the increased penetration resistance $q_{c,hc}$ due to increased expanding pressure required to overcome the additional frictional resistance developed along sand-glass interface. In this way we can postulate that the frictional effects are self-compensating and net effect on penetration resistance will be very small. In order to

assess estimate these frictional effects, let us consider the force diagram acting along cone tip as shown in Figure 5.11. From statics, the net load measured by the load cell F_{LC} is expressed as:

$$F_{LC} = F_{tip,hc} - F_r \tag{5-1}$$

By dividing both sides by cone projected area A_c

$$\frac{F_{LC}}{A_c} = \frac{F_{tip,hc}}{A_c} - \frac{F_r}{A_c} \tag{5-2}$$

$$q_{c,m} = q_{c,hc} - \sigma_{nf} \cdot \frac{As}{A_c} \tag{5-3}$$

where As is the half-circular cone surface area and $\sigma_{n,f}$ is the frictional resistance between cone flat side and glass sheet.

The 60° apex angle cone penetrometer used in this research has twice the cone surface area than the half-circular cone projected area.

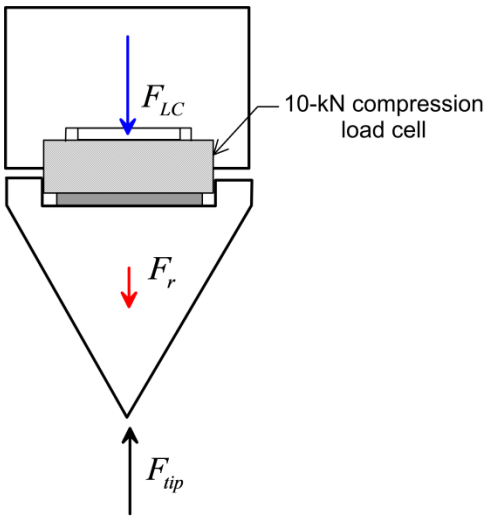

Figure 5.11 Penetrometer-glass friction effect on measured penetrometer tip load

The decreasing effect of friction between cone and glass can be derived by assuming the average stress state acting along the cone face (Salgado & Prezzi, 2007) as shown in Figure 5.12. If we consider the average major vertical principal stress acting at cone surface is equal to cone resistance ($q_{c,hc}$) than the average normal stress acting on cone surface can be found as ($\sigma_3 = q_{c,hc} / N_T$). The flow number (N_T) is obtained from

mobilized friction angle in transition zone ($N_T = 1+\sin\phi_T / 1-\sin\phi_T$). The mobilized transition zone friction angle ϕ_T depends upon initial relative density and horizontal effective stress and was estimated from $\phi_T - \phi_c$ graph published by Salgado & Prezzi (2007) for 33 degree critical state friction angle. The estimated N_T for initial relative densities of 45%, 85% and initial horizontal effective stress of 25 kPa are 3.537 and 3.851 respectively. The frictional resistance between cone and glass $\sigma_{n,f}$ can be found as:

$$\sigma_{nf} = \sigma_3 \tan\delta_{cone-glass} = \frac{q_{c,hc}}{N_T}\tan\delta_{cone-glass} \qquad (5\text{-}4)$$

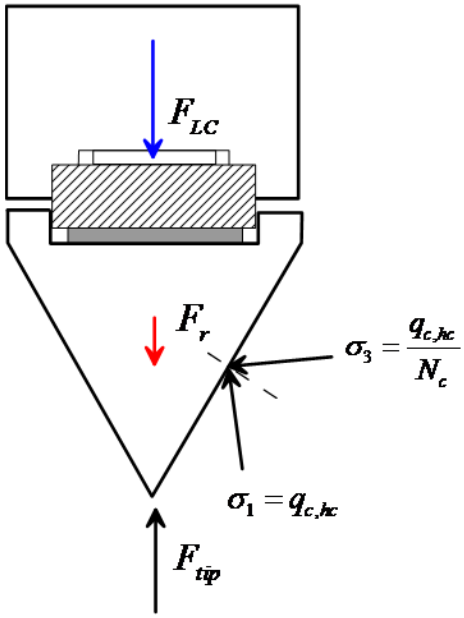

Figure 5.12 Assumed average stress field around cone (after Salgado & Prezzi, 2007)

To quantify the friction resistance σ_{nf} , we also performed interface friction tests between a brass-plate of similar roughness as that of the cone tip and a glass using direct shear testing apparatus. A 5mm thick glass sheet of size 60 × 60 mm was placed in lower half of the shear box as shown Figure 5.14. The brass plate was placed in the top half of

the shear box. The tests were conducted under normal stress ranging from 60 kPa to 442 kPa. The interface friction angle between the cone and glass was measured as 5.62 degrees. Figure 5.14 shows the test results. We also performed interface friction tests between sand particles and glass as discussed in section 5.2.8.2. The frictional resistance σ_{nf} between cone and glass, obtained from Equation (5-4), for loose and dense sands becomes:

$$\sigma_{nf-loose} = (0.0278)q_{c,hc}$$
$$\sigma_{nf-dense} = (0.0256)q_{c,hc} \quad (5\text{-}5)$$

The measured tip resistance from Equation (5-3) is calculated as:

$$q_{c,m-loose} = 0.944q_{c,hc}$$
$$q_{c,m-dense} = 0.948q_{c,hc} \quad (5\text{-}6)$$

Now we will attempt to estimate the increase in cone tip resistance due to frictional resistance between sand particles and the glass sheet. We used the cavity expansion analysis of Salgado and Randolph (2002) in order to estimate the friction effect on penetration resistance. If we consider the cavity expansion process in circular and half-circular calibration chamber test under same initial conditions, than the only difference in cavity expansion process in half-circular calibration chamber is the mobilization of additional resistance to overcome the frictional resistance between sand-glass interface (Figure 5.13). The cone resistance $q_{c,cc}$ in circular calibration chamber will be same as of penetration resistance in half-circular calibration chamber $q_{c,hc}$ in the absence of the frictional resistance q_{cf}. Mathematically we can express this as:

$$q_{c,cc} = q_{c,hc} - q_{cf} \quad (5\text{-}7)$$

The limit pressure required to create the cavity can be related in similar manner:

$$p_{L,cc} = p_{Lc,hc} - \tau_f \quad (5\text{-}8)$$

where p_{L-hc} is the limit pressure mobilized in half-circular calibration chamber; $p_{L,cc}$ is limit pressure mobilized in circular calibration chamber; τ_f is frictional resistance mobilized in half-circular calibration chamber.

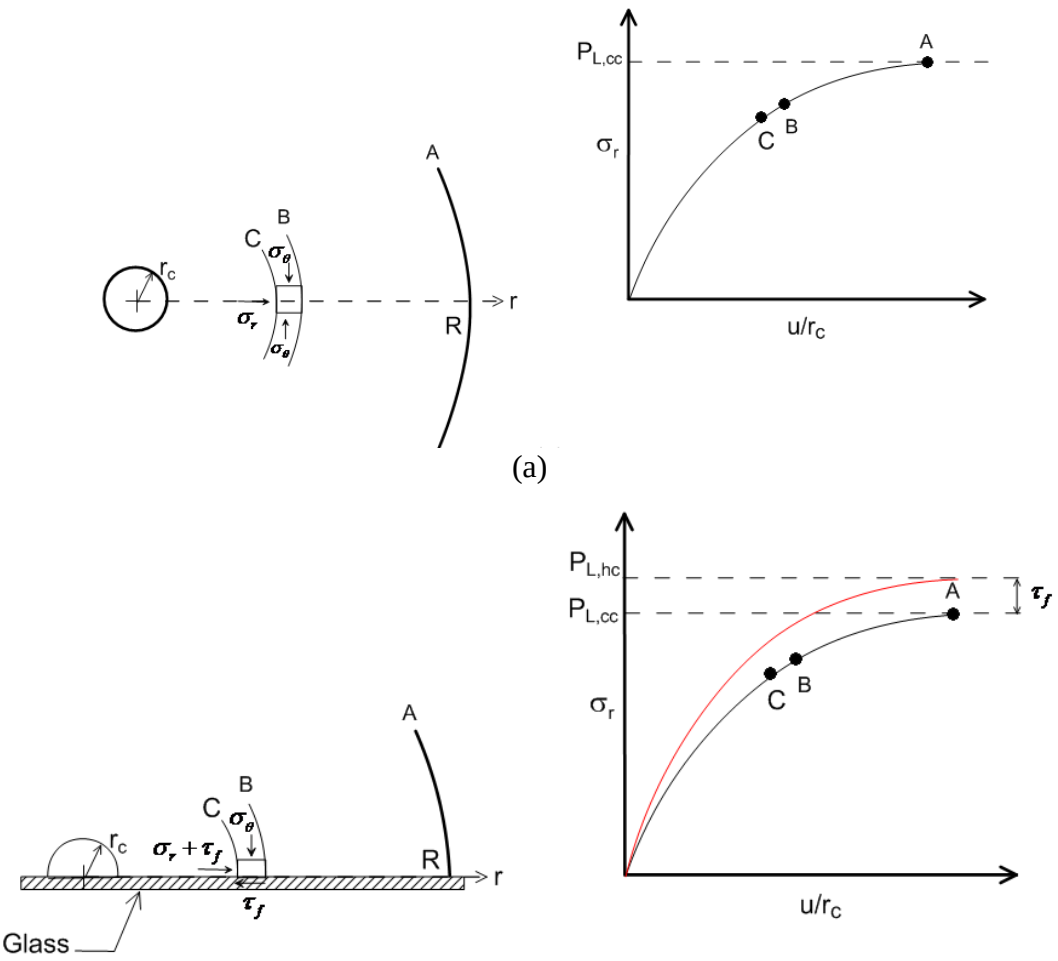

Figure 5.13 Cavity expansions process : (a) in the circular calibration chamber and (b) in the half-circular calibration chamber.

The cone resistance can be related with cavity limit pressure p_L using cavity expansion analysis of Salgado and Prezzi (2007) in a very simplified manner.

$$q_c = p_L N_q \qquad (5\text{-}9)$$

where N_q is cone factor and can be derived iteratively from cavity expansion solution of Salgado & Prezzi (2007). The N_q depends upon friction angle mobilized in transition zone ϕ_T and cone resistance itself. The mobilized transition zone friction angle ϕ_T depends upon initial relative density, horizontal stress. Since the sand along the cone

interface will be in critical-state, therefore any initial contribution of sand glass frictional angle on mobilized ϕ_T will have little influence on critical-state friction angle of sand. Therefore, the N_q mobilized for half-circular and circular calibration chamber tests with same initial conditions will be equal. The frictional resistance τ_f can be calculated from mobilized glass-sand frictional angle as:

$$\tau_f = \sigma_T \tan\delta_{sand-glass} = \frac{p_{L,hc}}{N_T}\tan\delta_{sand-glass} \qquad (5\text{-}10)$$

Combining Equation (5-7) and (5-9), the cone resistance in half-circular $q_{c,hc}$ is expressed as:

$$q_{c,hc} = (1+\frac{\tan\delta_{sand-glass}}{N_T})\, p_{L_{,cc}} N_q = (1+\frac{\tan\delta_{sand-glass}}{N_T}) q_c \qquad (5\text{-}11)$$

The N_T estimated from Salgado & Prezzi (2007) are 3.457 for loose and 3.851 for dense sand. The sand-glass interface friction angle measured from interface shear testing is as 8.54 degrees. Therefore, the increased cone resistance for half-circular calibration chamber can be estimated from the cone resistance measured in circular calibration chamber as:

$$\begin{aligned} q_{c,hc-loose} &= 1.043 q_{c,cc} \\ q_{c,hc-dense} &= 1.039 q_{c,cc} \end{aligned} \qquad (5\text{-}12)$$

From Equation (5-6) measured cone resistance can be related with cone resistance in circular chamber as:

$$\begin{aligned} q_{c,m-loose} &= 0.9845 q_{c,cc} \\ q_{c,m-dense} &= 0.984 q_{c,cc} \end{aligned} \qquad (5\text{-}13)$$

From Equation (5-13) the net measured cone resistance in loose and dense sand is a 1.5% smaller than the actual cone resistance as expected in a circular calibration chamber. This reduction is due to glass-cone tip friction that affects the tip load cell diaphragm deformation, which would be in absence of glass-tip friction. The increase in cone tip resistance due to increased cavity limit pressure required for overcoming the frictional resistance between sand particles and glass sheet has been suppressed by the tip-glass

friction effect. Since the effect of glass friction on measured cone resistance is small, In addition to that, we lubricated the flat side of the cone interfacing with the glass with grease to minimize the cone-glass friction effect and therefore, the frictional effect can be neglected in interpretation of cone resistance.

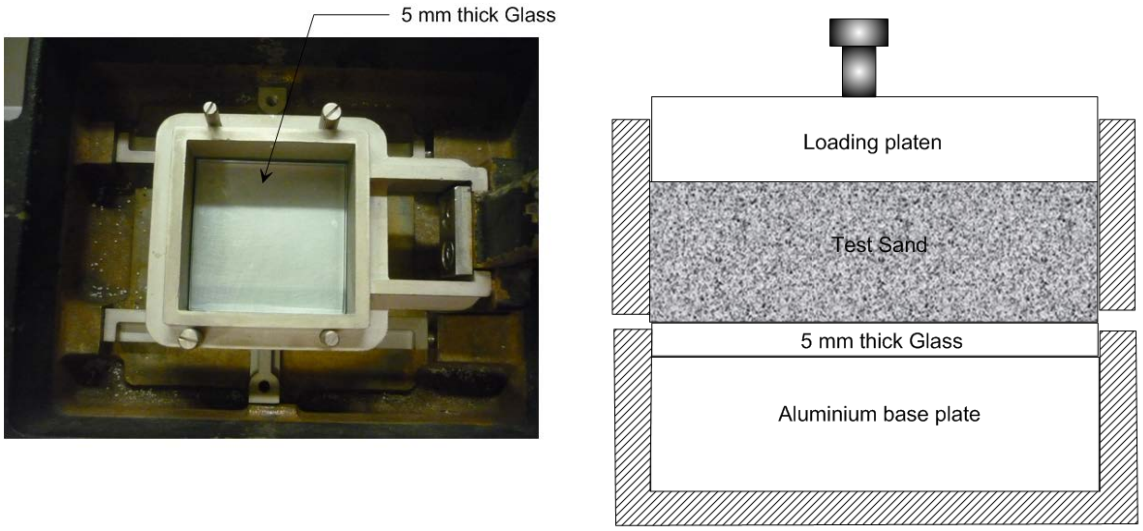

(a) (b)

Figure 5.14 Brass-glass interface friction test arrangement

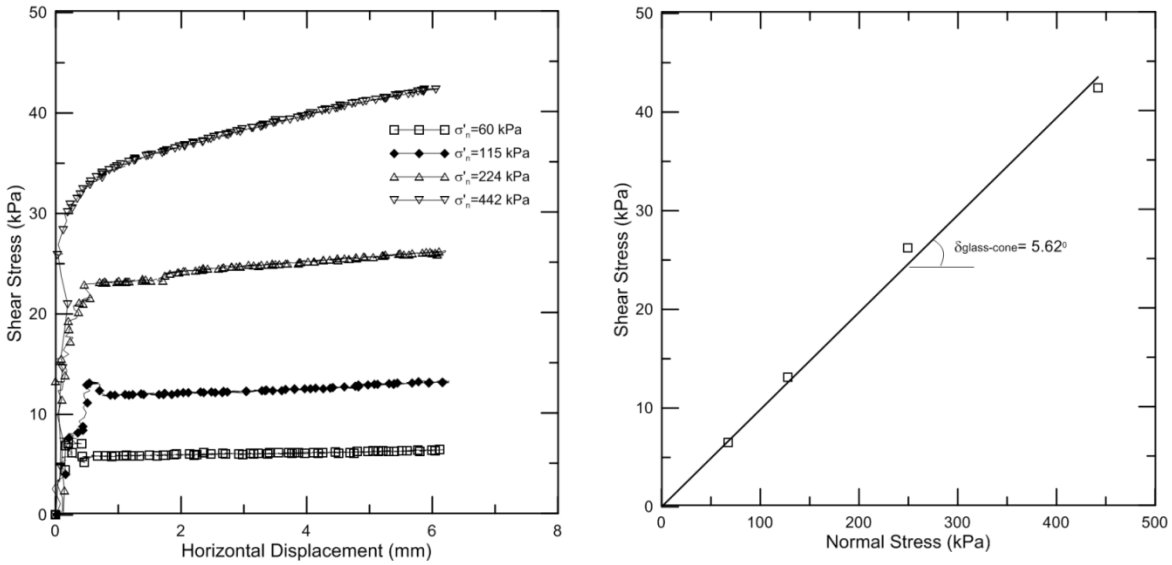

(a) Shear stress vs. horizontal displacement (b) Brass-glass interface friction angle

Figure 5.15 Cone-glass interface friction tests results

5.2.7.2 The Sand-Glass Friction Effects

The main objective of this study is to measure the displacement field during the continued cone penetration process using DIC technique. The cone penetration process is observed through Plexiglas observation windows. As the cone penetrates it starts displacing the sand vertically downward and radially. The sand particles slides along the glass observation windows and displacements are deduced by tracking the movement of these sliding sand particles. The stress ahead of advancing cone is also increased concurrently with the sand particles displacements. The friction between sand particles and observation glass window will affect the soil particle movement to some extent. In order to assess this frictional effect, we performed the interface testing between the testing sand and glass in direct shear test. The 5 mm thick glass sheet was placed at the bottom of shear box similar to Figure 5.11. The sand samples were prepared in upper half of the shear box with average relative density of (D_R) 65%. The interface tests were performed at the stress range of 25 kPa to 142 kPa. As can be seen in Figure 5.16, which shows the shear stress vs. horizontal displacement curves obtained from the interface direct shear tests, the response is almost perfectly plastic, with shear strength developing at very small displacements (of the order of 0.15-0.2 mm). The sand-glass interface friction angle is 8.5^o for this silica sand, which has angular particles; smaller interface friction angles are expected for the other sands considered in this study, which have rounded and sub-rounded particles. This value is in line with previous work done by White and Bolton (2004), who reported interface friction angles ranging from 9 to 10^o. The displacement required for mobilization of the interface friction is considerably less than the displacement that occurs during continued cone penetration. Thus, any interface friction is anticipated to have minimum or negligible effects on the motion of the sand particles near the cone and, therefore, can be disregarded in the interpretation of the displacement results. Only at locations far from the cone where the displacements in the absence of the glass would be very small would the displacements obtained from the DIC technique be, in relative terms, significantly less than the displacements that would be observed in the real problem. This only happens far from the cone and does not affect the solution to any meaningful extent.

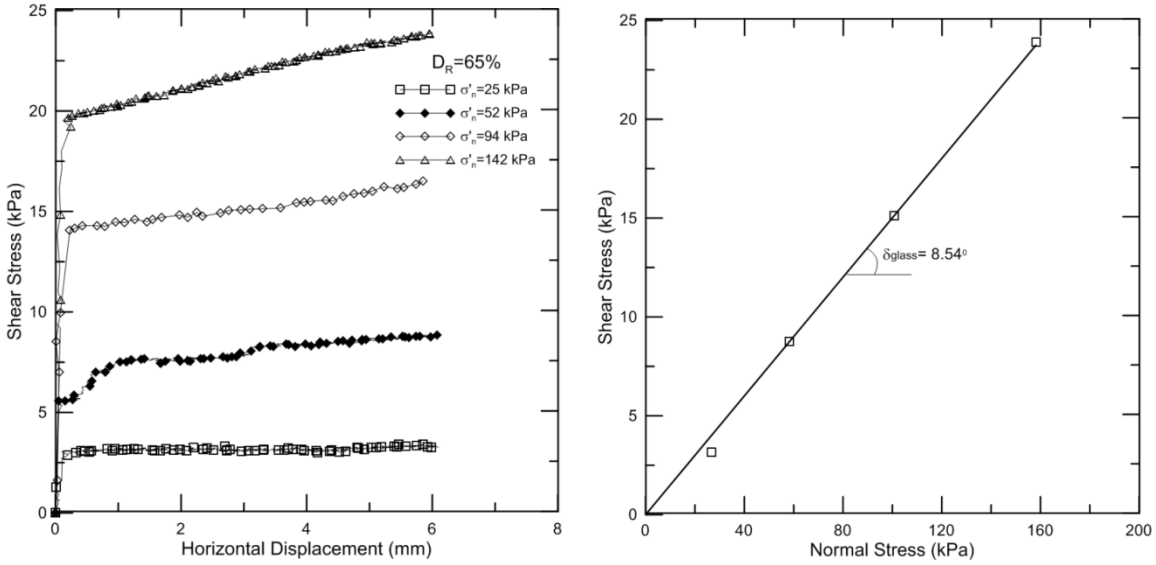

(a) Shear stress vs. horizontal displacement (b) Sand-glass interface friction angle

Figure 5.16 Glass-Sand interface friction test results

In order to investigate the total frictional drag effect of glass-sand interface on displacement in the entire soil model during cavity expansion, we performed the spherical cavity expansion analysis using finite element code PLAXIS. The cavity was expanded from initially small radius of 5 mm by employing incremental volumetric strain to reach the final cavity radius of 15 mm by using analysis procedure similar to Xu & Lehane (2008). Two cavity expansion numerical models with same soil conditions were considered as shown in Figure 5.17. The effect of interface friction was induced in the model by fixing the radial displacements initially along the cavity and then introducing the interface elements to allow for sliding along the sand-glass interface during cavity expansion process. The soil was modeled using Hardening Soil Model (HS) available in PLAXIS. The software uses Mohr-Coulomb (MC) elastic-plastic yield criterion for modeling of the interface. The interface model parameters are automatically computed from neighboring soil parameters by using the user-specified strength reduction factor, R_{inetr}. The reduction factor ($R_{\text{int}er} = \delta_{\text{int}erface} / \phi_{soil}$) was deduced from sand-glass interface

test results. The soil and interface model parameters used in the analysis are shown in Table 5.2.

Table 5.2 Model parameters used in interface analysis

Parameter	Soil (HS)	Interface (MC)	Unit
Unit Weight, γ,	14.5	14.5	kN/m^3
E_{50}^{ref} (P_{ref} = 100 kPa)	30000	-	kPa
E_{oed}^{ref} (P_{ref} = 100 kPa)	15500	-	kPa
E_{ur}^{ref} (P_{ref} = 100 kPa)	125000	-	kPa
E	-	12675	kPa
Peak friction angle, ϕ_p	36	8.54	degree
Dilatancy angle, ψ	3.63	0	degree
Power, m	0.45	-	
R_f	0.9	-	
R_{inter}	0.215	1	
Interface thickness t_{inter}		0.65	
Relative density, D_R	65	-	%

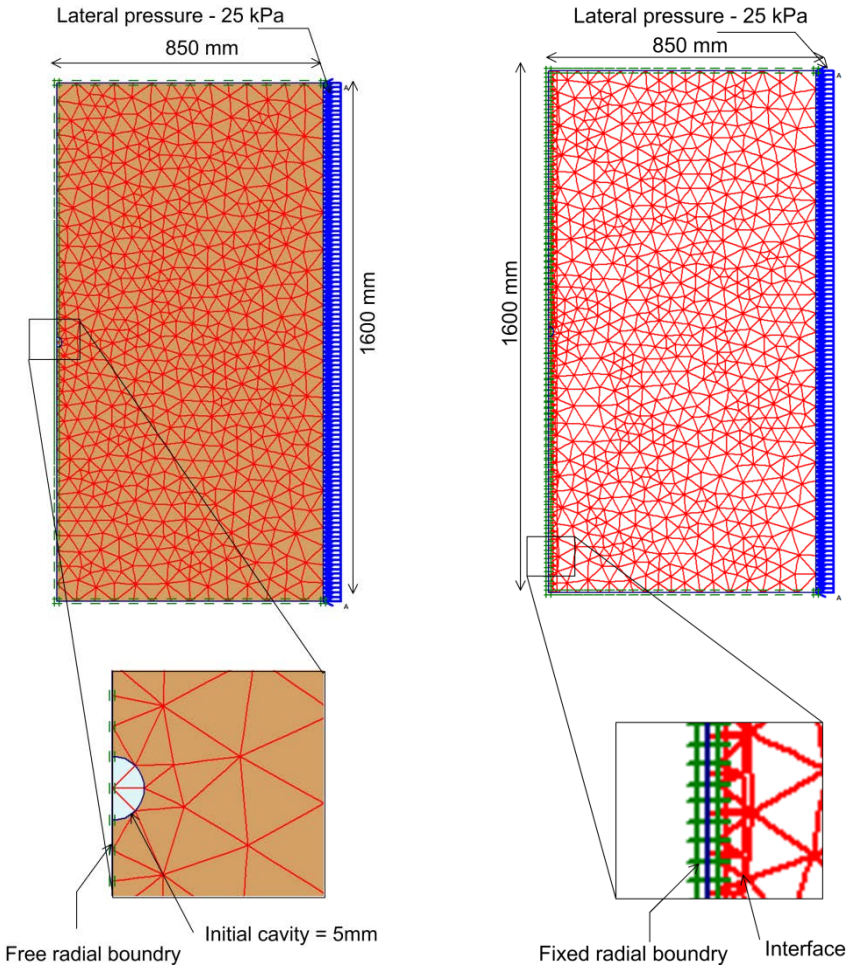

(a) (b)

Figure 5.17 Spherical cavity expansion models: (a) without interface friction, and (b) with interface friction.

The performance of interface model available in the PLAXIS finite element code was also compared with experimental interface test, by using the simple sliding block model. Then the verified interface properties were used in the cavity expansion analysis. Figure 5.18(a) shows the sliding block model and test results that compared well with experimental interface tests conducted at normal stress of 25 kPa (the initial average normal stress acting on the glass sheet under the surcharge of 50 kPa).

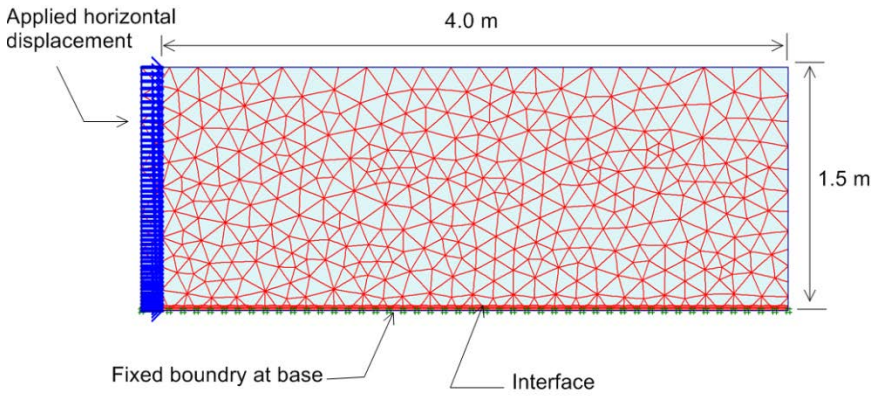

(a)

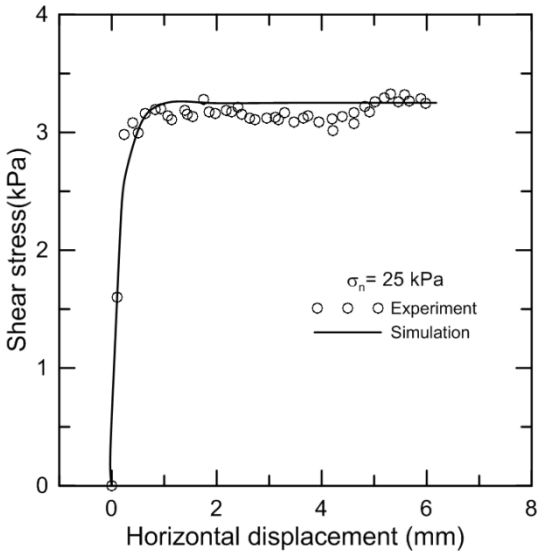

(b)

Figure 5.18 Interface test simulation: (a) sliding block model, and (b) test results.

Similar analyses were also performed for cylindrical cavity expansion to see the effect of glass friction on soil displacement. Figure 5.19 shows the effect of glass friction on displacement field in spherical and cylindrical cavity expansions respectively. The effect of glass friction in spherical cavity expansion is small as compared to cylindrical cavity expansion analysis owing to the fact that the different amount of circumstantial (normal stress acting at glass) stress is mobilized during spherical and cylindrical cavity

expansion process. These results from numerical study shows that the sand-glass interface friction effect on displacements are small and can be neglected in DIC displacement measurements.

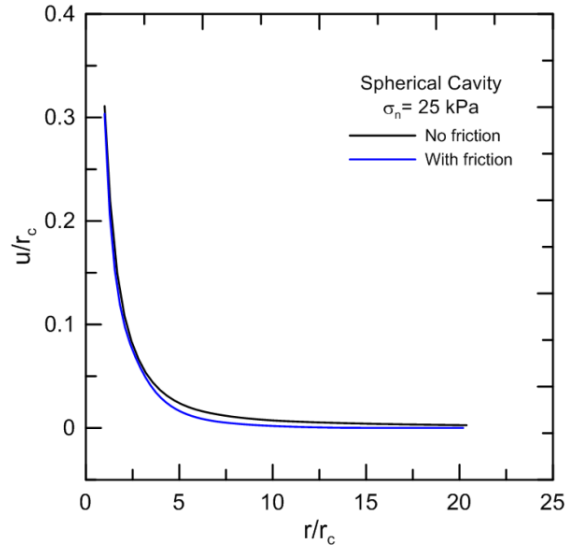

(a)

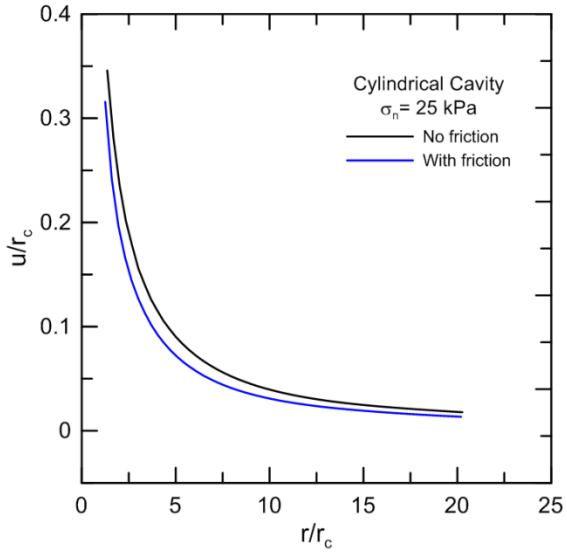

(b)

Figure 5.19 Glass-sand interface friction effect on displacements: (a) spherical cavity, and (b) cylindrical cavity.

5.3 Experimental Program

5.3.1 Test Matrix

Two series of cone penetration tests were conducted; one in uniform soil profiles and second in layered soil profiles. Sample density, sand type, cone size, surcharge stress level and cone tip geometry were varied during these cone penetration test series. A series of ten cone penetration tests were performed in the DIC chamber in uniform sand samples (Table 5.3). A total of eight tests were performed on the most crushable silica sand (#2Q-ROK) with and without surcharge. Out of these eight tests, three tests were performed without any surcharge to investigate the development of the slip mechanism at shallow penetration and the effect of stress level on the displacement field. Two tests were performed on the other two sands, ASTM 20-30 sand and Ohio Gold Frac sand. The tests are identified by a code that specifies the sand density (L=loose, MD=medium dense and D=dense), surcharge (0 or 50 kPa), test number (a number from 1 to 10) and sand type (#2Q-ROK, ASTM 20-30 and Ohio Gold Frac). For example, CPTL50-T4-#2Q-ROK identifies CPT number 4, performed on a loose #2Q-ROK sand sample with a surcharge of 50 kPa. Table 5.3 shows the cone penetration tests details conducted in uniform soil profile.

A series of 11 cone penetration tests were performed in layered samples. The tests are identified by a code that specifies the sand density (L = loose, MD = medium dense and D = dense), surcharge (50 kPa), test number (a number from 1 to 11) and sand type (#2Q-ROK). For example, CPTLOD50-T1-#2Q-ROK identifies CPT number 1, performed on a loose-over-dense #2Q-ROK sand sample with a surcharge of 50 kPa. A total of 8 tests were performed with the cone with diameter of d_c = 31.75mm in two-layered soil profile samples. The two-layered samples were prepared with strong over weak and weak over strong layers. Two tests, CPTLOD50-T9-mini and CPTDOL50-T10-mini, were also conducted in two-layered samples with the cone with diameter of $d_{c,mini}$ = 19.05 to investigate the cone size effect on penetration resistance when the probe is near a layer interface. One test, CPTD-L-D50-T11-#2Q-ROK, was conducted in a

three-layered sample with a loose sand layer sandwiched between two dense layers. Table 5.4 shows the test details conducted in layered soil profiles.

Table 5.3 Cone penetration test series in uniform soil profiles

Test Code	Surcharge (kPa)	Initial void ratio *e*	Relative Density D_R (%)	dc/D_{50}	$d_{chamber}/d_c$
CPTL0-T1-#2Q-ROK	0	0.849	45	41.0	53.0
CPTMD0-T2-#2Q-ROK	0	0.783	65		
CPTD0-T3-#2Q-ROK	0	0.718	85		
CPTL50-T4-#2Q-ROK	50	0.849	45		
CPTL50-T5-#2Q-ROK	50	0.855	42		
CPTMD50-T6-#2Q-ROK	50	0.790	63		
CPTD50-T7-#2Q-ROK	50	0.718	85		
CPTD50-T8-#2Q-ROK	50	0.7252	82		
CPTD50-T9-Ohio Gold Frac	50	0.578	87	53.0	
CPTD50-T10-ASTM 20-30	50	0.538	85	49.0	
CPTD50-T11-Mini-#2Q-ROK	50	0.849	45	25.0	85.0
CPTL50-T12-Mini-#2Q-ROK	50	0.718	85		
CPTL0-T13-#2Q-ROK	0	0.932	20	41.0	53.0
JPL0-T14-Flat-#2Q-ROK	0	0.932	20		

[1]L = loose; MD = medium dense; D = dense

In miniature cone tests, only the total cone resistance was measured; instrumentation of the tip failed because of its very small size.

Table 5.4 Cone penetration test series in layered soil profiles

Test Code	Soil Profile	Layer Thickness (mm)	Relative Density D_R (%)
CPTLOD50-T1-#2Q-ROK	Loose over dense	390/610	45/85
CPTLOD50-T2-#2Q-ROK	Loose over dense	390/610	43/85
CPTDOL50-T3-#2Q-ROK	Dense over loose	420/580	85/43
CPTDOL50-T4-#2Q-ROK	Dense over loose	390/610	85/42
CPTMDOD50-T5-#2Q-ROK	Medium dense over dense	390/610	65/85
CPTDOMD50-T6-#2Q-ROK	Dense over medium dense	410/590	85/63
CPTLOMD50-T7-#2Q-ROK	Loose over medium dense	390/610	42/65
CPTMDOL-T8-#2Q-ROK	Medium dense over loose	365/635	65/43
CPTLOD50-T9-mini-#2Q-ROK	Loose over dense	355/645	45/85
CPTDOL50-T10-mini-#2Q-ROK	Dense over loose	355/645	85/45
CPTD-L-D50-T11-#2Q-ROK	Dense -loose - dense	300/150/550	74/46/74

5.3.2 Test Procedure

5.3.2.1 Sample Preparation

The test sand samples were prepared by air pluviation using a large pluviator placed above the chamber at a fixed position such that the sand drop height was greater than the critical fall height. The critical height was determined as 500 mm, obtained through calibration. The target sample densities were achieved by changing the flow rate through addition or removal of a diffuser sieve. The drop height was reduced for preparation of loose sand samples. While carefully maintaining the drop height, a half-circular pluviator placed inside the chamber was slowly raised as the sample was prepared. For sample density verification, during sample preparation, nine miniature two-inch-diameter thin tube samplers were placed at three different levels within the sand sample. The density variation was determined to be within 2-3%. Figure 5.20 shows the typical relative density achieved at each level in uniform soil test series. The average

density values (±3%) achieved during samples preparation are 85%, 65% and 46% for dense, medium dense and loose sand respectively.

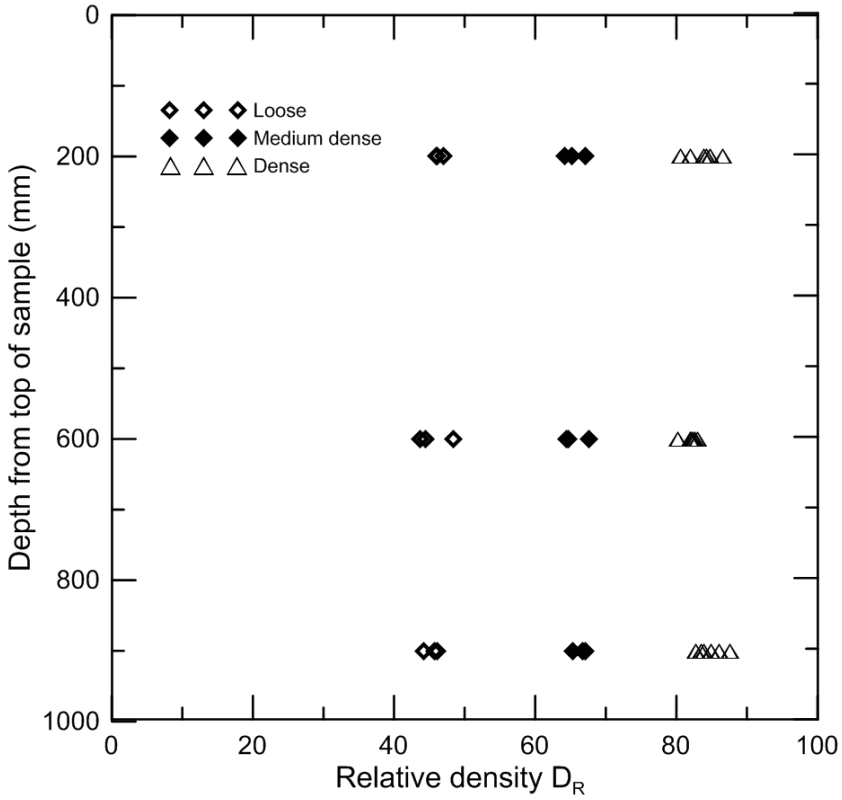

Figure 5.20 Typical relative density at each level of soil samples

5.3.2.2 Sensor Arrangement

In addition to cone tip load sensor and jacking load cell installed at head of cone penetrometer a base load cell was mounted directly below the cone penetration path to monitor the chamber base boundary stress during consolidation and penetration phase of test. The monitoring of the chamber base pressure served as termination criteria for tests to avoid the base boundary effects on tip resistance. In layered soil profile test a miniature pressure transducer was also installed at the layer interface to samples the sensing distance from interface. In few tests the lateral stress was also measured by installing the mini pressure transducer at a distance of 2 cone radius behind the cone tip. In two tests a miniature pressure transducer were also installed at the chamber wall to evaluate the

lateral boundary effects during cone was penetrated. Figure 5.21 shows the sensors arrangement in a penetration test.

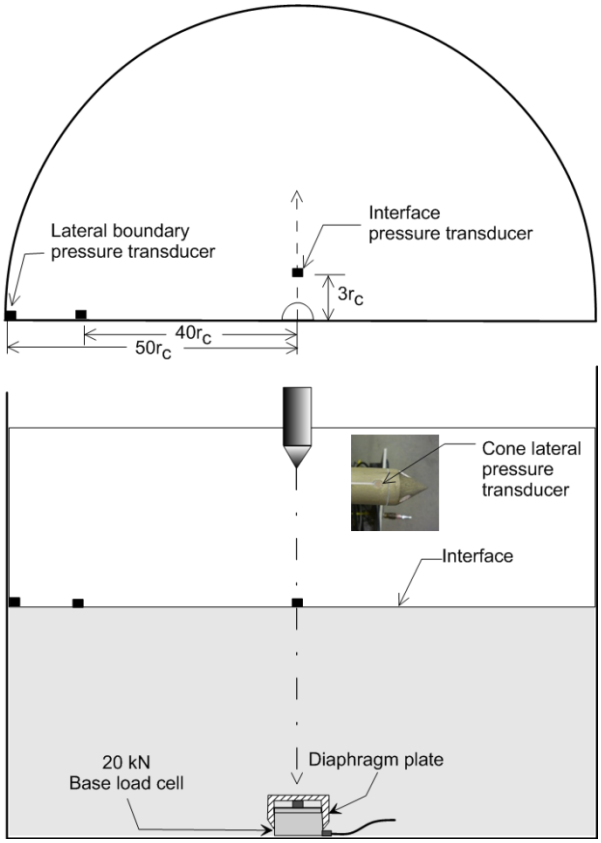

Figure 5.21 Sensors arrangement for penetration test

5.3.2.3 Sample Consolidation

After sample preparation, the pressure bladder is installed on the top of sand and a reaction plate is placed above it and secured with bolts. The consolidation pressure of 50 kPa is applied gradually through a high-pressure air line. Sufficient time is allowed for stabilization of the consolidation pressure, which is then monitored during the entire duration of the test through a pressure transducer. A small fluctuation of ± 2-3 kPa was observed in the applied consolidation pressure due to the automatic starting and tripping of air compressor during the test. Figure 5.22 shows the time history plots of the applied surcharge pressure during loose, medium dense and dense sand tests after the start of cone penetration.

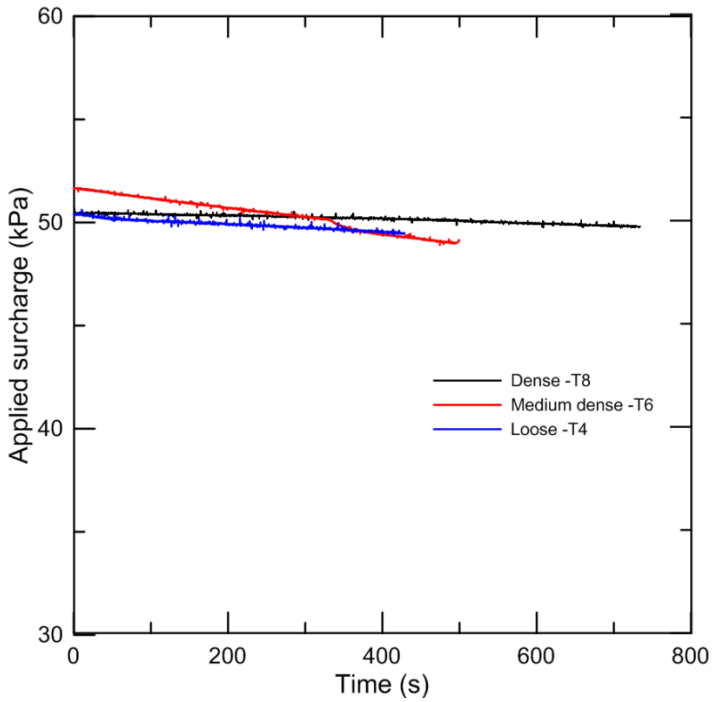

Figure 5.22 Time history of applied surcharge during penetration tests

5.3.2.4 Jack Positioning and Penetrometer Alignment

Precise alignment of the cone penetrometer is critical for the elimination of possible sand intrusion between the cone and the glass sheet. The cone penetrometer mounted on the jacking system is positioned precisely with the help of the screw handle of the jack mechanical alignment system to align it with the glass sheet. Three sets of cam follower are slightly pressed against the cone for precise cone guidance during penetration as shown in Figure 5.23.

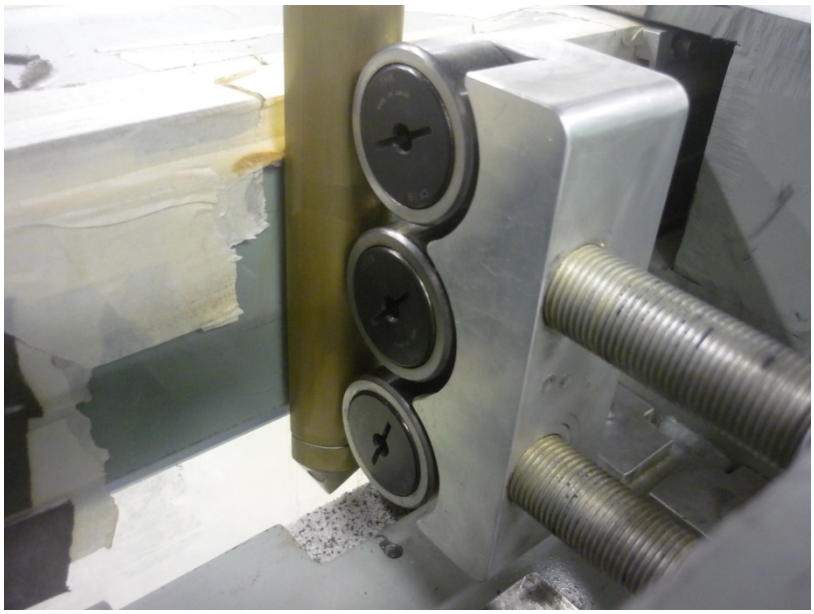

Figure 5.23 Alignment of penetrometer against glass with Cam-Followers

5.3.2.5 Camera Alignment and Lighting

Correct camera alignment with respect to observation windows is critical to avoid additional image distortion due to misalignment. A three-axis leveling system is used to level the cameras and a cross-hair target was used to align each individual camera with the corresponding observation window. Compact fluorescent lights (CFL) were used to illuminate the observation windows. This lighting arrangement does not produce excessive heat and produces sufficient bright light to illuminate the soil observation plan. Careful alignment of lights was done to reduce the amount of light reflection and generate uniform illumination.

5.3.2.6 Probe Penetration and Data and Image Acquisition

The data and image acquisition software is synchronized manually. The image recording starts after selecting the image capture frame rate of 2 frames per second. The cone penetration started with speed of 0.802 mm/min. The data and image acquisition software is stopps after the cone has reached to the desired penetration depth. The sensor and image data are transferred to external hard drives for DIC analysis.

5.3.2.7 Post-Test Observations

After completion of a test, close up images were also recorded with digital handheld microscope in a few tests to observe the shear band formation and extent of particle crushing along the penetrometer shaft. A few sand samples were also recovered from the cone penetration path in order to quantify the particle crushing.

5.4 Summary

In this chapter, the cone penetrometer test procedures and the test program were discussed in detail. The sizes of calibration chamber and model penetrometer are considered appropriate to avoid the significant chamber boundary and particle size effects. Use of additional pressure sensors allowed assessment of the chamber lateral and base boundary effects. The glass friction effects on penetration resistance and soil displacement were evaluated in detail, and these effects were found to be small under present experimental conditions. Repeatability and uniformity of sample density was evaluated.

CHAPTER 6. CONE PENETRATION TESTS IN UNIFORM SAND

6.1 Introduction

This chapter presents the results and interpretation of cone penetration tests in uniform sand sample. A series of ten cone penetration tests were performed in the DIC chamber in uniform sand samples (Table 5.3). A total of eight tests were performed on the most crushable silica sand (#2Q-ROK) with and without surcharge. Out of these eight tests, three tests were performed without any surcharge to investigate the development of the slip mechanism at shallow penetration and the effect of stress level on the displacement field. Two tests were performed on the other two sands, ASTM 20-30 sand and Ohio Gold Frac sand. The tests are identified by a code that specifies the sand density (L = loose, MD = medium dense and D = dense), surcharge (0 or 50 kPa), test number (a number from 1 to 10) and sand type (#2Q-ROK, ASTM 20-30 and Ohio Gold Frac). For example, CPTL50-T4-#2Q-ROK identifies CPT number 4, performed on a loose #2Q-ROK sand sample with a surcharge of 50 kPa. The results are divided into two parts, firstly, the results from conventional sensors are presented and secondly, the results from Digital Image Correlation (DIC) analysis are discussed. The DIC data includes the displacement and strain paths during incremental and continued cone penetration are presented. Table 5.3 shows the details of each test, includes the initial density, soil type, and penetrometer type. Mainly results from two types of test series are included, one from the tests without surcharge in order to investigate the shallow penetration mechanism and other, with surcharge for deep penetration analysis.

6.2 Cone Penetration Resistance

The cone tip resistance was measured by a 10-kN embedded compression load cell as shown in Figure 4.16 and total jacking force was also measured by a 20-kN in-line compression/tension load cell as shown in Figure 4.17. Cone resistance profiles were obtained from the measurements made by the load cell embedded inside the cone tip; these are illustrated in Figure 6.1 and Figure 6.2. Figure 6.1(a) shows cone resistance profiles for the tests performed in loose, medium dense and dense sand samples without surcharge loading (CPTL0-T1-#2Q-ROK, CPTMD0-T2-#2Q-ROK & CPTD0-T3-#2Q-ROK). Figure 6.1(b) shows the q_c profiles for all the cone penetration tests performed with a surcharge of 50 kPa in the #2Q-ROK silica sand. Cone resistance increases with increasing initial sample relative density in all tests. In the loose and medium dense sand samples, cone tip resistance tends to stabilize earlier than in the dense sand sample.

Figure 6.2(a) shows the cone resistance profiles for the tests performed in dense samples ($D_R \approx 85\%$) prepared with two different silica sands (#2Q-ROK and Ohio Gold Frac) considered in this study. These results clearly show the effect of particle crushing on cone resistance, as the more crushable sand (#2Q-ROK) offers less resistance to cone penetration than the sand of intermediate crushability (Ohio Gold Frac). The effect of particle shape and size on crushability and cone resistance can also be inferred from the cone resistance comparison shown in Figure 6.2(a), as the #2Q-ROK sand (CPTD50-T8-#2Q-ROK) has angular particles, whereas Ohio Gold Frac sand (CPTD50-T9-Ohio Gold Frac) has sub-rounded particles. The more angular the particles, the more crushable the sand, and the smaller the cone resistance is. Figure 6.2(b) shows the measured cone penetration resistances and the predicted cone resistances for #2Q-ROK obtained using CONPOINT (Salgado, 2002), which is based on cylindrical cavity expansion theory. The predicted cone resistances are within ±20% of the measured cone resistances.

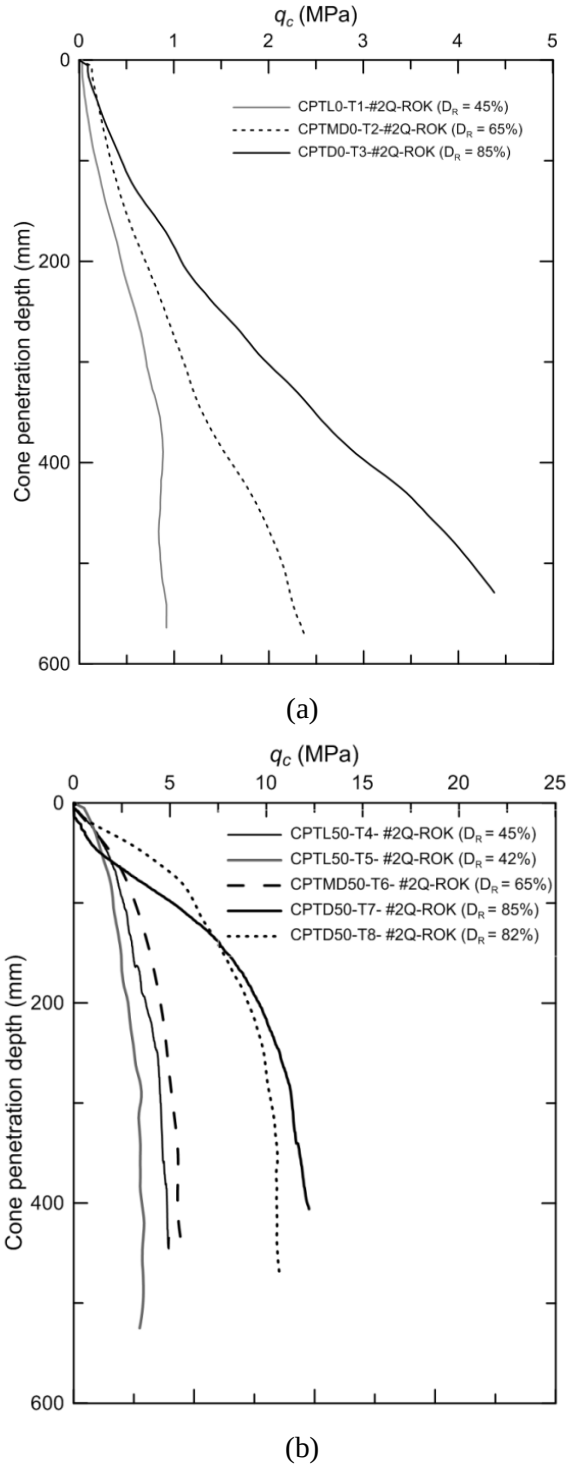

Figure 6.1 Cone resistance profile for penetration tests in #2Q-ROK sand: (a) tests without surcharge and (b) tests with a surcharge of 50 kPa.

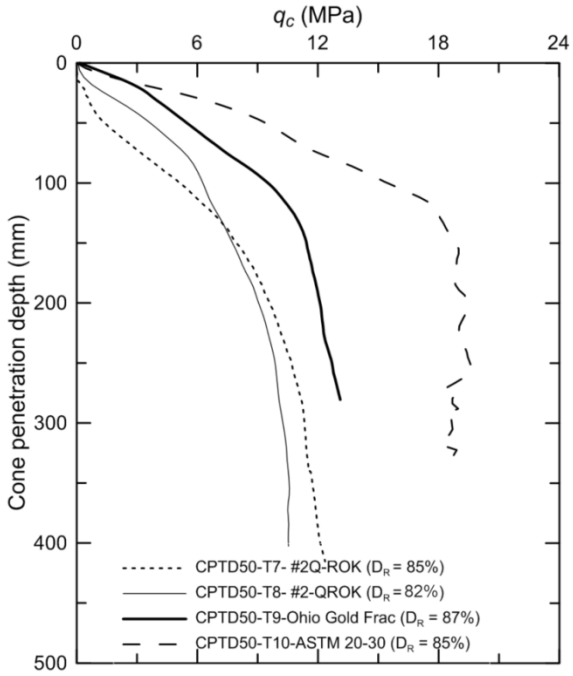

(a)

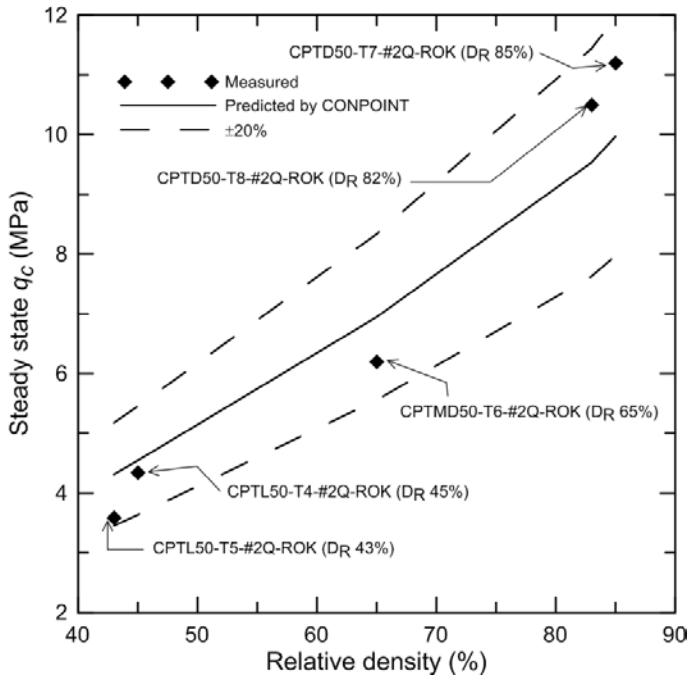

(b)

Figure 6.2 Comparison of cone resistance profiles between: (a) #2Q-ROK and Ohio Frac sand and (b) measured steady state resistance of #2Q-ROK and predicted by CONPOINT.

6.2.1 Total Cone Resistance

Figure 6.3 shows the total cone resistance measured during cone penetration tests with surcharge. The total cone resistance measured in crushable silica sand (#2Q-ROK) increases with density and the steady resistance of 0.8 kN for loose, 1.8 kN and 4.5 kN for the dense sand are observed. A smaller cone resistance of 1.5 kN in miniature cone test (CPTD-T11-Mini) is observed and resistance gets dropped at very deep penetration. A slight increase in cone resistance is observed in case of dense and medium dense sand due to the cone proximity to the chamber base boundary at the penetration depth of 400mm for dense penetration test (CPTD-T7) and 500 mm for the medium dense sand test (CPTMD-T6).

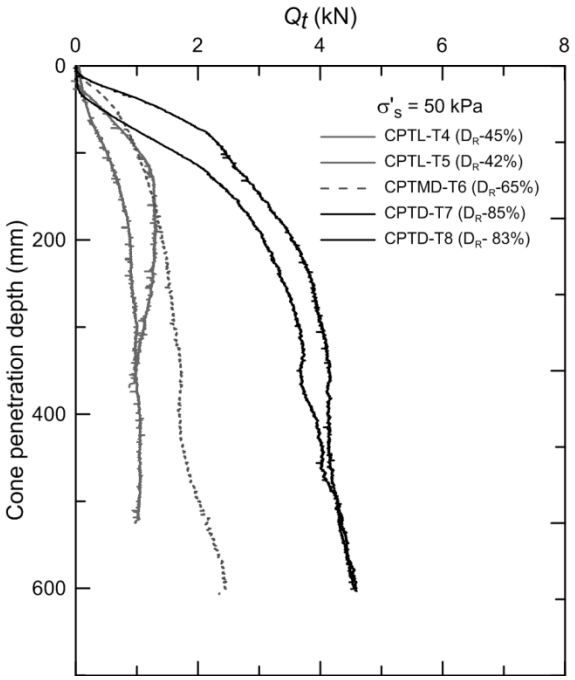

Figure 6.3 Total cone resistance in penetration tests with surcharge

6.3 DIC Results

Digital images acquired during the cone penetration tests were analyzed using the DIC technique to obtain the soil displacement fields at different penetration depths, as discussed earlier. The following measurements were obtained from the DIC analysis:

(a) incremental displacement field resulting from incremental cone penetration;
(b) soil displacement paths during continued cone penetration;
(c) post-penetration accumulated displacement field;
(d) strain and rotation paths during incremental and continued cone penetration;
(e) post-penetration accumulated strain and rigid body rotation field.

Figure 6.4 shows the coordinate reference system used to report the DIC results. The cone penetration depth from the top of sample at any given time is denoted by h^*. The vertical position of an element is given by h, which is the distance of a point in the domain with respect to the cone tip ($h = 0$ at the cone tip, positive above the cone tip and negative below it). Results are typically presented with h and h^* normalized by the cone radius (h/r_c and h^*/r_c). The radial position r is the horizontal distance from the cone penetration axis to a point in the domain, whereas the depth z is the vertical distance from the sample surface to a point in the domain. Both r and z can be normalized with respect to the cone radius (r/r_c and z/r_c).

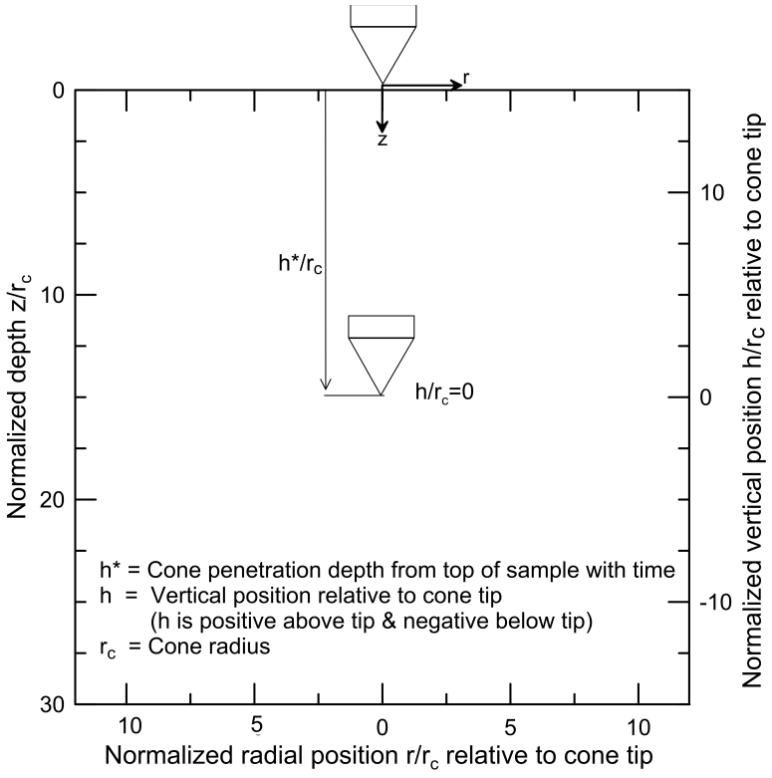

Figure 6.4 Coordinate reference system for DIC data

6.3.1 Displacements during Surcharge

Figure 6.5(a) shows the displacement vector plot during surcharge of 50 kPa in loose test (CPTL-T4). The maximum vertical displacement of 2.21 mm was recorded at the top of sample as seen in Figure 6.5(b) showing the profile of vertical displacement and strain along the cone penetration path at center of observation window. The corresponding maximum volumetric strain of 1.8% was calculated.

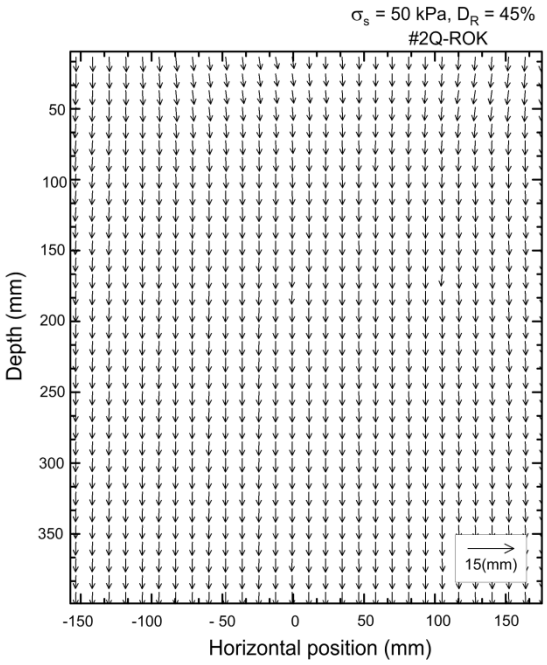

(a)

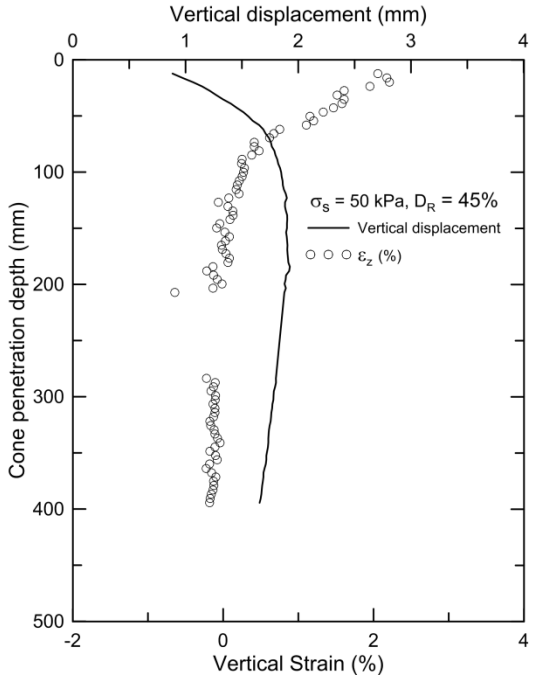

(b)

Figure 6.5 Displacement during surcharge loading in loose test CPTL-T4: (a) vector plot, and(b) vertical profile at center of soil model.

6.3.2 Soil Displacement Pattern during Cone Penetration

The deformation pattern around an advancing cone has historically been viewed through the prism of a slip mechanism (R. Salgado & Prezzi, 2007). Such a slip mechanism can be inferred from the observation of the soil displacement field in the immediate neighborhood of the cone tip for small increments of cone penetration. Paniagua et al. (2013) used 3D X-Ray CT and 3D DIC algorithms to study displacements and strains around a cone penetrometer pushed into silt, and observed also there a pattern consistent with the Salgado & Prezzi (2007) slip pattern. Figure 6.6 illustrates the evolution of the slip mechanism with increasing cone penetration for the CPTD0-T3-#2Q-ROK test. A free surface exists at the top of the sample since no surcharge was applied in this test. Image pairs of the cone penetration at three normalized penetration depths (h^*/r_c = 2, 6, and 22) were analyzed to obtain the incremental displacement fields at each of these normalized penetration depths for an incremental penetration of 2.075 mm [= 5 × 0.415mm = 2.075 mm increment of cone penetration between images i and (i+5)]. As the cone first enters the sample, a shallow slip surface forms, with the displacement vectors fanning out in a pattern similar to that of “classical” bearing capacity failure (R. Salgado, 2008), with the conical tip acting as a rigid driving wedge. The cone displacement in Figure 6.6 is shown in natural scale but the displacement vectors in these two figures are magnified 20 times to allow better visualization of the displacement field.

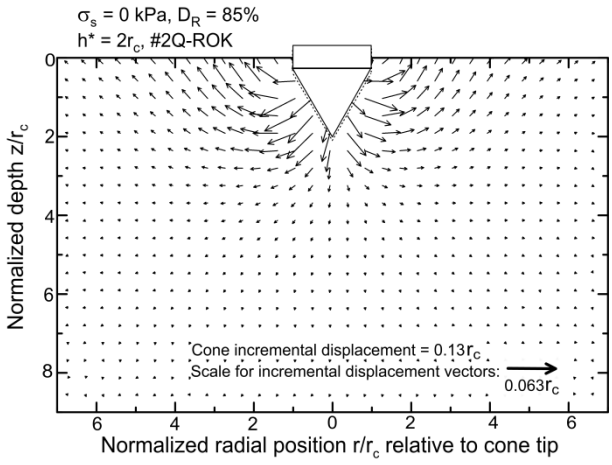

(a)

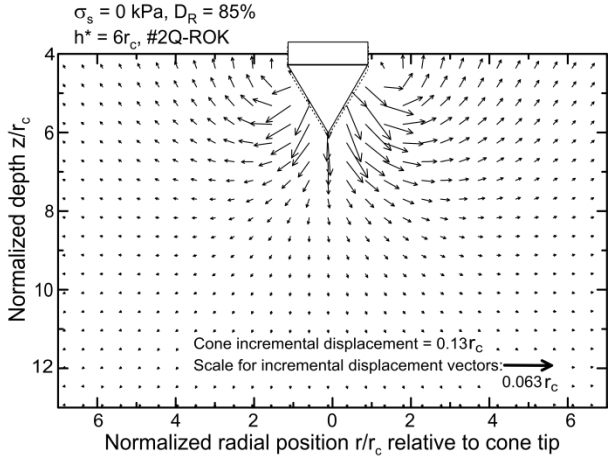

(b)

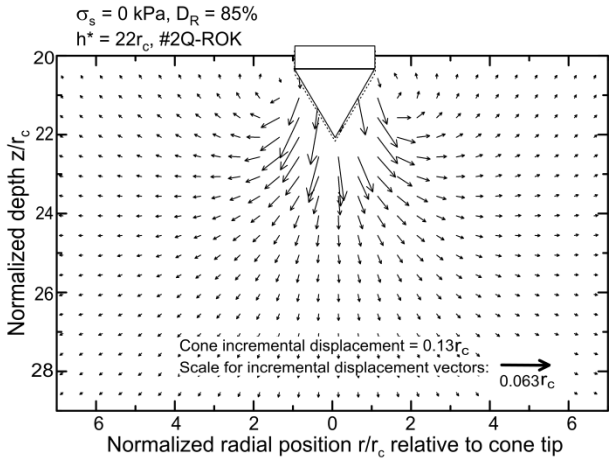

(c)

Figure 6.6 Evolution of the slip pattern with penetration for test CPTD-T3-#2Q-ROK (σ'_s= 0 kPa, D_R = 85%): (a) h^*/r_c =2, (b) h^*/r_c = 6, and (c) h^*/r_c = 22.

Figure 6.7 also plots the cone displacement in a 1:1 scale but soil displacements in a 20:1 scale. It compares the displacement field around the cone during an incremental penetration of 2.075 mm [= 5 × 0.415mm = 2.075 mm increment of cone penetration between images i and (i+5)] for three tests performed on samples of three different sands (CPTD50-T8-#2Q-ROK, CPTD50-T9-Ohio Gold Frac and CPTD50-T10-ASTM20-30) with approximately the same density (82%, 85% and 87%) subjected to the same surcharge (50 kPa). The figure shows the incremental displacement fields for two normalized depths, $h^*/r_c = 6$ and $h^*/r_c = 20$, corresponding to normalized depths just prior to and after the onset of particle crushing in the soil zone below the cone (particle crushing was visible to the naked eye through the observation window). The incremental displacement field for $h^*/r_c = 6$ (Figure 6.7(a), (b) and (c)) indicates that, immediately below the cone tip, the displacement vectors are nearly vertical, while further away from it, the displacement vectors have a larger radial component. A transition zone is observed where the incremental displacement vectors rotate from the vertical to the radial direction, as suggested in Salgado & Prezzi (2007); this zone is more clearly observed for the least crushable sand (ASTM20-30), for which the degree of incremental displacement vector rotation is more pronounced. The incremental displacement field for $h^*/r_c = 20$ (Figure 6.7 (d), (e) and (f)) illustrates that the overall incremental displacement field becomes more vertical for all sands as the cone penetrates to a depth at which the sand particles surrounding the conical tip undergo crushing (i.e., incremental displacement rotation is less pronounced after particle crushing becomes significant). In order to quantify the degree of incremental displacement rotation within the transition zone, the direction of the average incremental displacement vectors was calculated within a subdomain of the soil domain obtained by revolution of the cross section shown Figure 6.7. This subdomain is essentially a cylinder, except for the conical space occupied by the penetrometer tip, with radius $2d_c$ and length extending from the cone shoulder down to $1.25d_c$ below the cone tip. The average direction of the incremental displacement vectors is calculated using the product of the radius at which the displacement is observed and the magnitude of the displacement as a weight factor:

$$\theta_{ave} = \frac{\sum_{i=1}^{n_{el}} \theta_i l_i 2\pi r_i dr}{\sum_{i=1}^{n_{el}} l_i 2\pi r_i dr} \quad (6\text{-}1)$$

where:

$$\theta_i = \tan^{-1}\left(\frac{v_i}{u_i}\right) \quad (6\text{-}2)$$

$$l_i = \sqrt{u_i^2 + v_i^2} \quad (6\text{-}3)$$

and u_i and v_i are the radial and vertical displacements of every soil element i within the averaging zone, respectively, θ_i is the direction of the displacement vector of element i with respect to the horizontal, l_i is the magnitude of the displacement vector for element i, n_{el} is the number of soil elements within the subdomain where the average is calculated, and r_i is the radial distance between the element i and the cone axis.

As the cone penetrates to a depth in which the sand particles surrounding the conical tip start crushing, the overall incremental displacement fields become more vertical for all sands (the degree of incremental displacement rotation is less pronounced). A “cone punching” effect appears to be taking place due to particle crushing (Figure 6.7(d), (e) and (f)). After particle crushing, the direction of the average incremental displacement vectors with respect to the horizontal are 33^o, 40.1^o and 36.8^o for ASTM20-30 (the least crushable sand), Ohio Gold Frac, and #2Q-ROK (the most crushable sand), respectively. Outside the transition zone, the radial incremental displacements follow a pattern similar to that observed prior to particle crushing. However, the magnitude of the radial incremental displacement vectors decrease with pronounced particle crushing, while the magnitude of the vertical incremental displacement vectors increase immediately below the cone tip. The time history of the motion of various soil elements located in the vicinity of the cone path are shown later in the upcoming sections.

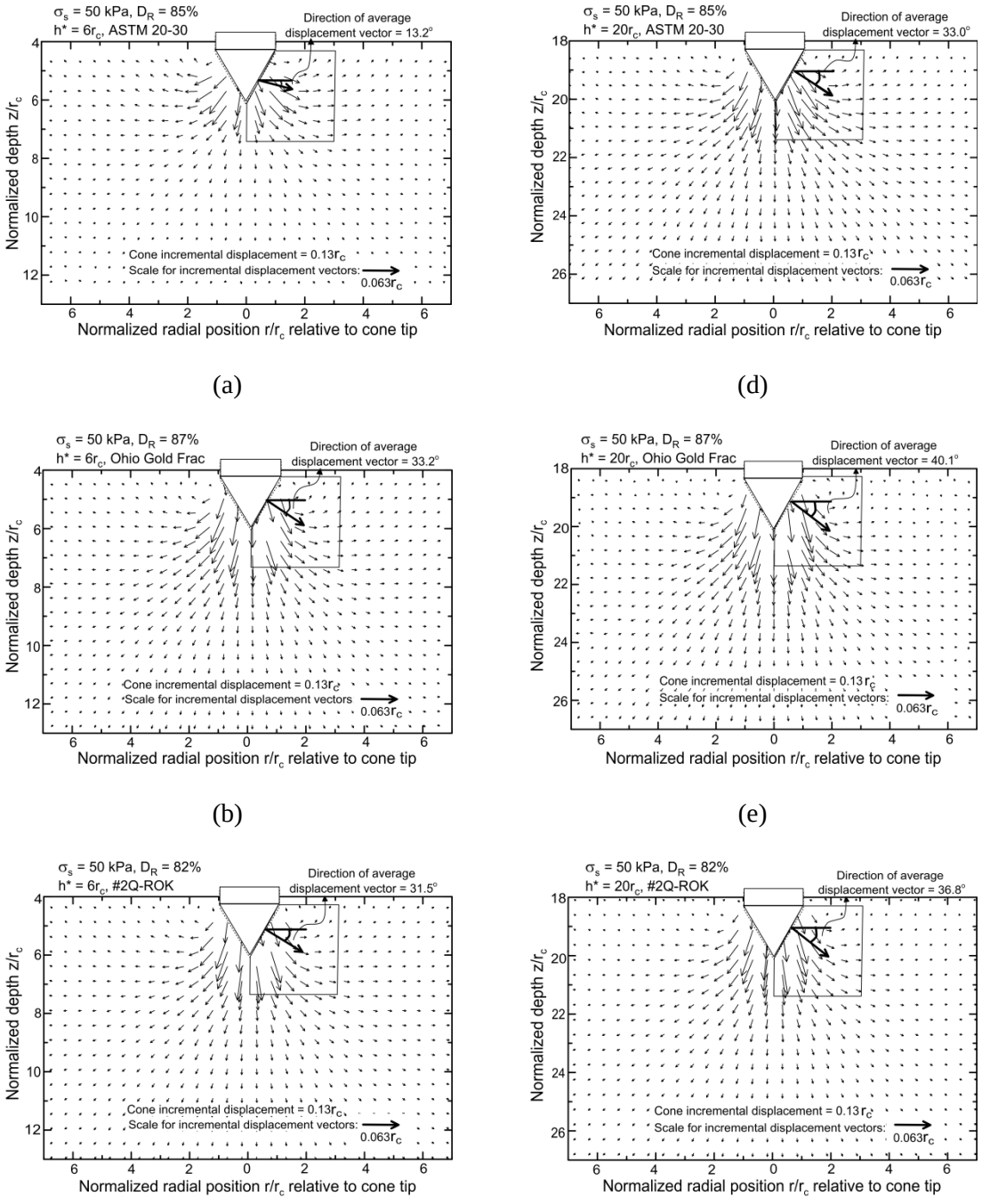

Figure 6.7 Soil displacement patterns for ASTM 20-30, Ohio Gold Frac, and #2Q-ROK silica sands prior to particle crushing ($h^*/r_c = 6$) and after particle crushing ($h^*/r_c = 20$): (a) ASTM 20-30 at $h^*/r_c = 6$, (b) Ohio Gold Frac at $h^*/r_c = 6$, (c) #2Q-ROK at $h^*/r_c = 6$, (d) ASTM 20-30 at $h^*/r_c = 20$, (e) Ohio Gold Frac at $h^*/r_c = 20$, and (f) #2Q-ROK at $h^*/r_c = 20$.

In order to assess the effect of the penetrometer tip geometry on the mobilized slip pattern, two tests were performed with rectangular flat-end and half-circular conical tip penetrometers in very loose sand samples (D_R = 15%) prepared using #2Q-ROK sand. Figure 6.8(a) shows the slip pattern at a depth h^*/r_c = 36, which was selected to ensure that a deep penetration mechanism had been mobilized, even with no surcharge. The mobilized slip pattern for the flat-end penetrometer has similar characteristics to that associated with deep cone penetration (Figure 6-8(b)) due to the formation of an "artificial cone" or "nose cone" just below the flat tip, something that has also been observed by other researchers (White & Bolton, 2004). However, in the displacement field of the flat-end penetrometer, there is a clear transition line extending from the flat tip shoulder at an inclination of 38.5^o with the horizontal, with sub-vertical displacement vectors parallel to it; in the case of the conical tip, the displacement vectors rotate from sub-vertical to horizontal with radial offset from the cone tip.

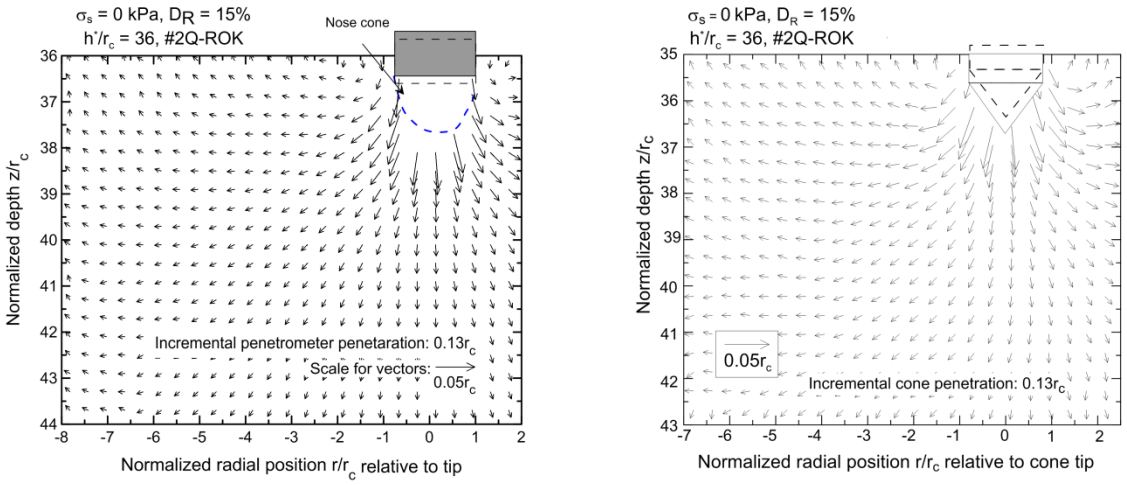

(a) (b)

Figure 6.8 Comparison of slip pattern for penetrometers with different tip geometry: (a) rectangular flat-end penetrometer and (b) half-circular conical tip penetrometer.

6.3.3 Characterization of Displacement Zones around the Cone

Four zones providing a general, qualitative sense of the displacement field and of processes taking place during cone penetration were identified based on the displacement patterns observed (Figure 6.9(a)): zone I – a vertical compression zone below the cone; zone II – a crushed particle band along the surface of the cone tip and shaft; zone III – a transition zone where the displacement vectors rotate from the vertical/sub-vertical direction to the radial direction; and zone IV – a zone in which the direction of the displacements is approximately radial.

Figure 6.9(b) shows a vector plot of the incremental displacement field obtained when the cone tip moved down from $h^* = 6r_c$ (initial position) to $h^* = 7r_c$ (final position) for CPTD50-T8-#2Q-ROK. The four zones are sketched in the same plot. In zone I, vertical compression of the soil dominates, and the incremental displacement vectors are mostly vertical. For small penetration increments, zone I extends from the cone tip to $h/r_c \approx -3.8$; for lower elevations, the incremental vertical displacement reduces to less than 10% of the maximum incremental vertical displacement observed in zone I. The maximum incremental vertical displacement is observed along the cone surface at $r/r_c \approx 0.5$ and $h/r_c = 0.866$

Zone II forms due to intense shearing and particle crushing that takes place below the cone. The particles crushed below the cone are displaced laterally as the cone advances, and stay roughly in the same place as the cone continues in its advance. The finely crushed sand particles can be observed coating the cone tip and the entire cone shaft in close-up views of the images captured during penetration. The maximum thickness of this zone, which was also observed by White & Bolton (2004) and Yang et al. (2010), is 1.5-4 D_{50} at $r/r_c \approx 0.5$ and $h/r_c = 0.866$.

Zone III exists immediately below the cone, where rotation of the incremental displacement field from a mainly vertical direction to the radial direction occurs, as can be seen in Figure 6.9(b). The inclination of the outer boundary of the transition zone III depends on sand crushability: the more crushable the sand, the less the boundary rotates outward (away from the cone). In zone IV, the incremental soil displacement field is

purely radial, resembling the field that would result from a cylindrical cavity expansion process, with minimal vertical incremental displacement observed.

Soil displacement in each of zones I though IV can be better understood by observing the displacement paths of key soil elements (labeled E_1 through E_6 in Figure 12(a)). Figure 6.10 shows the evolution of the normalized vertical and radial displacement increments $\Delta v/r_c$ and $\Delta u/r_c$ of elements E_1, E_2, E_3, E_4, E_5 and E_6 shown in Figure 6.9(a) due to a penetration of approximately $1r_c$ (= 1.05 r_c) from a depth $h^* = 20r_c$. The incremental change in the displacement field was deduced from the analysis of image sequences obtained in tests CPTD50-T10-ASTM20-30 and CPTD50-T8-#2Q-ROK. Figure 6.10(a) shows the displacement path of element E_1 located just below the cone tip in zone I. Element E_1 experiences a maximum vertical displacement increment $\Delta v = 0.68r_c$ for the least crushable sand (ASTM20-30) and $\Delta v = 0.49r_c$ for the most crushable sand (#2Q-ROK). The radial displacement change is negligible for both sands. It is seen in Figure 6.10(a) that particle tracking for element E_1 ends before cone penetration equal to r_c is achieved. For element E_2 next to the cone surface, maximum Δv values of $0.34r_c$ and $0.48r_c$ were observed for the least and most crushable sand, respectively (Figure 6.10(b)). The increase in the normalized vertical displacement increment observed for the most crushable silica sand #2Q-ROK is caused by the intense particle crushing occurring just below the cone tip. Element E_2 undergoes a maximum radial displacement increment equal to $0.17r_c$ for the ASTM20-30 sand and to $0.13r_c$ for the #2Q-ROK sand. Element E_3 (Figure 6.10(c)), located in the transition zone, experiences maximum radial and vertical displacement increments of $0.12r_c$ and $0.10r_c$ for ASTM 20-30 sand, and $0.12r_c$ and $0.16r_c$ for #2Q-ROK sand. The displacement paths of elements E_4, E_5 and E_6, located on the transition line between zone III and zone IV, indicate clearly that the radial component of the normalized displacement increment dominates there for both sands (see Figure 6.10(d), (e) and (f)). However, the values of the radial displacement increment of elements located at larger radial offsets from the cone tip (elements at positions E_5 and E_6) are smaller for the most crushable silica sand than those observed for the least crushable silica sand ($0.036r_c$ and $0.017r_c$ versus $0.067r_c$

and $0.02r_c$). These results suggest that deformation gets more localized near the cone in the most crushable sand.

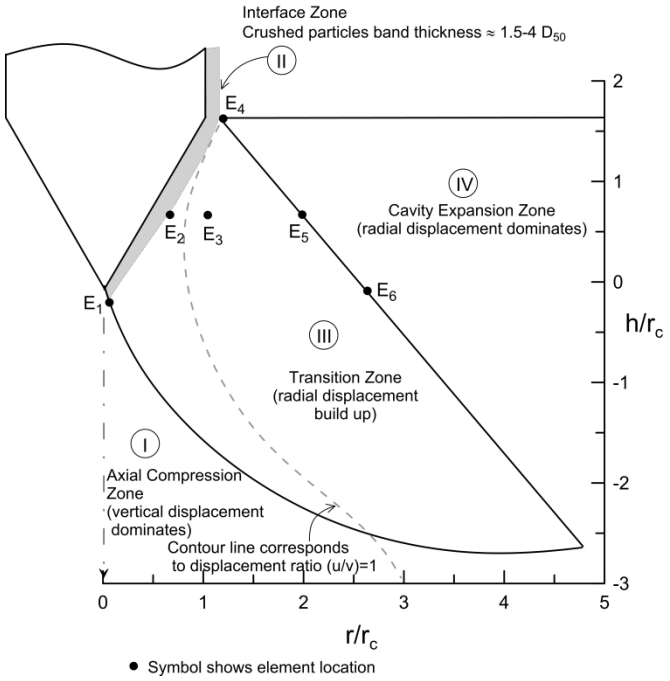

(a)

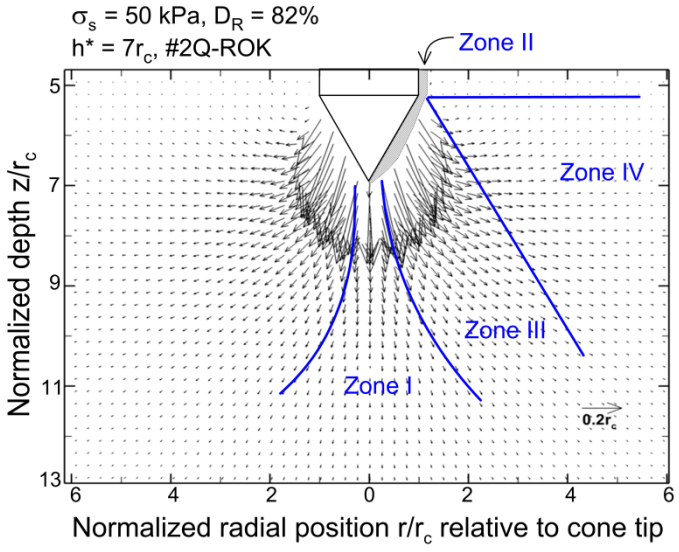

(b)

Figure 6.9 Characterization of displacement zones near the cone during a penetration equal to r_c: (a) displacement zones and (b) displacement field change.

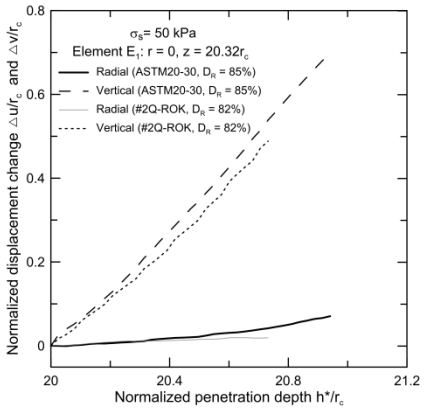

(a)

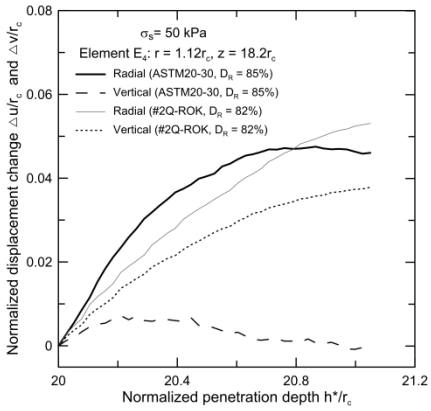

(d)

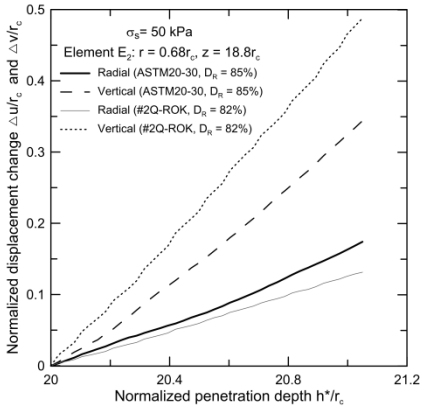

(b)

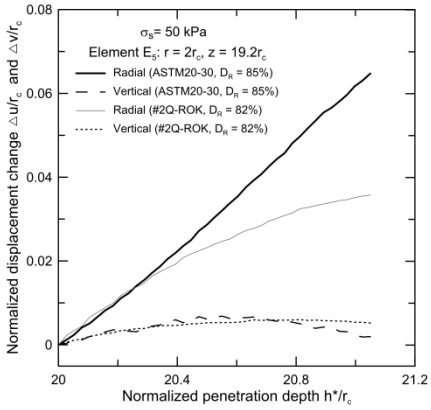

(e)

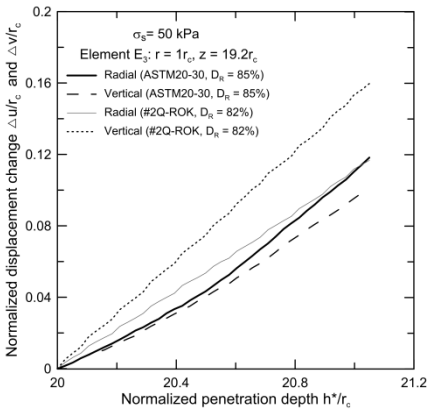

(c)

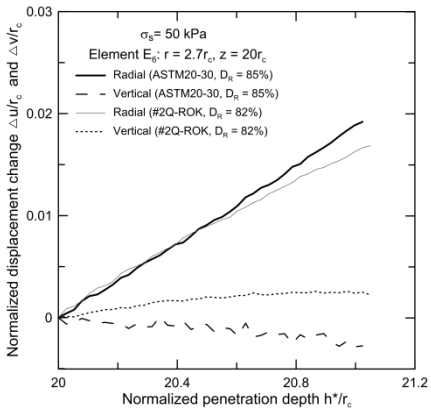

(f)

Figure 6.10 Evolution of radial and vertical displacement change for $1r_c$ penetration in the least crushable (CPTD50-T10-ASTM20-30) and most crushable (CPTD50-T8-#2Q-ROK) silica sands.

6.3.4 Displacement Paths during Continuous Penetration

Figure 6.11 show the displacement paths of nine elements located at different radial offsets from the cone penetration axis (r/r_c = 0, 0.5, 1, 1.5, 2, 3, 4, 6 and 8) for test CPTD50-T8-#2Q-ROK. The displacement paths follow the coordinates of the centroid of each of the soil elements during cone penetration from h^*=0 to h^*=30r_c. The characteristics of the displacement paths of each of these elements, located initially at a depth $z \approx 18r_c$, depend on their offset position with respect to the cone penetrometer path. The displacement paths for soil elements *A*, *B*, *C*, *D* and *E* located at r/r_c = 0.5, 1, 1.5, 2 and 3 show that these elements move away from the cone path, except near the end of the displacement paths, when the soil elements move slightly towards the cone shaft instead (see Figure 6.12). For elements *F*, *G* and *H* located at r/r_c = 4, 6 and 8, no inward displacement is observed at the end of the displacement paths. Vertical displacements, which accumulate below the cone tip, decay sharply with increasing radial distance from the cone penetration path. As can be seen in Figure 6.11, the soil displacement paths radiating from the cone tip are inclined, with radial and vertical displacements decaying with increasing radial distance from the cone tip. However, the rate of decay of the radial displacement with increasing distance from the cone path is lower than that of the vertical displacement.

Figure 6.12 shows close-up views of the displacement paths for elements *C* and *H* located at r/r_c = 1.5 and at r/r_c = 8, respectively. For element *C* (Figure 6.12(a)), the vertical component of displacement dominates initially, but, on further cone penetration, the displacement becomes more radial and, immediately after the cone shoulder crosses the elevation of element *C*, bends back towards the cone shaft. Figure 6.12(b) shows the displacement path of element *H*. The radial and vertical displacements are of approximately the same magnitude, with no inward displacement towards the shaft taking place as the cone penetrates beyond the elevation of this element. As shown in the Figure 6.12(a), the motion of element C undergoes a reversal, and its inward motion after this reversal is significantly less than its outward displacement. Given that the inward motion of element C is small, friction between the glass and the sand particles may have somewhat impeded the inward motion since the motion reversal is linked to unloading,

which is initially approximately elastic. As mentioned earlier, the glass-soil stress-strain relationship is a stiff, linear elastic curve, which makes it possible to estimate any drag that may have been present. The inward movement of element C and others like it reflect a decrease in radial stress after the cone shoulder crosses the element elevations, and this drop in radial stress, experienced on the penetrometer shaft, implies a drop of shear stress.

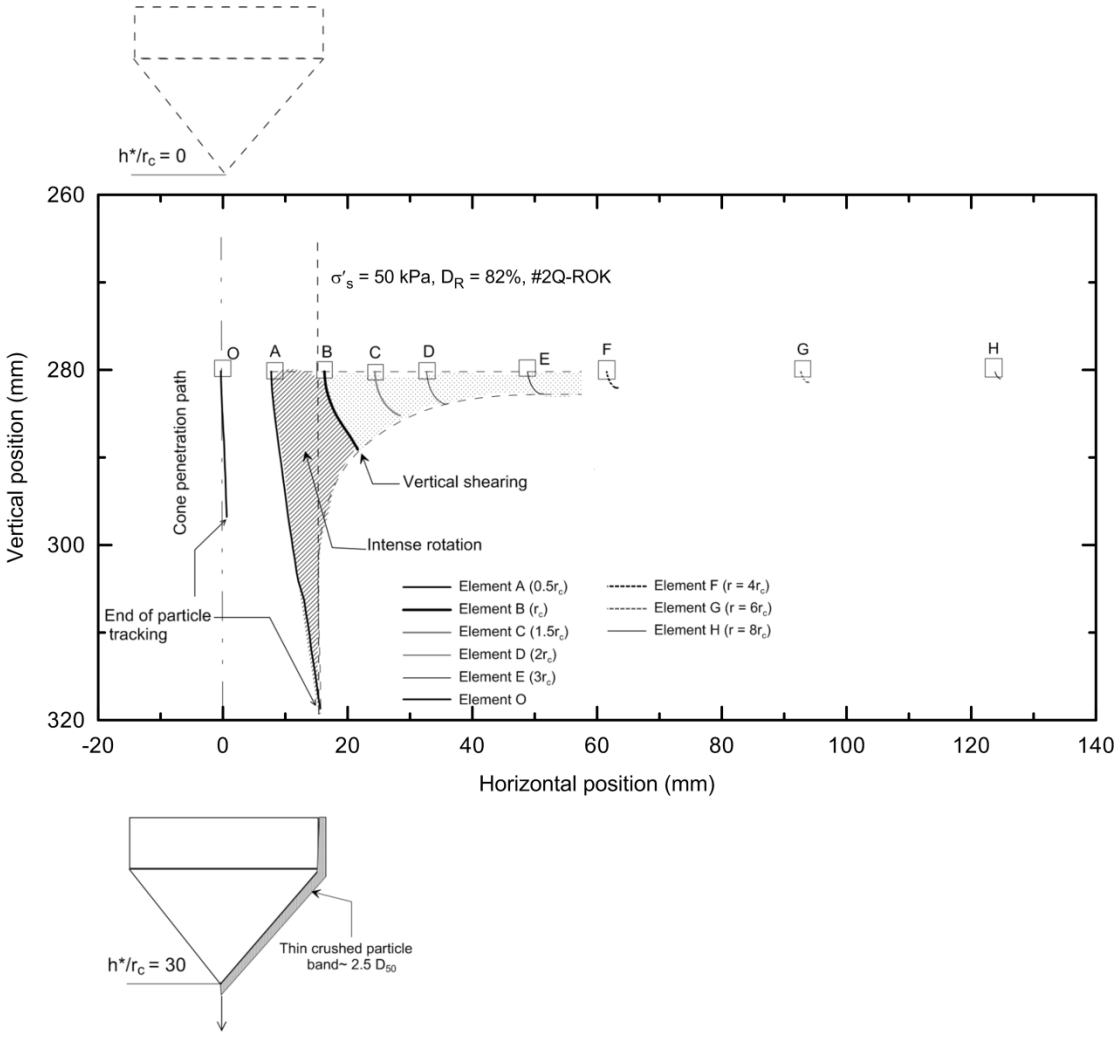

Figure 6.11 Displacement paths during cone penetration from $h^*=0r_c$ to $h^*=30r_c$ for soil elements *O*, *A*, *B*, *C*, *D*, *E*, *F*, *G* and *H*

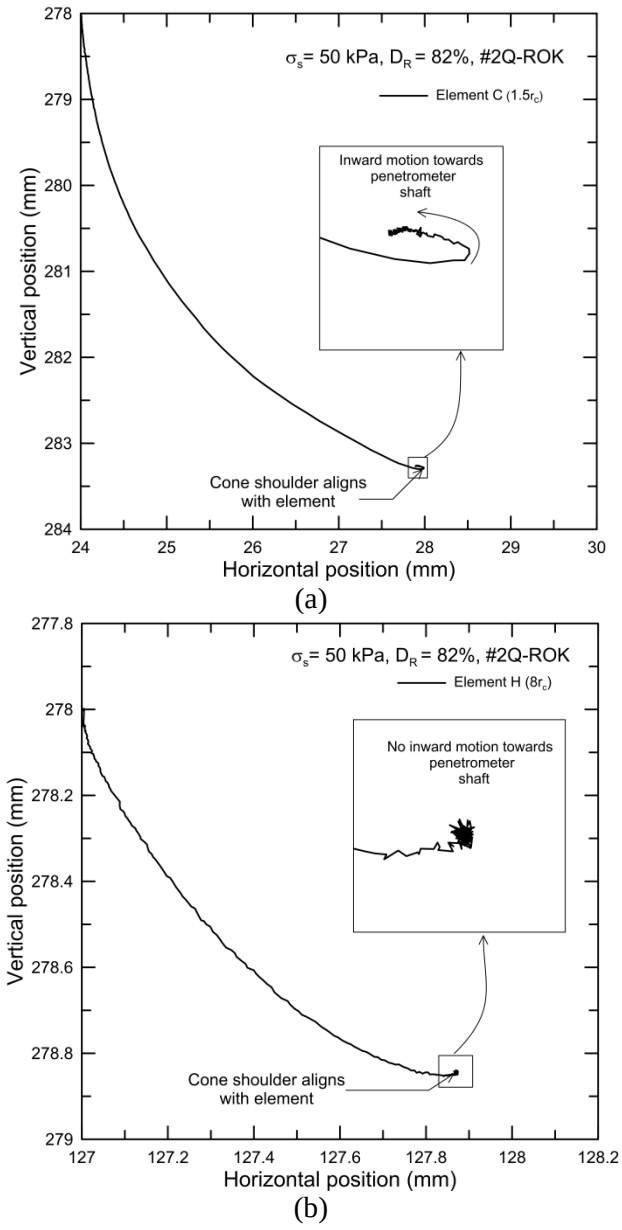

Figure 6.12 Displacement paths for: (a) element C and (b) element H.

Figure 6.13 and Figure 6.14 show the evolution of the normalized vertical and radial displacements of soil elements *B*, *C*, *D* and *E* as the cone penetrates from $h^* = 0$ to 23 and $25r_c$, respectively, for tests CPTL50-T4-#2Q-ROK and CPTD50-T8-#2Q-ROK. Initially, the soil elements are located at $z = 18r_c$ for the loose sand sample and at $z = 18.5r_c$ for the dense sample and at radial offsets of $1r_c$ (element *B*), $1.5r_c$ (element *C*), $2r_c$ (element *D*) and $3r_c$ (element *E*) from the cone penetration axis.

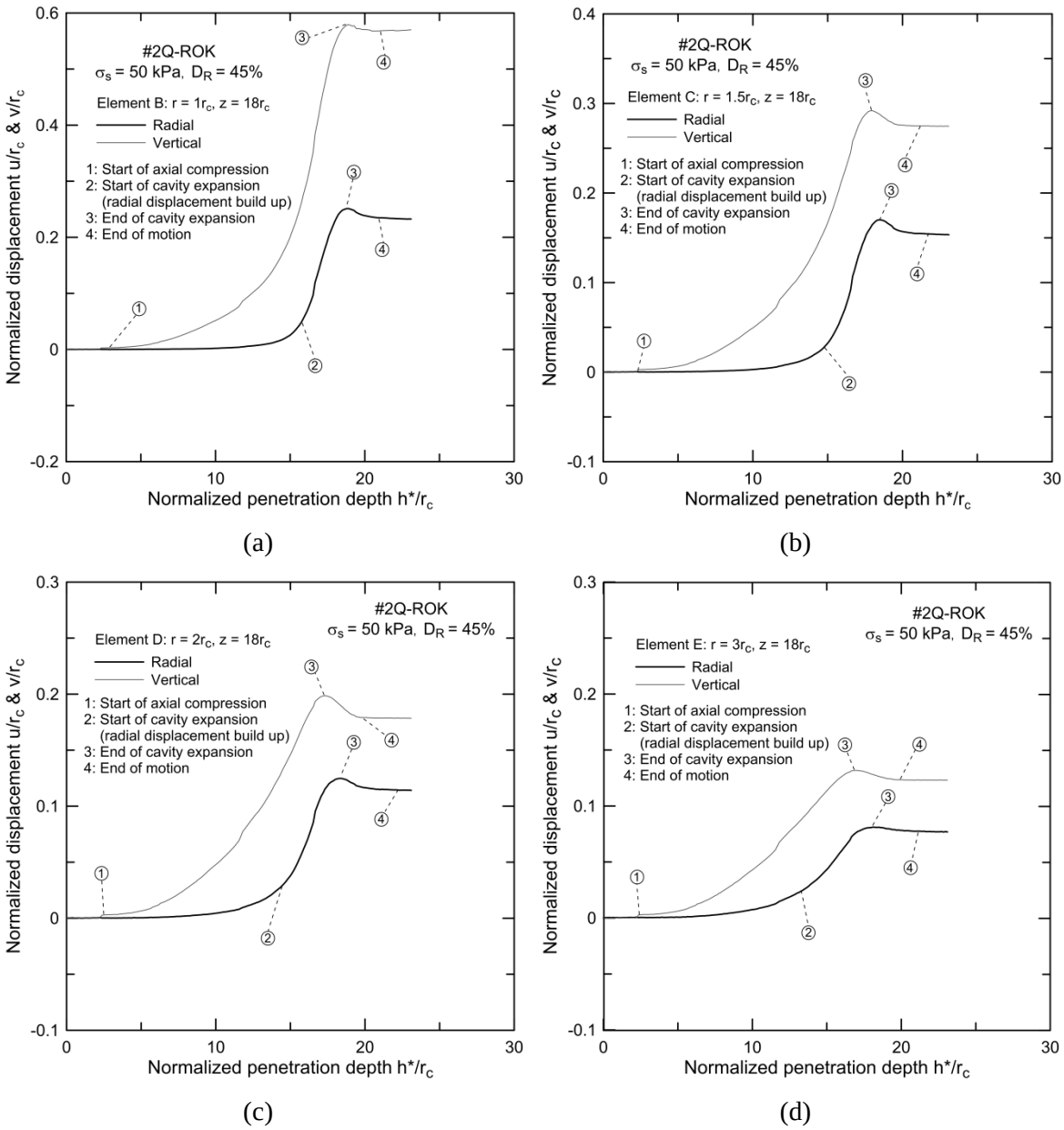

Figure 6.13 Evolution of normalized radial and vertical displacements of soil elements at different locations during continuous cone penetration from $h^* = 0r_c$ to $h^* = 23r_c$ for test CPTL50-T4-#2Q-ROK: (a) element B at $r = 1r_c$, (b) element C at $r = 1.5r_c$, (c) element D at $r = 2r_c$, and (d) element E at $r = 3r_c$.

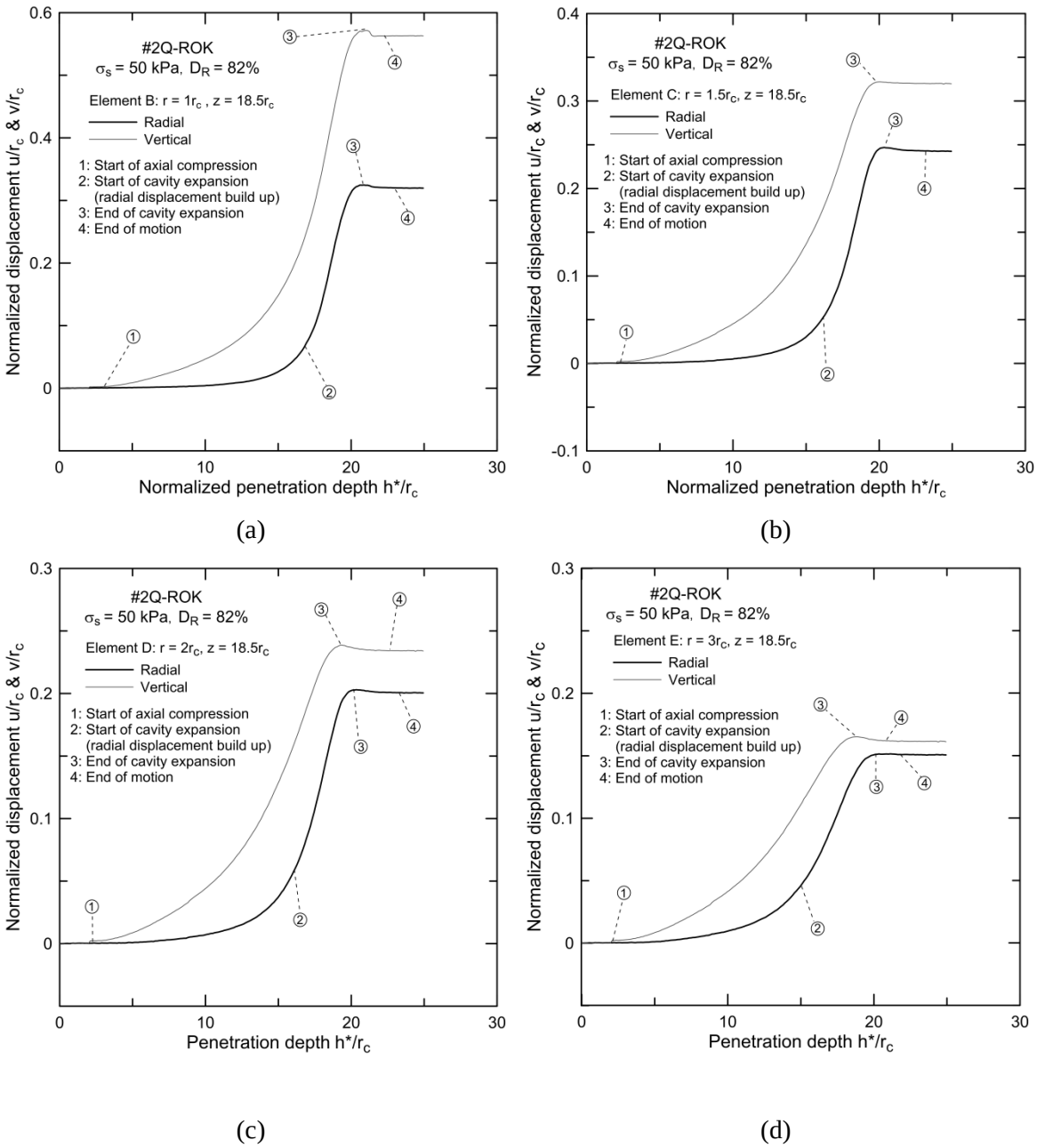

Figure 6.14 Evolution of normalized radial and vertical displacements of soil elements at different locations during continuous cone penetration from $h^* = 0r_c$ to $h^* = 25r_c$ for test CPTD50-T8-#2Q-ROK: (a) element *B* at $r=1r_c$, (b) element *C* at $r=1.5r_c$, (c) element *D* at $r=2r_c$, and (d) element *E* at $r=3r_c$.

Elements closer to the cone penetration path, such as element *B*, are the first elements to sense the approaching cone. This happens when the vertical distance from element *B* to the cone tip is equal to approximately 15 to 16 r_c for loose and dense sand samples, respectively. The normalized radial displacement of soil element *B* increases sharply when the cone tip reaches a distance of approximately 3-3.5 r_c from soil element *B* and then moves closer to it. We refer to this build up in radial stress as the cavity expansion stage (Figure 6.13 (a)), whose start is labeled as point 2 in Figure 6.13. Element *B* is displaced radially and downward as the cone passes by it. If one chooses to view the cone as stationary, then the element could be viewed as flowing around the cone face. The normalized radial soil displacement of element *B* peaks when the cone shoulder starts to align with it at the end of the cavity expansion process (see the peak in normalized displacements, identified as point 3 in Figure 6.13(a) and Figure 6.14(a)). During the cavity expansion process, particle crushing is observed near the cone tip, with the crushed particle band starting to form along the cone tip shoulder. A small reduction in normalized radial and vertical displacements takes place after the cavity expansion process (see points 3 and 4 in Figure 6.13(a) and Figure 6.14(a)). For the elements located farther away from the cone, the peak in normalized radial displacement is either less pronounced or no longer observed.

As the cone penetration continues, further vertical shearing is observed above the cone only within the thin crushed particle band (zone II) along the shaft. Particle movement is very random within the crushed particle band. As observed from close-up images of the cone penetration process, for tests performed with no surcharge (such as CPTD0-T3-#2Q-ROK), vertical particle movement is more pronounced in loose sand than in dense sand prior to particle crushing. In the case of the penetration tests performed in dense sand with the 50 kPa surcharge (such as CPTD50-T8-#2Q-ROK), noticeable particle crushing takes place below the cone tip. Figure 18 shows a close-up image of the soil in the zone ($1.25r_c \times 1r_c$) immediately next to the cone shaft for CPTD50-T8-#2Q-ROK. As shown in Figure 6.15, a very thin band of thickness equal to about $2.5D_{50}$ with highly crushed particles is observed right next to the cone shaft. Next

to this thin band, there is a $4D_{50}$-thick band consisting of moderately crushed sand particles.

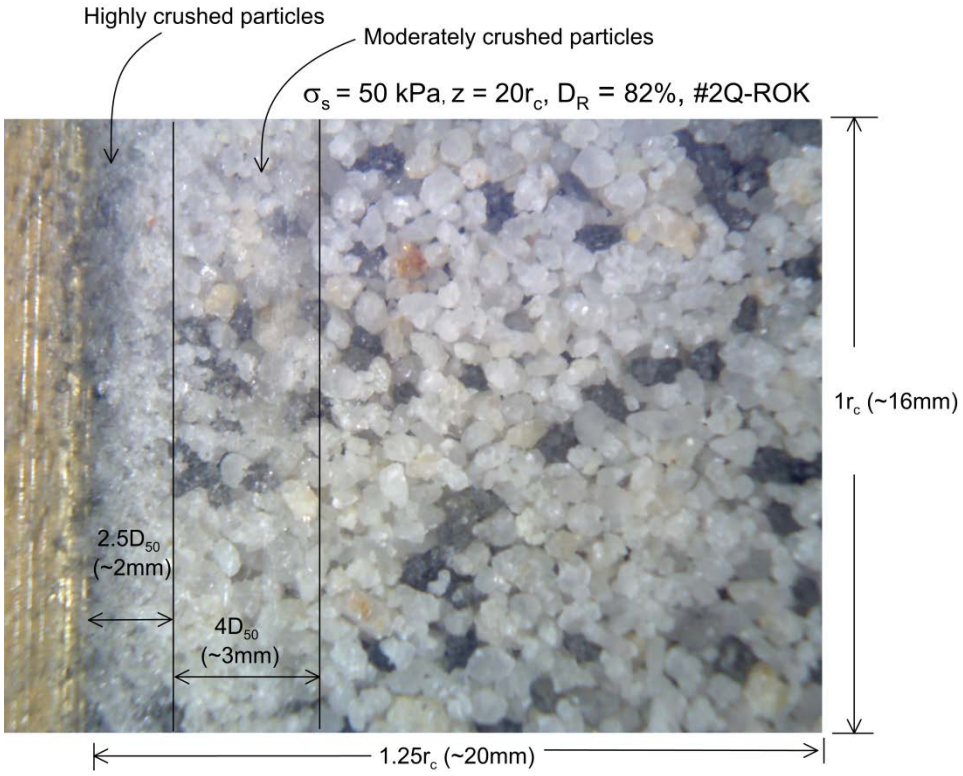

Figure 6.15 Close-up view of the interface zone along the penetrometer shaft for CPTD50-T8-#2Q-ROK

Radial displacement towards the cone shaft is indicative of a release in radial stresses (unloading in the radial direction), as previously observed in field penetration and model pile tests (Lehane et al., 1993; Gavin & Kelly, 2007) The larger the inward radial displacement, the greater the reduction in radial stress is. The amount of inward radial displacement is greater in loose sand (CPTL50-T5-#2Q-ROK) than in dense sand (CPTD50-T8-#2Q-ROK) (see Figure 6.13(b) and Figure 6.14(b)) due to less particle crushing. Therefore, it can be inferred that the reduction in radial stresses near the shaft is a density-dependent process. In order to quantify the inward radial displacement towards the cone shaft, we analyzed a thin soil disk (radius=$9r_c$ and thickness=$1r_c$) located at z = $18.5r_c$ during penetration from h^*/r_c =20 to h^*/r_c = 30, as shown in Figure 6.16. The radial displacement towards the cone shaft is more pronounced for loose sand than for medium

dense and dense sands. For all sands, negligible radial particle motion was observed for $r/r_c>4$.

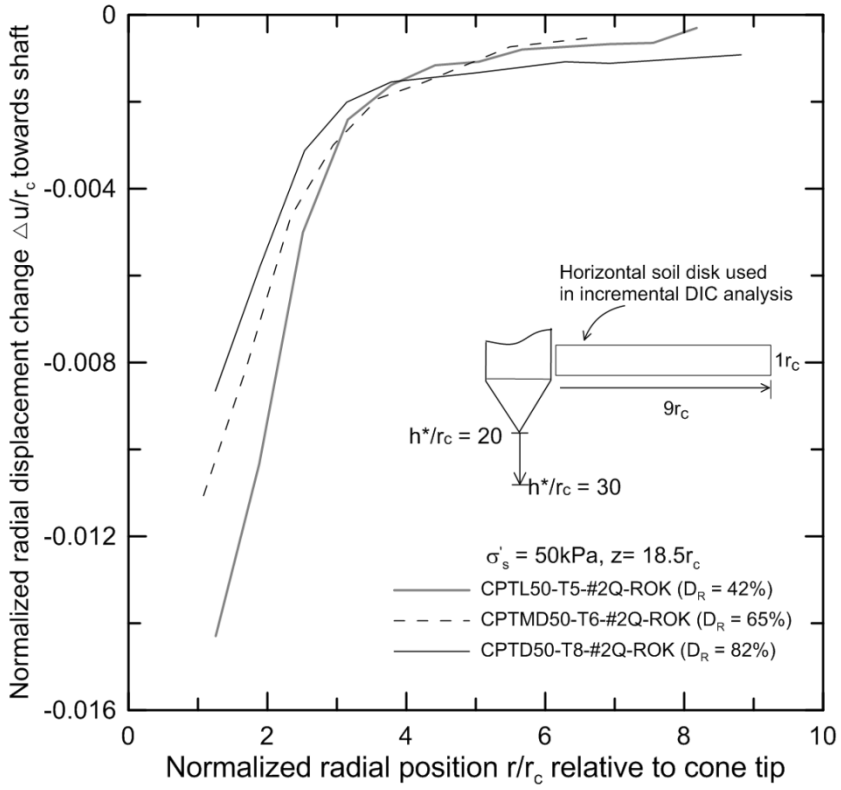

Figure 6.16 Normalized radial displacement change towards the cone shaft at depth z = 18.5r_c for penetration from h^*/r_c = 20 to h^*/r_c = 30r_c in CPTL50-T5-#2QROK, CPTMD50-T6-#2QROK and CPTD50-T8-#2QROK tests

6.3.5 Displacement Paths below Cone Tip

Figure 6.17 shows normalized radial and vertical displacement paths below the cone tip for $h^*/r_c \approx 20$ for tests performed on sand samples prepared with three different initial densities (CPTL50-T4-#2Q-ROK, CPTMD50-T6-#2Q-ROK & CPTD50-T8-#2Q-ROK). The normalized displacement paths are given for soil elements located at $r/r_c \approx 1$, 1.5, 2, 3, 5, and 8. Both the radial and vertical normalized displacements decrease with increasing r. The maximum value of the normalized radial displacement u/r_c, which is observed at an offset r/r_c = 1 along the shoulder of the cone tip for dense and medium dense sand(a) & (c)), is equal to 0.33, whereas u/r_c=0.28 at 0.5r_c below the cone tip for loose sand (Figure 6.18(e)). The normalized radial displacement decays sharply with

increasing vertical depth below the cone tip, becoming negligible ($u/r_c \approx 1\%$ of the maximum normalized radial displacement observed) at h/r_c equal to -10,-12 and -14 for loose, medium, and dense sands, respectively (Figure 6.17(a),(c) & (e)). The opposite trend is observed in the case of the maximum normalized vertical displacement. The maximum normalized vertical displacement v/r_c observed at $r/r_c = 1$ at $h = 0$ is equal to 0.8 for loose sand, as shown in Figure 6.17(f), and to approximately 0.6 for both the medium dense and dense sands, as shown in Figure 6.17(b) & (d), respectively. At larger r/r_c ($\approx$ 1.5, 2, 3, 5, and 8) from the cone tip, the rate of decay of the normalized vertical displacement is greater for the loose sand ($v/r_c \approx$ 0.30, 0.19, 0.13, 0.07 and 0.02) than for the dense ($v/r_c \approx$ 0.34, 0.26, 0.18, 0.11, and 0.08) and medium dense sands ($v/r_c \approx$ 0.32, 0.23, 0.16, 0.08 and 0.04). Figure 6.17 also shows that the vertical distance from the cone tip to the depth at which the normalized vertical displacement is equal to ≈1% of the maximum normalized vertical displacement, is slightly greater for the dense sand ($h/r_c \approx$ -14) than for the medium dense ($h/r_c \approx$ -12) and loose sands ($h/r_c \approx$-10).

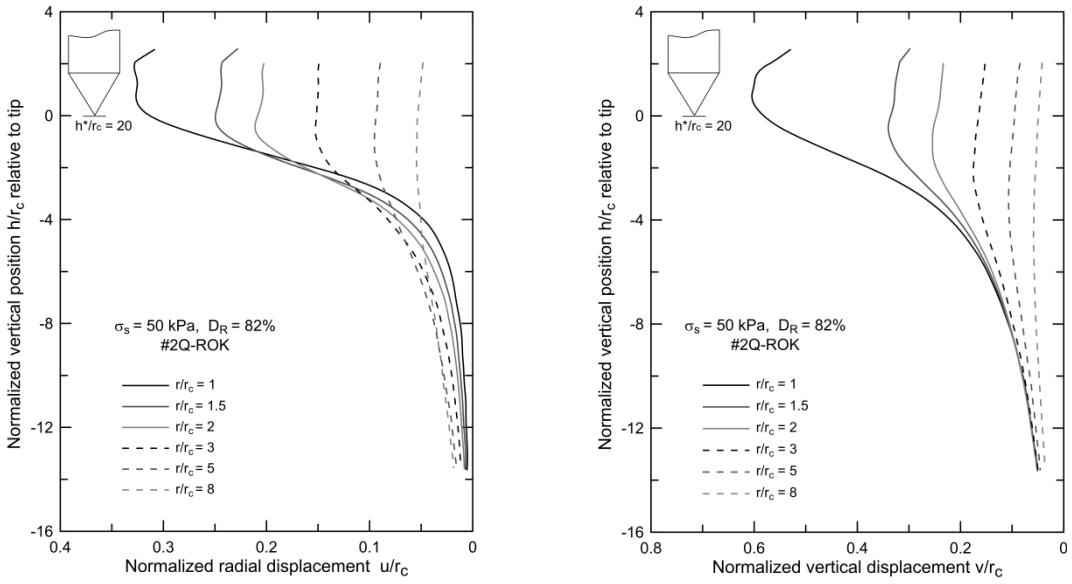

(a) (b)

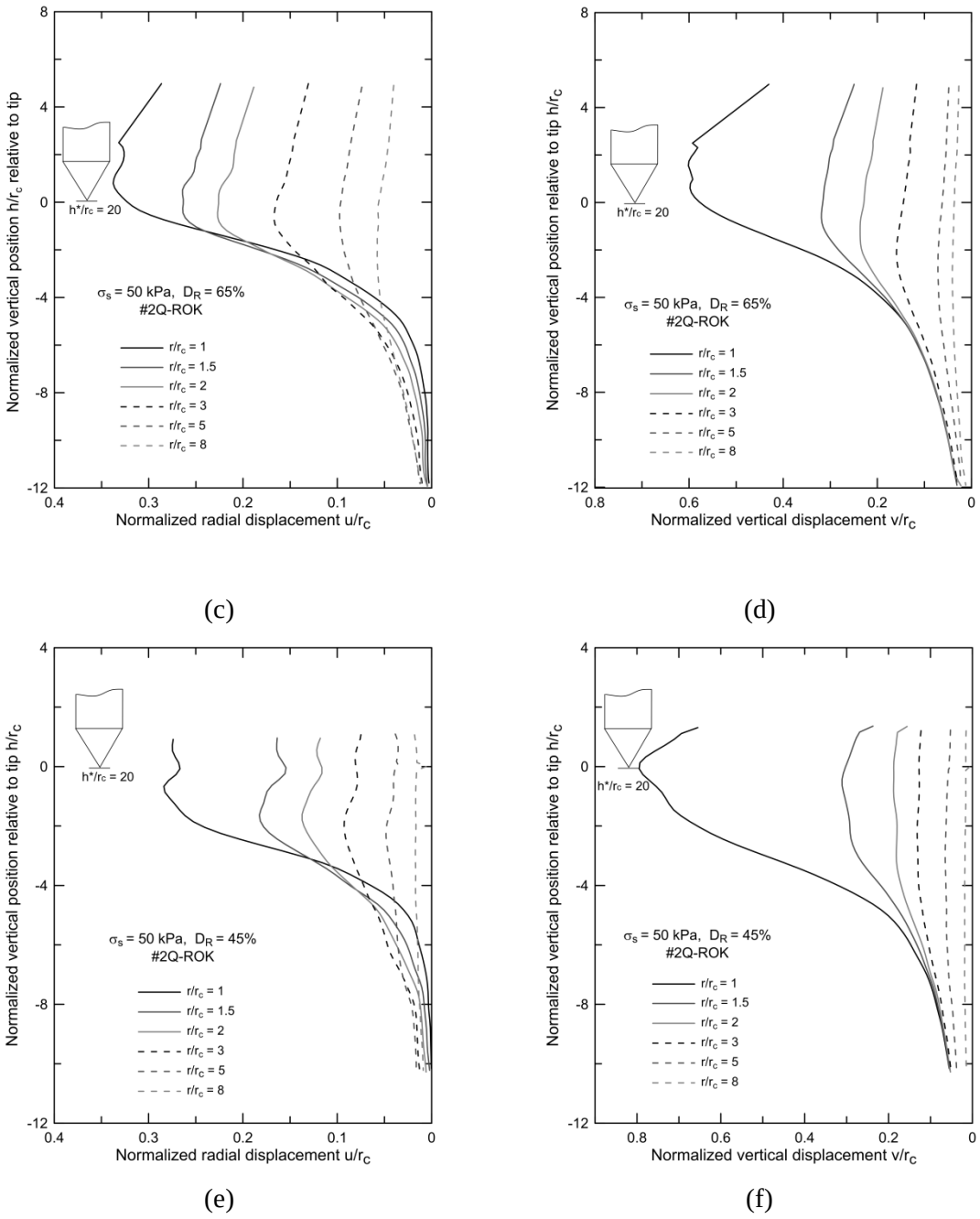

Figure 6.17 Displacement paths below the cone tip when the cone is at $h^*/r_c = 20$: (a) radial displacement path for CPTD50-T8-#2Q-ROK, (b) vertical displacement path for CPTD50-T8-#2Q-ROK, (c) radial displacement path for CPTMD50-T6-#2Q-ROK, and (d) vertical displacement path for CPTMD50-T6-#2Q-ROK (e) radial displacement path for CPTL50-T4-#2Q-ROK, and (f) vertical displacement path for CPTL50-T4-#2Q-ROK.

6.3.6 Post Penetration Displacement Field

The complete displacement field at any instance of the penetration process can be obtained by combining the displacement data from all observation windows. Figure 6.18 shows the normalized displacement fields obtained as the cone moved from a normalized cone penetration depth $h^*/r_c = 0$ to approximately 20 for tests CPTL50-T4-#2Q-ROK and CPTD50-T8-#2Q-ROK. At $h^*/r_c \approx 20$, the cone tip was located at a vertical distance of $40r_c$ from the chamber base boundary; at this position, there are no boundary effects on the displacement field. The contour plots of normalized radial and vertical displacements shown in Figure 6.18 are approximately symmetric. The radial displacement extends to larger offset distances from the center of the cone path in the dense than in the loose sand. Sharp vertical displacements are observed within a small zone in the vicinity of the cone shaft (from $r = 0$ to $r/r_c < 2$) for all sands. Below the cone tip, vertical displacement (v/r_c) contours ranging from 0.8 to 0.05 extend vertically to $h/r_c \approx -8$ and radially to $r/r_c \approx 5$ for the loose sand. For the dense sand, the vertical displacement contour extends to $h/r_c \approx -12$ vertically and to $r/r_c \approx 8$ radially. The vertical displacement contours shown in Figure 6.18 are cutoff at the bottom of the chart because they reach the cross bar of the calibration chamber, which prevents visualization of displacements.

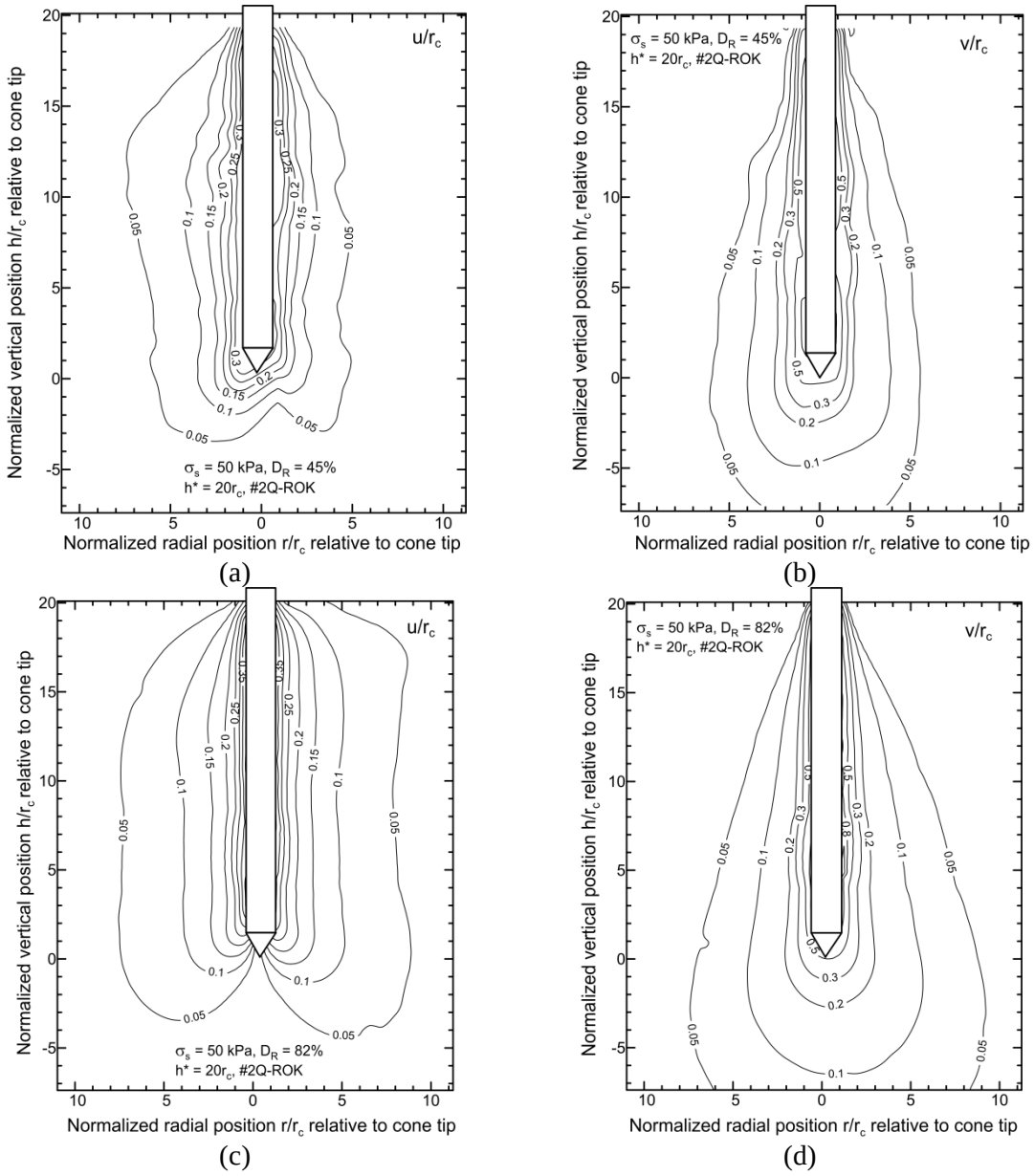

Figure 6.18 Normalized radial and vertical displacement after cone penetration to approximately h^*/r_c= 20: (a) radial displacement for CPTL50-T4-#2Q-ROK; (b) vertical displacement for CPTL50-T4-#2Q-ROK, (c) radial displacement for CPTD50-T8-#2Q-ROK, and (d) vertical displacement for CPTD50-T8-#2Q-ROK.

6.3.6.1 Influence of Density on Displacement Field

Figure 6.19 shows the influence of sand density on the radial and vertical displacement fields obtained for cone penetration from h^*/r_c=0 to normalized penetration depths h^*/r_c = 5, 10, 15 and 22.5. The displacement fields were obtained by considering a thin (~8mm) horizontal soil disk located at h/r_c = 1.732 for CPTL50-T4-#2Q-ROK and CPTD50-T8-#2Q-ROK. For h^*/r_c = 5 and 10, the normalized radial displacement profiles decay faster in loose sand than in dense sand (Figure 6.19(a), and(b)). The difference in radial displacements in the loose and dense sand decreases with increasing penetration depth (possibly due to densification of the loose sand with further penetration). As shown in Figure 6.20, the influence of the initial sand density on vertical displacements is negligible.

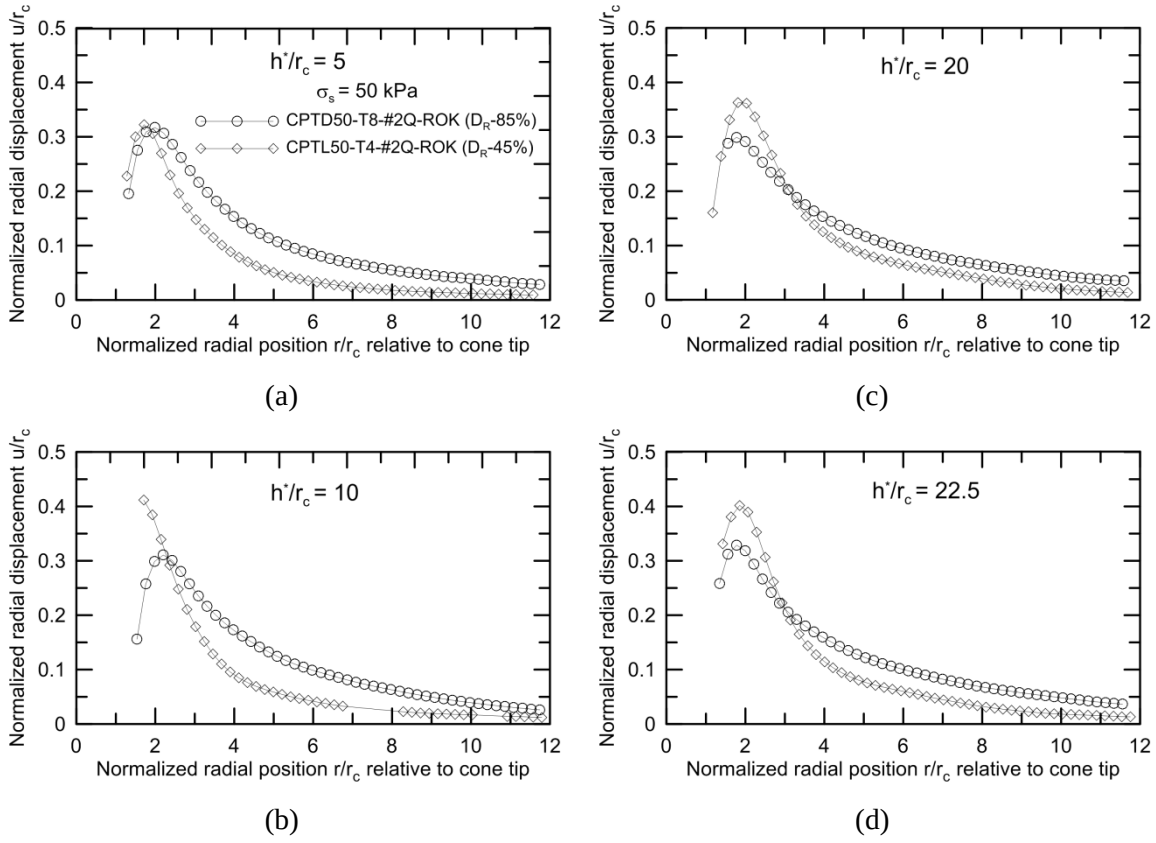

Figure 6.19 Influence of initial sand density on normalized radial displacements (u/r_c) for loose and dense tests at different penetration depths: (a) h^*/r_c = 5, (b) h^*/r_c = 10, (c) h^*/r_c = 20, and (d) h^*/r_c = 22.5.

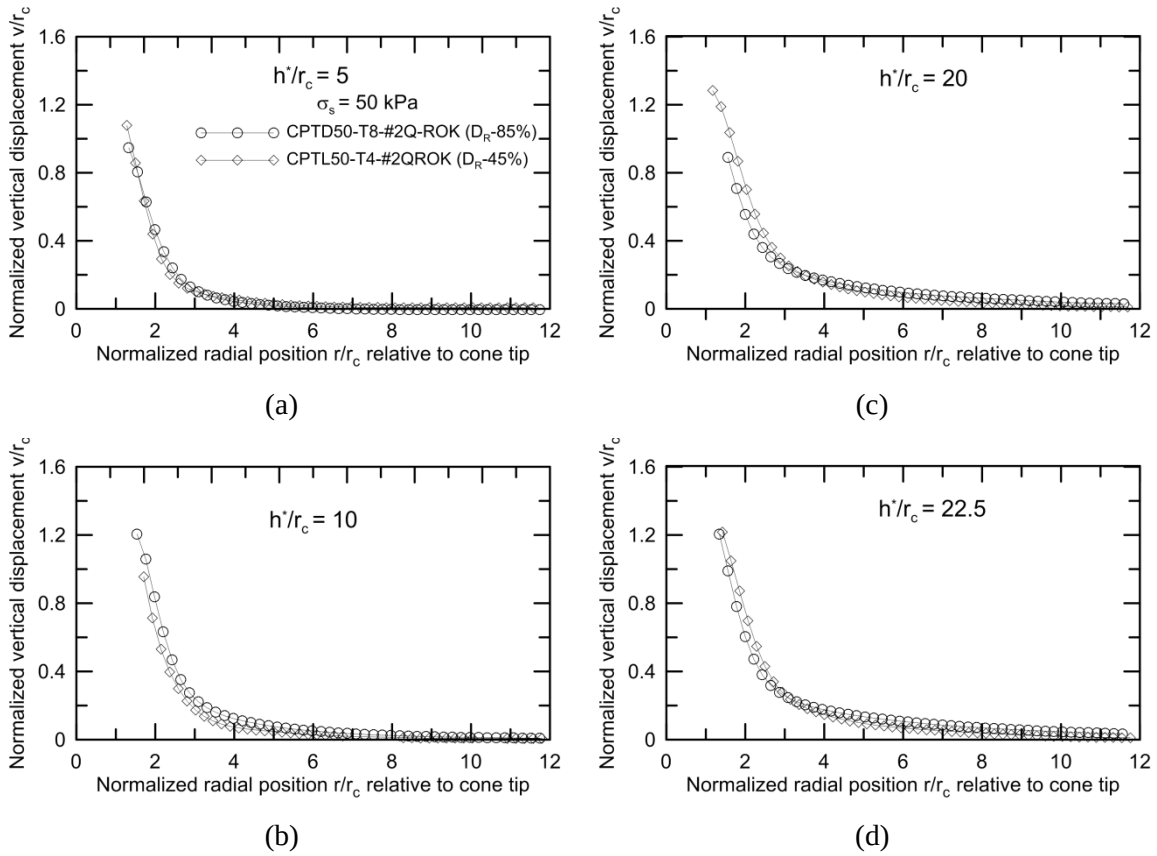

Figure 6.20 Influence of initial sand density on normalized vertical displacements (v/r_c) for loose and dense tests at different penetration depths: (a) $h^*/r_c = 5$, (b) $h^*/r_c = 10$, (c) $h^*/r_c = 20$, and (d) $h^*/r_c = 22.5$.

6.3.6.2 Influence of Stress Level on Displacement Field

Figure 6.21 and Figure 6.22 show the effect of the surcharge on the radial and vertical displacements respectively obtained for cone penetration from $h^*/r_c = 0$ to different normalized penetration depths $h^*/r_c = 5$, 10, 15 and 25. The displacement fields were obtained by considering a thin (~8mm) horizontal soil disk located at $h/r_c = 1.732$ for CPTL0-T3-#2Q-ROK (no surcharge) and CPTD50-T8-#2Q-ROK (50kPa surcharge). For normalized penetration depths $h^*/r_c = 5$ and 10, radial displacements become negligible at $r/r_c = 8$ for CPTD0-T3#2Q-ROK and at r/r_c=12 for CPTD50-T8#2Q-ROK. At $h^*/r_c = 20$ and 25, radial displacements are similar for both tests. Due to the heave observed during shallow penetration ($h^*/r_c = 5$) in the test performed with no confinement

(CPTD0-T3#2Q-ROK), the vertical displacement near the cone shaft is less than that obtained for the test performed with a 50 kPa surcharge (CPTD50-T8#2Q-ROK). For normalized penetration depths of 10, 20, and 25, vertical displacements become negligible at r/r_c =4 for the test without a surcharge and at r/r_c =8 for the test performed with a surcharge. Overall, based on the vertical displacements observed at these normalized penetration depths, the extent of the influence zone in the vicinity of the cone for the penetration test performed with a surcharge is twice that of the test performed without surcharge. However, the rate of decay in radial displacements is smaller than that of the vertical displacements.

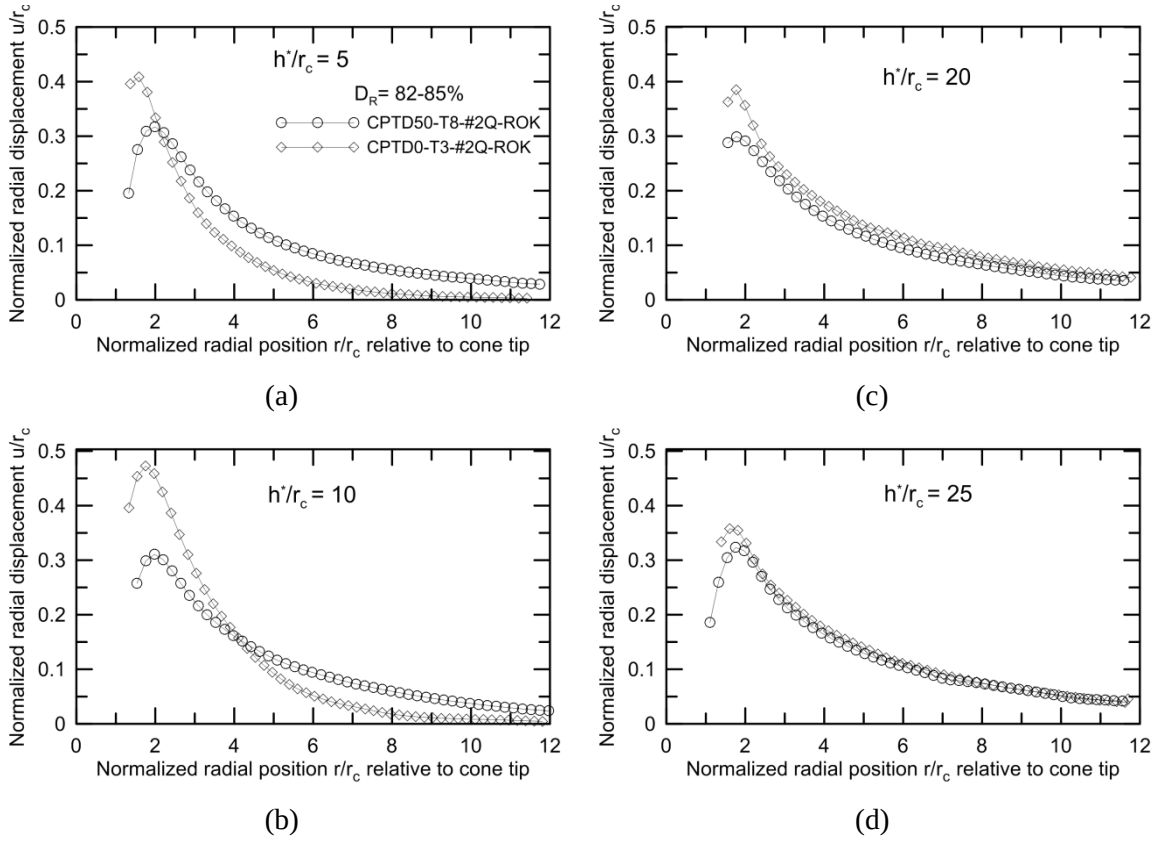

Figure 6.21 Influence of stress level on normalized radial displacements (u/r_c) for dense test CPTD0-T3-#2Q-ROK without surcharge and dense test CPTD50-T8-#2Q-ROK with surcharge of 50 kPa at increasing penetration depths: (a) h^*/r_c = 5, (b) h^*/r_c = 10, (c) h^*/r_c = 20, and (d) h^*/r_c = 25.

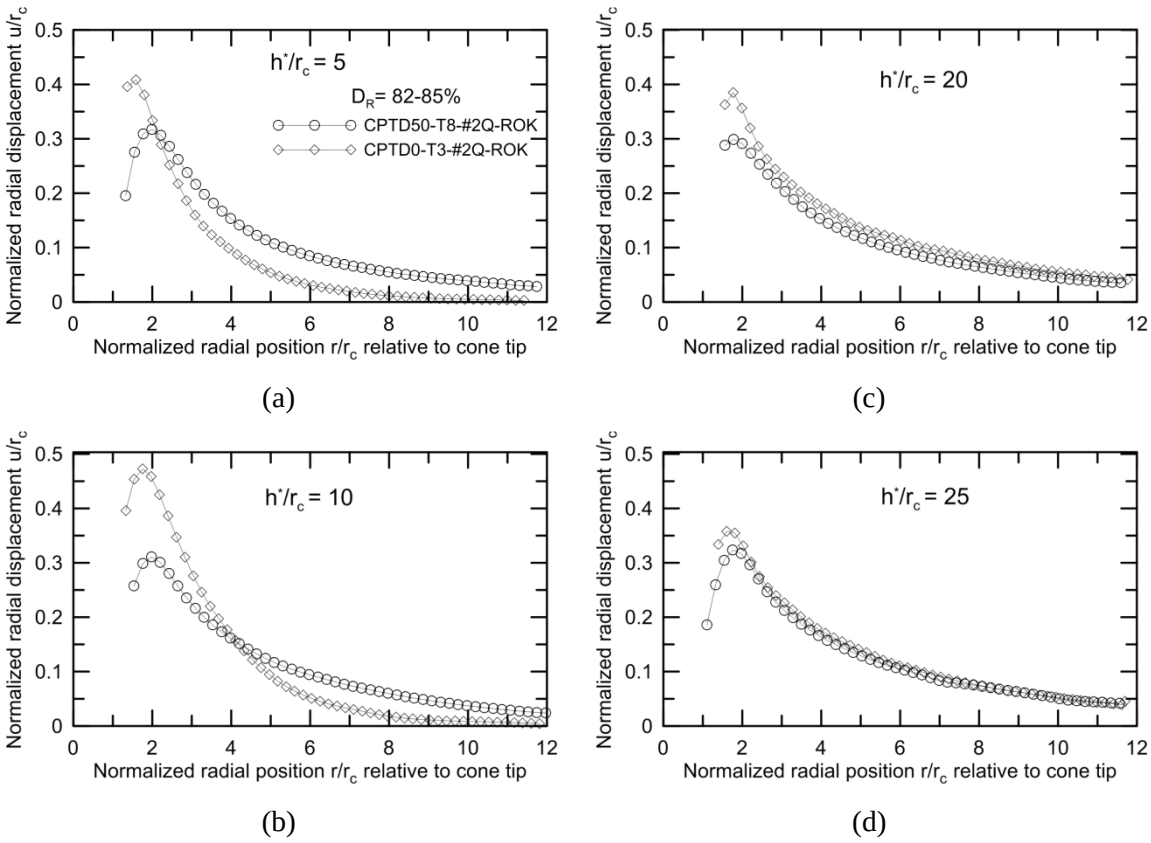

Figure 6.22 Influence of stress level on normalized vertical displacements (v/r_c) for dense test CPTD0-T3-#2Q-ROK without surcharge and dense test CPTD50-T8-#2Q-ROK with surcharge of 50 kPa at increasing penetration depths: (a) $h^*/r_c = 5$, (b) $h^*/r_c = 10$, (c) $h^*/r_c = 20$, and (d) $h^*/r_c = 25$.

.

6.3.6.3 Influence of Sand Type on Displacement Field

Figure 6.23 compares normalized radial and vertical displacement profiles for cone penetration from $h^*/r_c = 0$ to $h^*/r_c = 25$ for tests CPTD50-T8-#2Q-ROK, CPTD50-T9-Ohio Gold Frac and CPTD50-T10-ASTM20-30. The displacement fields were obtained by considering a thin (~8mm) horizontal soil disk located at $h/r_c = 1.732$. Sand particle crushability affects the extent of the zone within which non-negligible displacements are observed during deep penetration (Figure 6.23(c)). As shown in Figure Figure 6.23(a), the rate of decay in the normalized radial displacement is similar for the

three sands tested. There is a non-negligible effect of sand type on the normalized vertical displacement near the cone tip; away from the cone tip, this difference tends to disappear, as shown in Figure 6.23(b).

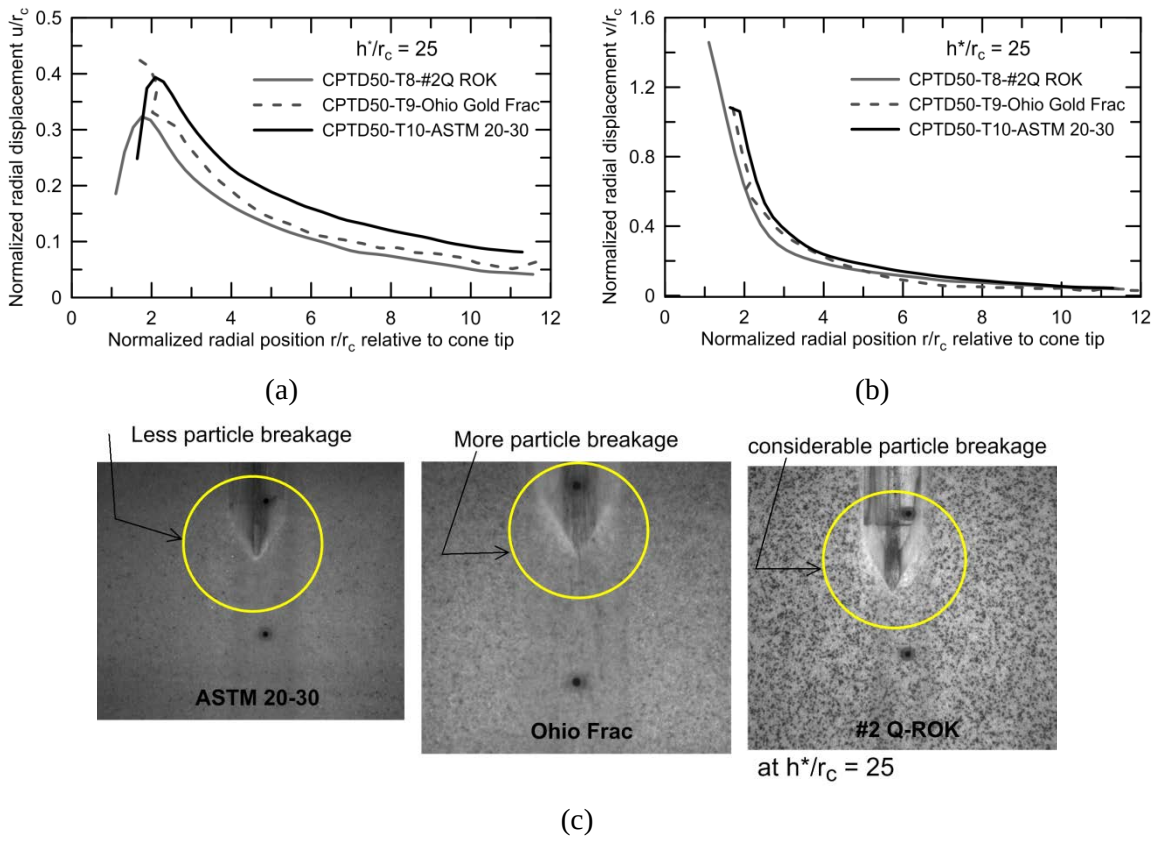

Figure 6.23 Influence of sand type on normalized vertical and radial displacements for cone penetration tests performed on dense sands from $h^*/r_c = 0$ to $h^*/r_c = 25$: (a) radial displacement and (b) vertical displacement (c) visual identification of degree of crushing for #2Q-ROK, Ohio Gold Frac and ASTM20-30 sands.

6.3.7 Comparison of Displacement Paths with Analytical Solutions

Figure 6.24 shows a comparison of normalized radial displacement profiles for a soil disk located at $z/r_c = 20$ when the cone penetrates from $h^*/r_c = 0$ till $h^*/r_c = 21.8$ obtained using image analysis for CPTL50-T4-#2Q-ROK and CPTD50-T8-#2Q-ROK with the cylindrical and spherical cavity expansion solutions of Salgado & Randolph (2001), which is coded in the cavity expansion analysis program CONPOINT (Salgado,

2002). The Bolton dilatancy soil model (Bolton, 1986) was used in these analyses with typical silica sand small-strain stiffness parameters (Salgado, 2008). The measured normalized radial displacements for tests performed on the dense sand samples (Figure 6.24(a)) plot between the upper and lower boundaries defined by the displacements obtained from cylindrical and spherical cavity expansion analyses. For the loose sand samples, predictions using spherical cavity expansion seem to be closer to the observed radial displacement at normalized radial positions larger than 6 (Figure 6.24(b)).

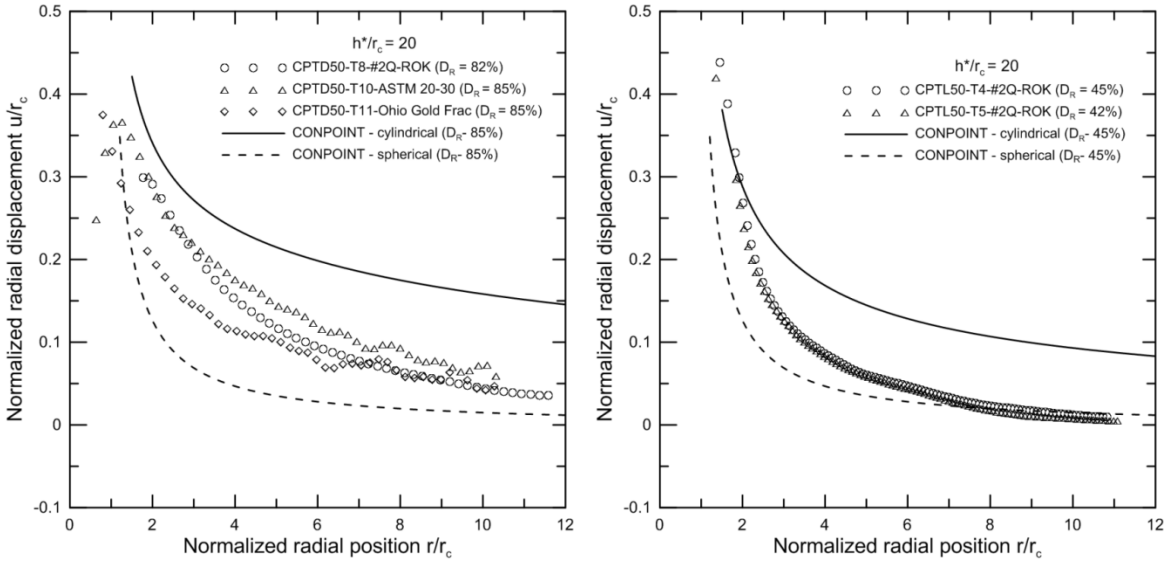

(a) (b)

Figure 6.24 Comparison of radial displacement paths with cavity expansion solutions: (a) dense sand, and (b) loose sand.

6.4 Strain Paths during Cone Penetration

The strain analysis is performed by calculation of the Green-Lagrange strain tensor using the post-processing tool of VIC-2D DIC software (Correlated Solutions, 2009) for each soil element. The radial strain E_{rr}, vertical strain E_{zz}, hoop strain $E_{\theta\theta}$ and shear strain E_{rz} are calculated for different stages of the cone penetration process. The hoop strain $E_{\theta\theta}$ is calculated from the radial displacement assuming that axisymmetric conditions hold true throughout the tests, as explained in section 3.5. In this study, the normal strains are taken as positive in compression and negative in tension. Similarly, contraction is taken as positive and dilation is taken as negative.

6.4.1 Effect of Size of Strain Window on Computed Strain Field

The accuracy of the computed strains depends upon the displacement field accuracy and the appropriate size of the defined strain window (Bing Pan, Xie, Guo, & Hua, 2007). In order to calculate reliable strain fields, a square strain window of size equal to or greater than $20D_{50}$ was selected, where D_{50} is obtained from gradation analysis (ASTM D6913-04) of the test sands. A parametric study was conducted to evaluate the influence of the strain window size on the computed strain for two different elements locations (see Figure 6.25(a)) -- one closer to the cone tip (such as Element B) and another slightly away from it (such as Element E) -- during an incremental cone penetration of 1 r_c from $h^*/r_c = 20$ to $h^*/r_c = 21$ for test CPTD50-T10-ASTM20/30. As shown in Figure 6.25(a), this size for the strain window is just large enough to contain enough particles to produce accurate strain computations. A smaller size would lead to erroneous computations, especially in the displacement zone closer to the cone tip, which has sharp displacement gradients, and a size much larger would move us away from the notion of a point in the continuum (or of a representative element volume (REV)). In the domain where the displacement gradients are relatively small (having relative uniform and small displacements), the size of the strain window has less influence on the strain calculation, as depicted in Figure 6.25(b).

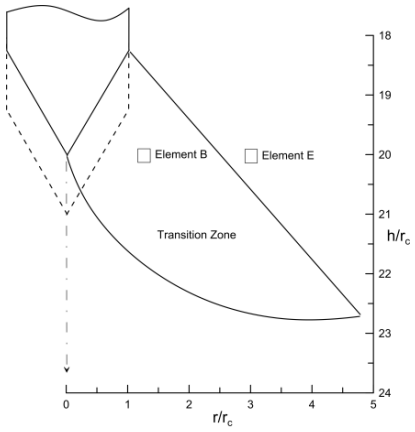

(a)

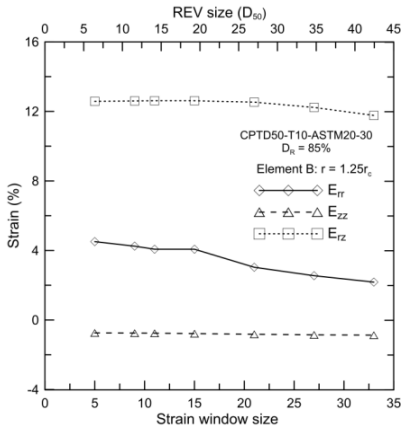

(b)

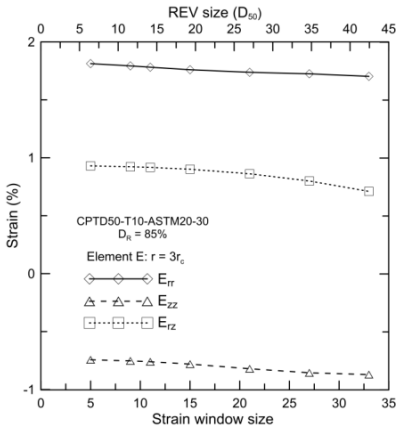

(c)

Figure 6.25 Effect of strain window size on the calculated strain: (a) element locations, (b) Element I, at $r = 1.25r_c$ and (c) Element II, at $r = 3r_c$.

6.4.2 Strain Patterns during Incremental Cone Penetration

6.4.2.1 Incremental Normal Strains Patterns

Figure 6.26 illustrates the spatial distribution of radial (E_{rr}) and vertical strain increments (E_{zz}) associated with increasing cone penetration for the CPTD0-T3-#2Q-ROK test. A free surface exists at the top of the sample since no surcharge was applied in this test. Image pairs of the cone penetration at three normalized penetration depths (h^*/r_c = 2, 6, and 22) were analyzed to obtain the strain increment fields at each of these normalized penetration depths corresponding to an incremental penetration of 2.075 mm ($0.13r_c$), [= 5 × 0.415mm = 2.075 mm increment of cone penetration between images i and (i+5)]. Closer examination of these strain increment plots (see Figure 6.26) show mobilization of fin-shaped zones of compressive radial strains (E_{rr}) around the cone tip, while tensile radial strain bulbs are present below the tip. The reverse trend is observed in the case of vertical strain (E_{zz}) increments, where compressive strain bulbs are present below the cone tip, while tensile vertical strains are observed next to and above the cone tip. The compressive radial strains fan out more radially at shallow penetration depth (h^*/r_c = 2) (Figure 6.26 (a), (c) & (e)); with increasing penetration depth, the orientation of the observed near-symmetrical, fin-shaped radial strain zones become more sub-vertical. The maximum contour of compressive radial strain increment of 2% is consistent with increasing penetration depths h^*/r_c = 2, 6 & 8, while an increase in compressive vertical strain increments (E_{zz} = 3%, 4% & 5%) is observed for h^*/r_c = 2, 6 & 8. Moreover, the size of the compressive vertical strain increments contour bulbs below the cone tip also increases from $2r_c$ to $3r_c$ with increasing penetration depth.

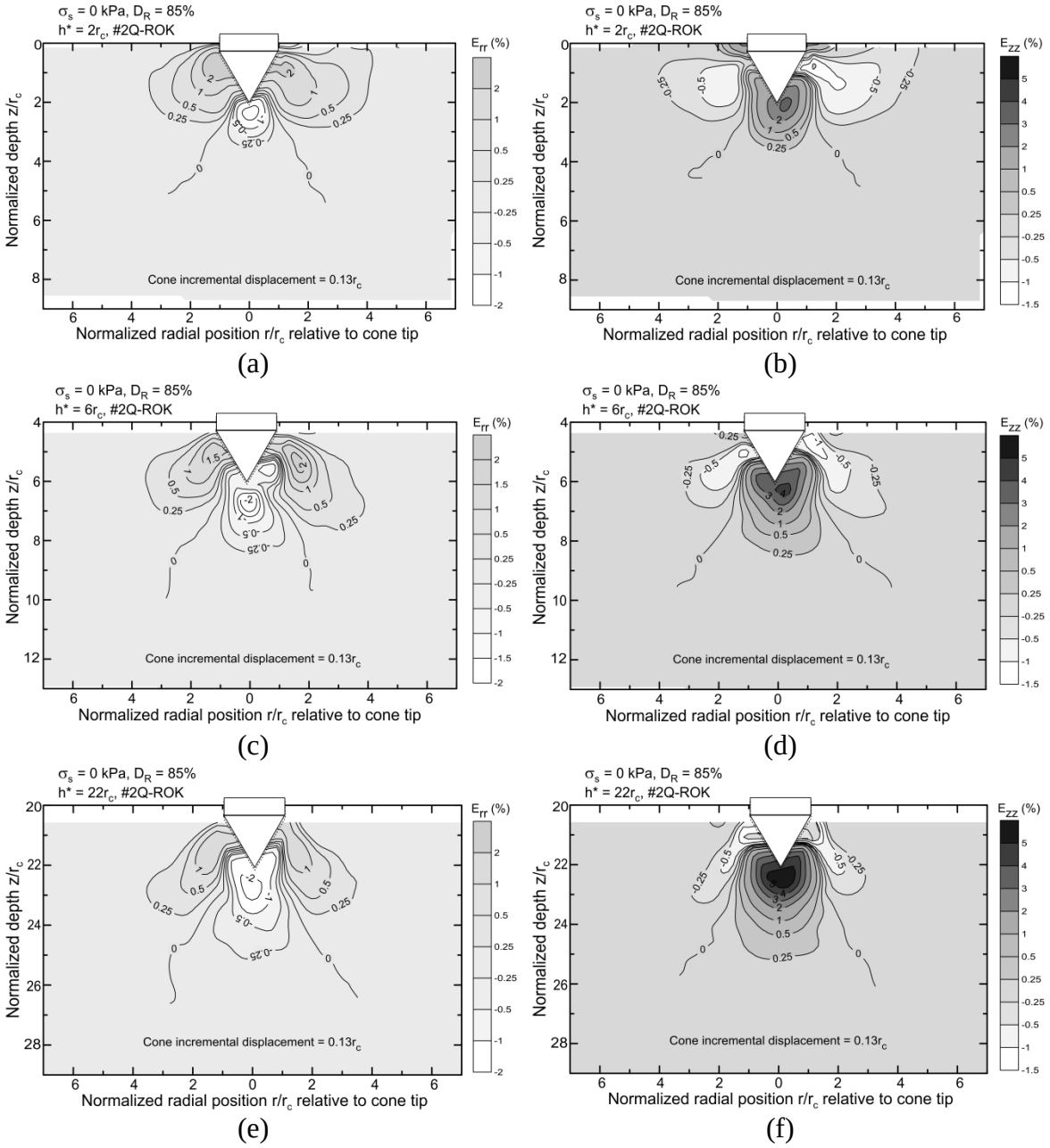

Figure 6.26 Normal strains increments for test CPTD-T3-#2Q-ROK (σ'_s= 0 kPa, D_R = 85%): (a) radial strain increment at h^*/r_c = 2, (b) vertical strain increment at h^*/r_c = 2, (c) radial strain increment at h^*/r_c = 6, (d) vertical strain increment at h^*/r_c = 6, (e) radial strain increment at h^*/r_c = 22 and (f) vertical strain increment at h^*/r_c = 22.

Figure 6.27 and Figure 6.28 compare the incremental radial (E_{rr}) and incremental vertical strain (E_{zz}) patterns around the cone during an incremental penetration of 2.075 mm ($0.13r_c$) for three tests performed on samples of three different sands (CPTD50-T8-#2Q-ROK, CPTD50-T9-Ohio Gold Frac and CPTD50-T10-ASTM20-30) with approximately the same density (82%, 85% and 87%) subjected to the same surcharge (50 kPa). These figures show the incremental strain fields for two normalized depths, $h^*/r_c = 6$ and $h^*/r_c = 20$, corresponding to normalized depths just prior to and after the onset of particle crushing in the soil zone below the cone (particle crushing was visible to the naked eye through the observation window).

The incremental radial strain (E_{rr}) pattern for $h^*/r_c = 6$ (Figure 6.27(a), (b) and (c)) indicates that, immediately below the cone tip, the radial strain increments are tensile, while, slightly above it, the compressive radial strain increments are observed. A wider zone of compressive radial strains is more clearly observed for the least crushable sand (ASTM20-30) than for the other two sands. The incremental radial strain patterns for $h^*/r_c = 20$ (Figure 6.27 (d), (e) and (f)) show a similar trend.

The incremental vertical strain (E_{zz}) bulbs (Figure 6.28) show that compressive vertical strain increments are observed below the cone tip and slightly above it ($h/r_c \approx 1$), and tensile vertical strain contours of comparatively lesser magnitudes (tensile strain of 1-2% versus 5% compressive strain) develop next to it. The mobilized compressive vertical strain bulbs are slightly shallower in the least crushable sand (ASTM 20-30) than in the other two sands for penetration depth of $h^*/r_c = 6$ (Figure 6.28 (a), (b) and (c)) and for the greater penetration depth $h^* = 20\ r_c$.

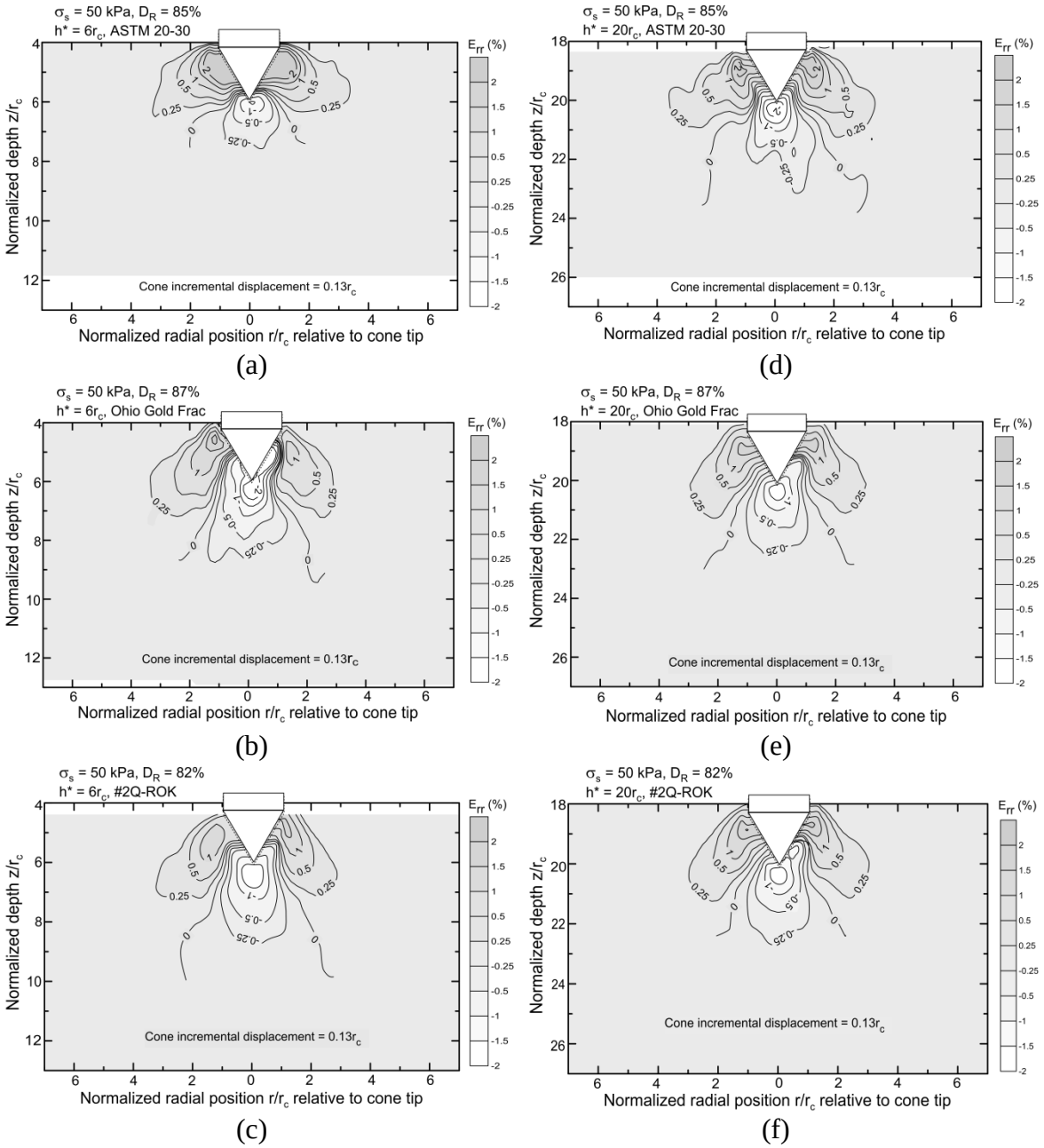

Figure 6.27 Radial strain (E_{rr}) increments for ASTM 20-30, Ohio Gold Frac, and #2Q-ROK silica sands prior to (h^*/r_c = 6) and after particle crushing (h^*/r_c = 20): (a) ASTM 20-30 at h^*/r_c = 6, (b) Ohio Gold Frac at h^*/r_c = 6, (c) #2Q-ROK at h^*/r_c = 6, (d) ASTM 20-30 at h^*/r_c = 20, (e) Ohio Gold Frac at h^*/r_c = 20, and (f) #2Q-ROK at h^*/r_c = 20.

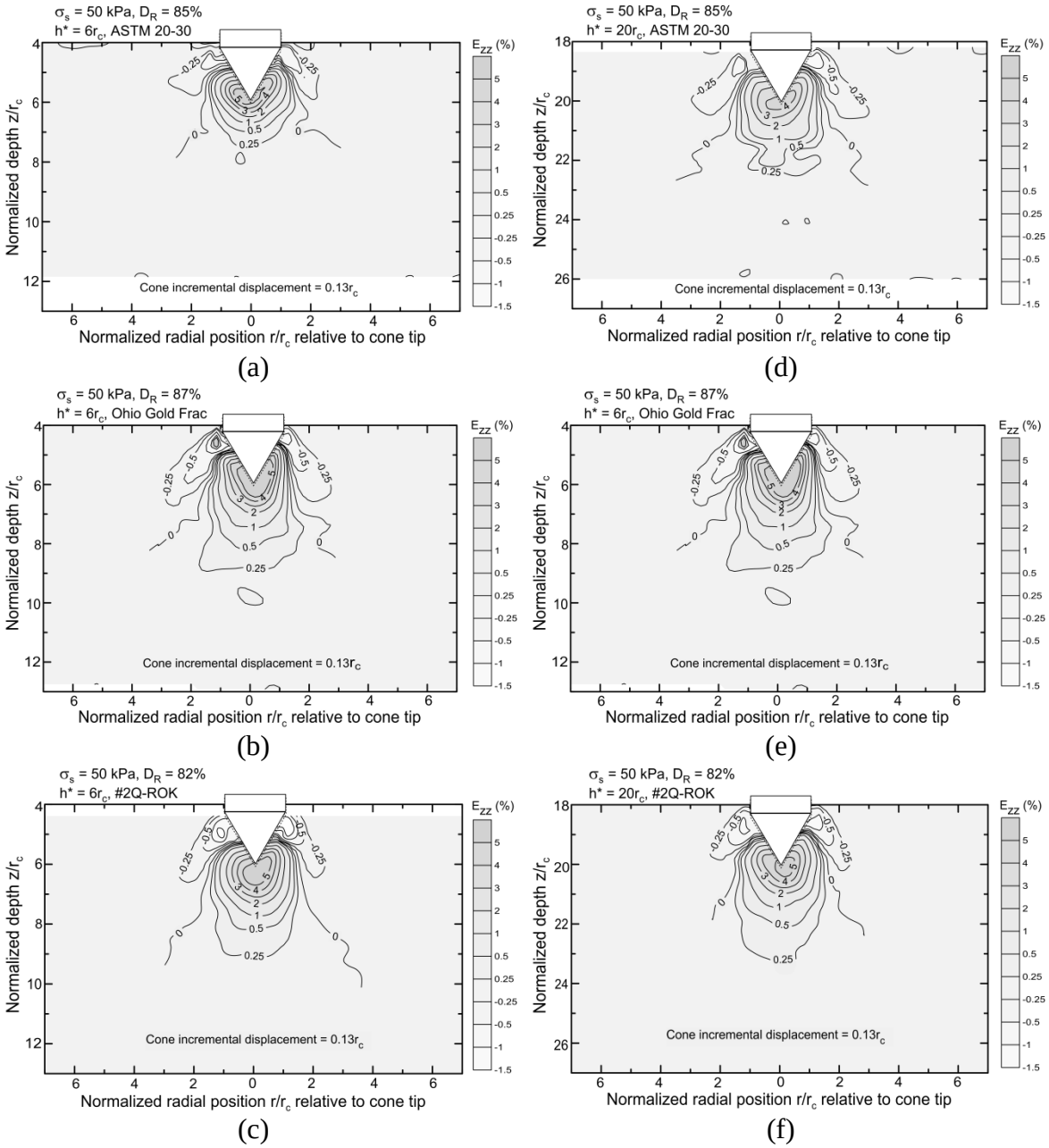

Figure 6.28 Vertical strain (E_{zz}) increments for ASTM 20-30, Ohio Gold Frac, and #2Q-ROK silica sands prior to (h^*/r_c = 6) and after particle crushing (h^*/r_c = 20): (a) ASTM 20-30 at h^*/r_c = 6, (b) Ohio Gold Frac at h^*/r_c = 6, (c) #2Q-ROK at h^*/r_c = 6, (d) ASTM 20-30 at h^*/r_c = 20, (e) Ohio Gold Frac at h^*/r_c = 20, and (f) #2Q-ROK at h^*/r_c = 20

6.4.2.2 Incremental Shear and Volumetric Strain Patterns

Figure 6.29 shows the evolution of incremental shear strain (E_{rz}) and volumetric strain (E_{vol}) for increasing penetration depth for the CPTD0-T3-#2Q-ROK test. The shear strain contours around the cone form a transition zone pattern radiating from the cone tip (Figure 6.29(a), (b) and (c)) similar to that indicated by Salgado & Prezzi (2007). Due to presence of the free surface, next to it, an upward shearing zone is also observed which tends to diminish at greater penetration depths, with h^*/r_c = 22 shown in Figure 6.29(c). This also shows in the incremental volumetric strain fields: at the shallow penetration depth of h^*/r_c = 2 (Figure 6.29(d)), dilation zone fans upward towards the free surface, but at greater penetration depths, h^*/r_c = 6 & 22 (Figure 6.29(e) and (f)), it tends to localize around the cone tip. The amount of dilation is greater at shallow depth (due to lower initial mean stress). A narrow contractive zone is also observed along the axis of penetration of the cone next to the dilative zone with maximum volumetric change of (1-2%).

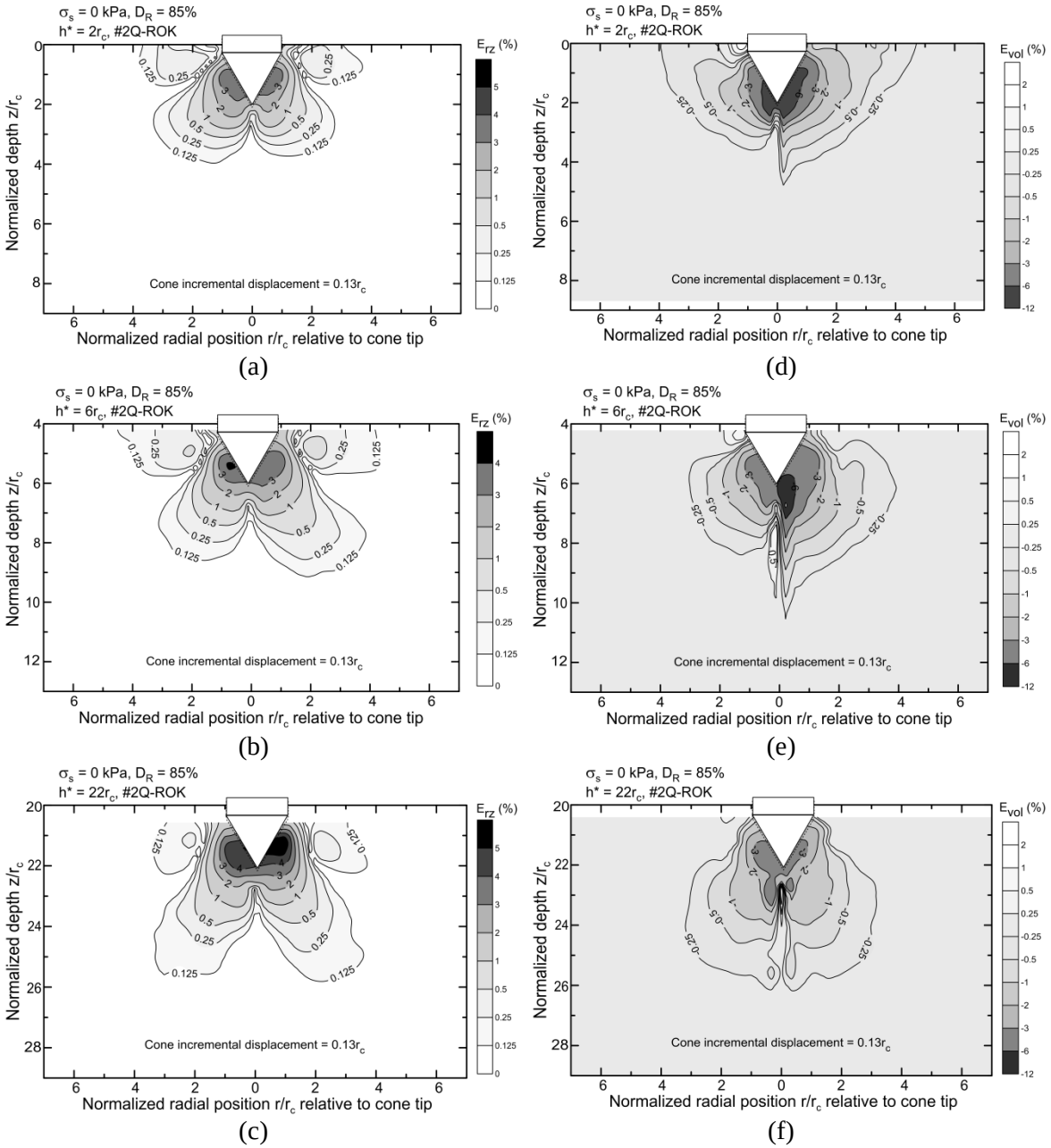

Figure 6.29 Evolution of the shear strain (E_{rz}) increments and volumetric (E_{vol}) strain increments with increasing penetration for test CPTD-T3-#2Q-ROK (σ'_s= 0 kPa, D_R = 85%): (a) E_{rz} at h^*/r_c = 2, (b) E_{rz} at h^*/r_c = 6, (c) E_{rz} at h^*/r_c = 22, (d) E_{vol} at h^*/r_c = 2, (e) E_{vol} at h^*/r_c = 6 and (f) E_{vol} at h^*/r_c = 22.

Figure 6.30 and Figure 6.31 compare the incremental shear (E_{rz}) and incremental volumetric strain (E_{vol}) patterns for three tests, with three different sands (CPTD50-T8-#2Q-ROK, CPTD50-T9-Ohio Gold Frac and CPTD50-T10-ASTM20-30). The transition zone, shaped as suggested by Salgado & Prezzi (2007), are clearly observed in these figures. However, in the test (CPTD50-T10-ASTM20-30) on the least crushable sand, a slightly wider and shallower shear zone is observed than in the tests with the other two sands (CPTD50-T8-#2Q-ROK, CPTD50-T9-Ohio Gold Frac) at the same normalized penetration depth $h^*/r_c = 6$. At deeper penetration depths, such as $h^*/r_c = 20$, the shearing zone patterns are similar and no clear effect of particle crushing is visible. Maximum incremental shear strain values of 4-6%, always corresponding to the incremental penetration of $0.013r_c$, are observed.

The incremental volumetric strain contour plots of tests conducted with a surcharge (Figure 6.31) indicate the presence of a contractive zone (~ maximum contraction of 2%), that is sandwiched between dilative zones (with a dilation of ~2-4%) along the axis of cone penetration. In the least crushable sand test (CPTD50-T10-ASTM20-30), more dilation is observed at deeper normalized penetration depth of $h^*/r_c = 20$ as compared to normalized penetration depth of $h^*/r_c = 6$, possibly due to considerable density and stress changes involved during the course of increased cone penetration (see Figure 6-32(a) & (d)); while, for the tests with other two sands (CPTD50-T8-#2Q-ROK, CPTD50-T9-Ohio Gold Frac), the dilation is slightly suppressed at deep penetration depths as depicted from the size of contours.

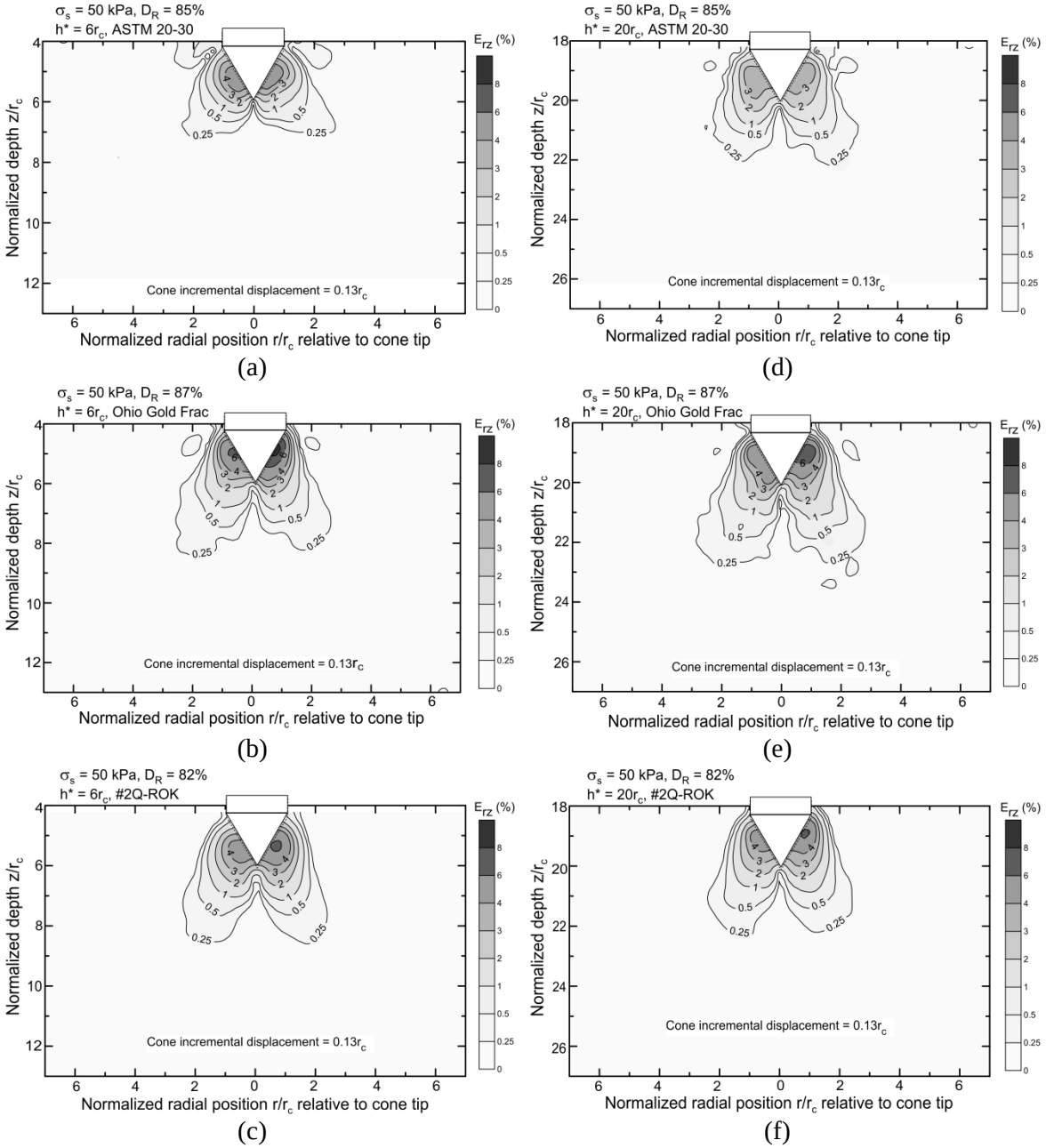

Figure 6.30 Shear strain (E_{rz}) increments for ASTM 20-30, Ohio Gold Frac, and #2Q-ROK silica sands prior to (h^*/r_c = 6) and after particle crushing (h^*/r_c = 20): (a) ASTM 20-30 at h^*/r_c = 6, (b) Ohio Gold Frac at h^*/r_c = 6, (c) #2Q-ROK at h^*/r_c = 6, (d) ASTM 20-30 at h^*/r_c = 20, (e) Ohio Gold Frac at h^*/r_c = 20, and (f) #2Q-ROK at h^*/r_c = 20.

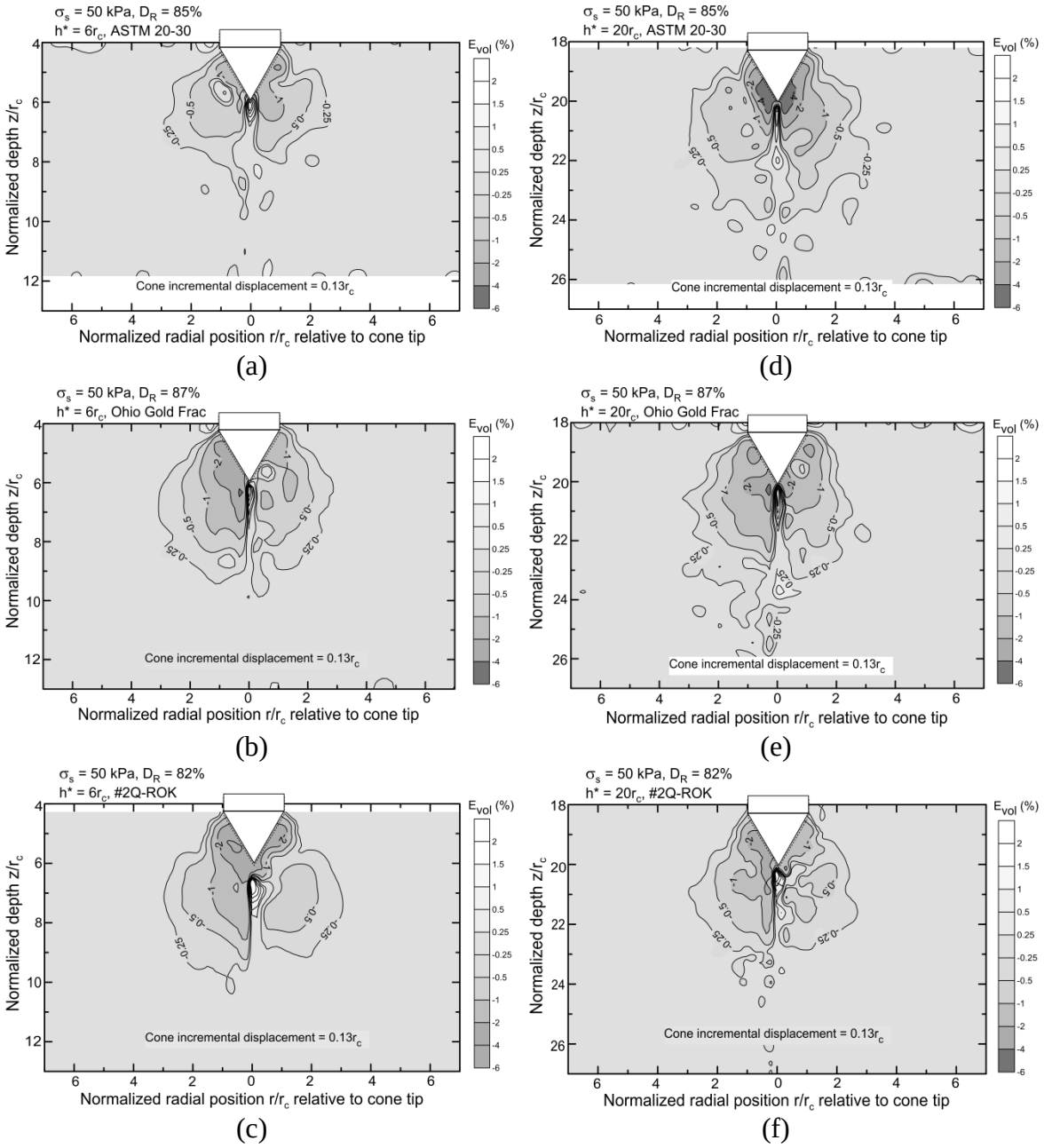

Figure 6.31 Volumetric strain (E_{vol}) increments for ASTM 20-30, Ohio Gold Frac, and #2Q-ROK silica sands prior to (h^*/r_c = 6) and after particle crushing (h^*/r_c = 20): (a) ASTM 20-30 at h^*/r_c = 6, (b) Ohio Gold Frac at h^*/r_c = 6, (c) #2Q-ROK at h^*/r_c = 6, (d) ASTM 20-30 at h^*/r_c = 20, (e) Ohio Gold Frac at h^*/r_c = 20, and (f) #2Q-ROK at h^*/r_c = 20.

6.4.3 Change in Normal Strains during Increased Cone Penetration

Figure 6.32 shows the spatial distribution of accumulated vertical and radial strains around the cone tip corresponding to $1r_c$ penetration, deduced from the sequence of images obtained when the cone tip moved from a depth $h^* = 20r_c$ (measured from the top of the sample) to $h^* = 21r_c$ for the tests CPTD50-T10-ASTM20-30 and CPTD50-T8-#2Q-ROK. These contour plots can be used to explain the mobilization of tip resistance. The zone of compressive strains mobilized below the cone tip is slightly wider for the most crushable sand than the least crushable sand (compare Figure 6.32(b) & (d)). For the tests performed, the transition from vertical compression to vertical extension takes place at inclinations of 52.4 and 49.2 degrees with the horizontal for the least crushable sand and the most crushable sand, respectively. The transition starts from the cone shoulder at $h/r_c = 1.71$ for the both test sands. The vertical extent of the straining zone below the cone tip corresponding to vertical strains greater than 0.5% is about $6r_c$ for both sands.

Figure 6.33 shows the evolution of vertical and radial strains for soil elements *O*, *A*, *B*, *C*, *D* & *E* initially located at the normalized vertical position of $z/r_c = 20$ (see Figure 6.11 for radial position of the elements) during an incremental cone penetration from $h^*/r_c = 20$ *to* $h^*/r_c = 21$ for tests CPTD50-T10-ASTM20-30 and CPTD50-T8-#2Q-ROK. A large vertical compressive strain is mobilized for element *O*, located immediately below the cone tip in both sands. Element *O* in the most crushable sand (#2Q-ROK) undergoes approximately 30% vertical compressive strain, which is slightly more than the 28% vertical compressive strain observed in the least crushable sand (ASTM 20-30). The radial extension of element *O* in both sands is similar, with 26% in the least crushable sand and 20% in the most crushable sand. These strain paths indicate that the soil element undergoes a loading path that approaches triaxial compression below the cone tip (see Figure 6.33(a)).

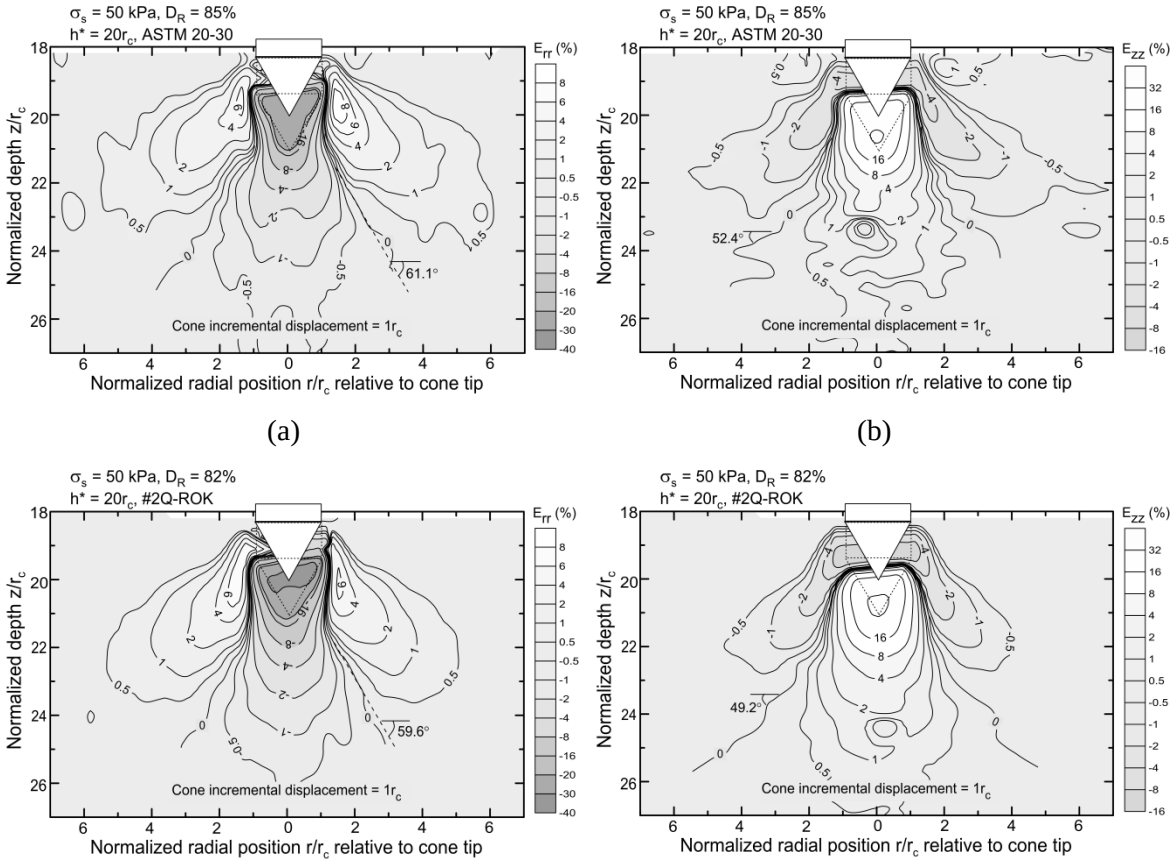

Figure 6.32 Vertical and radial accumulated strain patterns corresponding to a cone penetration of $1r_c$ during penetration from $h^*/r_c = 20$ to $h^*/r_c = 21$ in the least crushable (ASTM20-30) and most crushable (#2Q-ROK) silica sands: (a) radial strain for CPTD50-T10-ASTM20-30, (b) vertical strain for CPTD50-T10-ASTM20-30, (c) radial strain for CPTD50-T8-#2Q-ROK, and (d) vertical strain for CPTD50-T8-#2Q-ROK.

Soil element *A* (Figure 6.33(b)), located at r = $0.5r_c$, experiences increasing vertical compressive strain with increasing penetration. The least crushable sand (ASTM20-30) continues to experience less vertical compression (about 18%), while the most crushable sand (#2Q-ROK) experiences about 21% vertical compression. The radial extension experienced by element *A* in the least crushable sand (ASTM20-30) is slightly less (16%) than the 20% experienced by the most crushable sand (#2Q-ROK).

Element *B* (Figure 6.33(c)), located at $r = 1.25r_c$, undergoes vertical and radial compression simultaneously. The peak vertical compression in the least crushable sand is observed to be much smaller (about 0.5%) than in the most crushable sand (for which it is

about 2.5%). The compressive radial strain in the least crushable sand is slightly greater (about 4.0%) than in the most crushable sand (about 3.0%).

Element *C* (Figure 6.33(d)), located at $r = 1.5r_c$, undergoes radial compression of about 5% in the least crushable sand, which is smaller than the radial compression of about 6% experienced in the most crushable sand. At the same time, it undergoes vertical extension of about 2.5% in the least crushable sand and vertical extension of about 1.25% in the most crushable sand.

Element *D* (Figure 6.33(e)), located at $r = 2r_c$, undergoes about 3.6% and 4.5% radial compression in the least crushable sand and the most crushable sand, respectively. It undergoes vertical extension of about 2.6% in the least crushable sand and 2.2% in the most crushable sand.

Element *E* (Figure 6.33(f)), located at $r = 3r_c$, experiences about 1.7% radial compression in the least crushable sand, which is slightly greater than 1.3% radial compression experienced by the most crushable sand. The vertical extension of element E is about 0.7% and 0.5% in the least crushable sand and the most crushable sand, respectively.

Closer look at the strain paths shown in Figure 6.33 reveals that a transition in the loading path from paths resembling triaxial compression in a general way to paths resembling triaxial extension in a general way takes place below the cone tip during cone penetration with increasing radial distance from the cone tip.

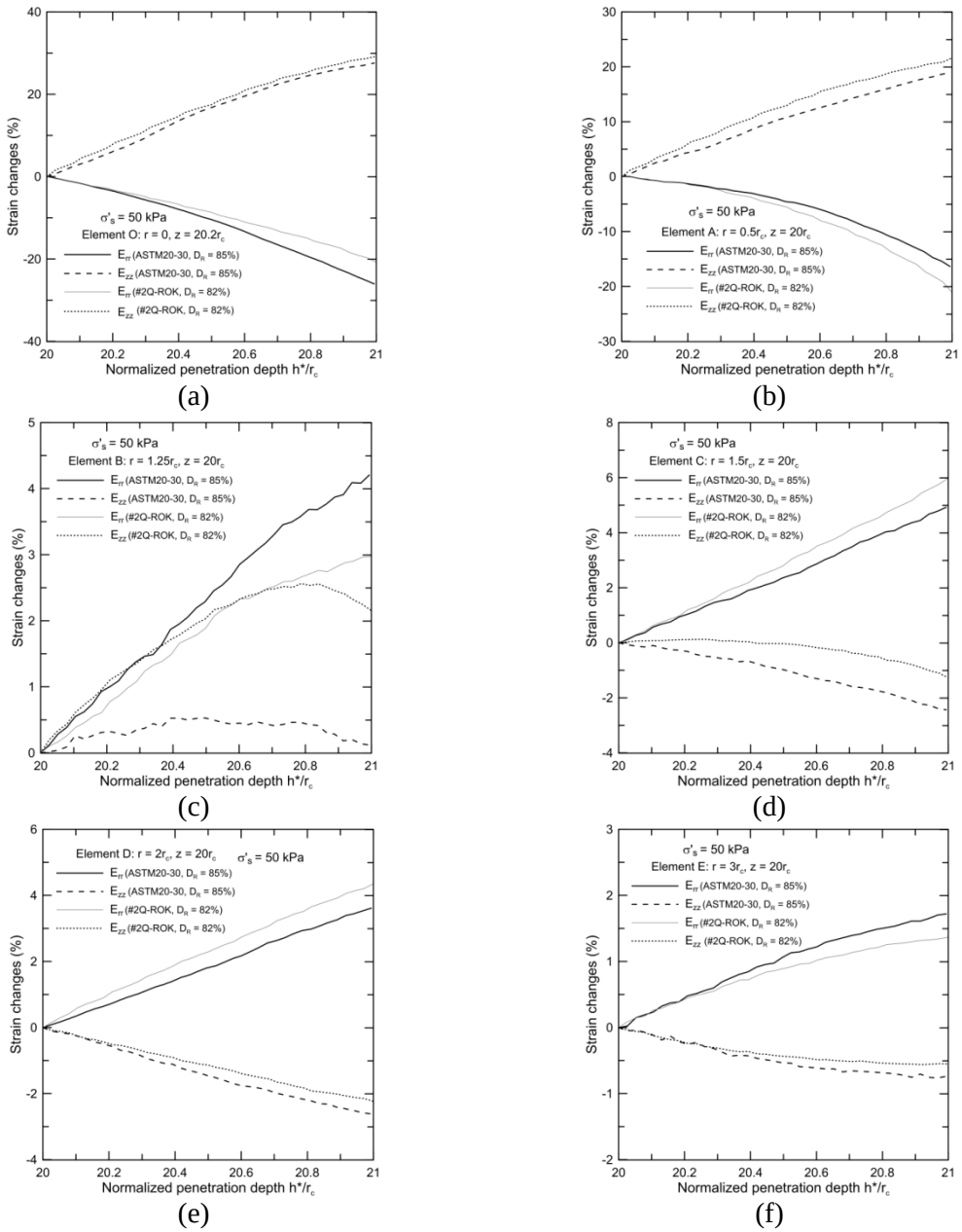

Figure 6.33 Evolution of accumulated radial and vertical strain for $1r_c$ penetration in the least crushable (CPTD50-T10-ASTM20-30) and the most crushable (CPTD50-T8-#2Q-ROK) silica sands: (a) element *O* at r = 0, (b) element *A* at r = $0.5r_c$, (c) element *B* at r = $1r_c$, (d) element *C* at r = $1.5r_c$, (e) element *D* at r = $2r_c$ and (f) element *E* at r = $3r_c$.

6.4.4 Strain Paths during Continued Cone Penetration

Figure 6.34 and Figure 6.35 show the strain paths of soil elements *O*, *B*, *C*, *D* and *E* for cone penetration from $h^* = 0\ r_c$ to $h^* = 23r_c$ for tests CPTL50-T4-#2Q-ROK and $h^* = 0r_c$ to $h^* = 25r_c$ for CPTD50-T8-#2Q-ROK. Figure 6.36 shows the strain paths of the same elements for miniature cone penetration from $h^* = 0r_c$ to $h^* = 50r_c$ (where r_c in these figures is the radius of the miniature cone) for test CPTD50-T11-Mini-#2Q-ROK. For tests CPTL50-T4-#2Q-ROK and CPTD50-T8-#2Q-ROK, the soil elements are located at $r = 0$ (element O), $r = 1.25r_c$ (element *B*), $r = 1.5r_c$ (element *C*), $r = 2r_c$ (element *D*) and $r = 3r_c$ (element *E*) (see Figure 6.11) at depth $z = 20r_c$ and $20.5r_c$ for the loose and dense sand sample, respectively. For test CPTD50-T11-Mini-#2Q-ROK, soil elements *O*, *B*, *C*, *D* and *E* are located at the same normalized offsets (normalized by the miniature cone radius) ($r = 0$,1.25 r_c, $1.5r_c$, $2r_c$ and $3r_c$) and the depth of these elements is almost identical for all three tests. Therefore, the effect of density on the strain paths can be evaluated for tests CPTL50-T4-#2Q-ROK and CPTD50-T8-#2Q-ROK and the effect of cone size on the strain paths can be studied for tests CPTD50-T8-#2Q-ROK and CPTD50-T11-Mini-#2Q-ROK (the initial state of stress for each element in these two tests are almost similar).

The strain paths of soil elements located at various distances from the penetration axis, shown in Figures 6.34, 6.35, and 6.36, have some notable features. There is initially vertical compression together with radial extension, starting at the point labeled as 1. That is followed by deformation generally consistent with a cavity expansion process (starting at 2 in Figures 6.34, 6.35, 6.36 and ending at 3), during which compressive radial strains increase substantially. Between 3 and 4 there is some radial relaxation and then stability, as the cone reaches a depth at which it no longer affects the soil element.

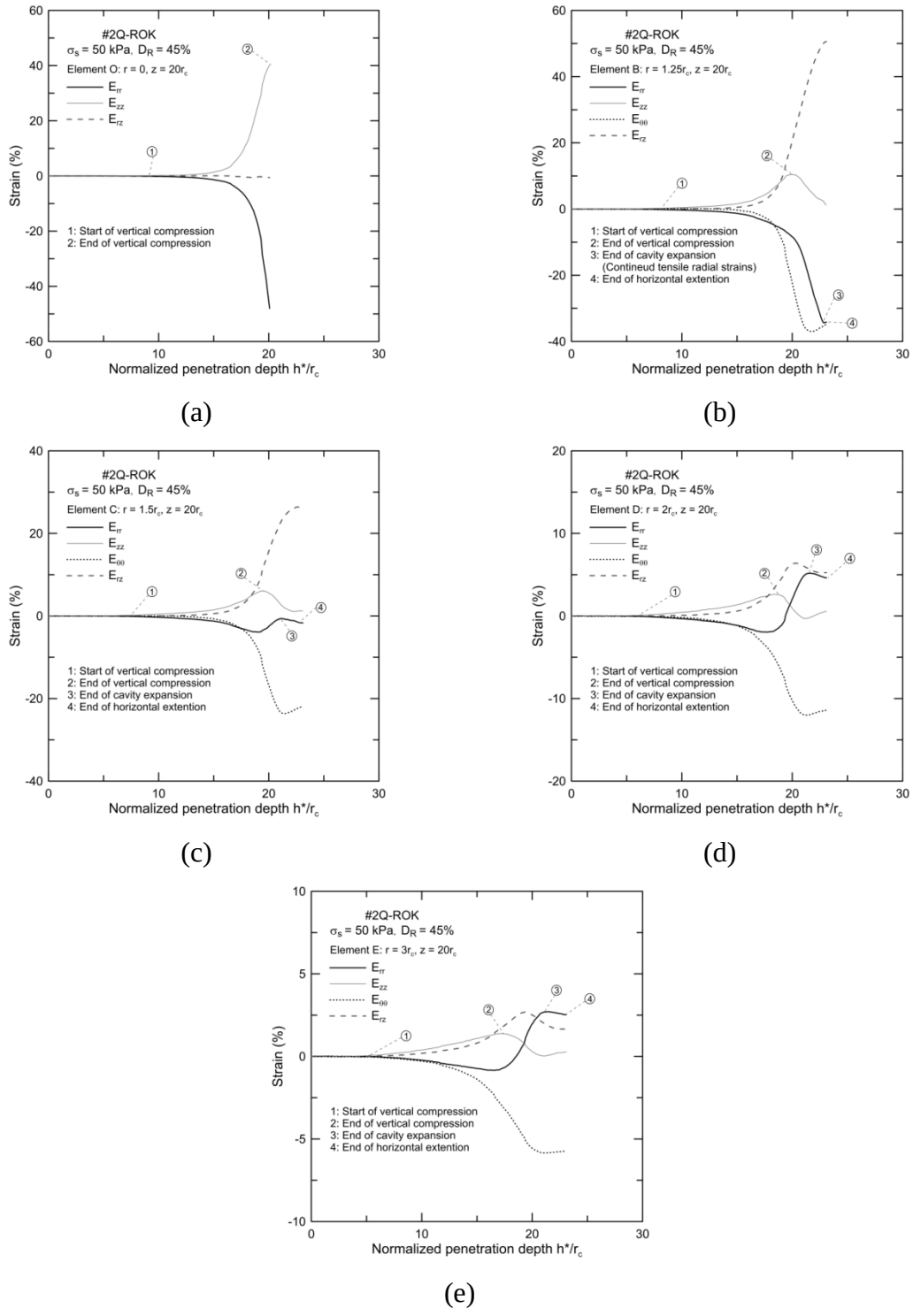

Figure 6.34 Strain paths during continuous cone penetration from $h^* = 0r_c$ to $h^* = 23r_c$ for test CPTL50-T4-#2Q-ROK for: (a) element *O* at $r = 0$ (b) element *B* at $r = 1.25r_c$, (b) element *C* at $r = 1.5r_c$, (b) element *D* at $r = 2r_c$, and (b) element *E* at $r = 3r_c$.

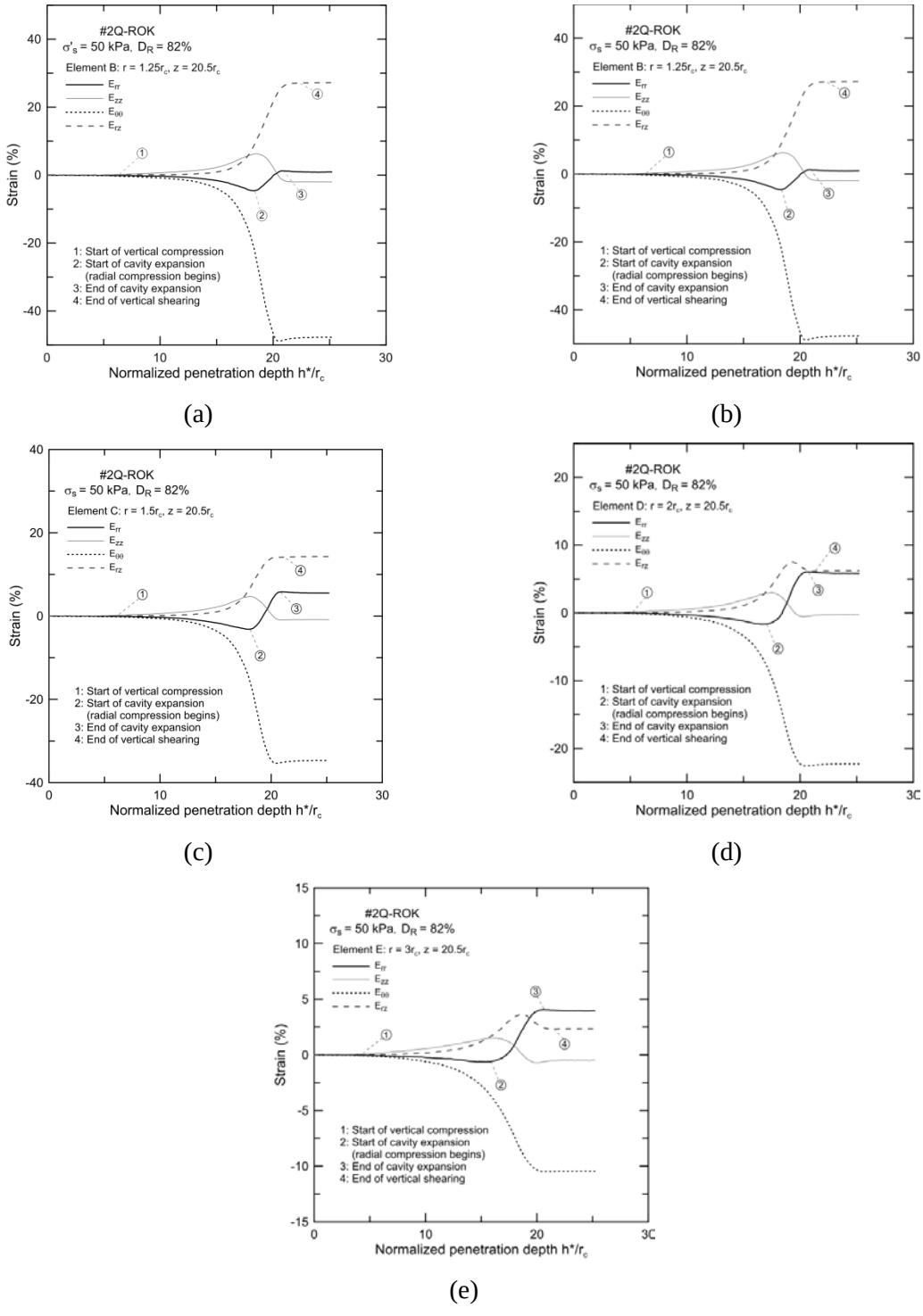

Figure 6.35 Strain paths during continuous cone penetration from $h^* = 0r_c$ to $h^* = 25r_c$ for test CPTD50-T8-#2Q-ROK for: (a) element *O* at $r = 0$, (b) element *B* at $r = 1.25r_c$, (c) element *C* at $r = 1.5r_c$, (d) element *D* at $r = 2r_c$, and (e) element *E* at $r = 3r_c$.

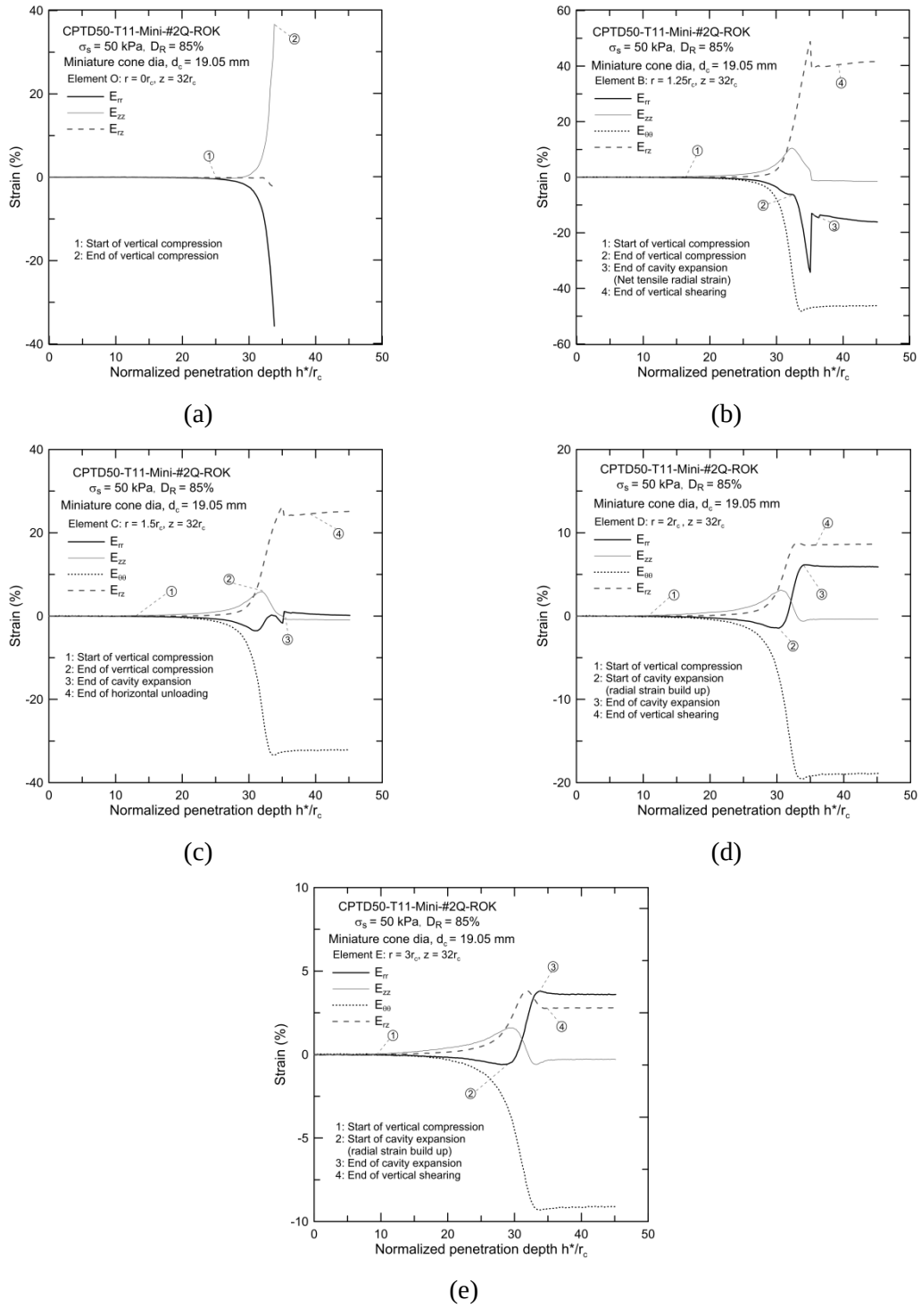

Figure 6.36 Strain paths during continuous cone penetration from $h^* = 0r_c$ to $h^* = 45r_c$ for test CPTD50-Mini-T11 for: (a) element *O* at $r = 0$ (b) element *B* at $r = 1.25r_c$, (c) element *C* at $r = 1.5r_c$, (d) element *D* at $r = 2r_c$ and (e) element *E* at $r = 3r_c$.

Analysis of Figures 6.34, 6.35, and 6.36 suggest that the position of the soil elements and the initial density of the soil samples determine the onset of deformation (vertical compression and radial extension) of the elements during the cone penetration process. The deformation of elements located immediately below the tip (Element O) takes place slightly after than the other elements (such as elements B, C, D and E) located at greater r/r_c. Table 6.1 lists the vertical position of the soil elements shown in Figures 6.34, 6.35, and 6.36, with respect to the cone tip, where they start deforming.

Table 6.1 Relative vertical position (h) of the soil elements with respect to the cone tip at the onset of deformation corresponding to 0.5% accumulated strain mobilization

Element	Test Code		
	CPTL50-T4-#2Q-ROK	CPTD50-T8-#2Q-ROK	CPTD50-T11-Mini-#2Q-ROK
O	7.28 r_c	8.24 r_c	6.32 r_c
B	9.64 r_c	11.68 r_c	11.325 r_c
C	9.37 r_c	11.18 r_c	11.25 r_c
D	9.37 r_c	10.68 r_c	10.83 r_c
E	8.98 r_c	10.92 r_c	10.22 r_c

At the onset of cavity expansion (starting at 2 in Figures 6.34, 6.35, and 6.36), soil elements, in general, undergo maximum vertical compression and begin a sharp transition from radial extension to radial compression. Figures 6.34, 6.35, and 6.36 show that the maximum vertical compression mobilizes in the elements slightly before the cone tip aligns vertically with the elements. Table 6.2 lists the vertical and radial strain experienced by the soil elements at the onset of the cavity expansion stage (at 2 in Figures 6.34, 6.35, and 6.36) for each of the three tests.

Table 6.2 Vertical and radial strains at the onset of cavity expansion

Element	Test					
	CPTL50-T4-#2Q-ROK		CPTD50-T8-#2Q-ROK		CPTD50-T11-Mini-#2Q-ROK	
	E_{zz} (%)	E_{rr} (%)	E_{zz} (%)	E_{rr} (%)	E_{zz} (%)	E_{rr} (%)
O	40.2	-48.0	30.6	-20.9	36.7	-35.7
B	10.4	-8.6	6.3	-4.6	10.5	-6.2
C	6.0	-3.5	4.7	-3.2	5.8	-3.0
D	2.6	-1.9	2.9	-1.5	3.1	-1.4
E	1.4	-0.8	1.5	-0.6	1.6	-0.6

Analysis of Table 6.2 reveals that the vertical and radial strain at the onset of cavity expansion do not significantly depend on the soil density (tests CPTL50-T4-#2Q-ROK and CPTD50-T8-#2Q-ROK). The strains for element *B* through *E* are reasonably consistent across tests, but there is a clear difference in the strains observed for element O (located directly on the axis of penetration), which undergoes considerably greater deformation for the loose test than for dense test, whereas the test for the smaller cone shows intermediate response.

Table 6.3 lists the vertical and radial strains of the elements at the end of the cavity expansion stage (at 3 in Figures 6.34, 6.35, and 6.36) for each of the three tests. At that stage, the vertical strains is tensile and radial strain is compressive for elements located at larger offsets from the cone penetration axis (r/r_c = 1.5, 2 and 3), except for elements located closer to the penetration axis at a radial offset of $r/r_c \sim 1.5$, such as Element *B,* which experience a continued buildup of tensile radial strain (see Figures 6.34(b), and 6.35(b)).

Table 6.3 Vertical and radial strains at the end of cavity expansion

Element	Test Code					
	CPTL50-T4-#2Q-ROK		CPTD50-T8-#2Q-ROK		CPTD50-T11-Mini-#2Q-ROK	
	E_{zz} (%)	E_{rr} (%)	E_{zz} (%)	E_{rr} (%)	E_{zz} (%)	E_{rr} (%)
O	N.A.	N.A.	N.A.	N.A.	N.A.	N.A.
B	2.5	-34.5	-1.9	1.3	-1.1	-13.1
C	2.7	-0.5	-0.9	5.8	-0.8	1.1
D	-0. 2	5.2	-0.5	6.1	-0.6	6.2
E	-0.05	2.7	-0.7	4.0	-0.6	3.8

Table 6.3 shows that, at the completion of cavity expansion, when the cone shoulder lines up with the elements vertical position (at 3 in Figures 6.34, 6.35, and 6.36), element *B* undergoes maximum vertical extension. In the tests with the larger cone, element *B* undergoes radial compression, whereas in the test with the miniature cone, it undergoes radial extension, due to scale effects as more vertical shearing is experienced by same element *B* in the miniature cone test as compared to large cone test (see Table 6.4). The deformation of elements rapidly decays with radial offset from the cone penetration axis. Comparison of the elements' responses in the loose and the dense sands (CPTL50-T4-#2Q-ROK and CPTD50-T8-#2Q-ROK) suggests that more vertical and radial extension are mobilized in the loose sand than the dense sand, and the compressive deformation of soil elements at greater radial offsets is more in the dense sand than the loose sand. The effect of cone size on the elements responses at the end of cavity expansion is not pronounced and is similar to the onset of cavity expansion (Table 6.2). The miniature cone (CPTD50-T11-Mini-#2Q-ROK) mobilizes almost similar vertical extension in the elements at the same normalized radial distance from the cone penetration path as compared to the larger cone (CPTD50-T8-#2Q-ROK). However, Element *B* in the test with the miniature cone undergoes radial extension, while it

undergoes radial compression in the test with the larger cone. Elements *C*, *D* and *E*, show comparable responses in the dense sand irrespective of the cone size. The maximum compressive radial strain is observed to be taking place in Element *D* located slightly away from the cone tip ($r/r_c = 2$).

The maximum shear strain (E_{rz}) for the elements located at closer position to cone penetration axis (such as elements *B* and *C* located at $r/r_c = 1.25$ & 1.5) is mobilized when the cone shoulder aligns with the vertical position of the soil elements (at 3 Figuress 6.34(b), 6.35(b) and 6.36(b) marks the end of cavity expansion). However, for elements at larger offsets (such as elements *D* and *E* located at $r/r_c = 2$ & 3), the peak shear mobilizes during the cavity expansion phase (between 2 & 3 Figures 6.34(d), 6.34(d) and 6.36(d)). After the mobilization of peak shear strain, shear healing takes place as the cone penetrates further below the vertical position of these soil elements, and eventually it stabilizes after penetration of 4-5 r_c, and further cone penetration does not affect these elements. Table 6.4 lists the maximum shear strain of each element for the three tests.

Table 6.4 Maximum shear strain experienced by soil elements

Element	Test Code		
	CPTL50-T4-#2Q-ROK	CPTD50-T8-#2Q-ROK	CPTD50-T11-Mini-#2Q-ROK
O	N.A.	N.A	N.A
B	50.5%	27.2%	48.8%
C	26.4%	14.1%	25.9%
D	6.4%	7.5%	8.8%
E	2.7%	3.6%	3.8%

As shown in Table 6.4, the soil elements undergo greater shearing in the loose sand than the dense sand. It can be seen that, for the dense soil samples, the soil elements

in the test with the miniature cone experience more shearing than those in the test with the larger cone. This trend is consistent with what was observed from the radial and vertical strains. From the results of these analysis, it can be inferred that a zone of localized intense shearing exists within the radial distance of $r = 2r_c$ from the cone penetration axis.

6.4.5 Loading Patterns

In addition to the strain paths discussed earlier, normal strain paths for additional soil elements located around the cone tip were analyzed in order to provide a better understanding of the complex loading pattern experienced by these elements during the incremental cone penetration process. Figure 6.37 shows the soil elements considered for the analysis of loading pattern near the cone tip.

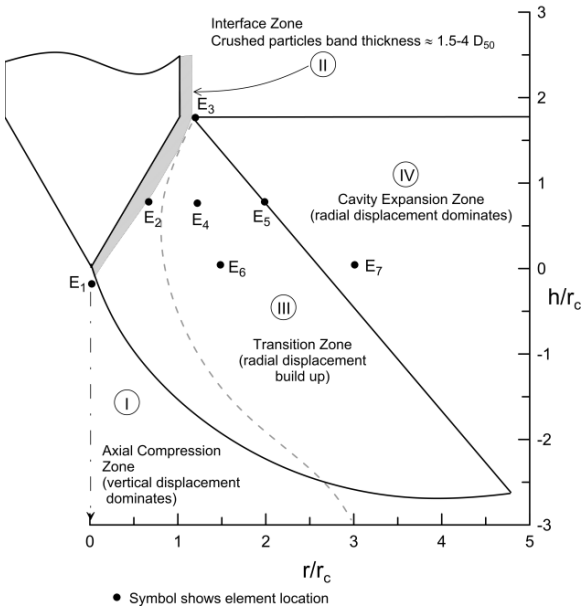

Figure 6.37 Soil elements considered for analysis of loading patterns near the cone tip.

Figure 6.38 shows the evolution of the vertical strain with change in the radial strain for seven soil elements E_1, E_2, E_3, E_4, E_5, E_6, & E_7 shown in Figure 6.38 for dense samples of the least crushable (CPTD50-T10-#ASTM20-30) and the most crushable (CPTD50-T8-#2Q-ROK) sands during cone penetration from $h^* = 20r_c$ to $h^* = 21r_c$. Element E_1

located immediately below the cone tip undergoes vertical compression and radial extension. The soil element experiences slightly more vertical compression (E_{zz} = 35.4%) and less radial extension (E_{rr} = -24.1%) in the most crushable sand than the least crushable sand (E_{zz} = 33.2% and E_{rr} = -25.5%). This shows the importance of crushing in the penetration process. Element E_2 shows an opposite loading pattern, undergoing less vertical compression (5%) and extensive radial extension (25%) in the most crushable sand as compared to increased vertical compression of 15.8% and less radial extension of 18.9% in the least crushable sand.

Elements E_4, E_5 and E_6 located in the transition zone display the same pattern of response, having dominant radial compression and a decreasing trend of vertical extension with increase of radial position r from the cone tip. This shows that the transition is taking place towards pure radial loading as experienced in the cavity expansion process. Element E_4 undergoes radial compression of 6.4% and vertical extension of 1.3% in the least crushable sand, and radial compression of 6.3% and vertical extension of 6.4% in the most crushable sand. Element E_5 experiences radial compression of 2.9% and vertical extension of 1.7% in the least crushable sand. Similarly, radial compression of 2.3% and vertical extension of 1.1% is observed in the most crushable sand. Element E_6 experiences dominant radial compression of 7.3% and vertical extension of 2.4% in the most crushable sand, as compared to the least crushable sand, for which element E_6 undergoes slightly less radial compression of 5.3% and increased vertical extension of 3.6%.

Element E_3, located next to the cone shoulder, undergoes radial compression of about 4% and vertical extension of about 3.5% in both the most crushable and the least crushable sands. The fact that the strains are comparable for both sands is due to the mean normal stress being much less for compression in the horizontal direction (the radial stress being much less than the vertical stress imposed on elements E_1 and E_2). Consequently, crushing is no longer observed to any significant extent once the cone shoulder levels with the element.

Element E_7 experiences slightly more radial compression of 1.9% in the least crushable sand as compared to 1.5% in most crushable sand, indicating the effect of

crushing on the extent of radial loading. For both sands, element E_7 undergoes vertical extension of 0.6%.

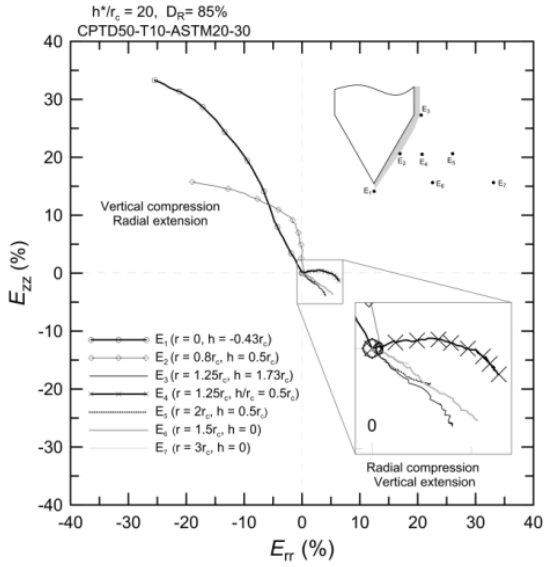

(a)

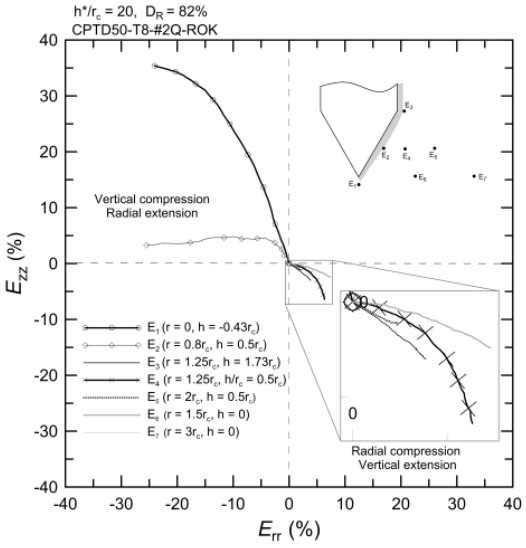

(b)

Figure 6.38 Evolution of normal strains during incremental penetration: (a) ASTM20-30 and (b) #2Q-ROK.

Taking the vertical direction as reference, soil elements undergo loading generally resembling triaxial compression below the cone tip (elements E_1 and E_2) and triaxial extension away from the cone tip (elements E_3, E_4, E_5, E_6, & E_7). The same general patterns are observed for both types of sands, with differences in magnitude due to difference in sand properties, crushability being a major factor.

Figure 6.39 shows the general modes of loading patterns in soil elements, as inferred from the strain paths of the soil elements shown in Figure 6-39 during incremental cone penetration process.

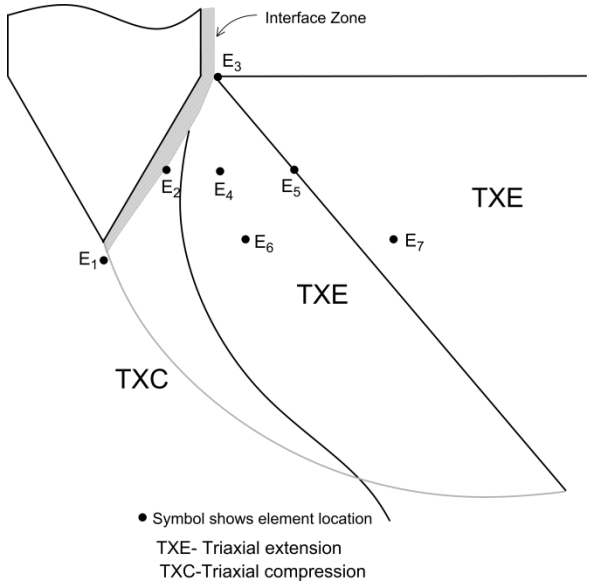

Figure 6.39 General modes of loading in soil elements during incremental cone penetration.

6.4.6 Strain Paths below Cone Tip

Assuming away any dependence on confining stress, the strain path (the sequence of strains experienced by an element as the cone passes by it) is the same as the sequence of strains experienced by elements at fixed r as h varies. Figure 6.40 and Figure 6.41 show paths for E_{rr}, E_{zz} , $E_{\theta\theta}$ and E_{rz} below the cone tip for $h^*/r_c \approx 20$ for tests performed

on sand samples prepared with two different initial densities (CPTL50-T4-#2Q-ROK & CPTD50-T8-#2Q-ROK). These strain paths are given for soil elements located at fixed $r/r_c \approx 1.25$, 1.5, 2, 3, 5, and 8 and with increasing depth h below the cone tip. The strain paths show that the soil elements are less deformed during the cone penetration process with increasing r and h below the cone tip. Sharp shearing of the soil can be seen around the cone at $r/r_c < 2$ (Figure 6.40, Figure 6.41 (a), (b) & (c)) and peak shear strain occurs when the soil has passed by the tip and element align with shoulder. The amount of shearing ($E_{rz} \approx$ 50%, 34% & 12% at $r/r_c \approx 1.25$, 1.5 & 2 respectively) in the loose test (CPTL50-T4-#Q2-ROK) is greater ($E_{rz} \approx$ 30%, 18% & 8% at same radial offset of $r/r_c \approx 1.25$, 1.5 & 2) than in the dense test (CPTD50-T8-#2Q-ROK). It can also be seen in Figure 6.40 and Figure 6.41 that the shear strain is greater than the normal strains for elements at less than $2r_c$ from the cone penetration axis and vertical distance of $2r_c$ below the cone tip. Also, it can be seen that vertical and radial strains, in general, show opposite trends, such that when the vertical strain is negative (extension), the radial strain is positive (compression) (TXE condition) or vice versa (TXC condition). At larger r/r_c ($\approx$ 2, 3, 5, and 8), the rate of decay of the radial compressive strain is greater for the loose sand ($E_{rr} \approx$ 5%, 3.8%, 1.5% and 0.5%) than for the dense sand ($E_{rr} \approx$ 6%, 4%, 2%, and 1%). At $r/r_c \approx 1.25$, greater tensile radial strains ($E_{rr} \approx$ -34% versus $E_{rr} \approx$ -5%) are present in the loose test (Figure 6.40 (a)) than in the dense test (Figure 6.41 (a)). The presence of tensile radial strains in both tests even after the soil is displaced by the cone shoulder is possibly due to the intense vertical shearing along the cone shaft.

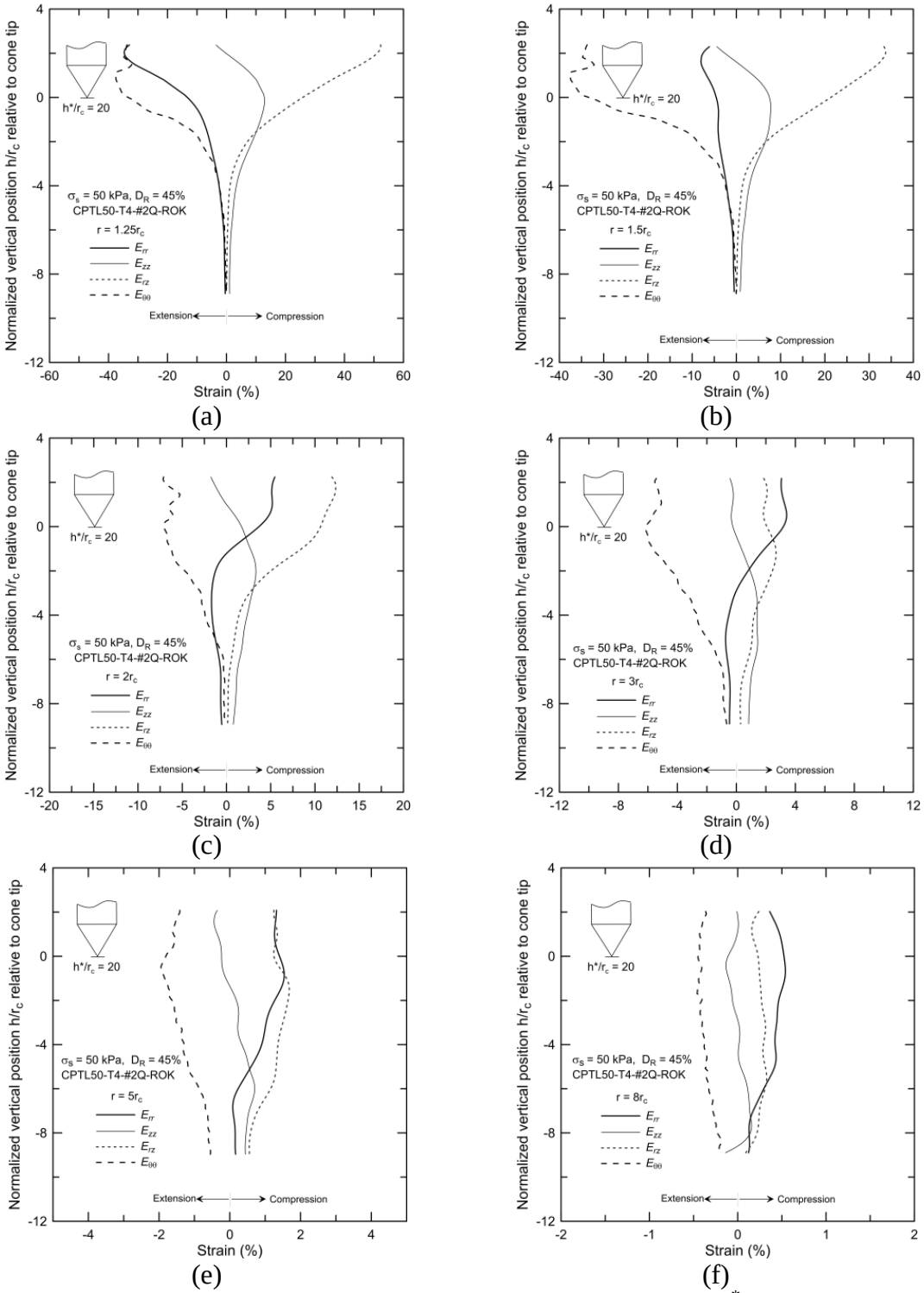

Figure 6.40 Strain paths below the cone tip when the cone is at $h^*/r_c = 20$ for test CPTL50-T4-#2Q-ROK: (a) $r = 1.25r_c$, (b) $r = 1.5r_c$, (c) $r = 2r_c$, (d) $r = 3r_c$, (e) $r = 5r_c$ and (f) $r = 8r_c$.

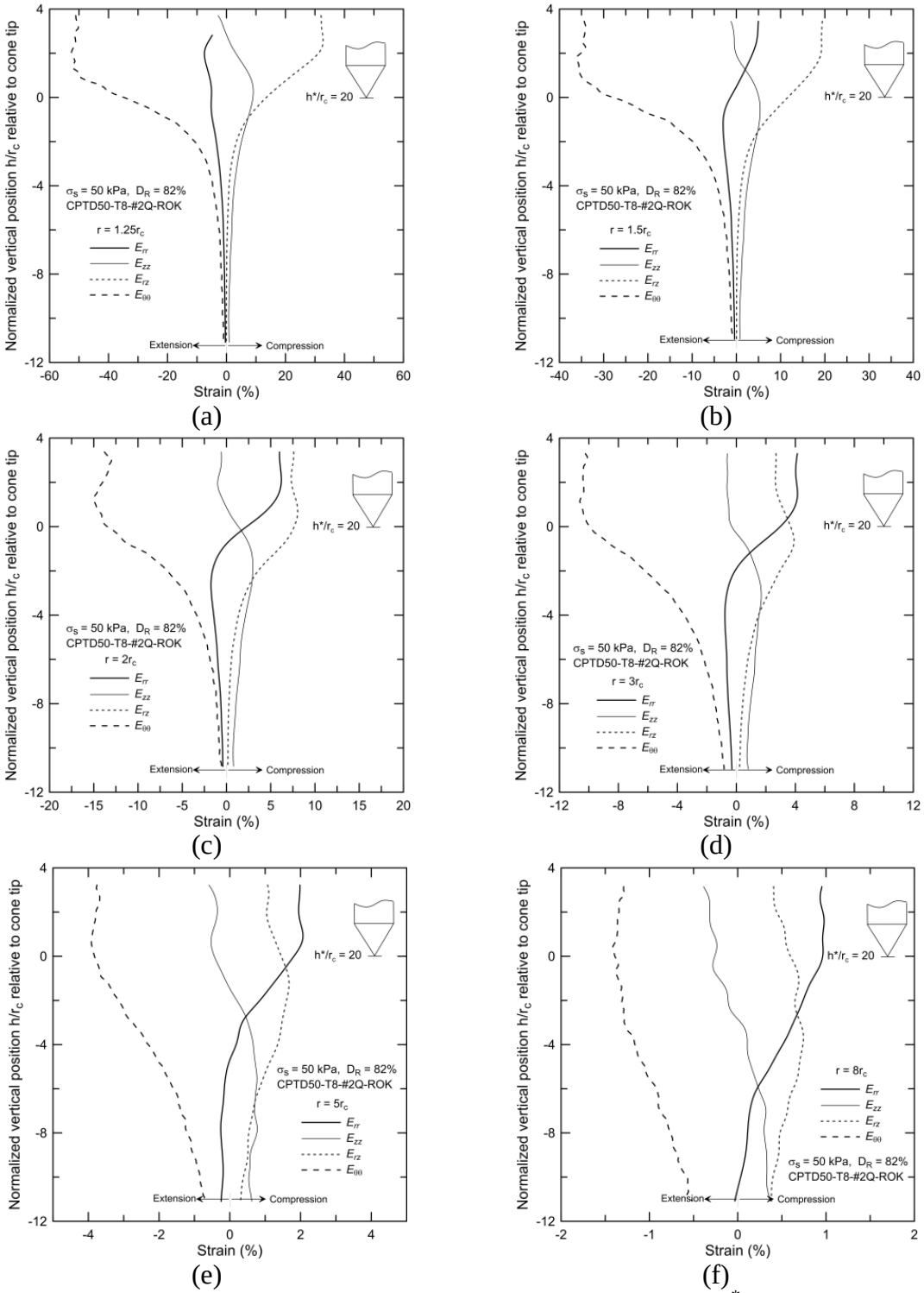

Figure 6.41 Strain paths below the cone tip when the cone is at $h^*/r_c = 20$ for test CPTD50-T8-#2Q-ROK: (a) $r = 1.25r_c$, (b) $r = 1.5r_c$, (c) $r = 2r_c$, (d) $r = 3r_c$, (e) $r = 5r_c$ and (f) $r = 8r_c$.

The maximum compressive vertical strain E_{zz} takes place below the cone tip and decays with increasing r. The rate of decay of compressive vertical strain at r/r_c (≈ 1.25, 1.5, and 2) is greater in dense (E_{zz} ≈ 10%, 5%, and 2.7%) than in loose sand (E_{zz} ≈ 13%, 8%, and 3%). The circumferential strain $E_{\theta\theta}$ remains tensile for both tests and for all r/r_c indicating that the soil elements move radially away from the cone penetration axis. Greater radial deformation takes place at r/r_c (≈ 1.25, 1.5, 2, 3, 5 and 8) in the dense sand ($E_{\theta\theta}$ ≈ 52%, 36%, 15%, 10.5%, 4%, and 1.4%) than in the loose sand ($E_{\theta\theta}$ ≈ 38%, 36%, 7%, 6%, 4%, 2%, and 0.5%).

6.4.7 Volumetric Strain Paths

6.4.7.1 Volume Change during Incremental Cone Penetration

Figure 6.42 compares the incremental volumetric strain for soil elements *O*, *B*, *C*, *D* and *E* located at normalized radial offsets of r/r_c = 0, 1.25,1.5, 2, & 3 from the cone penetration axis (see Figure 6.11) during an incremental cone penetration of $1r_c$ from h^*/r_c = 6 to h^*/r_c = 7 and again from h^*/r_c = 19 to h^*/r_c = 20 for tests CPTD50-T8-#2Q-ROK and CPTD50-T10-ASTM20-30. It should be noted that there was no visible particle crushing while the cone was advancing to depth h^*/r_c = 6. On the other hand, particle crushing was visible when the cone reached h^*/r_c = 20, with the amount of particle crushing being remarkably less in the least crushable sand (ASTM20-30) than in the most crushable sand (2Q-ROK).

Figure 6.42(a) and (b) show that element *O* located immediately below the cone tip at $z = 6r_c$ undergoes contraction of about E_{vol} ≈ 3.7 % in the least crushable sand while, for the most crushable sand, E_{vol} ≈ 20% prior to particle crushing (h^*/r_c = 6). After particle crushing (h^*/r_c = 20), element *O* located immediately below the cone tip at $z = 20r_c$ undergoes contraction of 16.8% and then attains stability at 16.2%, after a bit dilation in the least crushable sand versus 21.3% contraction in the most crushable sand. Obviously, the least crushable sand (ASTM20-30) shows the lesser contractive behavior at the shallow penetration and before particle crushing, whereas for the deep penetration, it undergoes more contraction due to excessive particle crushing. While the most

crushable sand shows almost same contractive behavior ($E_{vol} \approx$ 20% and 21.7 %) at shallow and deep penetration, possibly onset of particle crushing at shallow depth that may not visible by naked eye and excessive particle crushing at deep penetration.

Elements *B*, *C*, *D* and *E* undergo dilation in both sands for the shallow penetration; however the dilation of the most crushable sand is slightly greater than that of the least crushable sand. This response can be attributed to the difference of the particle shape in these sands, where the angular particles of the most crushable sand results in slight more dilation at relatively low stress level for the initial phases of the cone penetration. It is seen that dilation of both sands decays with increasing *r* from the cone penetration axis.

Figure 6.42(c) and (d) shows that the soil element *B* in both sands show contractive response during the deep incremental cone penetration from $h^*/r_c = 19$ to $h^*/r_c = 20$. A remarkable increase in contractive response from 3.7% to 16.8% is observed for the element *O* in least crushable sand (ASTM20-30) after particle crushing. As noted earlier, particle crushing has emerged at this depth, which is observed from close-up view of the tests images. A slightly lesser dilative response for other soil elements *B, C, D* and *E* is seen in both sands after the particle crushing than prior to particle crushing (Figure 6.42). The dilation of the soil element decays with increasing *r* from the cone penetration axis. The rate of decay of dilation for elements *B, C, D* and *E* located at r/r_c = 1.25, 1.5, 2, and 3 is more in most crushable sand ($E_{vol} \approx$ -7.7%, -4%, -2.2%, and -0.2%) as compared to least crushable sand ($E_{vol} \approx$ -9.4%, -8.2%, -4.2%, and -0.4%) at the deep penetration. It is also clear from responses of element *O* that the most crushable sand undergo more contraction as compared to the least crushable sand, which can be attributed to the excessive particle crushing in the most crushable sand at the deep penetration.

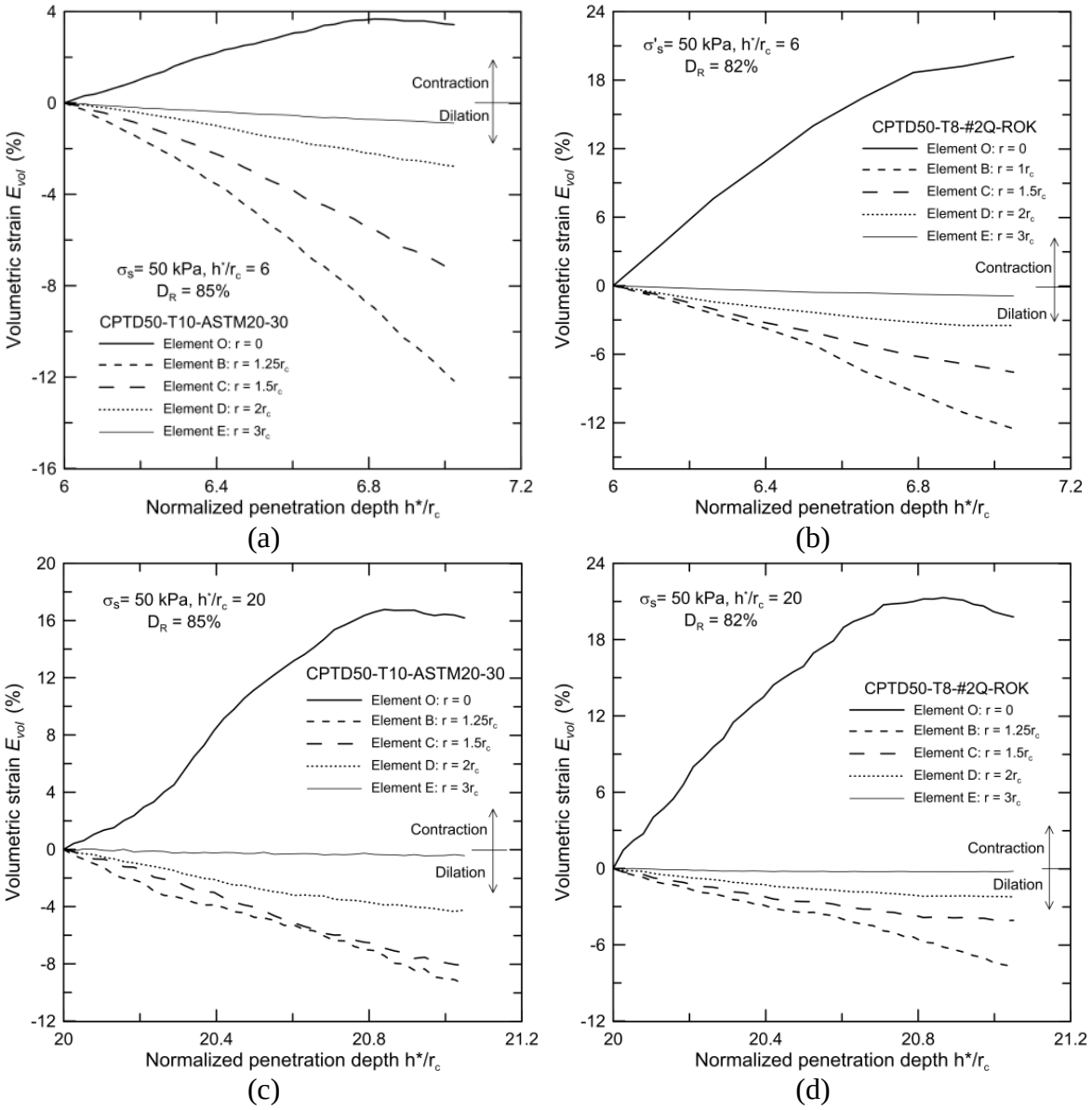

Figure 6.42 Evolution of volumetric strain for tests CPTD50-T8-#2Q-ROK and CPTD50-T10-ASTM20-30 prior to particle crushing ($h^*/r_c = 6$) and after particle crushing ($h^*/r_c = 20$): (a) ASTM 20-30 at $h^*/r_c = 6$,(b) #2Q-ROK at $h^*/r_c = 6$, (c) ASTM 20-30 at $h^*/r_c = 20$, and (d) #2Q-ROK at $h^*/r_c = 20$.

6.4.7.2 Evolution of volumetric Strain during Continuous Cone Penetration

Figure 6.43 shows the evolution of volumetric strain for soil elements *B*, *C*, *D*, *E*, *F*, *G* and *H* located at r/r_c = 1.5, 2, 3, 4, 5 and 8 at z = 18 and18.5 r_c for tests CPTL50-T4-#2Q-ROK, CPTD50-T8-#2Q-ROK and CPTD50-T11-Mini-#2Q-ROK for cone penetrations from $h^* = 0$ to $h^* = 23r_c$ and $25r_c$ (for miniature cone $h^* = 0$ to $h^* = 45r_c$).

As shown in Figure 6.43(a), (b) and (c), elements *B* near the cone penetration path (r/r_c = 1.25) shows strong dilative response for all tests. However, for the Elements *C*, *D*, *E* and *F* in the loose sand (CPTL50-T4-#2Q-ROK), a sharp reduction in dilative response is observed at greater r/r_c ($E_{vol} \approx$ -14%, -6%, -3%, and -1.5%) as compared to dense sand (CPTD50-T8-#2Q-ROK), in that a less decay in dilation is observed with increasing r/r_c ($E_{vol} \approx$ -27%, -15%, -7%, and -3.8%). At greater r/r_c of 5 and 8, a slight contraction ($E_{vol} \approx$ 0.25%, and 0.1%) is observed for Elements *G* and *H* for the loose sand, while in dense sand these elements shows dilative response ($E_{vol} \approx$ -2. 5%, and -0.8%). This clearly indicates the presence of reduced size of dilation zone of ($r/r_c \approx 5$) for the loose sand (CPTL50-T4-#2Q-ROK), as compared to dense sand (CPTD50-T8-#2Q-ROK), where all elements show dilative response ($r = 8r_c$) that is more pronounced near the cone penetration path.

In case of miniature cone penetration test in dense sand sample (CPTD50-T11-Mini-#2Q-ROK), all elements shows dilation similar to large cone test, however the amount of dilation is slightly less for elements (*D*, *E* and *F*) located further away of $r = 1.5r_c$.

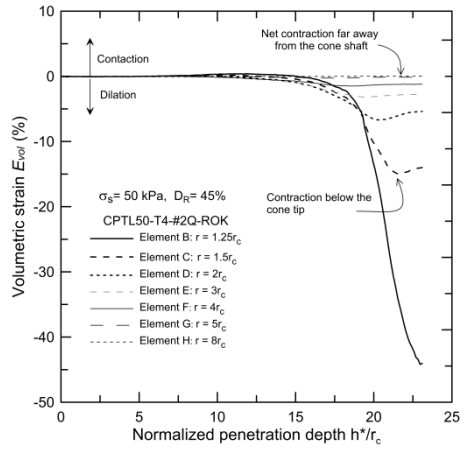

(a)

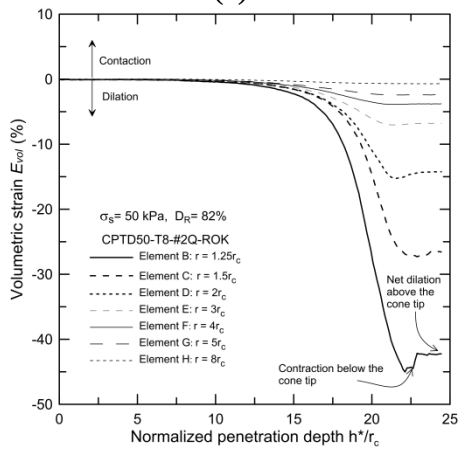

(b)

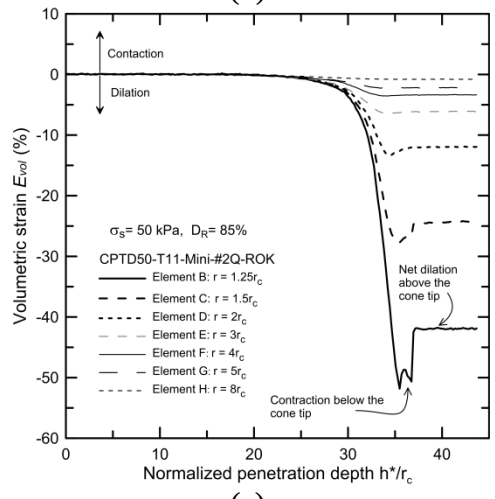

(c)

Figure 6.43 Evolution of volumetric strain paths of soil elements at r/r_c = 1.25, 1.5, 2, 3, 4, 5, and 8 during continuous cone penetration for tests: (a) CPTL50-T4-#2Q-ROK from $h^* = 0r_c$ to $h^* = 23r_c$, (b) CPTD50-T8-#2Q-ROK from $h^* = 0r_c$ to $h^* = 25r_c$, and (c) from $h^* = 0r_c$ to $h^* = 45r_c$ for CPTD50-T11-Mini-#2Q-ROK.

It should be noted that the actual magnitude of volumetric strain for elements in close proximity of the cone (r/r_c = 1.25 and 1.5) can be less than the calculated quantities (E_{vol} ≈ 40-50% for element *B* and E_{vol} ≈ 25-30% for element *C*) from the DIC analysis, since these elements must have undergone the critical state due to high shear strain mobilized (see Figure 6.34 (b), Figure 6.35(b)) and volume change is not expected after reaching the critical state.

6.4.7.3 Compression Zone Immediately below Cone Tip

Figure 6.44 shows the volumetric strain paths of elements *O* located at r = 0 and at depth z = $20r_c$, for tests CPTL50-T4-#2Q-ROK (during cone penetration from h^*= $0r_c$ to h^* = $23r_c$), CPTD50-T8-#2Q-ROK (during cone penetration from h^*= $0r_c$ to h^* = $25r_c$) and CPTD50-T11-Mini-#2Q-ROK (during cone penetration from h^*= $0r_c$ to h^* = $45r_c$). As shown in Figure 6.44, Element *O* undergoes contractions of ~12%, 6% and 4% in the tests on loose (CPTL50-T4-#2Q-ROK) and dense (CPTD50-T8-#2Q-ROK) sands with the regular-size cone and in the dense test with the miniature cone (CPTD50-T11-Mini-#2Q-ROK). In the loose sand sample, Element *O* contracts from the very beginning of cone penetration, but, for the dense sand samples, Element *O* initially dilates (E_{vol}~ -1.6) before the cone tip approaches it. Once the cone tip reaches Element *O*, it undergoes contraction also in dense sand. The amount of contraction for the larger cone (CPTD50-T8-#2Q-ROK) is slightly more (E_{vol} ≈ 6%) than for the miniature cone test (CPTD50-T11-Mini-#2Q-ROK) (E_{vol} ≈ 4%), possibly due to size effects. Due to intense particle crushing and disturbance of the soil element by the cone tip, further evaluation of these strain paths is not possible through image analysis in any of the three tests.

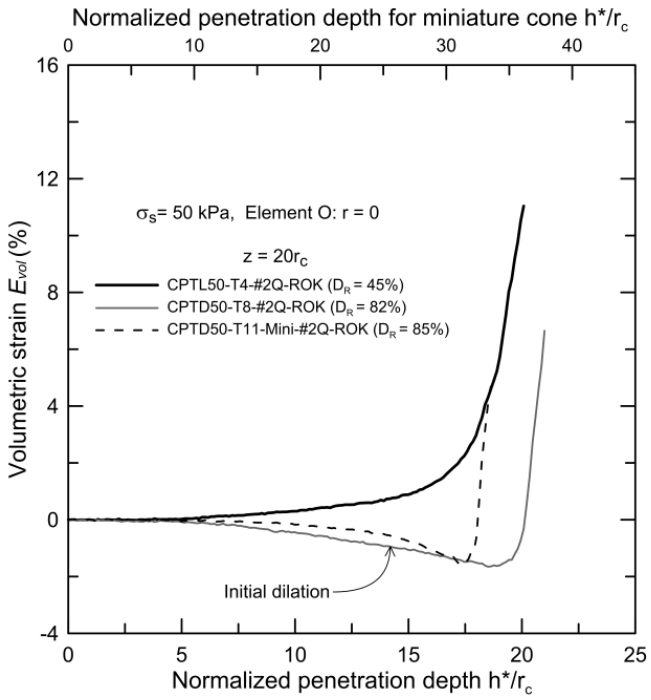

Figure 6.44 Volumetric strain path of soil Element *O* located at r =0 for cone penetration from h^* = 0r_c to h^* = 23-25r_c for tests CPTL50-T4-#2Q-ROK, CPTD50-T8-#2Q-ROK and CPTD50-T11-Mini-#2Q-ROK for the cone penetration from h^* = 0r_c to h^* = 45r_c.

6.4.8 Post-Installation Strain Field

Figure 6.45, and Figure 6.46 show spatial distribution of radial (E_{rr}), vertical (E_{zz}), shear (E_{rz}) and volumetric (E_{vol}) strains for tests CPTL50-T4-#2Q-ROK, and CPTD50-T8-#2Q-ROK at the completion of the cone penetration from h^* = 0r_c to h^*= 18r_c-20r_c. The cumulative strains are reported here at the end of cone penetration to the specified depth.

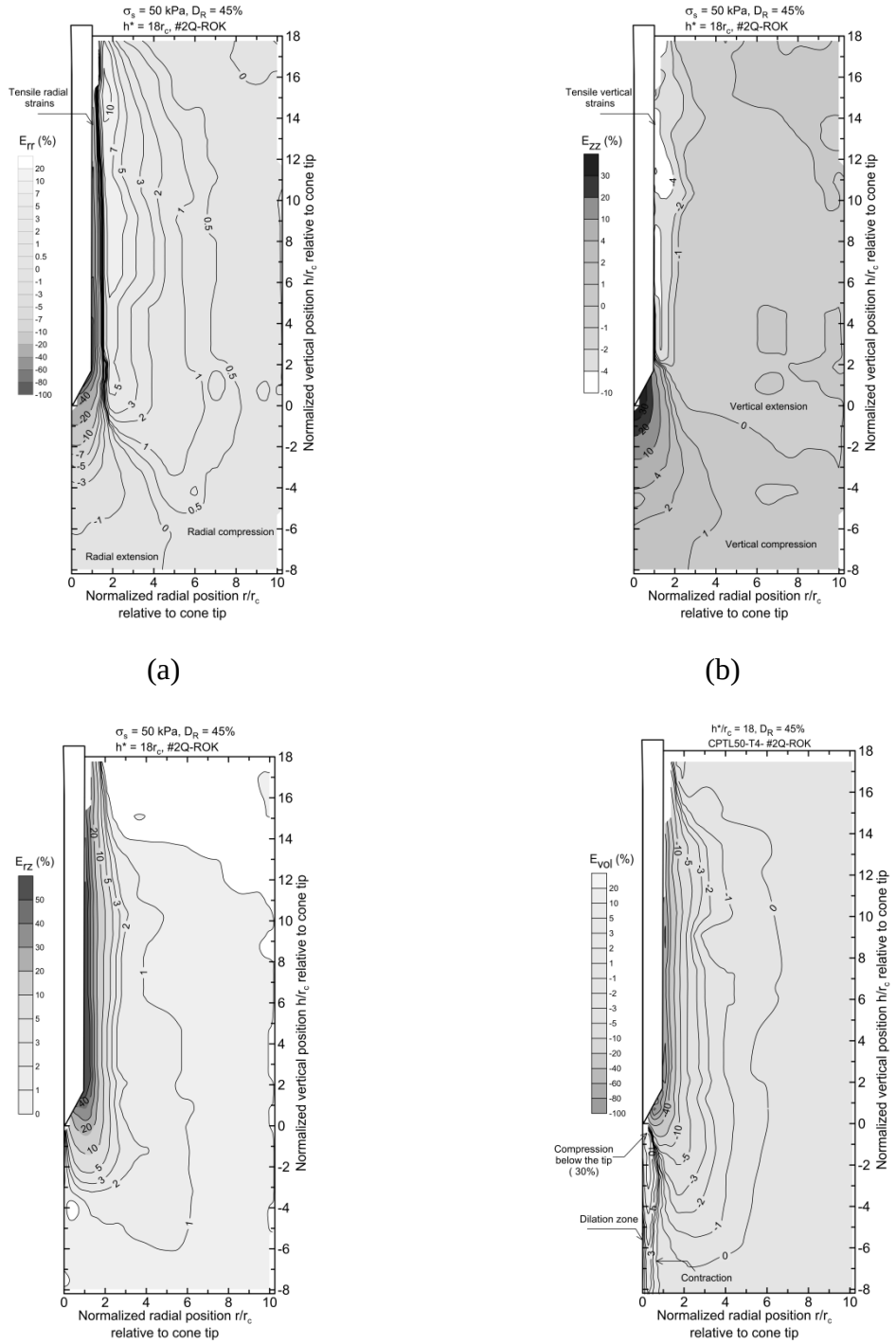

Figure 6.45 Post-installation, cumulative strain field after penetration from $h^*/r_c = 0$ to $h^*/r_c = 18$ for CPTL50-T4-#2Q-ROK test: (a) radial strain E_{rr}, (b) vertical strain E_{zz} , (c) shear strain E_{rz}, and (d) volumetric strain E_{vol}.

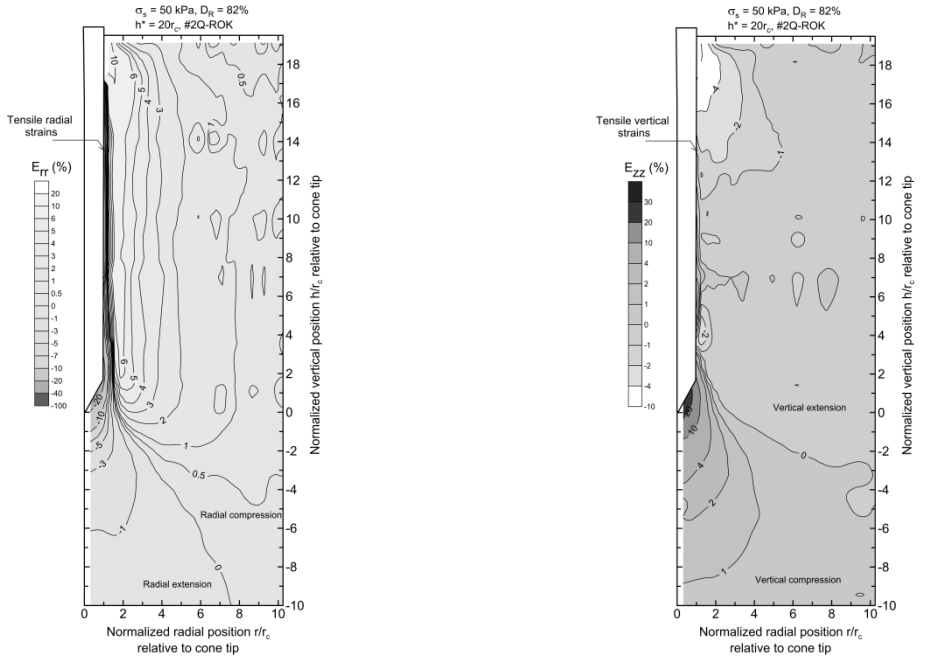

Figure 6.46 Post-installation, cumulative strain field after penetration from $h^*/r_c = 0$ to $h^*/r_c = 20$ for CPTD50-T8-#2Q-ROK test: (a) radial strain E_{rr}, (b) vertical strain E_{zz} , (c) shear strain E_{rz}, and (d) volumetric strain E_{vol}.

As shown in Figure 6.45 and 6.46 (parts (a) and (b)), for all tests, the vertical and radial extent of the vertical strain below the cone tip is greater than for the radial strain. On the other hand, the radial extent of radial strain is greater than that of the vertical strain around the cone shaft. Comparing the contour plots for all tests show that, as the soil becomes denser, the extent of radial strain increases in the radial direction. In other words, larger amount of soil volume undergoes radial strain in denser soil.

As shown in Figures 6.45, and 6.46, high tensile radial strains (E_{rr} < -30%) are mobilized immediately below the cone tip and along the cone shaft, and tensile vertical strains (E_{zz} >-2%) are mobilized away from the cone shaft. The compressive vertical strains are accumulated within a narrow band along the cone shaft (r/r_c = 0.5) during the cone penetration process. Very large compressive vertical strains (E_{zz} ≈ 40%) are observed below the tip.

As shown in Figures 6.45, and 6.46 (part c), the shear strain spatial distribution reveals that excessive shear strains (E_{rz} ≈40%) mobilize along the cone shaft and immediately below the cone tip.

As shown in Figures 6.45, and 6.46 (part d), the volumetric strain spatial distribution shows that different zones of dilation and compression below the cone tip and along the cone shaft exist for the loose and dense sands. The compression zone (as indicated in the figures) is observed immediately below the cone tip for all tests and it is wider and deeper in the loose sand than the dense sand. Significant dilation takes place away from the cone tip and along the cone shaft. The dilation zone along the cone shaft extends up to $r = 5r_c$ for the loose sand (CPTL50-T4-#2Q-ROK) and up to r ~ 8-10r_c in dense sand (CPTMD50-T8-#2Q-ROK). Below the tip, dilation is observed in denser sand. Pronounced contraction is observed for loose sand immediately below the tip.

6.5 Rigid-Body Rotation Paths

6.5.1 Rotation Paths during Incremental Cone Penetration

Figure 6.47 shows the evolution of rigid body rotation paths for soil elements *A*, *B*, *C*, *D*, and *E* initially located at the normalized vertical position of z/rc = 20 (see Figure 6.11 for radial position of the elements) during an incremental cone penetration from h^*/r_c = 20 to h^*/r_c = 21 for tests of least crushable sand (CPTD50-T10-ASTM20-30) and the most crushable sand (CPTD50-T8-#2Q-ROK). The soil elements located in close proximity to the cone undergo more extensive rigid-body rotations than elements located further away from the penetration axis.

Soil element *A* (Figure 6.47 (a)), located at r = 0.5r_c, experiences increasing rigid body rotation *R* with increasing penetration. The least crushable sand (ASTM20-30) ultimately experiences less rigid body rotation ($R \approx 25$ degrees) than the most crushable sand (#2Q-ROK) ($R \approx 44$ degrees). This trend is similar to that for vertical strains (see Figure 6.33(b)), which suggests that large vertical deformations are key in the development of extensive rotations.

Similarly, for elements *B*, *C* and *D* (Figure 6.47 (b), (c), and (d)), located at increasing r/r_c, the rigid body rotation *R* increases with crushability ($R \approx 16, 8.5, 2$ degrees versus $R \approx 14, 7.2, 1$ degrees).

Soil Element *E* (Figure 6.47 (e)), located at r = 3.0r_c, experiences almost no rigid-body rotation for an incremental cone penetration of $1r_c$. This indicates that the soil elements located within the transition zone (Zone III in Figure 6.9), in close proximity to the cone, undergo substantial rigid-body rotation, but elements located outside that zone undergo little to negligible rotation.

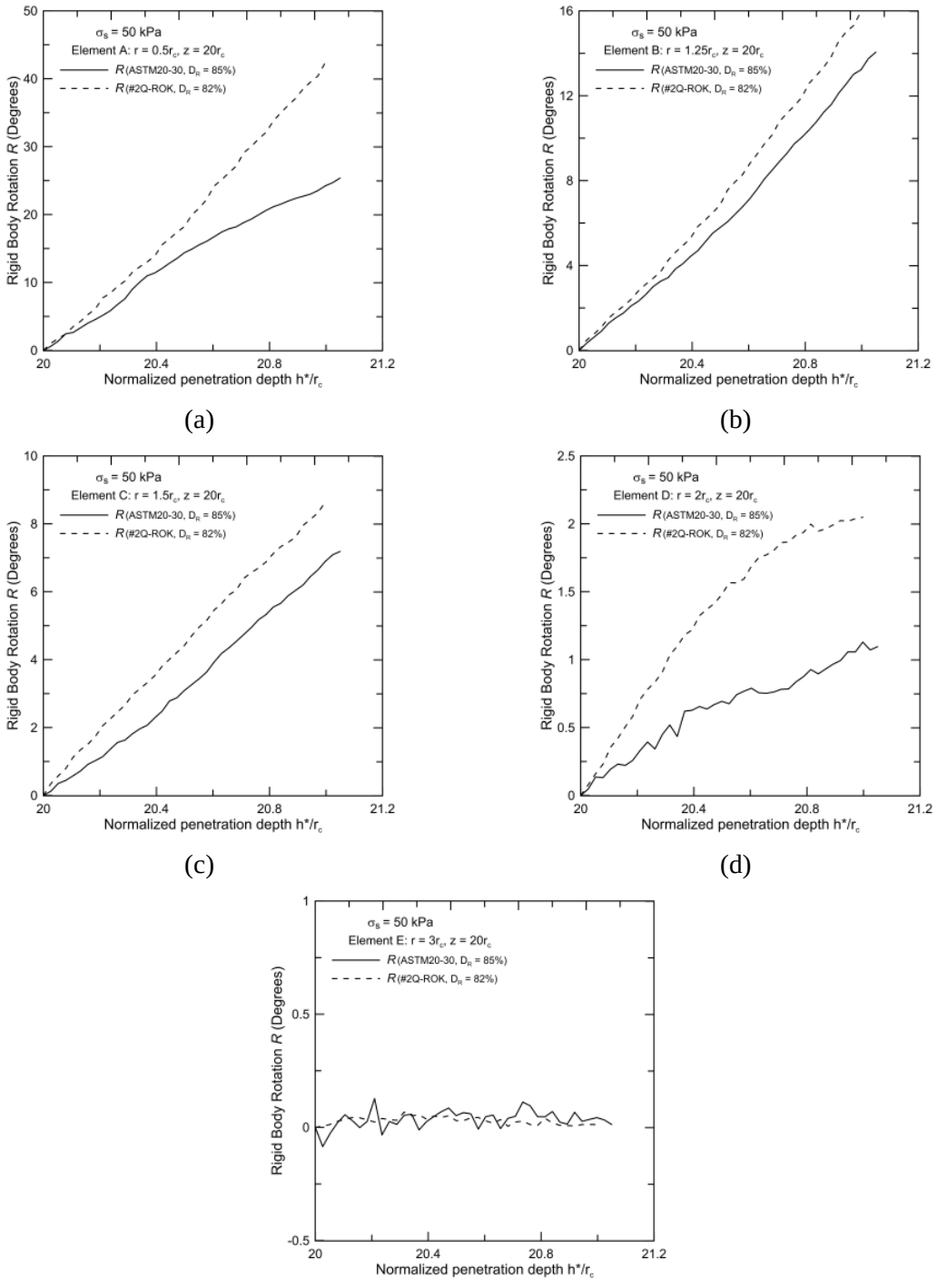

Figure 6.47 Evolution of rigid body rotation paths R for $1r_c$ penetration in the least crushable (CPTD50-T10-ASTM20-30) and the most crushable (CPTD50-T8-#2Q-ROK) silica sands: (a) element A at r = $0.5r_c$, (b) element B at r = $1r_c$, (c) element C at r = $1.5r_c$, (d) element D at r = $2r_c$ and (e) element E at r = $3r_c$.

Figure 6.48 shows the rigid body rotation patterns around the cone during incremental cone penetration from h^*/r_c = 20 to h^*/r_c = 21 for tests in the least crushable sand (CPTD50-T10-ASTM20-30) and most crushable sand (CPTD50-T8-#2Q-ROK). Counter-clockwise rotations are shown as positive, whereas clockwise rotations are negative. These patterns indicate that the rigid body rotation is taking place only within a transition zone similar to that identified by Salgado & Prezzi (2007). Extensive rigid body rotations are experienced by the soil elements in the most crushable sand (#2Q-ROK) (Figure 6.48(b)), and comparatively less rotation is present in the least crushable sand (ASTM20-30) (Figure 6.48(a)). The depth and radial extent of the zone undergoing rigid body rotation is about $3r_c$ in both sands.

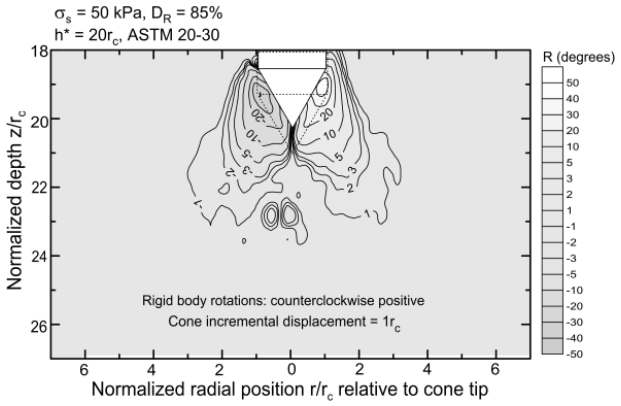

(a)

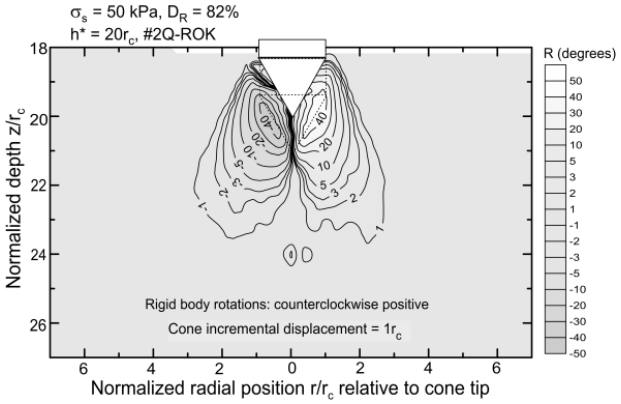

(b)

Figure 6.48 Rigid body rotation patterns for $1r_c$ penetration from h^*/r_c = 20 to h^*/r_c = 21 in the least crushable and the most crushable silica sands tests: (a) ASTM20-30 and, (b) #2Q-ROK.

6.5.2 Rotation Paths during Continuous Cone Penetration

Figure 6.49 shows the rigid body rotation paths of soil elements *B, C, D,* and *E* for cone penetration from $h^* = 0\ r_c$ to $h^* = 23$ and $25r_c$, respectively, for tests CPTL50-T4-#2Q-ROK and CPTD50-T8-#2Q-ROK. Figure 6.49(c) shows the rigid body rotation paths of the same elements for the miniature cone penetration from $h^* = 0r_c$ to $h^* = 45r_c$ (where r_c is the radius of the miniature cone) for test CPTD50-T11-Mini-#2Q-ROK. Soil Elements *B* and *C,* located at $r/r_c = 1.25$ & 1.5, undergo greater rigid body rotation ($R \approx$ 38.5 and 24.5 degrees) in loose (CPTL50-T4-#2Q-ROK) than in dense sand (CPTD-T8-#2Q-ROK) ($R \approx 27.5$ and 17.8 degrees). Soil elements *D* and *E* located at greater r/r_c (2 & 3) undergo slightly greater rigid-body rotations in dense sand ($R \approx 7.8$ and 3 degrees) than in loose sand ($R \approx 7$and 2 degrees). This indicates that the rigid body rotations are correlated with the amount of vertical deformations.

Figure 6.49(c) shows that the soil Elements *B, C, D* and *E* undergo greater rigid body rotations for the miniature cone penetration test ($R \approx 35.6$, 22.9, 9.2, and 3 degrees) than for the large cone test ($R \approx 27.5$, 17.8, 7.8, and 3 degrees) all else being approximately the same. This is likely due to intensive shearing in miniature cone than the larger cone test (see Table 6.4) and the presence of some scale effects.

6.5.1 Post-Installation, Cumulative Rigid Body Rotations

Figure 6.50, shows spatial distribution of rigid body rotations (R) for tests CPTL50-T4-#2Q-ROK, and CPTD50-T8-#2Q-ROK at the completion of the cone penetration from $h^* = 0r_c$ to $h^* = 18r_c$ and $20r_c$ respectively. The cumulative rigid body rotations experienced by the soil elements are reported here at the end of cone penetration to the specified depth. As indicated by Figure 6.50, intense rotation takes place below the cone tip at closer $r/r_c \approx 1.5$ and decays rapidly with increasing r/r_c in loose test than the dense test. The degree of rigid body rotation in the loose test ($R \approx$ 30-40 degrees) is greater in closer proximity of cone ($r/r_c \approx 1.5$) than the dense test ($R \approx$ 20-30 degrees) and seems to be correlated with magnitude of shearing (see Figure 6.45(c) and Figure 6.46(c)). The extent

of rotation zone below the cone tip is slightly less in case of dense sand test than the loose sand test and along the cone shaft is almost similar in both loose and dense sand tests.

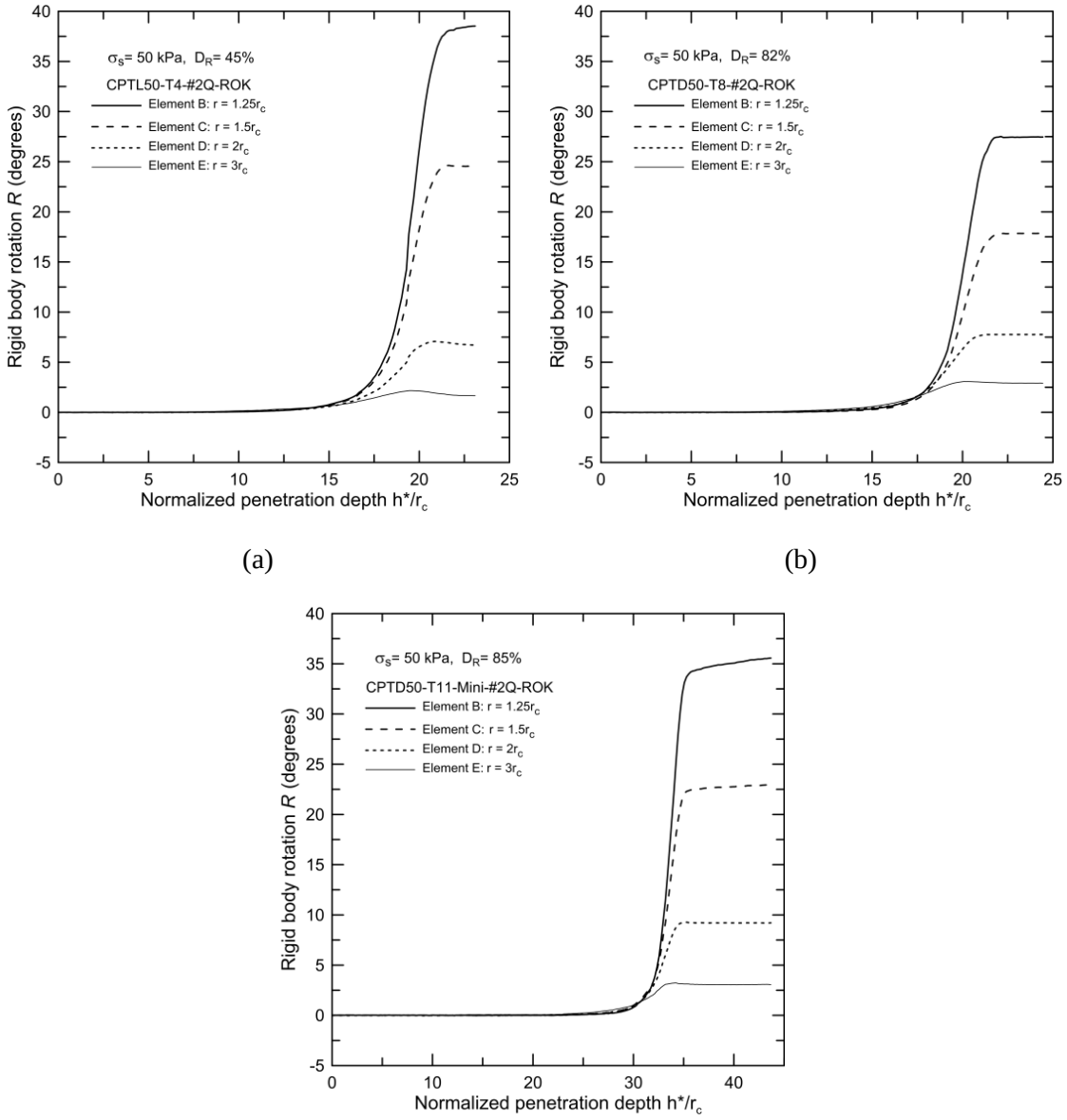

Figure 6.49 Rotation paths during continuous cone penetration from $h^* = 0r_c$ to $h^* = 23$-$25r_c$ for tests CPTL50-T4-#2Q-ROK, CPTD50-T8-#2Q-ROK and CPTD50-T11-Mini-#2Q2ROK during cone penetration from $h^* = 0r_c$ to $h^* = 45r_c$ for: (a) element *B* at $r = 1.25r_c$, (c) element *C* at $r = 1.5r_c$, (d) element *D* at $r = 2r_c$, and (e) element *E* at $r = 3r_c$.

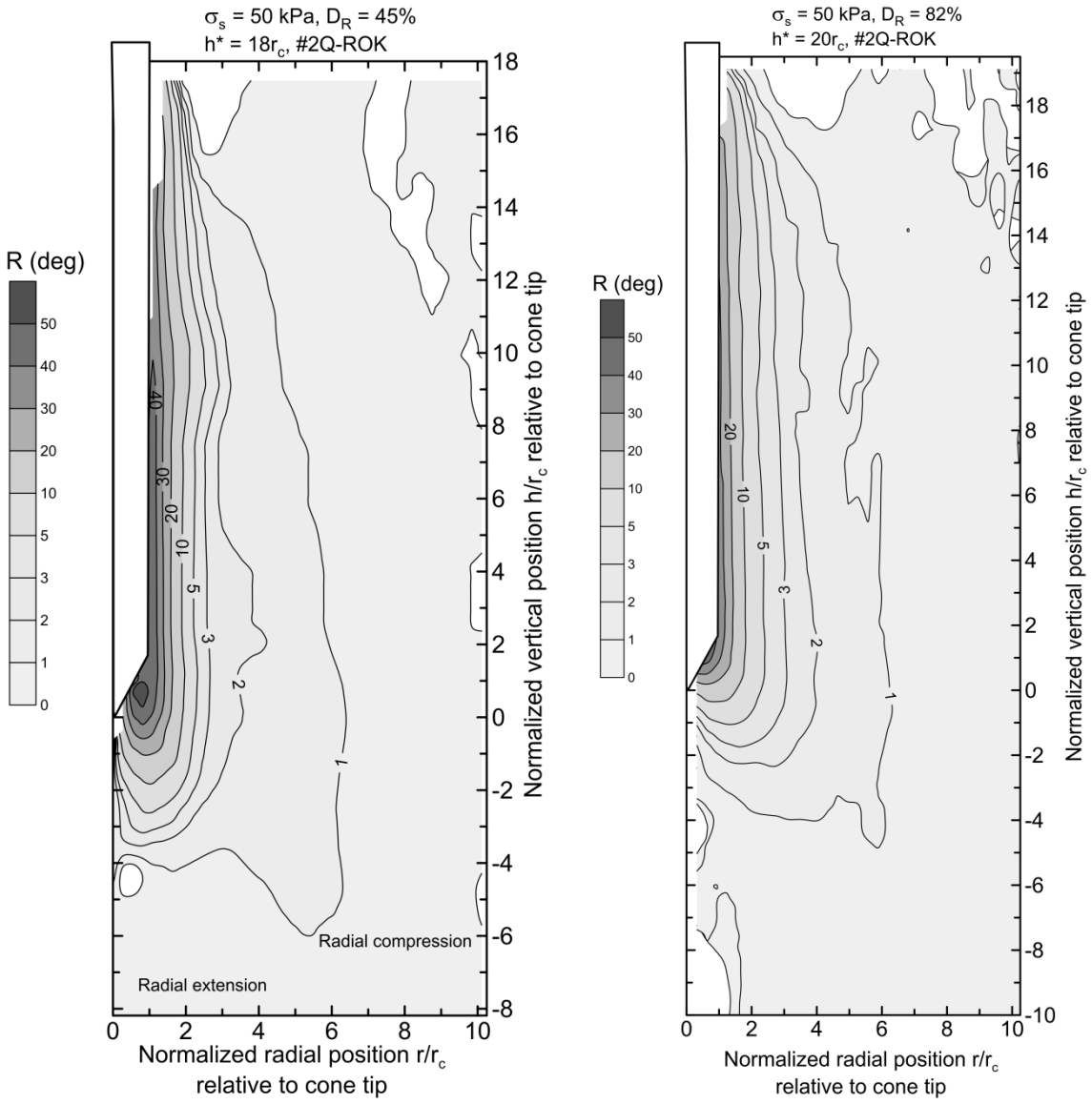

(a) (b)

Figure 6.50 Post installation rigid body rotation field after penetration from h^*/r_c = 0 to h^*/r_c = 18-20 for loose and dense sand tests: (a) CPTL50-T4-#2Q-ROK, and (b) CPTD50-T8-#2Q-ROK.

6.6 Summary

This chapter presented results of model cone penetration tests performed in the uniform sand samples. The characteristics of mobilized slip patterns and the effect of sand particle crushability on the observed failure mechanism were discussed in detail. Near- and far-field displacements were discussed in detail. The displacement and strain paths of soil elements located at various locations during cone penetration were discussed in detail. The displacement, strain and rigid-body rotation fields were presented. The influence of density, stress level, penetrometer size and particle crushability on the displacement and strain field were also evaluated.

CHAPTER 7. CONE PENETRATION TEST RESULTS IN LAYERED SAND

7.1 Introduction

This chapter presents and interprets the results of cone penetration tests in layered sand samples. The literature review in Chapter 2 concluded that few experimental studies have been performed for evaluation of cone penetration resistance in layered soil profiles. The objective of the tests presented here is to investigate the effect of layering on the cone penetration resistance and soil displacement field. The results are divided into two parts: first, the results from conventional sensors are presented; second, the results from Digital Image Correlation (DIC) analysis are discussed. The DIC analyses seek, in particular, to observe the soil layer interface as the cone approaches and then crosses it. Stress measurements from miniature pressure transducers, as discussed in section 5.3.2.2, were also made to investigate the generated stress distribution at the layer interface during the penetration process. Table 5.4 shows the details of each test, including the initial density and thickness of every layer as well as the type of penetrometer used. All tests were conducted with 50 kPa surcharge and #2Q-ROK silica sand. The effect of penetrometer size on the influence zone of the penetrometer was also investigated by using a miniature cone penetrometer in two-layered sand samples.

7.2 Sensing and Development Depths

The sensing depth (H_s) may be defined as the vertical distance from a given interface between layers of different density at which the interface starts affecting the tip resistance of an approaching cone. Similarly, the development depth (H_d) is the vertical distance from the layer interface, after the cone has crossed it, at which the tip resistance of the advancing penetrometer ceases to be affected by the presence of the overlying layer. Figure 7-1 illustrates these definitions schematically.

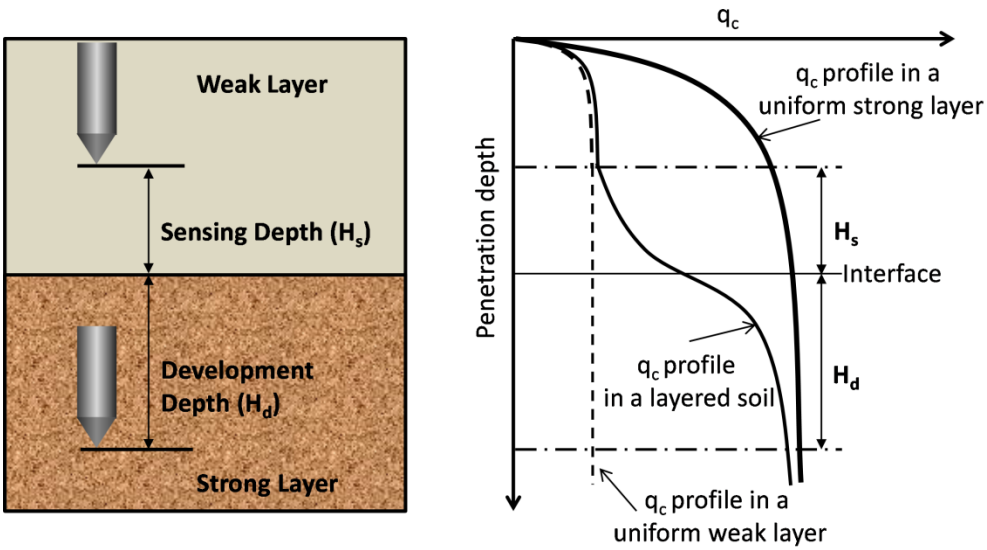

Figure 7.1 Sensing and development depths

The cone resistance depends on the relative density of the sand, the lateral effective stress and the intrinsic properties of the soil (R. Salgado, Mitchell, & Jamiolkowski, 1997; R. Salgado & Prezzi, 2007). An idealized slip pattern is shown in Figure 7-2 for uniform soil. As the cone approaches an interface, it is reasonable to expect that the mechanism will flatten if approaching denser sand and will stretch both vertically and radially if approaching looser sand. The theoretical mechanism reaches down to a depth of the order of two cone diameters below the tip of the cone, depending on the relative density and confining stress.

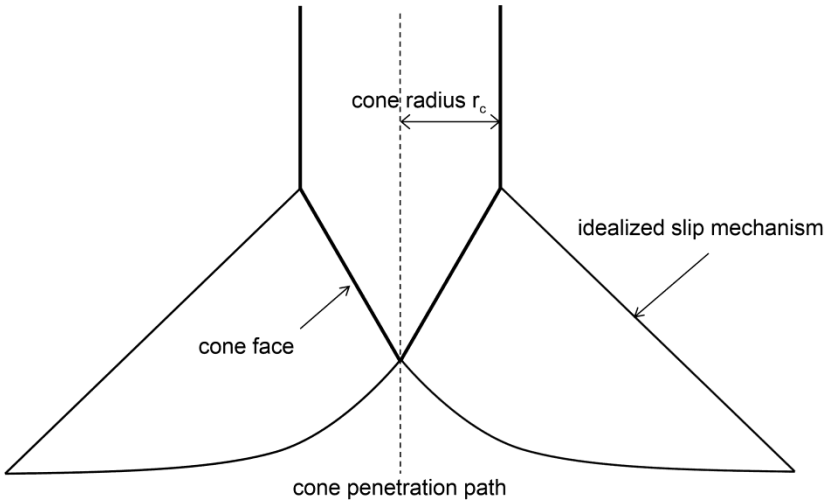

Figure 7.2 Idealized slip mechanism for computing cone resistance from cavity expansion limit pressure (R. Salgado & Prezzi, 2007).

Eight cone penetration tests were performed in layered soil profiles using cones with diameters of d_c equal to 31.75 mm and 19.05 mm. Pressure transducers were embedded in the samples at the layer interfaces to detect any rise in radial stress due to an approaching cone penetrometer. Table 7-1 shows the values of the sensing depth H_s inferred from the cone resistance profiles, the radial stress measurements and the soil displacements at the interface determined using DIC. The choice of radial stress as an indicator is related to the notion that the layer interface starts affecting the cone resistance more substantially when substantial stress rotation starts taking place in its neighborhood; this is also related to the dependence of q_c on lateral effective stress (R. Salgado et al., 1997; R. Salgado & Prezzi, 2007). The specifics of the experiments and the estimation of the sensing and development depths are discussed in subsequent sections.

Table 7.1. Summary of sensing and development depths from test results

Test	Sensing depth H_s (d_c)	Development depth H_d (d_c)
CPTLOD50-T1-#2Q-ROK	2.6 (5.3)	5.3 (5.9)
CPTLOD50-T2-#2Q-ROK	2.9 (5.1)	5.4 (6.5)
CPTDOL50-T3-#2Q-ROK	3.9 (4.3)	2.1 (5.1)
CPTDOL50-T4-#2Q-ROK	3.9 (4.1)	2.5 (5.2)
CPTMDOD50-T5-#2Q-ROK	4.4	5.9
CPTDOMD50-T6-#2Q-ROK	3.0	5.3
CPTLOMD50-T7-#2Q-ROK	2.7	6.0
CPTMDOL50-T8-#2Q-ROK	2.7	1.3
CPTLOD50-T9-mini-#2Q-ROK	(5.1)	(5.0)
CPTDOL50-T10-mini-#2Q-ROK	(4.8)	(6.1)

Note: Values in parentheses were measured based on the total cone resistance Q_t.

7.2.1 Sensing and Development Depths from Cone Resistance

Figure 7.3 shows the cone resistance profiles for a loose sand (D_R = 45%) sample (CPTL50-T4-#2Q-ROK), a dense sand (D_R = 85%) sample (CPTD50-T7-#2Q-ROK) and loose-over-dense sand samples (D_R = 45%/85% and D_R = 43%/85%) samples (CPTLOD50-T1-#2Q-ROK and CPTLOD50-T2-#2Q-ROK) for tests performed with a 50 kPa surcharge. The depth h^* of the penetrometer from the top of the sample may be viewed as a proxy for time, and snapshots of the soil displacement field will later be labeled by the value of h^* that they correspond to.

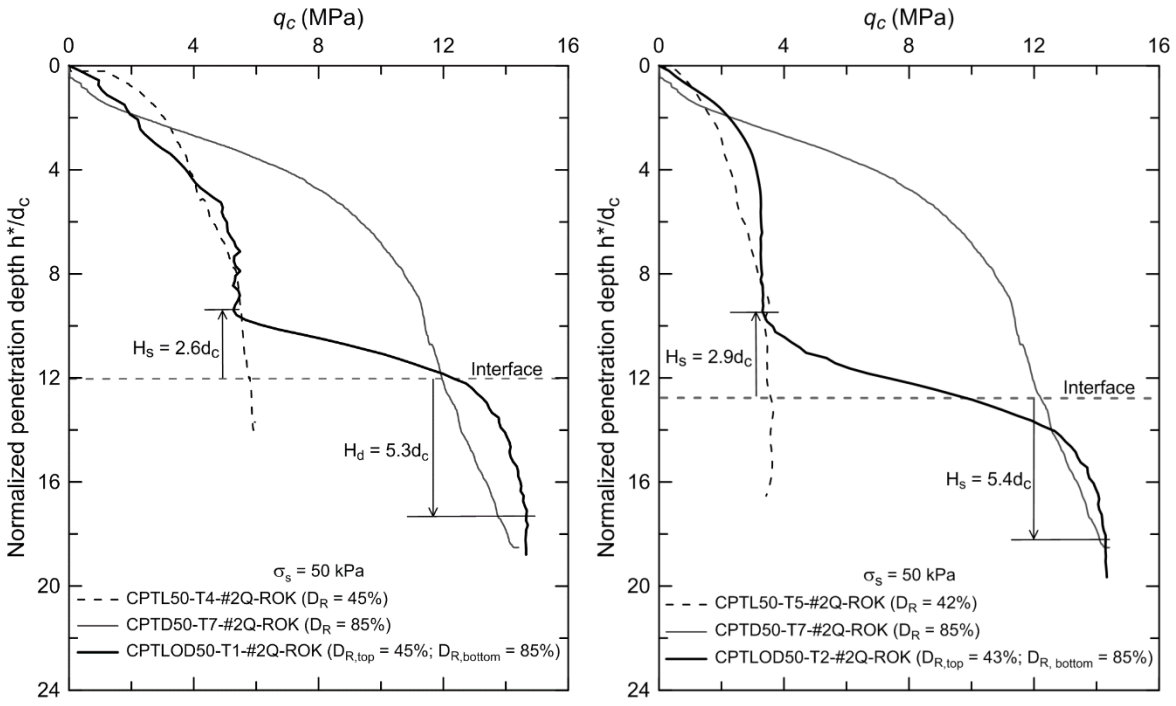

(a) (b)

Figure 7.3 Cone resistance vs. normalized penetration depth profiles for tests performed in loose (CPTL50-T4-#2Q-ROK), dense (CPTD50-T7-#2Q-ROK) and loose-over-dense samples: (a) CPTLOD50-T1-#2-ROK and (b) CPTLOD50-T2-#2-ROK.

The tip resistance in the loose-over-dense samples (Figure 7.3(a) and (b)) compares well with that of the loose sand sample until the cone is $2.6d_c$ and $2.9d_c$ above the interface, respectively, after which it starts sensing the presence of the underlying dense sand layer. Once the penetrometer enters the dense sand layer, the tip resistance continues to rise, stabilizing only at a vertical distance of $5.3d_c$ and $5.4d_c$ from the interface, as shown in Figure 7.3(a) and (b), respectively. Figure 7.4 shows the tip resistance profile for the dense-over-loose sand samples (CPTDOL50-T3-#2Q-RO; D_R = 85%/42%; and CPTDOL50-T4-#2Q-RO; D_R = 85%/44%) for a test performed with 50 kPa surcharge along with the tip resistance profiles for the tests performed in the loose (CPTL50-T5-#2Q-ROK, D_R = 42%) and dense (CPTD50-T7-#2Q-ROK, D_R = 85%) sand samples with similar initial density and surcharge.

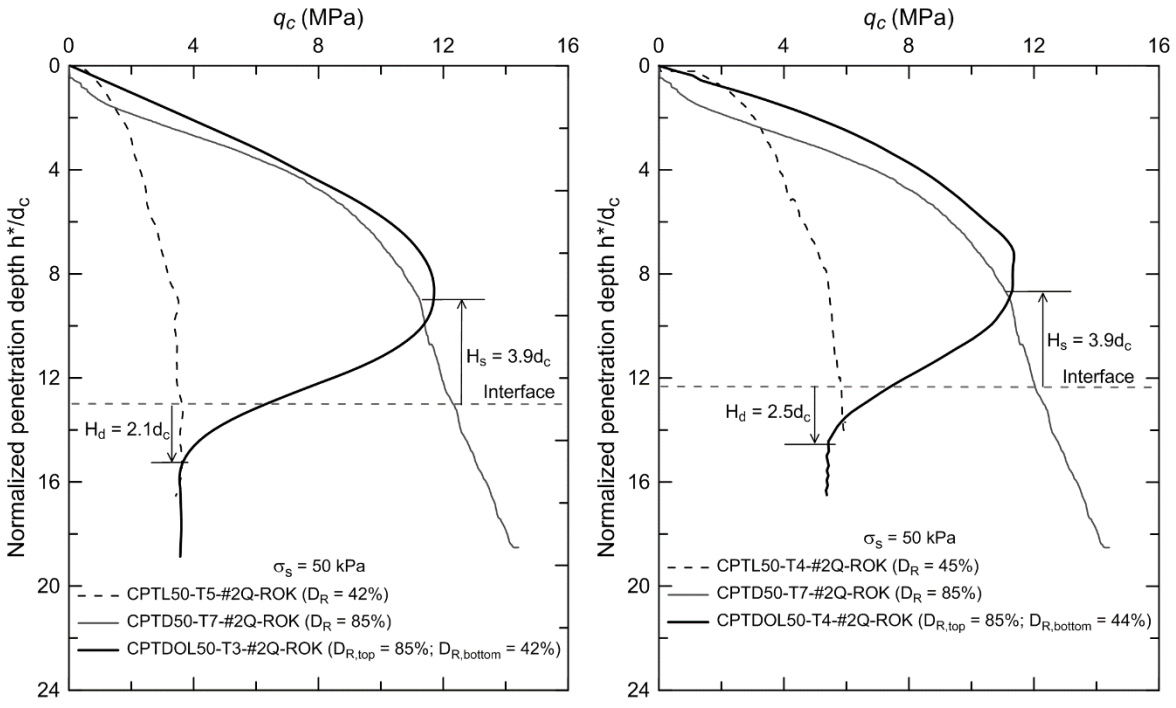

(a) (b)

Figure 7.4 Cone resistance vs. normalized penetration depth profiles for tests performed in loose (CPTL50-T5-#2Q-ROK), dense (CPTD50-T7-#2Q-ROK) and dense-over-loose samples: (a) CPTDOL50-T3-#2Q-ROK and (b) CPTDOL50-T4-#2Q-ROK.

The tip resistance profiles of Figure 7.4 show that, for the dense-over-loose sand sample, the tip resistance starts decreasing when the penetrometer tip starts sensing the presence of the underlying loose sand layer at a vertical distance of $3.9d_c$ above the interface. Development depths of $2.1d_c$ and $2.5d_c$ were identified based on the tip resistance profile of the layered samples, as the tip resistance in the underlying loose sand layer of the layered sample starts to match well the tip resistance observed in the uniform loose sand sample (CPTL50-T5-#2Q-ROK, D_R = 42%) at that depth.

Figure 7.5 shows the tip resistance profiles for tests performed in medium dense (CPTMD50-T6-#2Q-ROK, D_R = 63%), dense (CPTD50-T7-#2Q-ROK, D_R = 85%) and medium dense-over-dense (CPTMDOD50-T5-#2Q-ROK; D_R = 65%/85%) sand samples.

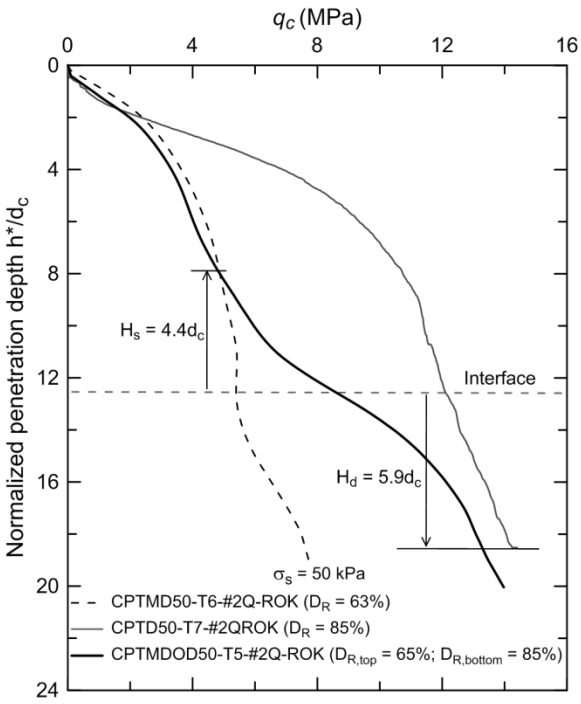

Figure 7.5 Cone resistance vs. normalized penetration depth profiles for tests performed in medium dense (CPTMD50-T6-#2Q-ROK), dense (CPTD50-T7-#2Q-ROK) and medium dense-over-dense (CPTMDOD50-T5-#2Q-ROK) sand samples.

The tip resistance profile of the medium dense-over-dense sand sample (Figure 7.5) shows that the cone starts sensing the presence of the underlying dense sand layer at a vertical distance of 4.4d_c above the interface, where a clear increase in tip resistance is observed. The development depth is 5.9d_c. Comparison of Figure 7.3 and Figure 7.5 show that the sensing depth for the test performed on the medium dense-over-dense sand sample (CPTMDOD50-T5-#2Q-ROK) is greater than that in the loose-over-dense sand sample (CPTLOD50-T1-#2Q-ROK), which indicates that, with the underlying layer unchanged, the sensing depth is directly affected by the density of the layer that the penetrometer is currently traversing.

Figure 7.6 shows the tip resistance profiles for the medium dense (CPTMD-T6-#2Q-ROK), dense (CPTD-T7-#2Q-ROK) and dense-over-medium dense (CPTDOMD50-T6-#2QROK; layer with D_R = 85% over layer with D_R = 63%) sand samples. For test CPTDOMD50-T6-#2QROK, the sensing and development depths are 3.0d_c and 5.3d_c, respectively. The sensing depth observed for test CPTDOMD50-T6-#2QROK (H_s=3.0d_c)

is smaller than that of test CPTMDOD50-T5-#2Q-ROK (H_s=4.4d_c). This shows the effect of the underlying layer on sensing depth. This result suggests that a penetrometer can sense a stiffer layer earlier (at a larger distance from the layer).

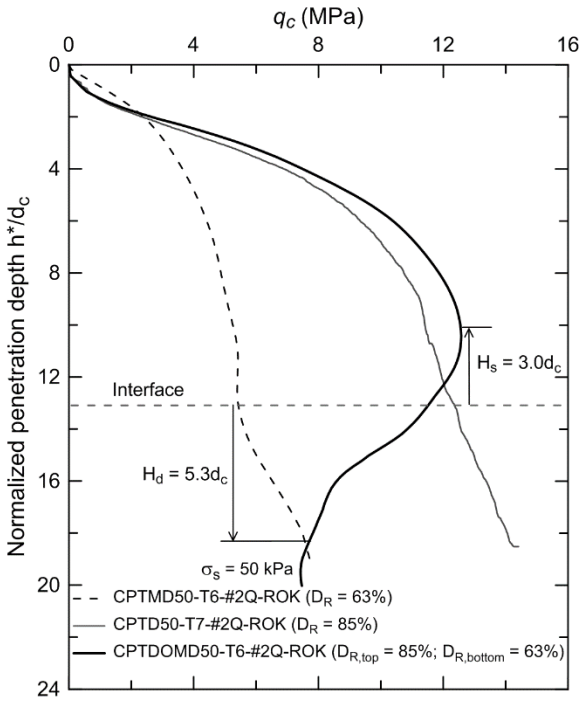

Figure 7.6 Cone resistance vs. normalized penetration depth profiles for tests performed in medium dense (CPTMD50-T6-#2Q-ROK), dense (CPTD50-T7-#2Q-ROK) and dense-over-medium dense (CPTDOMD50-T6-#2Q-ROK) sand samples.

Figure 7.7 shows the cone resistance profiles for tests performed in the loose (CPTL50-T5-#2Q-ROK), medium dense (CPTMD50-T6-#2Q-ROK) and loose-over-medium dense (CPTLOMD50-T7-#2Q-ROK; layer with D_R = 42% over layer with D_R = 63%) sand samples. The tip resistance starts to increase for the loose-over-medium dense sand sample (CPTLOMD50-T7-#2Q-ROK) as the cone tip is about 2.7d_c above the interface. At 6.0d_c below the interface, the tip resistance becomes similar to what was observed in uniform medium dense sand layer. Medium dense samples are notoriously challenging to prepare with a high degree of uniformity, so there is greater variability than there is for either loose or dense sand (Salgado et al. 1998; Salgado et al. 1997).

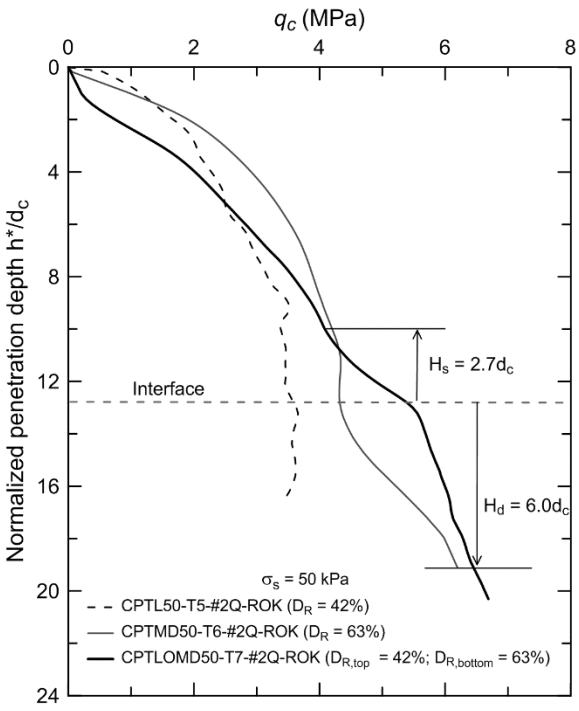

Figure 7.7 Cone resistance vs. normalized penetration depth profiles for tests performed in loose (CPTL50-T5-#2Q-ROK), medium dense (CPTMD50-T6-#2Q-ROK), and loose-over-medium dense (CPTLOMD50-T7-#2Q-ROK) sand samples.

Figure 7.8 shows the cone resistance profiles for the tests performed in the loose (CPTL50-T5-#2Q-ROK), medium dense (CPTMD50-T6-#2Q-ROK) and medium dense-over-loose (CPTMDOL50-T8-#2Q-ROK; layer with D_R = 65% over layer with D_R = 43%) sand samples. The sensing and development depths for test MDOL50-T8-#2Q-ROK are identified at 2.7d_c and 1.3d_c, respectively. In penetration from a medium dense into a loose sand sample, the vertical compression induced by the cone below the tip will densify the loose sand to some extent. This causes some density equalization for the two layers, leading to a smoother transition in cone resistance values from one layer to the other.

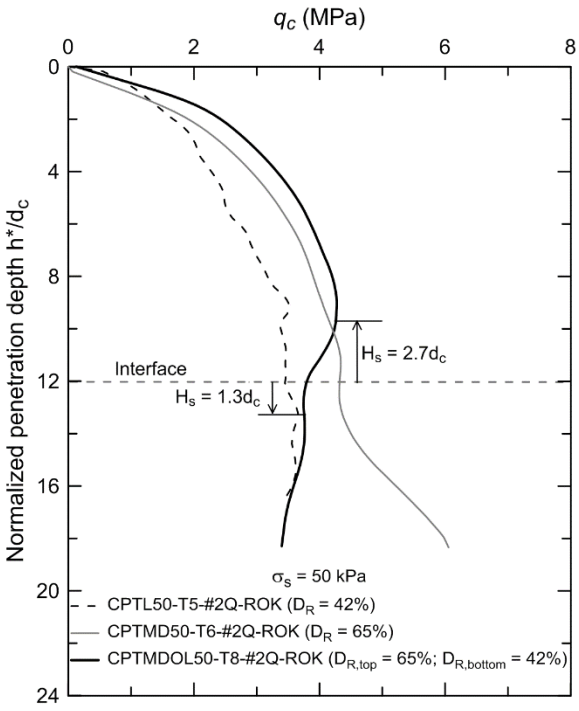

Figure 7.8 Cone resistance vs. normalized penetration depth profiles for tests performed in loose (CPTL50-T5-#2Q-ROK), medium dense (CPTMD50-T6-#2Q-ROK), and loose-over-medium dense (CPTMDOL50-T8-#2Q-ROK) sand samples.

Four tests were performed with a miniature cone of diameter $d_{c,mini}$ = 19.05 mm in loose (CPTL50-T13-Mini-#2Q-ROK), dense (CPTD50-T14-Mini-#2Q-ROK, loose-over-dense (CPTLOD50-T9-Mini-#2Q-ROK) and dense-over-loose (CPTDOL50-T10-Mini-#2Q-ROK) sand samples. It was not possible to embed a load cell at the tip of the miniature cone penetrometer. Therefore, only the total jacking load Q_t required to push the miniature cone penetrometer through the sand samples is reported in this section. The jacking load was measured through a load cell mounted on top of the penetrometer. The objective of these tests is to investigate the effect of penetrometer diameter on the total load Q_t in two-layered soil profiles.

Figure 7.9 shows the total jacking load profiles for tests performed on loose (CPTL50-T4-#2Q-ROK), dense (CPTD50-T7-#2Q-ROK), loose-over-dense (CPTLOD50-T1-#2Q-ROK, with D_R = 45%/85%; and CPTLOD50-T2-#2Q-ROK, with D_R = 43%/85%) and dense-over-loose (CPTDOL-T3-#2Q-ROK, with D_R = 85%/43%; and CPTDOL-T4-#2Q-ROK, with D_R = 85%/44%) sand samples with a cone diameter of

31.75mm. Comparison of Figure 7.9 with Figure 7.3 and Figure 7.4 reveals that the total jacking load (axial load) and the tip resistance mobilized for penetration into layered sand samples are affected in a similar manner by layers of different densities. The axial load starts increasing in the loose-over-dense sand samples (CPTLOD50-T1-#2Q-ROK and CPTLOD50-T2-#2Q-ROK) at a distance of $5.3d_c$ and $5.1d_c$ ahead of the interface and reaches the total load associated with the dense sand sample after the cone has penetrated a further $5.9d_c$ and $6.5d_c$ into the underlying layer, respectively. Similarly, for the dense-over-loose sand sample (CPTDOL-T3-#2Q-ROK and CPTDOL-T4-#2Q-ROK), the axial load starts decreasing at a distances $4.3d_c$ and $4.6d_c$ ahead of the interface, respectively, and matches well with the axial load measured for the loose sand sample at $5.1d_c$ and $5.2d_c$ beyond the interface, respectively.

Based on the axial load profiles shown in Figure 7.9, the total jacking load is affected by the presence of an underlying layer earlier than the tip resistance (see Figure 7.3 and Figure 7.4) and requires a greater penetration distance, once it passes the interface, to reach an axial load approximately equal to that of the uniform sand. It can be inferred from these results that the sensing and development depths obtained from the axial load profiles are conservative estimates, in the sense that they tend to be slightly greater than estimates from the cone resistance profiles.

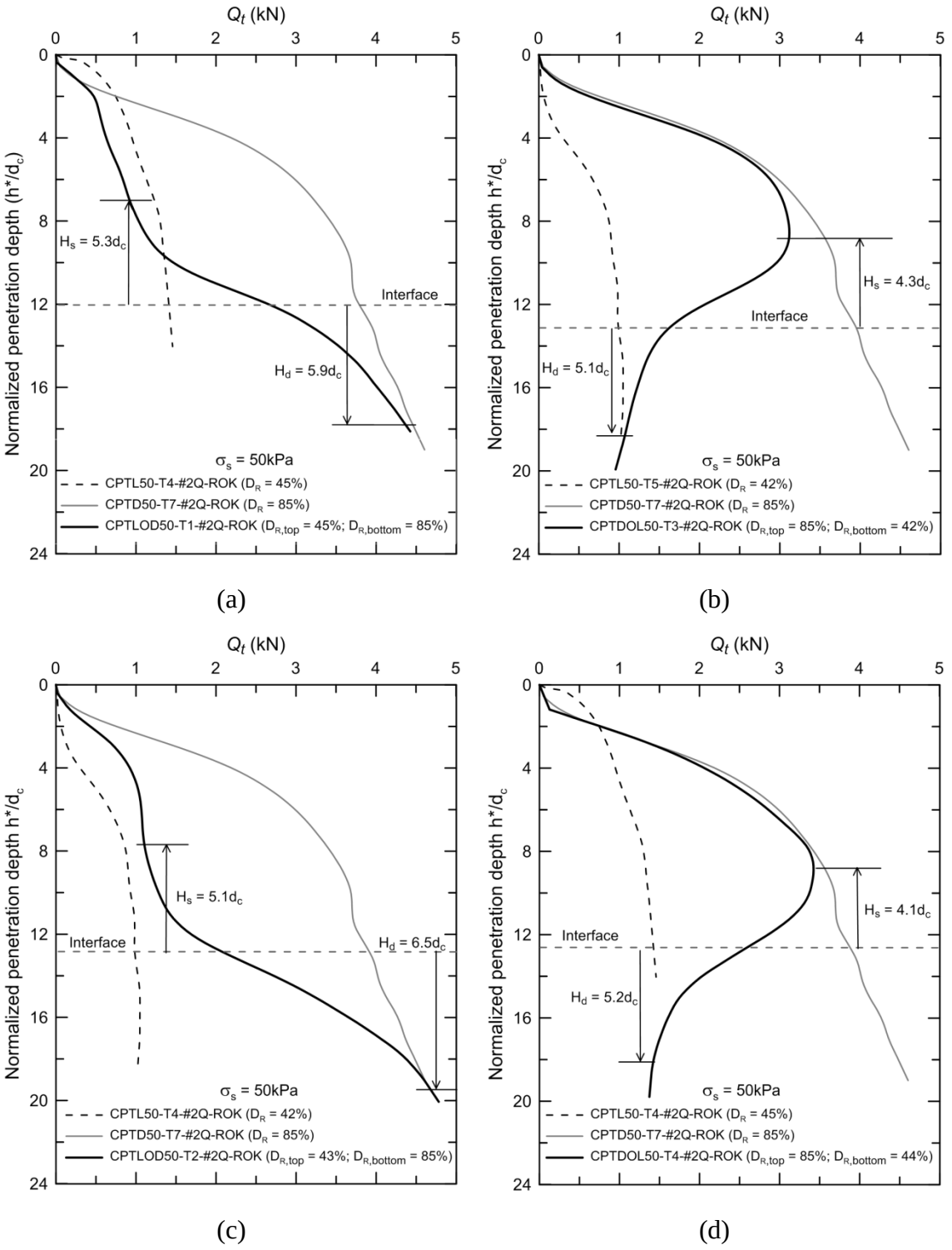

Figure 7.9 Total resistance vs. normalized penetration depth for loose (CPTL50-T4-#2Q-ROK), dense (CPTD50-T7-#2Q-ROK) samples and : (a), loose-over-dense (CPTLOD50-T1-#2Q-ROK), (b) dense-over-loose (CPTDOL50-T3-#2Q-ROK), (c) loose-over-dense (CPTLOD50-T2-#2Q-ROK) and (d) dense-over-loose (CPTDOL50-T4-#2Q-ROK)

Figure 7.10 shows the axial load profiles for the loose (CPTL50-T13-mini-#2Q-ROK, D_R = 45%), dense (CPTD50-T14-mini-#2Q-ROK, D_R = 85%) and loose-over-dense (CPTLOD50-T9-mini-#2Q-ROK; D_R = 45%/85%) sand samples. The axial load starts to increase at a distance of $5.1d_c$ from the interface as it approaches it and then matches the total load measured in the dense sand test once it reaches a distance of $5.0d_c$ from the interface.

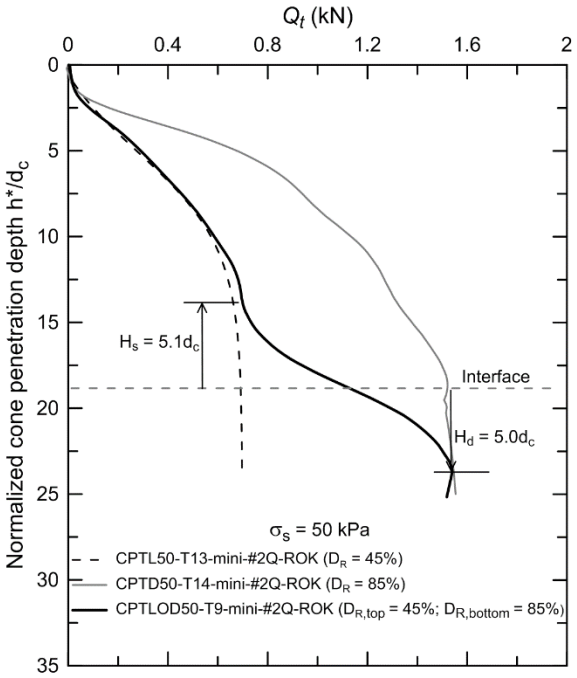

Figure 7.10 Total resistance vs. normalized cone penetration depth for tests performed in loose (CPTL50-T13-mini-#2Q-ROK), dense (CPTD50-T14-mini-#2Q-ROK), and loose-over-dense (CPTLOD50-T9-mini-#2Q-ROK) sand samples with a miniature cone penetrometer.

Figure 7.11 shows the axial load profiles for a test performed in a dense-over-loose sand sample (CPTDOL50-T10-mini-#2Q-ROK; D_R = 85%/45%), along with the tests in loose (CPTL50-T13-mini-#2Q-ROK) and dense (CPTD50-T14-mini-#2Q-ROK) sand samples. The axial load in the dense-over-loose sand sample starts decreasing at a distance of $4.8d_c$ above the interface and stabilizes at a distance of $6.1d_c$ below the interface in the loose sand layer.

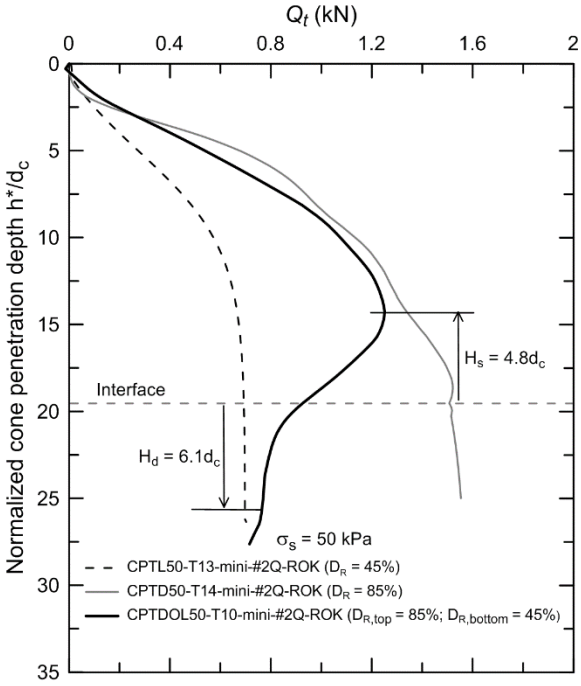

Figure 7.11 Total resistance vs. normalized penetration depth profiles for tests performed in loose (CPTL50-T13-mini-#2Q-ROK), dense (CPTD50-T14-mini-#2Q-ROK), and dense-over-loose (CPTDOL50-T10-mini-) samples with miniature cone penetrometer.

Comparison of Figure 7.10 and Figure 7.11 with Figure 7.9(a) and (b) show that the sensing and development depths observed from the total axial load profiles are in close agreement, suggesting that the sensing and development depths are independent of the size of the penetrometer so long as the penetrometer size remains large in comparison with soil particle size (R Salgado, 2013).

Figure 7.12 shows the tip resistance profile for a test performed in a three-layered sand sample with a loose sand layer sandwiched between two dense sand layers. The first layer is 300 mm thick with a relative density of 85% (dense sand). The second layer is 150 mm thick with a relative density of 46% (loose sand) and the third layer is 550 mm thick with a relative density of 85% (dense sand). The tip resistance profiles for the tests performed in the loose (CPTL50-T4-#2Q-ROK) and dense (CPTD50-T8-#2Q-ROK) sand samples with D_R = 45% and D_R = 82% are also plotted in Figure 7.12 for

comparison; it is clear that they bound the q_c profile for the test with the three layers. Only $2.5d_c$ further penetration was needed for q_c to drop to the value expected for the loose layer based on the test in a uniform sample with the same density. At that location, the distance from the bottom dense sand layer is only $2.4d_c$, and the cone was already sensing the presence of the denser layer, with q_c increasing from that location.

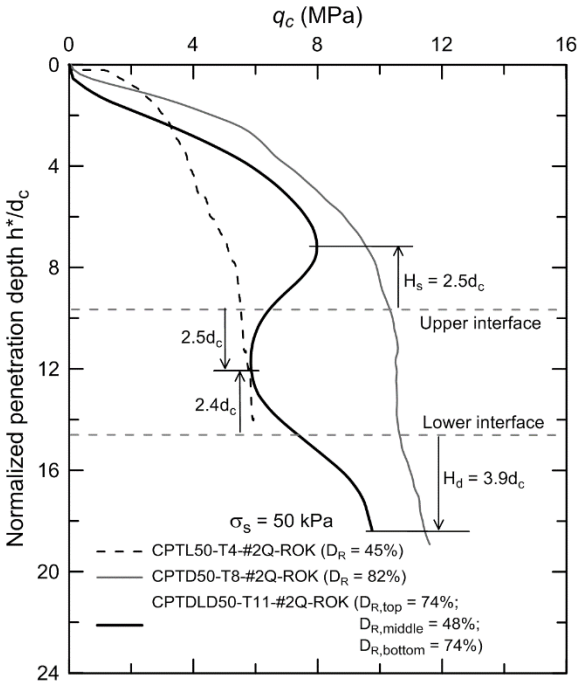

Figure 7.12 Cone resistance vs. normalized penetration depth in loose (CPTL50-T4-#2Q-ROK), dense (CPTD50-T8-#2Q-ROK) and dense-loose-dense (CPTDLD50-T11-#2Q-ROK) sand samples.

7.2.2 Sensing and Development Depths from Radial Stress Measurements

Figure 7.13 shows the radial stress measurements made using a miniature pressure transducer placed at the interface between layers for the tests performed on the loose-over-dense (CPTLOD50-T1-#2Q-ROK), dense-over-loose (CPTDOL50-T3-#2Q-ROK), medium dense-over-dense (CPTMDOD50-T5-#2Q-ROK), dense-over-medium dense (CPTDOMD50-T6-#2Q-ROK), loose-over-medium dense (CPTLOMD50-T7-#2Q-ROK), medium dense-over-loose (CPTMDOL50-T8-#2Q-ROK) and dense-over-loose-over-dense (CPTDLD50-T11-#2Q-ROK) sand samples. The pressure sensor was positioned at a normalized radial distance $r/r_c = 3$ from the cone penetration path. In the dense-over-loose-over-dense test, the pressure transducer embedded at the upper interface was damaged, thus only radial stress measurements from the pressure transducer at the lower interface were obtained.

The observed sensing depths for each test were superimposed on Figure 7.13(a) to (d) for comparison purposes. As shown in Figure 7.13(a) to (d), the radial stress at the interface, in general, starts increasing before the cone starts sensing the presence of the interface, which indicates that the soil at the interface is affected by the cone earlier than the cone senses it.

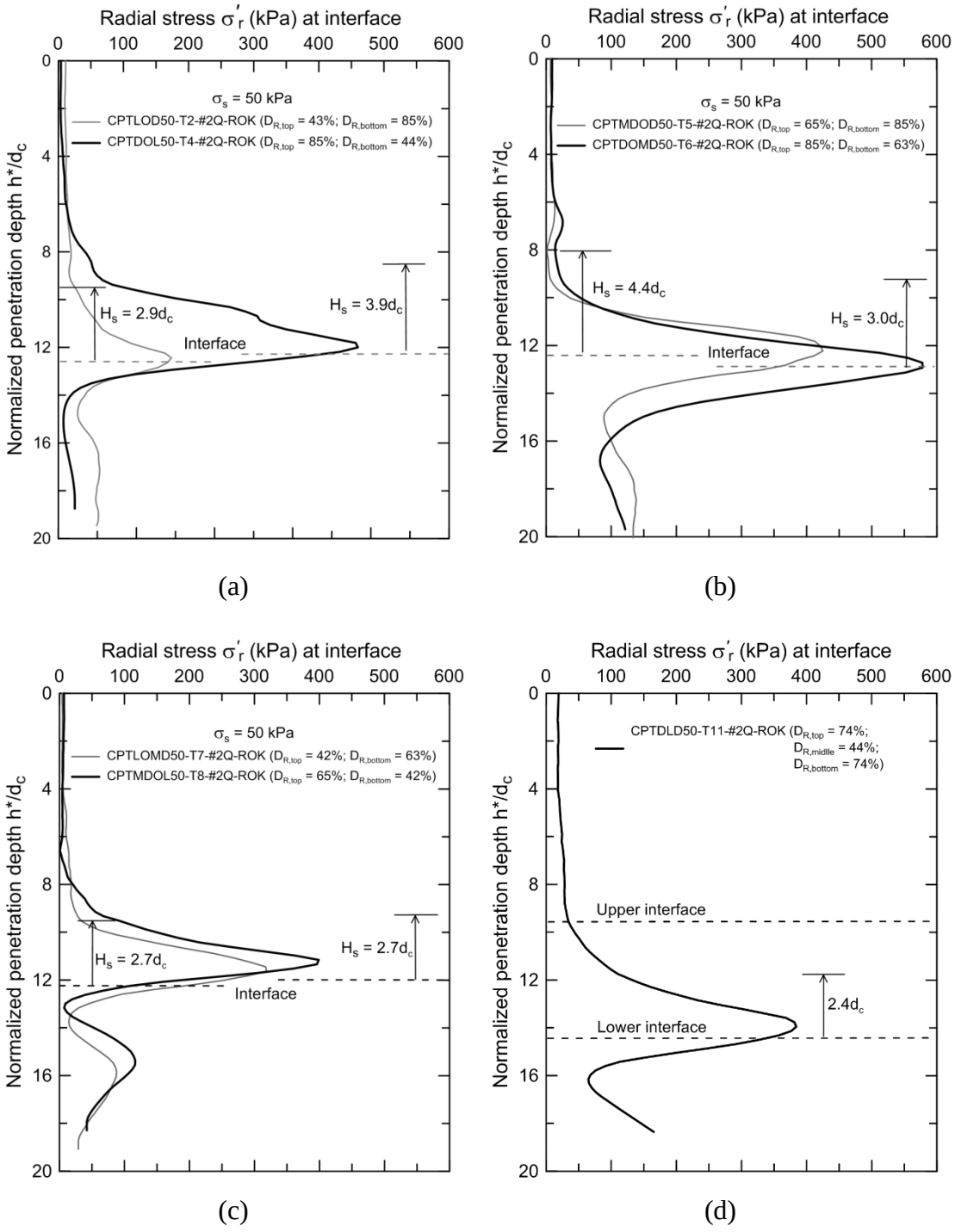

Figure 7.13 Interface radial stress measurements made in the following tests: (a) CPTLOD50-T2-#2Q-ROK and CPTDOL50-T3-#2Q-ROK, (b) CPTMDOD50T5-#2Q-ROK and CPTDOMD50-T6-#2Q-ROK, (c) CPTLOMD50-T7-#2Q-ROK and CPTMDOL50-T8-#2Q-ROK, and (d) CPTDLD50-T11-#2Q-ROK.

7.3 Radial and Vertical Displacement Path

Figure 7.14 shows the normalized radial displacement paths of a soil element located at the layer interface at a radial distance $r = 3r_c$ from the cone penetration path. The radial displacement paths were obtained using the DIC analysis of the cone penetration tests performed on layered sand samples. The sensing depths observed from the cone resistance profiles are shown on every plot to visualize the state of the element's radial displacement when the vertical distance from the cone tip to the interface is equal to the sensing depth. As shown in Figure 7.14, the radial displacement starts to increase well before the cone tip senses the existence of the underlying layer (sensing depth). In all cases, the maximum normalized radial displacement occurs slightly after the cone tip passes the interface.

Figure 7.15 shows the normalized vertical displacement paths of a soil element located at the layer interface at a radial distance $r = 3r_c$ from the cone penetration path. As in Figure 7.14, the sensing depths observed from the cone resistance profiles are superposed on every plot to illustrate the state of the element's vertical displacement when the vertical distance from the cone tip to the interface is equal to the sensing depth. Figure 7.15 (a), (c) and (d) show that the soil elements at the layer interfaces reach their maximum vertical displacements slightly before the cone reaches the layer interfaces for the loose-over-dense and dense-over-loose, loose-over-medium dense, medium dense-over-loose and dense-over-loose-over-dense sand samples. For medium dense-over-dense and dense-over-medium dense sand samples the maximum normalized vertical displacement occurs when the cone reaches the interface. It is clear from Figure 7.15 that the soil element starts moving vertically well before the cone senses the underlying layer.

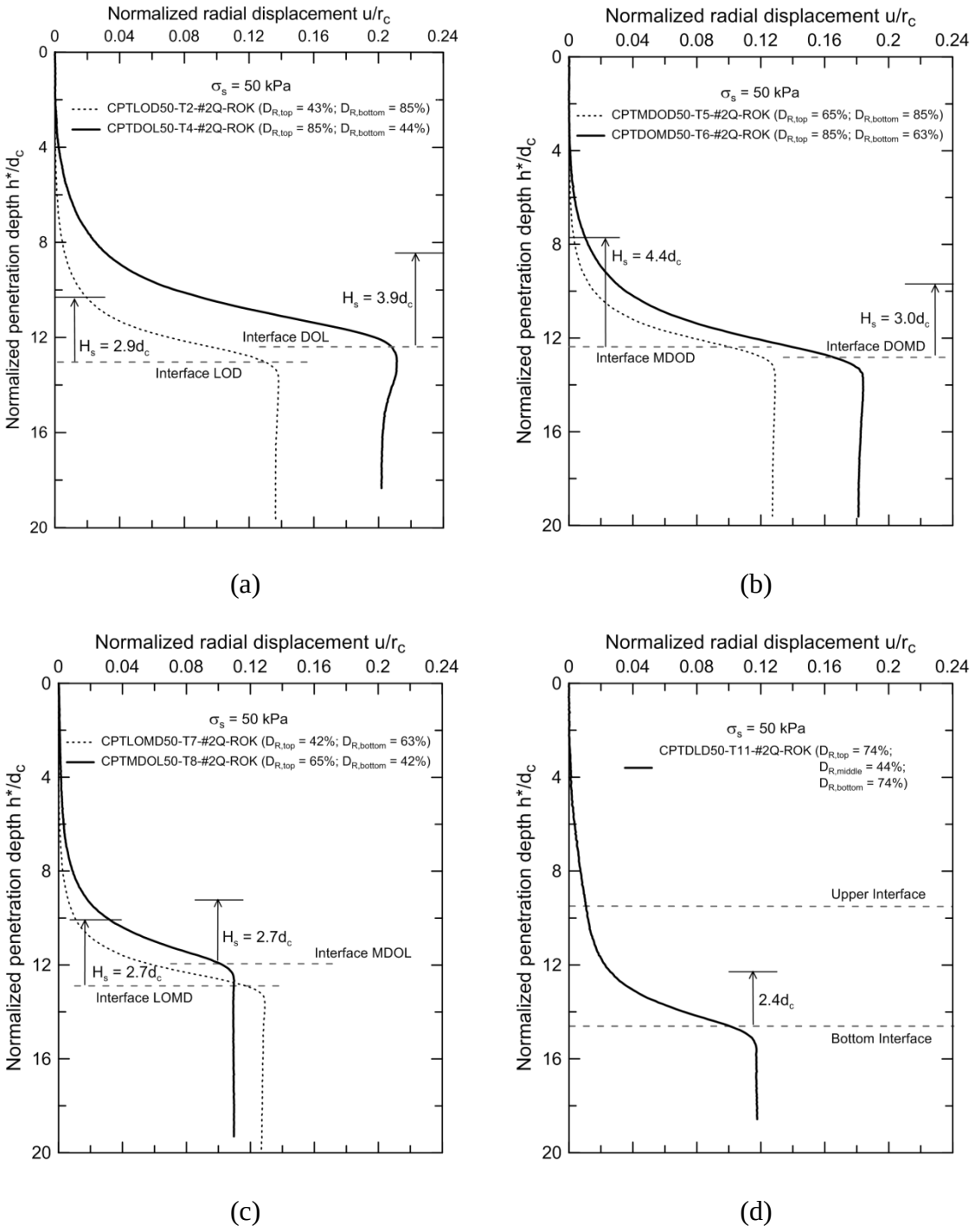

Figure 7.14 Normalized radial displacement path of a soil element located at the layer interface at $r = 3r_c$ for tests: (a) CPTLOD50-T2-#2Q-ROK and CPTDOL50-T4-#2Q-ROK, (b) CPTMDOD50-T5-#2Q-ROK and CPTDOMD50-T6-#2Q-ROK, (c) CPTLOMD50-T7-#2Q-ROK and CPTMDOL50-T8-#2Q-ROK and (d) CPTDLD50-T11-#2Q-ROK.

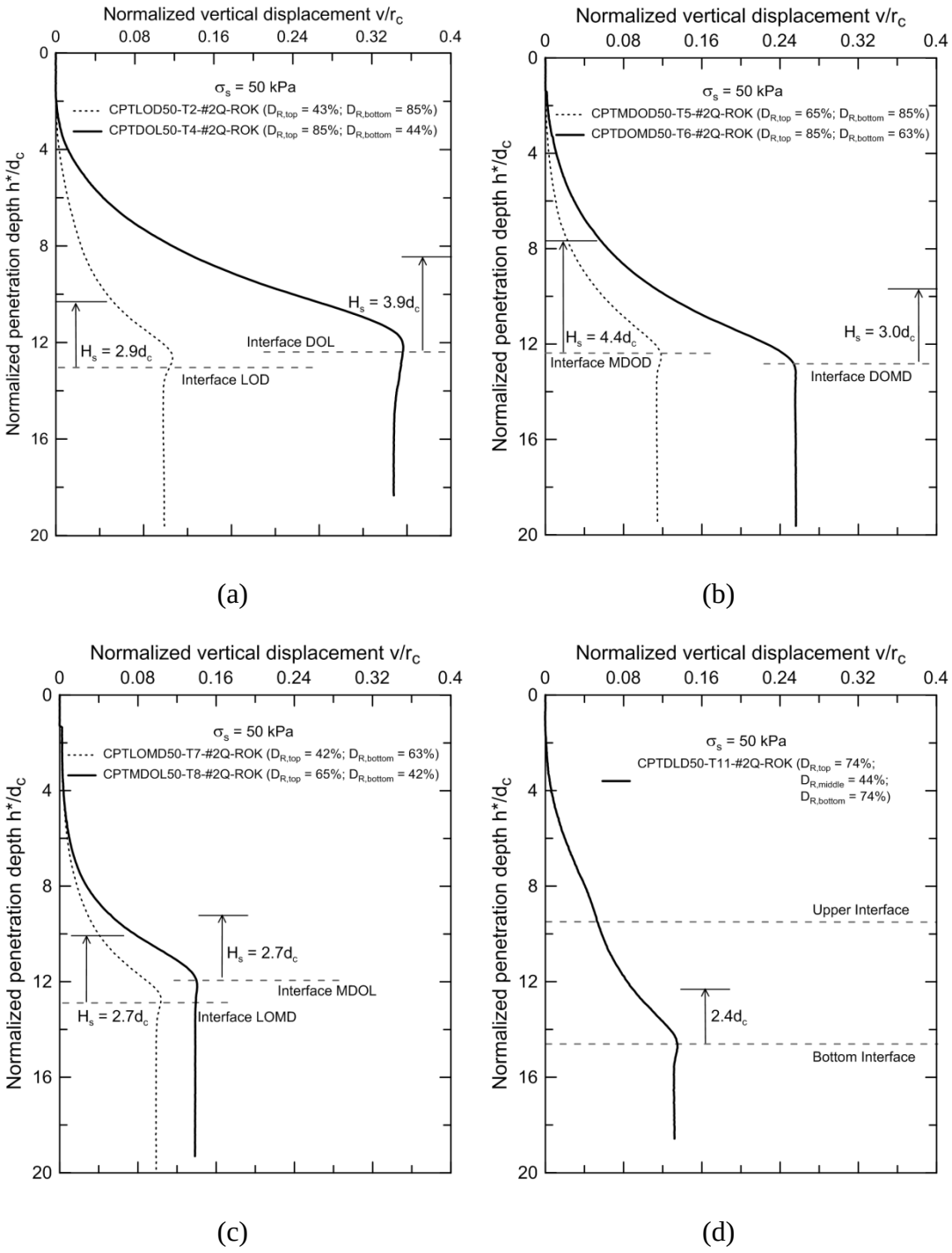

Figure 7.15 Normalized vertical displacement of a soil element path located at the layer interface at $r = 3r_c$ for tests: (a) CPTLOD50-T2-#2Q-ROK and CPTDOL50-T4-#2Q-ROK, (b) CPTMDOD50-T5-#2Q-ROK and CPTDOMD50-T6-#2Q-ROK, (c) CPTLOMD50-T7-#2Q-ROK and CPTMDOL50-T8-#2Q-ROK and (d) CPTDLD50-T11-#2Q-ROK.

7.4 Sensing Depth and the Displacement Pattern at the Layer Interface

Figure 7.16 shows the normalized displacements of the layer interface when the cone tip traverses the interface from H_s above the interface to H_d below the interface for the loose-over-dense (CPTLOD50-T2-#2Q-ROK) and dense-over-loose (CPTDOL50-T4-#2Q-ROK) sand samples. The vertical distance of a point in the domain with respect to the cone tip is represented by h, with $h = 0$ at the cone tip, $h > 0$ above the cone tip and $h < 0$ below it. The vertical distance to a point in the soil mass from the soil interface from the soil surface is given by z and z_i, respectively. Figure 7.16(a) shows that once the cone passes the interface in a loose-over-dense sand sample, the interface does not move further (the curves for $h = 1/4H_d$, $1/2H_d$, $3/4H_d$ and $1H_d$ overlap in Figure 7.16(a)). In the case of the dense-over-loose sand sample (Figure 7-16(b)), the interface still moves after the cone passes it until it reaches a depth $z_i = 3/4H_d$ measured from the interface. Comparing Figure 7.16(a) and Figure 7.16(b) reveals that when the cone tip reaches $h = H_s$ ($H_s = 2.9$ for test CPTLOD50-T2-#2Q-ROK and 3.9 for test CPTDOL50-T4-#2Q-ROK), the interface of the dense-over-loose sample moves more than the loose-over-dense sample.

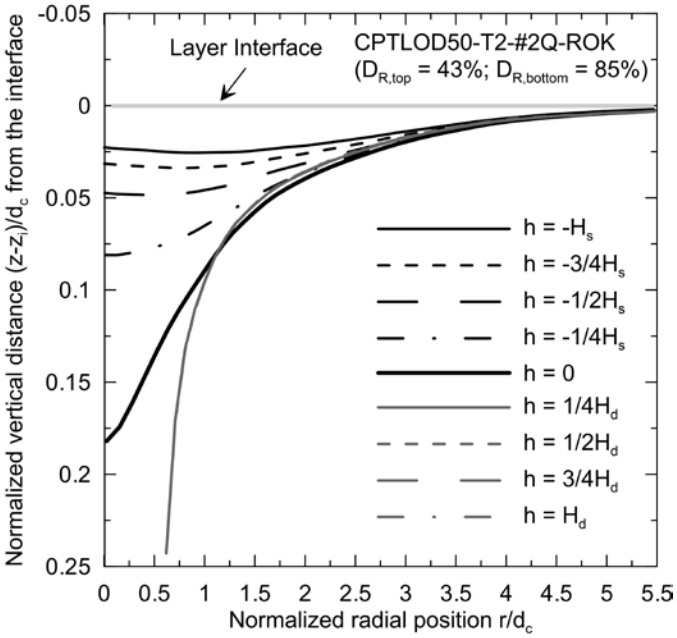

(a)

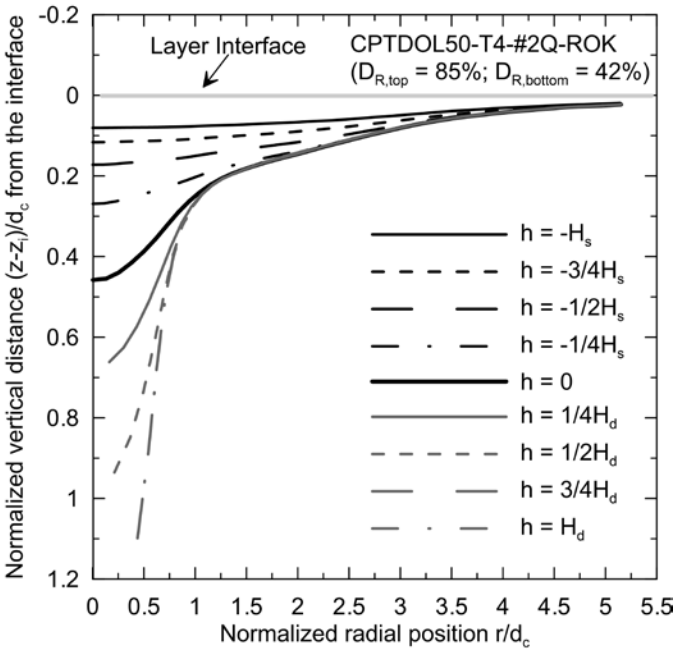

(b)

Figure 7.16 Evaluation of interface vertical displacement for: (a) loose-over-dense (CPTLOD50-T2-#2Q-ROK) sand sample and (b) dense-over-loose (CPTLOD50-T4-#2Q-ROK) sand sample.

7.5 Effect of the Layer Interface on Displacement Patterns

Figure 7.17 and Figure 7.18 show the spatial distribution of the normalized incremental radial displacement u/r_c and vertical displacement v/r_c for the loose-over-dense (CPTLOD50-T2-#2Q-ROK) sand sample. Figure 7.17 and Figure 7.18 show also the soil normalized incremental displacement vectors for $1r_c$ cone penetration when the cone tip reaches $h_i = h^*\text{-}z_i$ = $-H_s$, $-3/4H_s$, $-1/2H_s$,$-1/4H_s$, 0, $1/4H_d$, $1/2H_d$, $3/4H_d$ and H_d. Closer look at radial (Figure 7.17) and vertical (Figure 7.18) incremental displacement contour plots reveals that the size of radial and vertical displacement "bulb" increases as the cone moves from the loose to the dense layer. Figure 7.17(e) and Figure 7.18(e) show that, as the cone approaches the interface, the displacement vectors on the interface and near the cone tip face become horizontal.

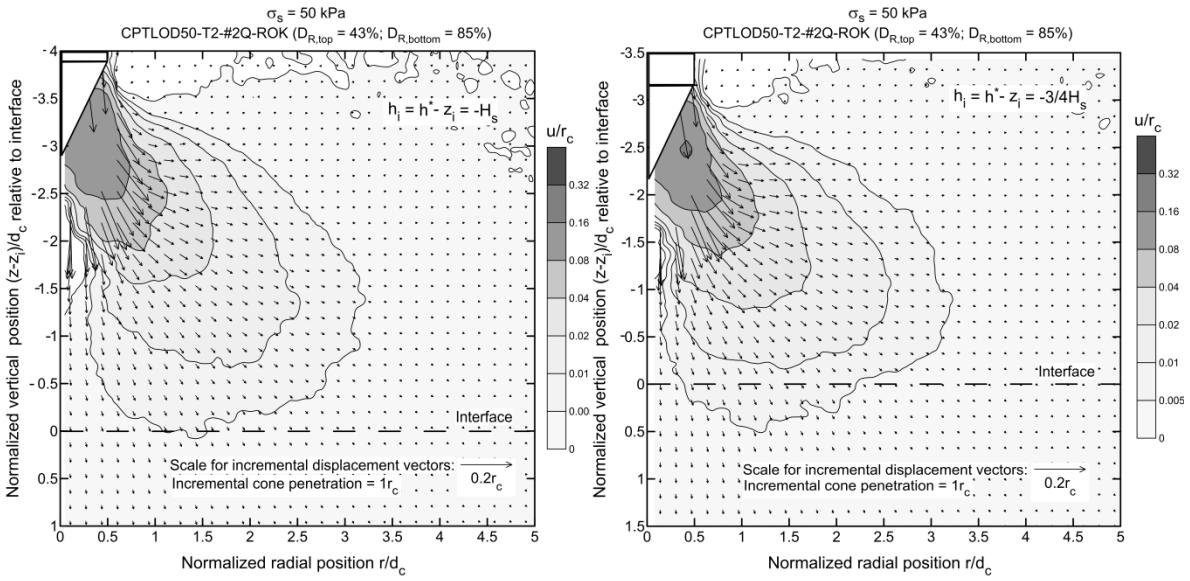

(a) (b)

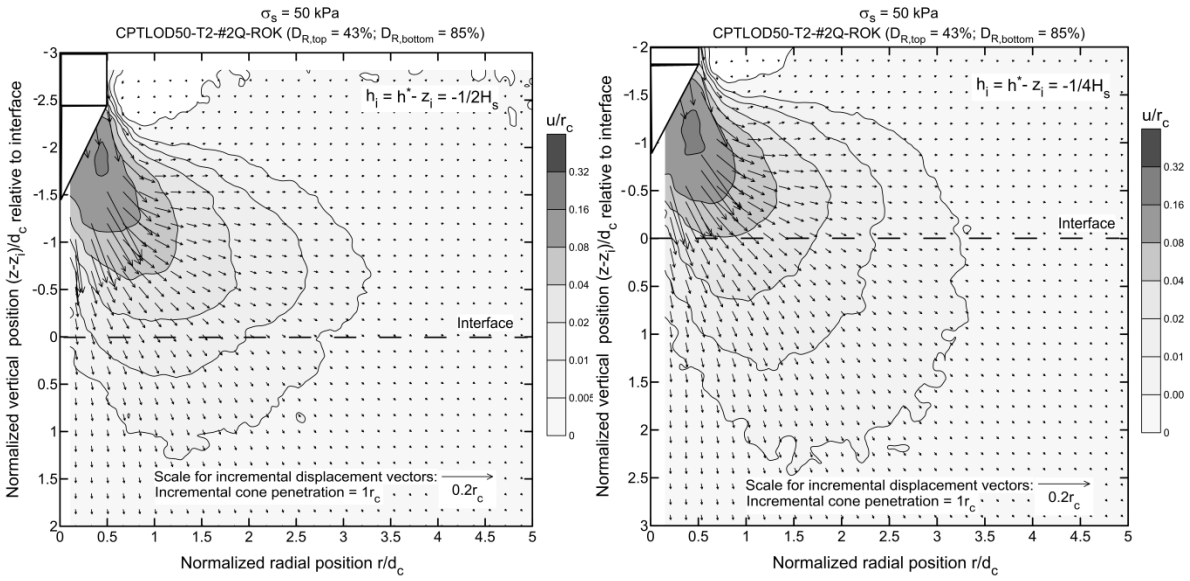
σs = 50 kPa
CPTLOD50-T2-#2Q-ROK (DR,top = 43%; DR,bottom = 85%)
hi = h*- zi = -1/2Hs
Interface
Scale for incremental displacement vectors:
Incremental cone penetration = 1rc
0.2rc
Normalized vertical position (z-zi)/dc relative to interface
Normalized radial position r/dc
u/rc
0.32
0.16
0.08
0.04
0.02
0.01
0.005
0
(c)
σs = 50 kPa
CPTLOD50-T2-#2Q-ROK (DR,top = 43%; DR,bottom = 85%)
hi = h*- zi = -1/4Hs
Interface
Scale for incremental displacement vectors:
Incremental cone penetration = 1rc
0.2rc
Normalized vertical position (z-zi)/dc relative to interface
Normalized radial position r/dc
u/rc
0.32
0.16
0.08
0.04
0.02
0.01
0.00
0
(d)
σs = 50 kPa
CPTLOD50-T2-#2Q-ROK (DR,top = 43%; DR,bottom = 85%)
hi = h*- zi = 0
Interface
Scale for incremental displacement vectors:
Incremental cone penetration = 1rc
0.2rc
Normalized vertical position (z-zi)/dc relative to interface
Normalized radial position r/dc
u/rc
0.32
0.16
0.08
0.04
0.02
0.01
0.00
0
(e)
σs = 50 kPa
CPTLOD50-T2-#2Q-ROK (DR,top = 43%; DR,bottom = 85%)
Interface
hi = h*- zi = 1/4Hd
Scale for incremental displacement vectors:
Incremental cone penetration = 1rc
0.2rc
Normalized vertical position (z-zi)/dc relative to interface
Normalized radial position r/dc
u/rc
0
(f)

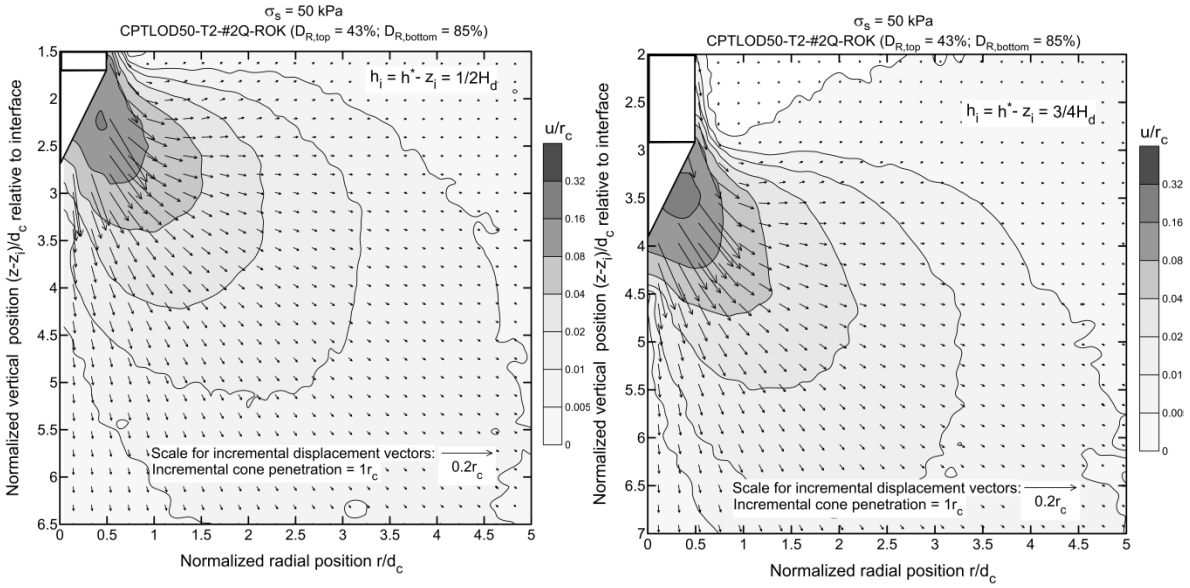

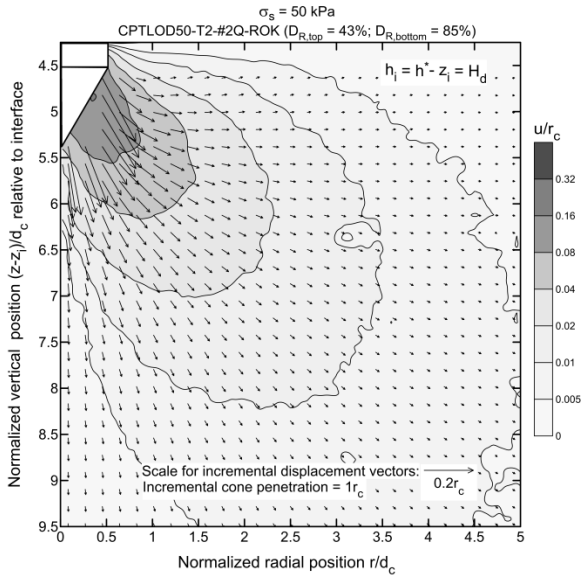

Figure 7.17 Evolution of normalized incremental radial displacement field after $1r_c$ incremental cone penetration at various cone penetration depths in loose-over-dense sample (CPLOD50-T2 -#2QROK) at: (a) $h_i = -H_s$, (b) $h_i = -3/4H_s$, (c) $h_i = -1/2\ H_s$, (d) $h_i = -1/4\ H_s$, (e) $h_i = 0$, (f) a) $h_i = 1/4H_d$, (g) $h_i = 1/2H_d$, (h) $h_i = 3/4\ H_d$, and (i) $h_i = H_d$.

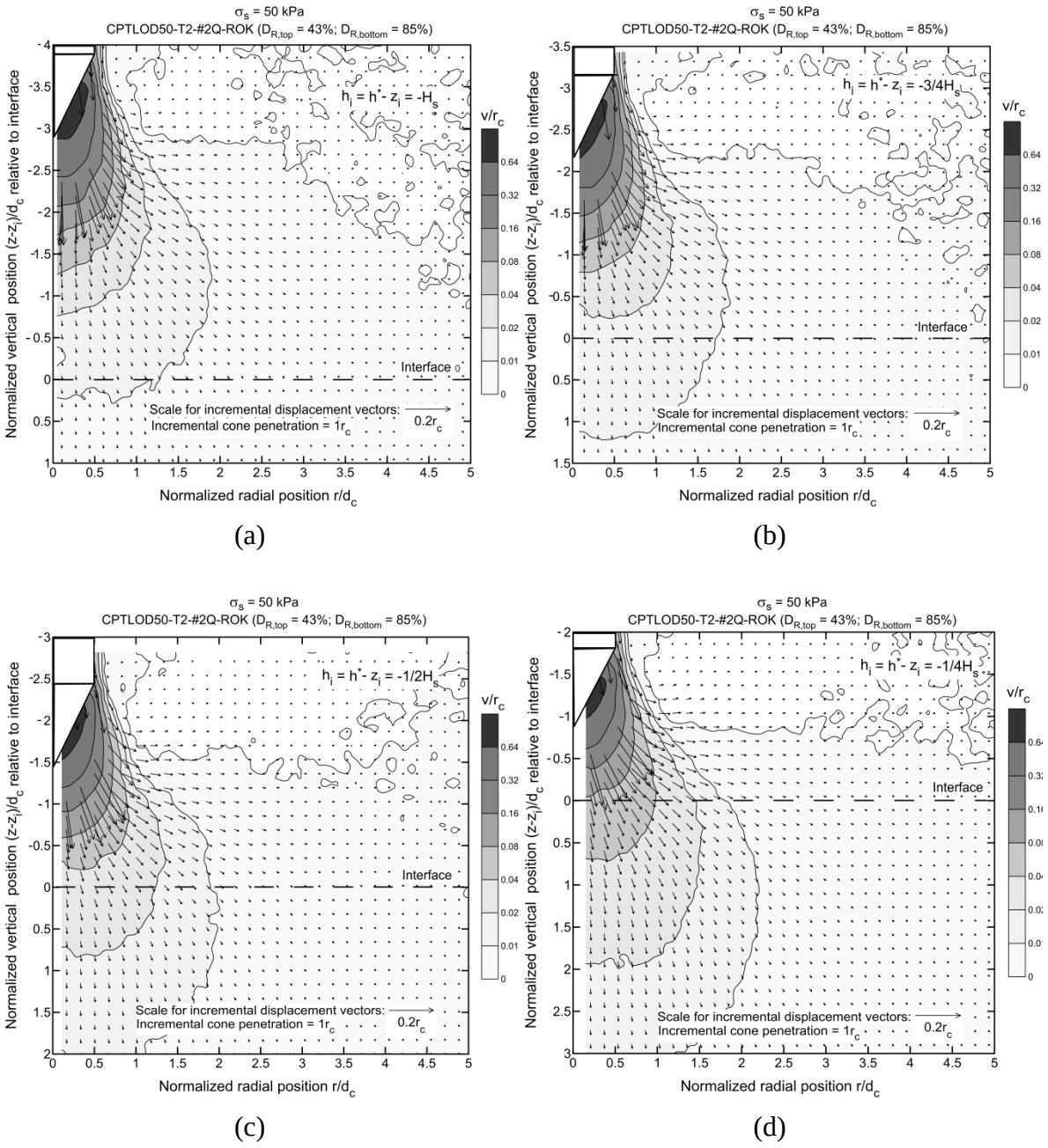
σs = 50 kPa
CPTLOD50-T2-#2Q-ROK (DR,top = 43%; DR,bottom = 85%)
hi = h* - zi = -Hs
hi = h* - zi = -3/4Hs
hi = h* - zi = -1/2Hs
hi = h* - zi = -1/4Hs
Interface
Scale for incremental displacement vectors:
Incremental cone penetration = 1rc
0.2rc
v/rc
0.64
0.32
0.16
0.08
0.04
0.02
0.01
0
Normalized vertical position (z-zi)/dc relative to interface
Normalized radial position r/dc
(a)
(b)
(c)
(d)

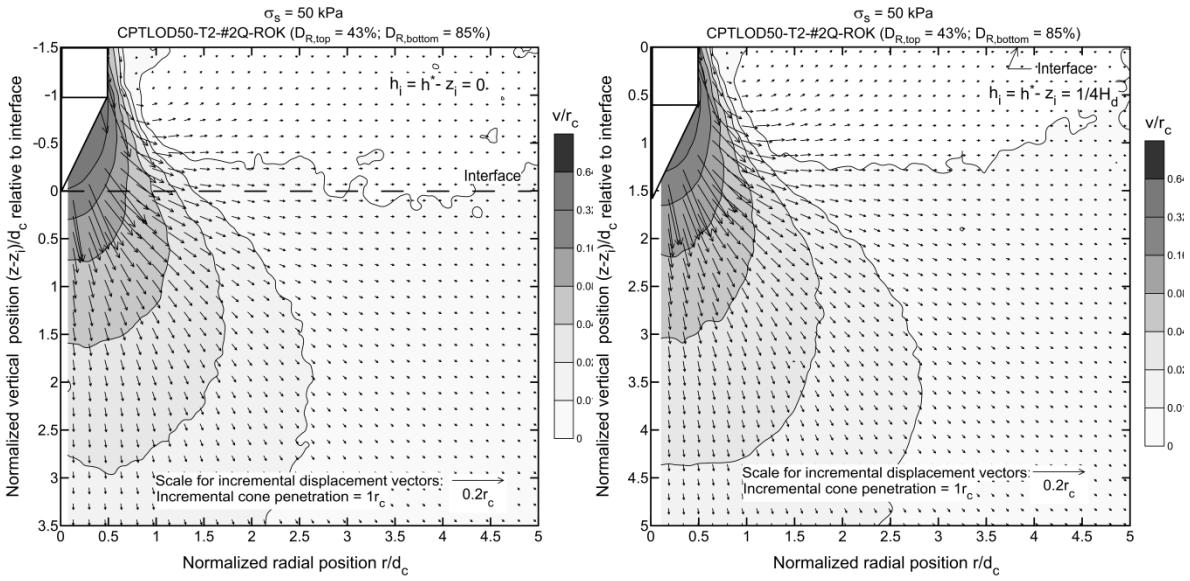
σs = 50 kPa
CPTLOD50-T2-#2Q-ROK (DR,top = 43%; DR,bottom = 85%)
hi = h*- zi = 0.
Interface
Scale for incremental displacement vectors:
Incremental cone penetration = 1rc
0.2rc
v/rc
Normalized vertical position (z-zi)/dc relative to interface
Normalized radial position r/dc

(e)

σs = 50 kPa
CPTLOD50-T2-#2Q-ROK (DR,top = 43%; DR,bottom = 85%)
Interface
hi = h*- zi = 1/4Hd
Scale for incremental displacement vectors:
Incremental cone penetration = 1rc
0.2rc
v/rc
Normalized vertical position (z-zi)/dc relative to interface
Normalized radial position r/dc

(f)

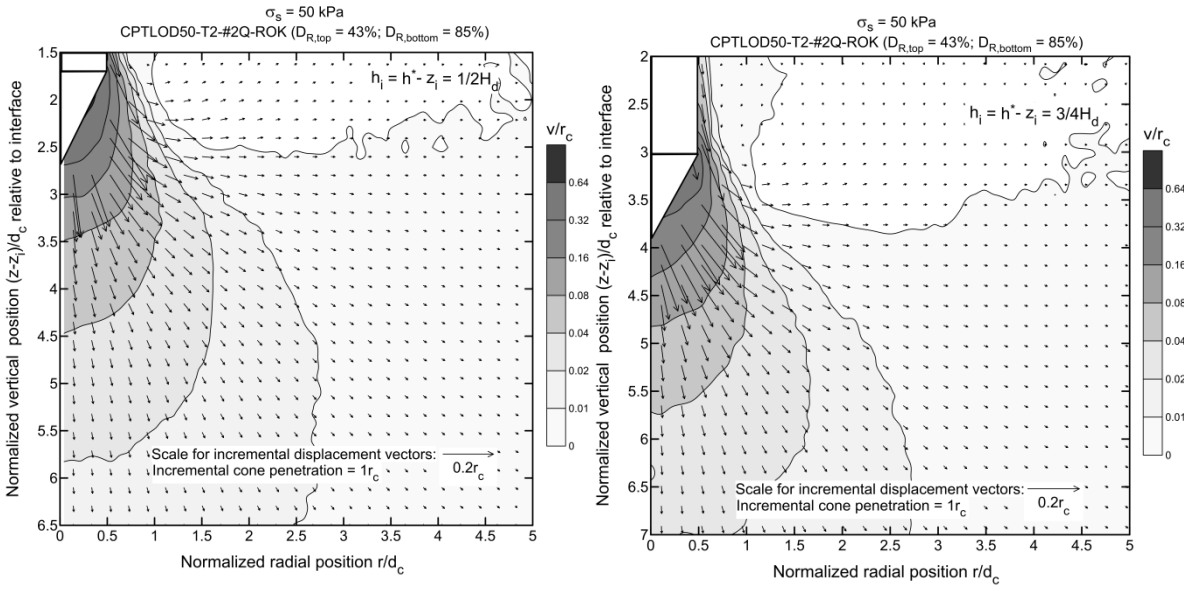
σs = 50 kPa
CPTLOD50-T2-#2Q-ROK (DR,top = 43%; DR,bottom = 85%)
hi = h*- zi = 1/2Hd
Scale for incremental displacement vectors:
Incremental cone penetration = 1rc
0.2rc
v/rc
Normalized vertical position (z-zi)/dc relative to interface
Normalized radial position r/dc

(g)

σs = 50 kPa
CPTLOD50-T2-#2Q-ROK (DR,top = 43%; DR,bottom = 85%)
hi = h*- zi = 3/4Hd
Scale for incremental displacement vectors:
Incremental cone penetration = 1rc
0.2rc
v/rc
Normalized vertical position (z-zi)/dc relative to interface
Normalized radial position r/dc

(h)

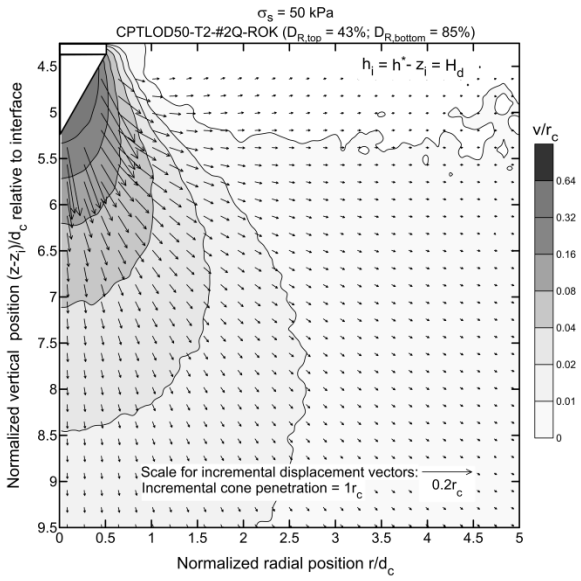

(i)

Figure 7.18 Evolution of normalized incremental vertical displacement field after $1r_c$ incremental cone penetration at various cone penetration depths in loose-over-dense sample (CPLOD50-T2 -#2QROK) at: (a) h_i = -H_s, (b) h_i = -3/4H_s, (c) h_i = -1/2 H_s, (d) h_i = -1/4 H_s, (e) h_i = 0, (f) a) h_i = 1/4H_d, (g) h_i = 1/2H_d, (h) h_i =3/4 H_d, and (i) h_i = H_d.

Figure 7.19 and Figure 7.20 show the spatial distribution of the normalized incremental radial u/r_c and vertical v/r_c displacements obtained from the DIC analysis for the dense-over-loose (CPTDOL50-T4-#2Q-ROK) sand sample. Figure 7.19 and Figure 7.20 also show also the soil normalized incremental displacement vectors for $1r_c$ cone penetration when the cone tip reaches $h_i = h^*-z_i$ = -H_s, -3/4H_s, -1/2H_s,-1/4H_s, 0, 1/4H_d, 1/2H_d, 3/4H_d and H_d in the loose-over-dense (CPTLOD50-T2-#2Q-ROK) sand sample. Unlike what was seen in Figure 7.17 and Figure 7.18 for the loose-over-dense sand sample, Figure 7.19 and Figure 7.20 show that that the size of the radial and vertical displacement bulbs gradually decrease as the cone approaches a loose layer from a dense one. In this case, the radial displacement vectors appear to be sub-vertical near the cone face when the cone reaches the interface (see Figure 7.19e and Figure 7.20e).

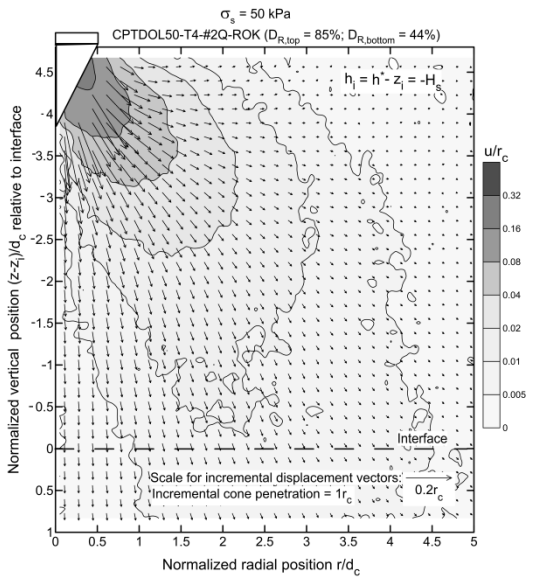
σs = 50 kPa
CPTDOL50-T4-#2Q-ROK (DR,top = 85%; DR,bottom = 44%)
hi = h* - zi = -Hs
Interface
Scale for incremental displacement vectors:
Incremental cone penetration = 1rc
0.2rc
u/rc
0.32
0.16
0.08
0.04
0.02
0.01
0.005
0
Normalized vertical position (z-zi)/dc relative to interface
Normalized radial position r/dc

(a)

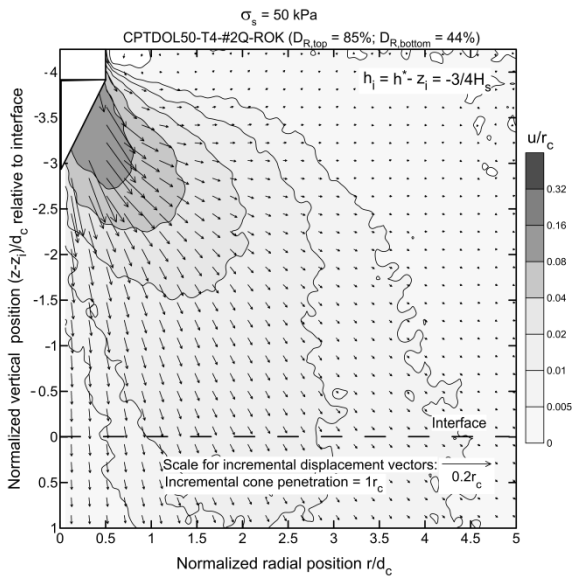
σs = 50 kPa
CPTDOL50-T4-#2Q-ROK (DR,top = 85%; DR,bottom = 44%)
hi = h* - zi = -3/4Hs
Interface
Scale for incremental displacement vectors:
Incremental cone penetration = 1rc
0.2rc
u/rc
0.32
0.16
0.08
0.04
0.02
0.01
0.005
0
Normalized vertical position (z-zi)/dc relative to interface
Normalized radial position r/dc

(b)

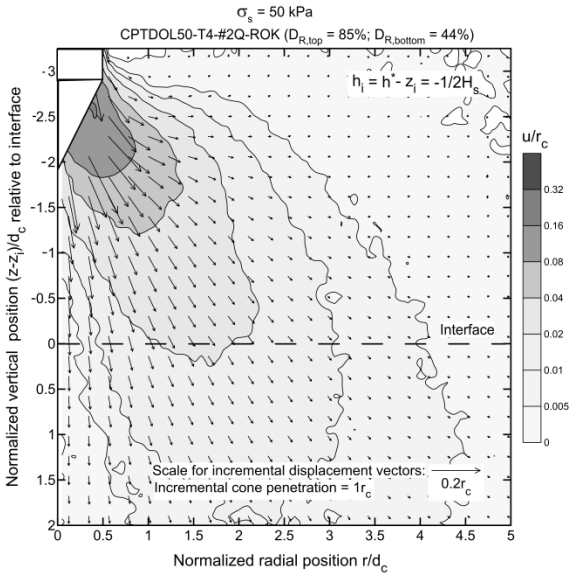
σs = 50 kPa
CPTDOL50-T4-#2Q-ROK (DR,top = 85%; DR,bottom = 44%)
hi = h* - zi = -1/2Hs
Interface
Scale for incremental displacement vectors:
Incremental cone penetration = 1rc
0.2rc
u/rc
0.32
0.16
0.08
0.04
0.02
0.01
0.005
0
Normalized vertical position (z-zi)/dc relative to interface
Normalized radial position r/dc

(c)

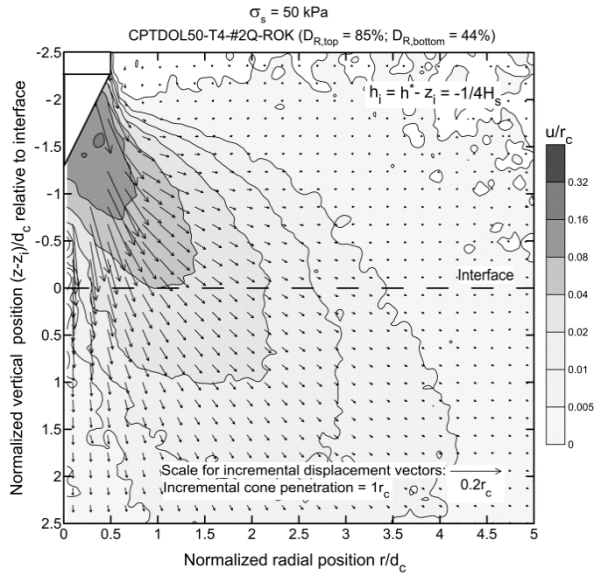
σs = 50 kPa
CPTDOL50-T4-#2Q-ROK (DR,top = 85%; DR,bottom = 44%)
hi = h* - zi = -1/4Hs
Interface
Scale for incremental displacement vectors:
Incremental cone penetration = 1rc
0.2rc
u/rc
0.32
0.16
0.08
0.04
0.02
0.01
0.005
0
Normalized vertical position (z-zi)/dc relative to interface
Normalized radial position r/dc

(d)

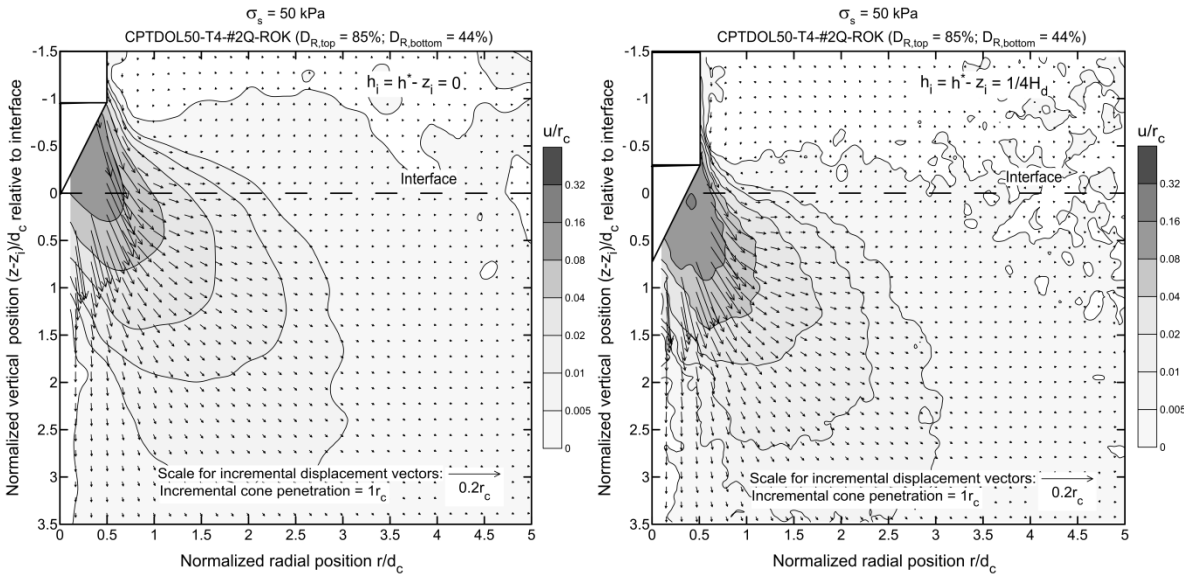
σs = 50 kPa
CPTDOL50-T4-#2Q-ROK (DR,top = 85%; DR,bottom = 44%)
hi = h* - zi = 0
Interface
u/rc
0.32
0.16
0.08
0.04
0.02
0.01
0.005
0
Scale for incremental displacement vectors:
Incremental cone penetration = 1rc
0.2rc
Normalized vertical position (z-zi)/dc relative to interface
Normalized radial position r/dc

(e)

σs = 50 kPa
CPTDOL50-T4-#2Q-ROK (DR,top = 85%; DR,bottom = 44%)
hi = h* - zi = 1/4Hd
Interface
u/rc
0.32
0.16
0.08
0.04
0.02
0.01
0.005
0
Scale for incremental displacement vectors:
Incremental cone penetration = 1rc
0.2rc
Normalized vertical position (z-zi)/dc relative to interface
Normalized radial position r/dc

(f)

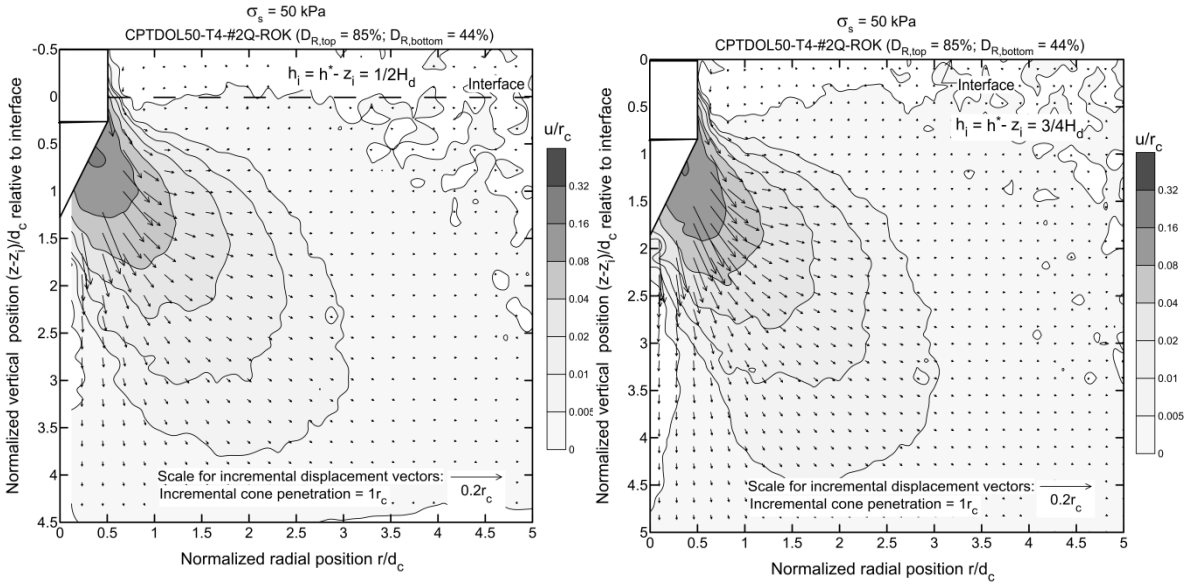
σs = 50 kPa
CPTDOL50-T4-#2Q-ROK (DR,top = 85%; DR,bottom = 44%)
hi = h* - zi = 1/2Hd
Interface
u/rc
0.32
0.16
0.08
0.04
0.02
0.01
0.005
0
Scale for incremental displacement vectors:
Incremental cone penetration = 1rc
0.2rc
Normalized vertical position (z-zi)/dc relative to interface
Normalized radial position r/dc

(g)

σs = 50 kPa
CPTDOL50-T4-#2Q-ROK (DR,top = 85%; DR,bottom = 44%)
Interface
hi = h* - zi = 3/4Hd
u/rc
0.32
0.16
0.08
0.04
0.02
0.01
0.005
0
Scale for incremental displacement vectors:
Incremental cone penetration = 1rc
0.2rc
Normalized vertical position (z-zi)/dc relative to interface
Normalized radial position r/dc

(h)

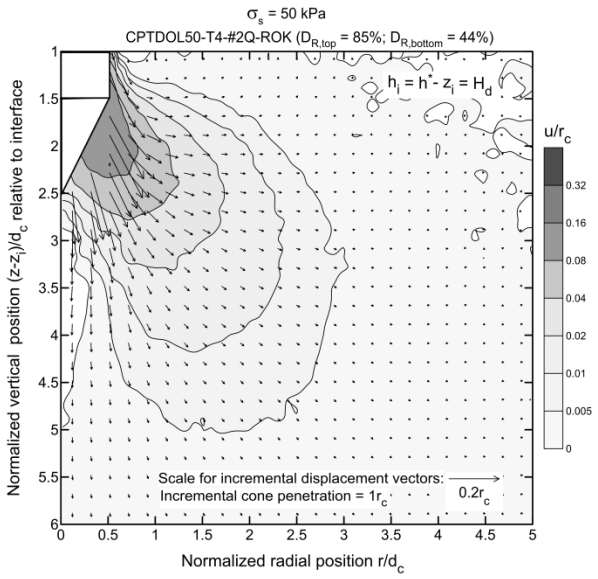

(i)

Figure 7.19 Evolution of normalized incremental radial displacement field (represented by contours) and resultant displacement (represented by arrows) after $1r_c$ incremental cone penetration at various cone penetration depths in dense-over-loose sample (CPTDOL50-T4 -#2QROK) at: (a) $h_i = -H_s$, (b) $h_i = -3/4H_s$, (c) $h_i = -1/2\ H_s$, (d) $h_i = -1/4\ H_s$, (e) $h_i = 0$, (f) a) $h_i = 1/4H_d$, (g) $h_i = 1/2H_d$, (h) $h_i = 3/4\ H_d$, and (i) $h_i = H_d$.

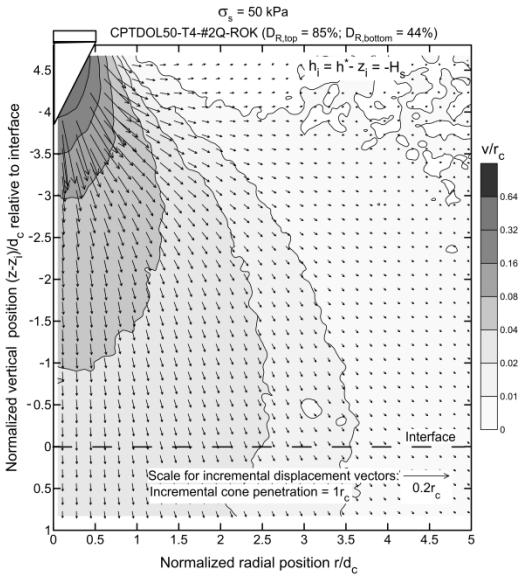
σs = 50 kPa
CPTDOL50-T4-#2Q-ROK (DR,top = 85%; DR,bottom = 44%)
hi = h* - zi = -Hs
v/rc
0.64
0.32
0.16
0.08
0.04
0.02
0.01
0
Interface
Scale for incremental displacement vectors:
Incremental cone penetration = 1rc
0.2rc
Normalized vertical position (z-zi)/dc relative to interface
Normalized radial position r/dc

(a)

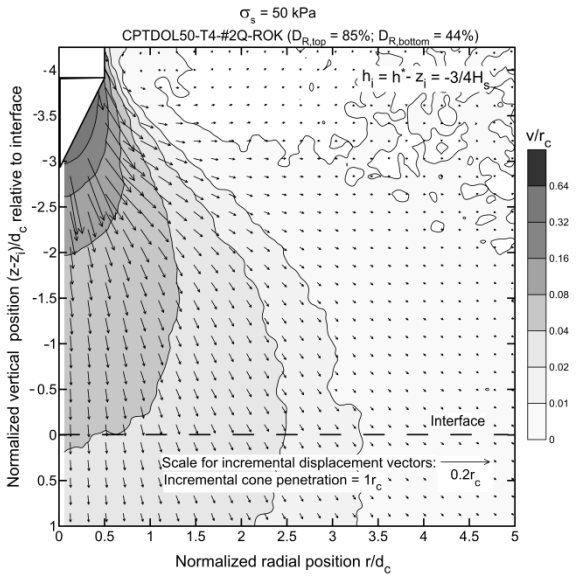
σs = 50 kPa
CPTDOL50-T4-#2Q-ROK (DR,top = 85%; DR,bottom = 44%)
hi = h* - zi = -3/4Hs
v/rc
0.64
0.32
0.16
0.08
0.04
0.02
0.01
0
Interface
Scale for incremental displacement vectors:
Incremental cone penetration = 1rc
0.2rc
Normalized vertical position (z-zi)/dc relative to interface
Normalized radial position r/dc

(b)

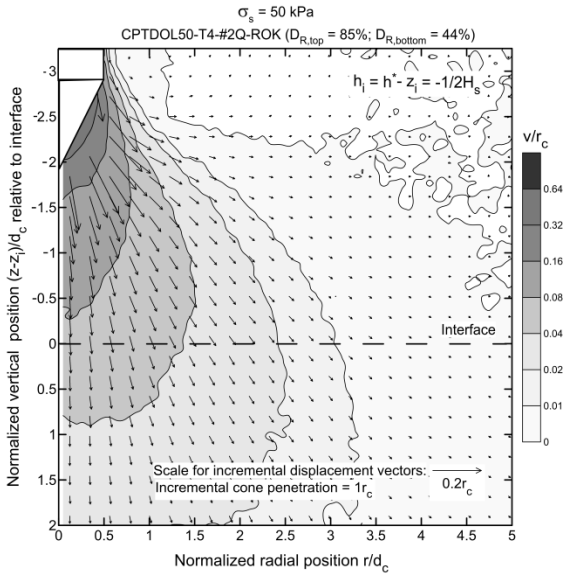
σs = 50 kPa
CPTDOL50-T4-#2Q-ROK (DR,top = 85%; DR,bottom = 44%)
hi = h* - zi = -1/2Hs
v/rc
0.64
0.32
0.16
0.08
0.04
0.02
0.01
0
Interface
Scale for incremental displacement vectors:
Incremental cone penetration = 1rc
0.2rc
Normalized vertical position (z-zi)/dc relative to interface
Normalized radial position r/dc

(c)

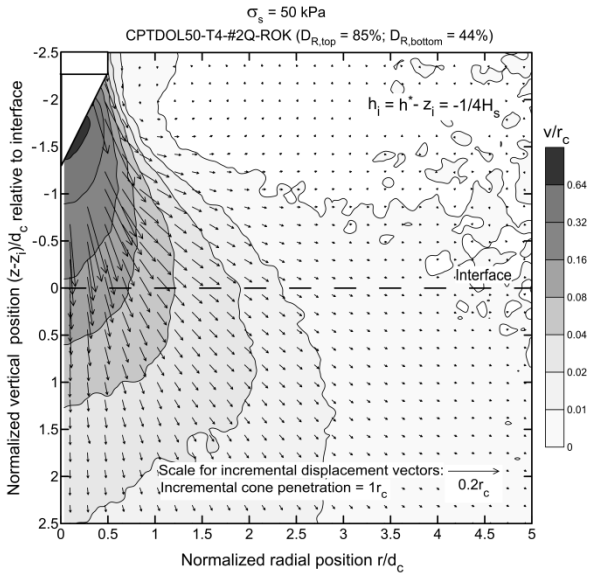
σs = 50 kPa
CPTDOL50-T4-#2Q-ROK (DR,top = 85%; DR,bottom = 44%)
hi = h* - zi = -1/4Hs
v/rc
0.64
0.32
0.16
0.08
0.04
0.02
0.01
0
Interface
Scale for incremental displacement vectors:
Incremental cone penetration = 1rc
0.2rc
Normalized vertical position (z-zi)/dc relative to interface
Normalized radial position r/dc

(d)

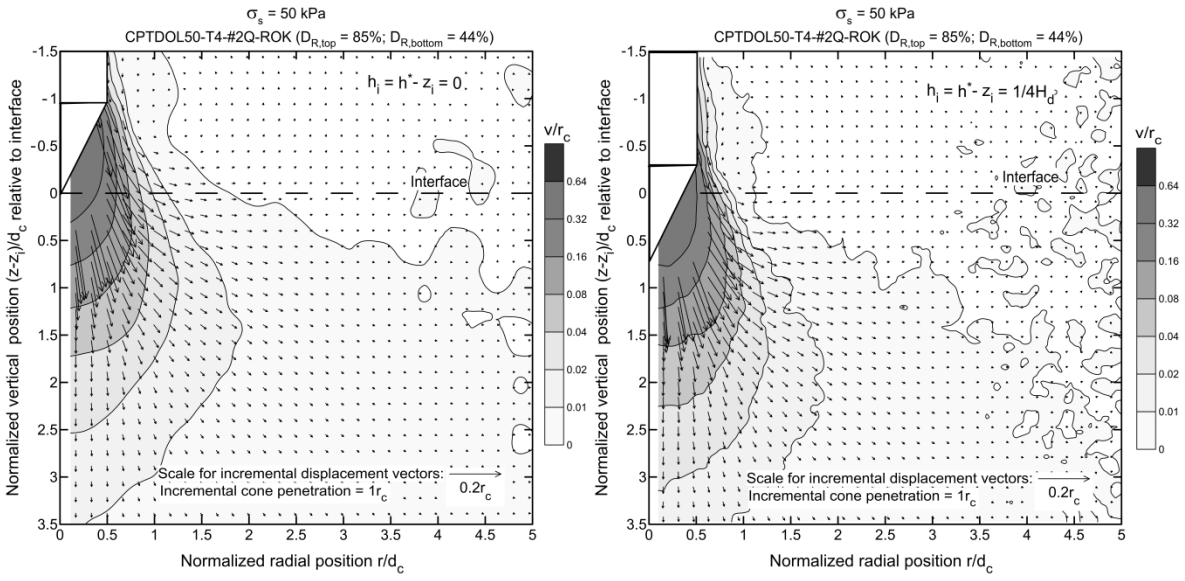
σs = 50 kPa
CPTDOL50-T4-#2Q-ROK (DR,top = 85%; DR,bottom = 44%)
hi = h*- zi = 0
Interface
Scale for incremental displacement vectors:
Incremental cone penetration = 1rc
0.2rc
v/rc
0.64
0.32
0.16
0.08
0.04
0.02
0.01
0
Normalized vertical position (z-zi)/dc relative to interface
Normalized radial position r/dc

(e)

σs = 50 kPa
CPTDOL50-T4-#2Q-ROK (DR,top = 85%; DR,bottom = 44%)
hi = h*- zi = 1/4Hd
Interface
Scale for incremental displacement vectors:
Incremental cone penetration = 1rc
0.2rc
v/rc
0.64
0.32
0.16
0.08
0.04
0.02
0.01
0
Normalized vertical position (z-zi)/dc relative to interface
Normalized radial position r/dc

(f)

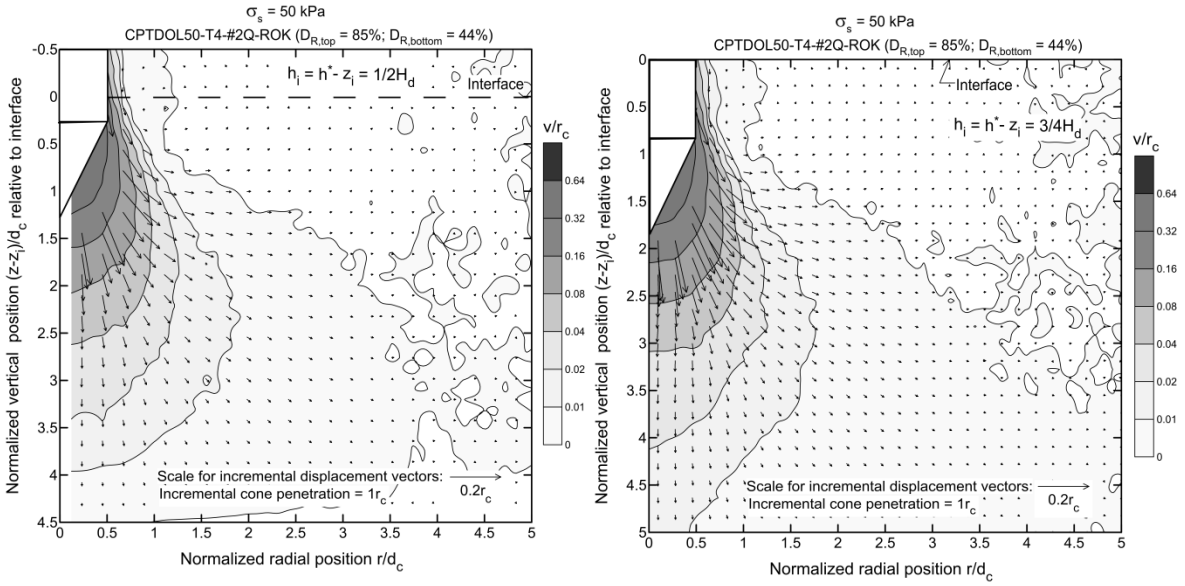
σs = 50 kPa
CPTDOL50-T4-#2Q-ROK (DR,top = 85%; DR,bottom = 44%)
hi = h*- zi = 1/2Hd
Interface
Scale for incremental displacement vectors:
Incremental cone penetration = 1rc
0.2rc
v/rc
0.64
0.32
0.16
0.08
0.04
0.02
0.01
0
Normalized vertical position (z-zi)/dc relative to interface
Normalized radial position r/dc

(g)

σs = 50 kPa
CPTDOL50-T4-#2Q-ROK (DR,top = 85%; DR,bottom = 44%)
Interface
hi = h*- zi = 3/4Hd
Scale for incremental displacement vectors:
Incremental cone penetration = 1rc
0.2rc
v/rc
0.64
0.32
0.16
0.08
0.04
0.02
0.01
0
Normalized vertical position (z-zi)/dc relative to interface
Normalized radial position r/dc

(h)

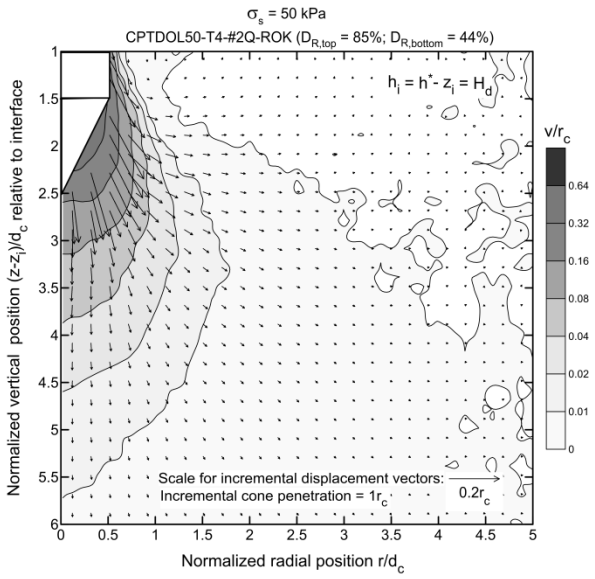

(i)

Figure 7.20.Evolution of normalized incremental vertical displacement field (represented by contours) and resultant displacement (represented by arrows) after $1r_c$ incremental cone penetration at various cone penetration depths in dense-over-loose sample (CPTDOL50-T4 -#2QROK) at: (a) h_i = -H_s, (b) h_i = -3/4H_s, (c) h_i = -1/2 H_s, (d) h_i = -1/4 H_s, (e) h_i = 0, (f) a) h_i = 1/4H_d, (g) h_i = 1/2H_d, (h) h_i =3/4 H_d, and (i) h_i = H_d.

7.6 Summary

This chapter presented results of cone penetration tests in layered sand samples. The distance from the layer interface at which the cone resistance first starts changing because of the proximity of the cone to the layer interface is referred to as the sensing distance. The distance from the layer interface at which the cone resistance ceases to be affected by the layer interface that the cone is moving away from is known as the sensing distance. The sensing and development distances were evaluated from the cone resistance profiles obtained for layered and uniform sand samples. The displacements obtained from DIC analyses for soil elements at the interface were evaluated in connection with the sensing and development distances. The radial stress at the layer interface was also measured during the tests.

CHAPTER 8. CONCLUSIONS AND RECOMMENDATIONS

8.1 Summary and Conclusions

The literature contains a limited number of experimental studies in which any attempt has been made at obtaining experimentally displacement and strain fields around a cone penetrometer in sand. Quality experimental work for the validation of large-deformation, large-displacement, large-rotation problems like the cone penetration problem. Some studies restrict themselves to plane strain boundary conditions, others are influenced by non-negligible scale effects or sand intrusion during deep penetration. Therefore, the main objective of this study was to observe the displacement field during cone penetrometer advancement through soil under realistic conditions and collect reliable, high-quality data that could be used for validation of theoretical results when these become available. For this purpose, a new experimental methodology with suitable testing facility was needed.

A half-circular calibration chamber was designed and developed to allow the observation of soil displacements as the half-circular penetrometer moves through the soil specimen. A dedicated digital image acquisition system, consisting of three machine vision digital cameras, frame grabbers and host PC was acquired. A specifically half-circular bladder was developed for applying different stress boundary conditions on the sand model. A half-circular penetrometer with 60° half-conical tip with 10-kN load cell was developed for the tests. A special Cam-follower roller and precise jack positioning system were developed to overcome the challenge of sand intrusion. The developed testing facility is extremely useful, enabling the study of various complex boundary-value problems, such as the CPT, axial and lateral loading of single piles and pile groups.

The soil displacements were deduced from digital image correlation (DIC); in some parametric analyses, particle image velocimetry (PIV) was also used. The DIC analysis was performed using a commercial software, VIC-2D, and EDPIV was used for the PIV analyses. The improved accuracy in displacement measurements was obtained by manually coloring the test sand in bulk.

Apart from the #2Q-ROK silica sand used as the main test sand, trial testing was also performed with four other silica sands. A series of 13 tests were performed in uniform sand test samples prepared at different densities (i.e., dense, medium dense and loose sands) in order to compare the effect of density on the soil displacements. The effect of surcharge was also studied by conducting three tests at low confinement level.

A series of 11 tests were performed in layered sand specimens in order to investigate the effect of layering on cone penetration resistance. During all tests, the jacking load and the penetrometer tip load were measured along with radial stress measurements at layered interfaces in few tests.

The conclusions drawn from the present thesis can be summarized as follows:

1. The crushability of sand influences the penetration resistance and associated slip pattern during the cone penetration process. The more crushable the sand, the the less the penetration resistance. Crushing affects the extent and magnitude of displacements, strains and rotations in the soil.
2. Four distinct zones were identified around the cone tip. Immediately below the cone tip, the displacement vectors were nearly vertical, while further away from it, the displacement vectors had a larger radial component. This is largely consistent with the coupling of a cavity expansion analysis with a separate analysis to handle the intense stress rotation observed around the cone to calculate cone resistances for a given soil state. In the zone just below the cone, the incremental displacement vectors were mostly sub-vertical for the least crushable sand, while they were mostly vertical for the most crushable sand.
3. A very thin, crushed particle band of thickness equal to about $2.5D_{50}$ formed at the interface with the cone surface due to intense shearing and particle crushing below the cone. This thin particle band was surrounded by a $4D_{50}$-thick band

consisting of moderately crushed sand particles. A transition zone, where the incremental displacement vectors rotated from approximately vertical to radial orientations, was also observed. A drop of radial stress was observed for elements to the side of the cone path after the cone moved down below the elevation of the elements.

4. Crushability played a clear role in the geometry of the displacement field. Greater crushability causes steep displacement vectors near and below the cone and produce sharper transitions to radial displacements in the outer zone in the soil. The magnitude of the radial incremental displacement vectors in this outer zone decreased and that of the vertical incremental displacement vectors near the cone increased with increasing particle crushing. This suggests that deformation gets more localized near the cone in crushable sand. At shallow penetration, these differences are sharp for sands with different crushability; for deep penetration, every sand crushes, and the differences are less pronounced.
5. The strain paths of soil elements located at various distances from the penetration axis have some notable features, defining four different stages of complex loading patterns observed during cone penetration. There is initially vertical compression together with radial extension. That is followed by deformation generally consistent with a cavity expansion process, during which compressive radial strains increase substantially. On further cone penetration there is some radial relaxation and then stability, as the cone reaches a depth at which it no longer affects the soil element. These deduced strain paths cane be used for validation and calibration of soil models and theoretical solutions.
6. A complex volumetric behavior is observed along the cone penetration axis and immediately below the tip, involving contraction due to particle crushing. The dilation zone is relatively small in loose sand.
7. The sensing and development distances are tied to the stiffness of the upper and lower layers. In general, the cone can sense the underlying layer earlier in denser soil than in less dense soils. The cone resistance in the underlying layer ceased being affected by the overlying layer earlier in looser than in denser layers. The

results from pressure transducers and DIC analysis showed that elements at the soil interface actually sense the penetrating cone earlier than the cone s the interface, which can be interpreted as the cone resistance being overwhelming affected by the response of soil very close to the cone.

8. In design of piles or interpretation of CPT results, it is important to know the values of the sensing and development depths. Values were provided based on the tests performed. Consideration of sensing and development distances together enables one to establish the resolution of CPT results (meaning the thinner layer detectable by a cone penetrometer), which, in sand, based on the results obtained in the present research, is of the order of 2.6 to 4.4 cone diameters.

8.2 Recommendations for Future Research

This dissertation investigated the displacement field during model half-circular cone penetration in uniform and layered sand profiles in a half-circular calibration chamber using DIC technique. Building on this, there are several areas where future work can be undertaken. Some recommendations for future research are suggested as follows:

1. The penetration tests should be conducted in conjunction with stress measurement in the sand mass, in order to have complete insights into the CPT boundary value problem experimentally. For that, location-based stress sensors with specific calibration can be used. The data on displacement paths presented in this work can be utilized for sensor calibration, which must account for movement of the sensor. The measured stress and strains obtained from DIC can be utilized to validate theoretical models.
2. The evolution of sand fabric and crushability can be observed by image analysis of test images acquired using the digital-hand held microscope or zoomed lenses, during the loading and installation of the model penetrometer. The use of a solidifying agent can also be incorporated for recovery of samples for microscopic observations and validating the image analysis results.

3. The effect of installation methods on influence zones below the penetrometer/model pile in the multilayered soil profile should be studied. These tests should also be verified in circular calibration chamber involving different installation methods.
4. The interface zone behavior under cyclic and monotonic loading can be studied with the use of close-up images in order to obtain reliable data for theoretical element test validations. The model penetrometers with different surface roughness should also be used to investigate the effect of surface roughness on interface zone behavior.
5. Experimental work can be carried out with different model penetrometers, such as half-circular open ended pipe pile, half-H pile, etc., to study the plugging behavior and installation of open-ended piles.

LIST OF REFERENCES

LIST OF REFERENCES

Abdel-aziz I., Y., & Karara M., H. (1971). *Direct linear transformation from comparator coordinates into object space coordinates in close-range photogrammetry*. Proceeding of Symposium on close-range photgrammetry, Urbana, Illinois,1-18.

Ahmadi, M. (2000). *Analysis of Cone Resistance in Sand.* PhD Thesis, The University of British Columbia.

Ahmadi, M. M., & Robertson, P. K. (2005). Thin-layer effects on the CPT q_c measurement. *Canadian Geotechnical Journal*, *1317*(42), 1302–1317.

Ahmadi, M. M., & Robertson, P. K. (2008). A Numerical Study of Chamber Size and Boundary E ects on CPT Tip Resistance in NC Sand. *Scientia Iranica*, *15*(5).

Allersma, H. G. B., & Broere, W. (2002). Optical Analysis of Stress around a Penetrating Probe in Granular Material. In *Physical Modeling in Geotechnics* (pp. 149–54). Swets and Zeitlinger.

Balachowski, L. (2007). Size effect in centrifuge cone penetration tests. *Archives of Hydro-Engineering and Environmental Mechanics*, *54*(3), 161–181.

Baligh, M. M. (1985). Strain path method. *Journal of Geotechnical Engineering Division, ASCE*, *111*(9), 1109–1135.

Berg, P. van den. (1994). *Analysis of soil penetration*. Phd Thesis, Delft University.

Berg, P. Van Den, Borst, R. De, & Huetink, H. (1996). An Eulerean Finite Element Model. *International Journal for Numerical and Anaylytical Methods in Geomechanics*, *20*(January 1995), 865–886.

Bolton, M. D. (1986). The strength and dilatancy. *Geotechnique*, *36*(1), 65–78.

Brandon, T. L., & Clough, G. W. (1991). Methods of sample prepration in Verginia Tech Calibration Chamber. In *Proc. 1st Int. Symp. on Penetration Testing* (pp. 119–133).

Collins, I. F., Pender, M. J., & Yan, W. (1992). Cavity expansion in sands under drained loading conditions. *Int. J. Numer. Analyt. Meth. Geomech.*, *16*, 3–23.

Committee, B. C. P. (1971). Field tests on piles in sand. *Soils and Foundations*, *11*(2), 29–49.

Correlated Solutions. (2009). VIC-2D. Retrieved from http://www.correlatedsolutions.com/index.php/products/vic-2d

D.J.M., N.-T., Cheng, X. H., van Nes, J., & Zitha, P. L. J. (2005). Application of x-ray computed tomography to cone penetartion tests in sands. In *GSP 138 Site Characterization and Modeling* (pp. 1–12).

D6913-04, A. S. (2013). Standard Test Methods for Particle-Size Distribution of Soils Using Sieve. In *Annual book of ASTM standards* (Vol. 04).

Danziger, F. A. B., & Janeiro, R. De. (2012). Rate Effect on Cone Penetration Test in Sand. *Geoetchnical Engineering Journal of the SEAGS & AGSSEA*, *43*(4), 72–80.

Davis, R. O., & Selvadurai, A. P. S. (1996). *Elasticity and Geomechanics*. Cambridge University Press.

De Pater, C. J., & Nieuwenhuis, J. D. (1987). Method for measuring the deformations of a sand surface. *Geotechnique*, (April), 581–585.

Durgunoglu, H. T., & Mitchell, J. K. (1976). Static penetration resistance of soils. I: Analysis. In *Proceedings of the ASCE Specialty Conference on In-Situ Measurement of Soil Properties* (Vol. 1, pp. 151–171). New York: ASCE.

Foray, P. (1991). Scale and Boundary effects on calibration chamber pile tests. In A.-B. Huang (Ed.), *First International Symposium on Calibration Chmaber TestingCalibration Chamber Testing* (pp. 147–160). Elsevier.

Gavin, K. G., & Kelly, B. C. O. (2007). Effect of Friction Fatigue on Pile Capacity in Dense Sand. *Journal of Geotechnical and Geoenvironmental Engineering Engineering Research*, *133*(1), 63–71.

Ghionna, V., & Jamiolkowski, M. (1991). A critical apraisal of calibration chamber testing of sands. In *Proc., 1st Int. Symp. on Calibration Chamber Testing* (pp. 13–39). New York: Elservier.

Gui, M. W., Bolton, M. D., Garnier, J., Corte, J. F., Bagge, G., Laue, J., & Renzi, R. (1998). Guidelines for cone penetration tests in sand. In *Centrifuge 98* (pp. 155–160). Balkema.

Gui, M. W., Laue, J., Renzi, R., Garnier, J., Bolton, M. D., Bagge, G., & Corte, J. F. (1999). Centrifuge cone penetration tests in sand. *Géotechnique*, *49*(4), 543–552.

Gupta, R. C. (1992). Finite Strain Analysis For Deep Cone Penetration. *Journal of Geotechnical Engineering*, *117*(10), 1610–1630.

Hardin, B. O. (1985). Crushing of soil particles. *Journal of Geotechnical Engineering ASCE*, *111*, 1177–1192.

Heerema, E. P. (1980). Predicting pile driveability: heather as an illustration of the friction fatigue theory. *Ground Engineering*, *13*(Apr), 15–37.

Heikkilä, J., & Silvén, O. (1997). A Four-step Camera Calibration Procedure with Implicit Image Correction. *IEEE Transactions on Pattern Analysis and Machine Intelligence*, *22*(10), 1066–1077.

Houlsby, G. T., Evans, K. M., & Sweeney, M. A. (1988). End bearing capacity of model piles in layered carbonate soils. In *Engineering for Calcareous Sediments* (pp. 209–214).

Huang, A.-B., Ma, M. Y., & Lee, J. S. (1993). A micromechanical study of penetration tests in granular material. *Mechanics of Materials*, *16*(1-2), 133–139.

Huang, A.B. and Hsu, H. . (2011). Cone penetration tests under simulated field conditions. *Geotechnique*, *55*(5), 345–354.

Jardine, R., Chow, F., Overy, R., & Standing, J. (2005). *ICP design methods for driven piles in sands and clays* (pp. 15–26).

Kobayashi, T., & Fukagawa, R. (2003). Characterization of deformation process of CPT using X-ray TV imaging technique. *Deformational Characteristics of Geomaterial*, *180*, 43–47.

Lehane, B. M. (2012). Relating foundation capacity in sands to CPT q c. In *ISC 4* (pp. 63–81).

Lehane, B. M., & Gill, D. R. (2004). Displacement fields induced by penetrometer installation in artificial soil. *IJPMG*, *1*, 25–36.

Lehane, B. M., Jardine, R. J., Bond, a. J., & Frank, R. (1993). Mechanisms of Shaft Friction in Sand from Instrumented Pile Tests. *Journal of Geotechnical Engineering*, *119*(1), 19–35.

Lehane, B. M., Schneider, J. A., & Xu, X. (2005). The UWA-05 method for prediction of axial capacity of driven piles in sand. In *Advances in Foundations* (pp. 1–6).

Li, Y., Li, J., & Zhang, S. (2010). Model Test research on the Compaction Effect of Jacked Pile in Layered soil. In *Deep Foundations and Geotechnical In Situ Testing* (pp. 238–245).

Liu, W. (2010). Axisymmetric Centrifuge Modelling of Deep Penetration. Phd Thesis, Nottingum University.

Loukidis, D., & Salgado, R. (2008). Analysis of the shaft resistance of nondisplacement piles in sand. *Geotechnique*, *58*(4), 283–296.

Mayne, P. W., & Kulhawy, F. H. (1991). Calibration chamber database and boundary effects correction for CPT data. In *Proc., 1st Int. Symp. on Calibration Chamber Testing (ISOCCT1)* (pp. 257–264). Elsevier, Potsdam, N.Y.

Mitchell, J. K., & Soga, K. (2005). Soil Composition and Engineering Properties. In *Fundamentals of Soil Behaviour* (3rd ed., pp. 83–108). John Wiley & Sons.

Ni, Q., Hird, C. C., & Guymer, I. (2010). Physical modelling of pile penetration in clay using transparent soil and particle image velocimetry. *Géotechnique*, *60*(2), 121–132.

Pan, B. (2010). Recent Progress in Digital Image Correlation. *Experimental Mechanics*, *51*(7), 1223–1235.

Pan, B., Qian, K., Xie, H., & Asundi, A. (2009). Two-dimensional digital image correlation for in-plane displacement and strain measurement: a review. *Measurement Science and Technology*, *20*(6), 062001.

Pan, B., Xie, H., Guo, Z., & Hua, T. (2007). Full-field strain measurement using a two-dimensional Savitzky-Golay digital differentiator in digital image correlation. *Optical Engineering*, *46*(3), 033601.

Paniagua, P., Andò, E., Silva, M., Emdal, A., Nordal, S., & Viggiani, G. (2013). Soil deformation around a penetrating cone in silt. *Géotechnique Letters*, *3*(4), 185–191.

Parkin, A. K., & Lunne, T. (1982). Boundary effects in the laboratory calibration of a cone penetrometer for sand. In *Proc. 2nd Euro. Symp. on Penetration Testing* (pp. 761–767). Amsterdam.

Porcino, D., Fioravante, V., Vn, G., & Pedroni, S. (2003). Interface Behavior of Sands from Constant Normal Stiffness Direct Shear Tests. *Geotechnical Testing Journal*, *26*(3), 1–13.

Pournaghiazar, M., Khalili, N., & Russell, a. R. (2012). Linking cone penetration resistances measured in calibration chambers and the field. *Géotechnique Letters*, *2*(April-June), 29–35.

Rad, N. S., & Tumay, M. T. (1987). Factors Affecting Sand Specimen Preparation by Raining. *Geotechnical Testing Journal*, *10*(1), 31–37.

Randolph, M. F., Dolwint, J., & Beck, R. (1994). Design of driven piles in sand. *Geotechnique*, *44*(3), 427–448.

Robinsky, E. I., & Morrison, C. F. (1964). Sand displacement and compaction around piles. *Canadian Geotechnical Journal*, *1*(2), 81–93.

Salgado, R. (1993). *Analysis of penetration resistance in sands*. *Civil and Environmental Engineering*. University of California, Berkeley, Berkeley.

Salgado, R. (2002). CONPOINT Beta Version : User's Manual, A Cavity Expansion Analysis Program for the Determination of Cone Penetration Resistance and Cavity Limit Pressure.

Salgado, R. (2008). *The Engineering of Foundations* (p. 888). McGraw-Hill.

Salgado, R. (2013). The mechanics of cone penetration : Contributions from experimental and theoretical studies. In *International Conference on Geotechnical and Geophysical Site Characterization, ISC-4* (pp. 131–153).

Salgado, R. (2013). The mechanics of cone penetration: Contributions from experimental and theoretical studies. In *Geotechnical and Geophysical Site Characterization 4 - Proceedings of the 4th International Conference on Site Characterization 4, ISC-4* (Vol. 1, pp. 131–153).

Salgado, R., Mitchell, J. K., & Jamiolkowski, M. (1997). Cavity expansion and penetration resistance in sands. *Journal of Geotechnical and Geoenvironmental Engineering*, *123*(4), 344–354.

Salgado, R., & Prezzi, M. (2007). Computation of cavity expansion pressure and penetration resistance in sands. *International Journal of Geomechanics*, *7*(4), 251–265.

Salgado, R., & Randolph, M. F. (2001a). Analysis of cavity expansion in sand. *International Journal of Geomechanics*, *1*(2), 175–192.

Salgado, R., & Randolph, M. F. (2001b). Analysis of Cavity Expansion in Sand. *The International Journal of Geomechanics*, *1*(2), 175–192.

Salgado, R., Mitchell, J.K. and Jamiolkowski, M. (1998). Calibration Chamber Size Effects on Penetration Resitance in Sand. *Journal of Geotechnical and Geoenvironmental Engineering*, *124*(9), 878–887.

Salma, C. C., Theurer, C., & Henriksen, S. W. (1980). *Manual of Photogrammetry* (Fourth., pp. 172–270).

Schnaid, F., & Houlsby, G. T. (1991). An assessment of chamber size effects in the calibration of in situ tests in sand. *Géotechnique*, *41*(3), 437–445.

Sutton, M. A., Orteu, J., & Schreier, H. W. (2009). *Image Correlation for Shape, Motion and Deformation Measurements*. Boston, MA: Springer US.

Susila, E., & Hryciw, R. D. (2003). Large displacement FEM modelling of the cone penetration test (CPT) in normally consolidated sand. *International Journal for Numerical and Analytical Methods in Geomechanics*, *602*(January), 585–602.

Taylor, R. N. (1995). Centrifuge in Modelling: Principal and Scale Effects. In R. N. Taylor (Ed.), *Geotechnical Centrifuge Technology* (First., pp. 19–33). Champan& Hall.

Teh, C. I. (1987). *An Analytical Study of Cone Penetration Test*. Phd Thesis, University of Oxford.

Tolooiyan, a., & Gavin, K. (2011). Modelling the Cone Penetration Test in sand using Cavity Expansion and Arbitrary Lagrangian Eulerian Finite Element Methods. *Computers and Geotechnics*, *38*(4), 482–490.

Uesugi, M., & Kishida, H. (1987). Tests of the interface between sand and steel in the simple shear apparatus. *Géotechnique*, *37*(1), 45–52.

Vesic, A. S. (1972). Expansion of cavities in infinite soil mass. *J. Soil Mech. Found. Div., ASCE, March*, 265–290.

Vreugdenhil, R., Davis, R. O. B., & Berrill, J. (1994). Interpretation Of Cone Penetration Results In Multilayered Soils, *18*(November 1993), 585–599.

Wereley, S. T. (2010). PIV Course Notes ME-575.

Wereley, S. T., & Gui, L. (2003). A correlation-based central difference image correction (CDIC) method and application in a four-roll mill flow PIV measurement, *34*, 42–51.

Wesley, L. D. (2011). Interpretation of calibration chamber tests involving cone penetrometers in sands. *Geotechnique*, *52*(4), 289–293.

White, D. J. (2002). *An investigation into the behaviour of pressed-in piles*. Phd Thesis University of Cambridge.

White, D. J., & Bolton, M. D. (2004). Displacement and strain paths during plane-strain model pile installation in sand. *Géotechnique*, *54*(6), 375–397.

White, D. J., Take, W. A., & Bolton, M. D. (2003). Soil deformation measurement using particle image velocimetry (PIV) and photogrammetry. *Géotechnique*, *53*(7), 619–631.

White, D. J., Take, W. A., Bolton, M. D., & Munachen, S. E. (1999). A deformation measurement system for geotechnical testing based on digital imaging , close-range photogrammetry , and PIV image analysis. In *15th International Conference on Soil Mechanics and Geotechnical Engineering* (pp. 539–542). Istanbul, Turkey.

XU, X. (2007). Investigation of the End Bearing Performance of Displacement Piles in Sand. Phd Thesis, The University of Western Australia.

Xu, X., & Lehane, B. M. (2008). Pile and penetrometer end bearing resistance in two-layered soil profiles. *Géotechnique*, *58*(3), 187–197.

Yang, J. (2006). Influence Zone for End Bearing of Piles in Sand. *Geotechnical and Geoenvironmental Engineering*, *132*(September), 1229–1237.

Yasufuku, N., & Hyde, A. F. L. (1995). Pile end-bearing capacity in crushable sands. *Geotechnique*, *45*(4), 663–676.

Yu, H. S., & Carter, J. P. (2006). Rigorous Similarity Solutions for Cavity Expansion in Cohesive-Frictional Soils, *2*(2), 233–258.

Yu, H. S., Falagush, O., & Mcdowell, G. R. (2012). A particle refinement method for simulating DEM of cone penetration testing in granular materials. *Géotechnique Letters*, *2*(July-September), 141–147.

Yu, H. S., & Houlsby, G. T. (1991). Finite cavity expansion in dilatant soils: Loading analysis. *Geotechnique*, *41*(2), 173–183.

Yu, H.S. and Mitchell, J. K. (1998). Anaylsis of Cone Resistance: Review of Methods. *Geotechnical and Geoenvironmental Engineering*, *124*(2), 140–149.

Zhu, B. T., Jardine, R. J., Tsuha, C. H. C., Foray, P., & Yang, Z. X. (2010). Sand grain crushing and interface shearing during displacement pile installation in sand. *Géotechnique*, *60*(6), 469–482.

VITA

VITA

Mazhar Iqbal Arshad was born in Sahiwal formely Montgomery, Pakistan. After his high school education, he joined the Pakistan Army as technical cadet in Military College of Engineering in April, 1991. He obtained his Bachelor of Science in Civil Engineering from the Military College of Engineering, and was awarded Army Chief of Staff Gold medal on excellence performance in the undergraduate study. After obtaining military training at Paksitan Military Academy, he was commissioned in the Pakistan Army Corps of Engineers as a Lieutenant in 1995. He served in various command, staff positions in the Military including Grade-III Operational Staff in an Infantry Brigade. He was seconded abroad on deputation to take part in the United Nations Peace Keeping Mission in Sierra Leone (UNAMSIL) in 2004. He took active part during rescue and rehabilitation pahses of 2005 Earthquake in Pakistan. He also served as garrison engineer, in Pakistan Navy during construction and operatons of deep sea-port Gawadar. After being awarded a competitive scholarship for graduate studies abroad from the Pakistan Army, Mazhar joined Purdue University's School of Civil Engineering in 2007, where he received his Master's Degree in 2009 before continuing towards a Ph.D.

Mazhar is married to Farhat Sultana, and has a son, Mustafa. At present, he holds the rank of Major in the Pakistan Army, posted to Military College of Engineering as a Instructor. He will continue to serve his country, in the Army, after receiving his doctoral degree.